CRANFIELD UNIVERSITY

HENRY OBEDIAH AGU

THE EFFECT OF 3D PRINTED MATERIAL PROPERTIES ON SHAPED CHARGE LINER PERFORMANCE

CRANFIELD UNIVERSITY
Defence and Security

PhD
Academic Year: 2016 - 2019

Supervisor: Professor Amer Hameed
Associate Supervisor: Dr Gareth Appleby-Thomas
September 2019

CRANFIELD UNIVERSITY

CRANFIELD UNIVERSITY

Defence and Security

PhD

Academic Year 2016 - 2019

HENRY OBEDIAH AGU

The effect of 3D printed material properties on shaped charge liner performance

Supervisor: Professor Amer Hameed

Associate Supervisor: Dr Gareth Appleby-Thomas

September 2019

This thesis is submitted in partial fulfilment of the requirements for the degree of PhD

ABSTRACT

Shaped charges operate by explosively loading a (typically metallic) liner to produce a jet travelling at extremely high velocity (9-12 km/s). Such explosive loading involves highly non-linear transient phenomena. As such, a very wide range of physical processes must be considered to enable accurate characterisation of such events – with material behaviour within these (pressure / strain-rate) regimes providing insight into problems ranging from shaped charge performance itself through to formation of new material phases at high pressures. Unlike other high strain impact events, the shaped charge phenomenon results in hydrodynamic material flow of the liner which is an integral aspect of the shaped charge design. As such, the study of shaped charge liners has been the subject of numerous scientific research studies for over 50 years since its discovery. When explosively loaded, the liner is stretched extensively during their elongation to form a jet. The jet length depends on the ductility of the liner material, and this is strongly linked to the microscopic crystal structure, which depends on the original material properties and the processes used to produce the liners.

There are several processes currently used for liner production. This thesis outlines the different liner production techniques, their advantages/disadvantages and explores the potential of employing additive manufacturing (3D printing) technique for shaped charge liner production. As 3D printed parts are being considered as a possible replacement for conventionally processed parts, this PhD work fits into this long-term vision; with built parts compared in density and mechanical strength to their bulk material equivalents. More so, 3D printing is shown to present some potential benefits for the production of efficient liners including high precision, cost-effectiveness and the potential to realise customized geometries. The use of fine powders may also allow alternative microstructures to be produced with potentially interesting results. This element of the study forms the first part of this thesis, aimed at investigating the mechanism elucidating the performance of 3D printed liners processed through

direct metal laser sintering process (selective laser sintering) and filament deposition modelling processes (Polylactic Acid).

The next part of this work provided additional insights on the additive manufactured processed employed through investigation of the dynamic behaviour of polylactic acid, employed in the filament deposition modelling process and static (optical and scanning micrographs) observation of the laser sintered liners in their as - manufactured and deformed state, in comparison with traditional machined liners. Autodyn 2D numerical hydrocode was employed to understand how temperature influences the deformation pattern (grain refinement); providing new insights on liner deformation.

Finally, a novel computational technique to determine the Virtual Origin of shaped charges was developed to provide a ready route to predict more accurate SC performance.

Keywords:

Virtual origin, shell jetting analysis, microstructure, liners, additive manufacturing, jet tip velocity, copper, aluminium, filament deposition modelling, selective laser sintering, standoff distance, grain size, equation of state.

ACKNOWLEDGEMENTS

I would like to express my deepest gratitude to the Chief of the air staff, Air Marshal Abubarkar Sadique for giving me this very rare opportunity to undertake this PhD programme. I am sincerely grateful for this opportunity and will remain indebted to the service of our dear nation. I would also like to thank Professor Amer Hameed for his guidance and support. I could not have hoped for a better PhD mentor in this amazing once in a lifetime journey. Additionally, I would like to express my sincere gratefulness to Dr. Gareth Appleby-Thomas, the co-supervisor. To put it simply, my progress would have been very different if you had not been around. My special thanks to Dr. David Wood who selflessly helped me on numerous occasions without hesitation. I would also like to thank all my colleagues especially Denny Lesmana, Dan Burton, Brianna Fitzmaurice, Caitlin Gilroy, and Alabri Mohammed for being great friends. Professor Ian Horsefall is appreciated for his advice at the beginning of the programme. I would like to thank Adrian Musty, John Painter, Karl Norris and Col Liz for their assistance at different stages of the research.

Finally, I would like to thank my lovely wife, Praise Adaeze Agu for her immense support and to our wonderful kids; Success, Samuel and Jeremy, you have all contributed in making my stay great fun. My Mother, Mrs Felicia Agu is specially appreciated for her prayers and counsel throughout the period.

Above all, I would like to express my deepest gratitude to God Almighty for his divine guidance in my life, family and career.

TABLE OF CONTENTS

LIST OF FIGURES

LIST OF TABLES

LIST OF EQUATIONS

1 General Introduction

1.1 Research background

High value well-protected targets are defeated by applying kinetic energy that overmatches the critical limit of such targets. The shaped charge is an effector, designed primarily to enhance the effects of explosive charges by focusing the resultant detonation to facilitate disruption of targets (ranging from oil-bearing strata in the oil exploration industry through to high-density targets such as armour in the defence sphere). When a shaped charge is initiated, the resultant detonation wave from the high explosive accelerates the liner rapidly resulting in the formation of high velocity jet travelling with a tip velocity of around 9-12 km/s accompanied by a slower moving slug with a velocity of less than 2 km/s. The hypervelocity jet is oftentimes directed to penetrate high density materials, ranging from armour to rocks or oil well strata in the defence and commercial industries, respectively. The penetration depth is usually employed as a measure of performance and achieving greater penetration is one of the primary objectives of every shaped charge designer.

The shaped charge comprises of a high explosive, detonator and a conical liner (other shapes are available) housed in a casing. Wave-shapers are occasionally employed to improve the angle at which the detonation wave impacts the liners with the overall aim of improving penetration. A lot of effort has been put into improving shaped charge performance over the years by varying one or more of the parameters both independently and collectively. For example, the effect of various explosive types, liner material, and casing amongst others have been investigated. Critical among these parameters is the liner because of the crucial role it plays in the jet formation process. Upon detonation, the liner collapses and is squeezed out under intense pressure to form the jet. As such, any design inaccuracies, eccentricity or asymmetry in the liner micro or macro structure is amplified.

For optimal liner performance, a number of factors, such as quality of the raw material, homogeneity, and microstructure have to be considered. The resultant liner microstructure has been correlated to the processing technique employed and several liner production techniques have been investigated, for example, machining, wire drawing, cold forging, powder metallurgy, etc. Although these techniques have been employed extensively in the production of shaped charge liners, they have been fundamentally shown to present some disadvantages ranging from poor microstructure, high cost of production, liner dimensional inaccuracies as well as asymmetries. For example, traditional machined liners have a poor crystal structure and using this approach, it is extremely difficult to fabricate liners from high density materials such as Tungsten and Tantalum (such materials have an inherent advantage in terms of resultant penetration efficiency).

The first part of this thesis explored the possibility of employing additive manufacturing technique, commonly referred to as 3D printing, for the production of shaped charge liners. This technique may present a viable alternative considering its potential of producing parts with density comparable to the theoretical maximum density and mechanical strength of the original material. Aside from its ability to process high density material with ease, the process is relatively cheap when larger quantities are required and capable of fabricating liners with complex geometries, with little or no material wastage. In this thesis, two different additive manufacturing techniques were explored; the selective laser sintering (SLS) technique and the filament deposition modelling (FDM) technique using aluminium and copper cones (typical of shaped charge liner materials). Both static (microscopic) and dynamic (flash X-ray) analysis were employed to investigate the characteristics of the liners produced. A numerical hydrocode, ANSYS Autodyn 2D, which has been validated in previous work was revalidated here by firing 50 mm Charge Diameter (CD) shaped charges into steel targets at a stand-off of 3 CDs. Optical micrographs were employed to underpin interpretation of the mechanism elucidating their resultant performance with further insight gained through a detailed metallurgical study of the initial (liner)

and ending (slug) microstructure of the laser sintered liner. Plate impact experiments were also conducted to develop an Equation-of-State for the polylactic acid employed in the FDM process with the aims of both enhancing understanding of this core material in the dynamic regime and also ensuring more accurate numerical simulations via use of real-world materials data.

Finally, the second part of the thesis was focused on developing a novel technique for simplifying the onerous task of determination of the virtual origin of shaped charges. This was necessary to improve the accuracy of predicted penetration depth when employing the Allison and Vitalli analytical formulae for determination of the VO position in shaped charges without the use of cost intensive experimental technique.

Together, these two elements of the thesis provide a unique set of tools to enable rapid design, development and manufacture of optimised shaped charge systems.

1.2 Organisation of the thesis

The thesis is written in paper format with each chapter forming an entire paper; some of which (3 chapters) has already been published in appropriate peer-reviewed academic journals (International Journal of Impact Engineering and Journal of Dynamic Behaviour of Materials – chapters 6, 7 and 8) attached at Appendixes 1,2 and 3. In order to provide an appropriate background, chapter 2 (which is further described below) was included to give an overall description of shaped charges along with a review of the important literature in this area. A brief overview of the focus of chapters 2 to 10 is presented below.

- **Chapter 2 – Literature Review**: In chapter 2, some basic concepts of shaped charges are introduced including the principle underlying jet formation, particulation and penetration. Factors that influenced the performance of shaped charges are then outlined. The various liner manufacturing processes and their effect on the jet performance are also discussed, highlighting the advantages and disadvantages of each

technique. The use of additive manufacturing is introduced, hypothesised and discussed – with this forming the basis of the subsequent research work. Some key analytical models detailing jet formation and penetration are also introduced.

- **Chapter 3 – Numerical Method and Parametric Study**: An overview of the numerical hydrocode, ANSYS Autodyn 2D employed in the numerical study was presented in chapter 3. The hydrocode was validated and mesh sensitivity study was conducted on a baseline 50 mm cone diameter shaped charge. The chapter concludes with parametric studies on the effect of environment, confinement, liner strength and head height on the performance of shaped charges.

- **Chapter 4 – Experimental Investigation of Shaped Charge Liners Produced from Selective Laser Sintering Process:** In this chapter, the feasibility of employing a selective laser sintering technique for the production of shaped charge liners is investigated. The study aims to elucidate mechanisms underpinning their resultant behaviour. Results were compared with the literature while performance was interrogated via comparison of variations in penetration depths for laser sintered and conventionally machined liners respectively, with experiments backed by hydrocode simulations. Optical examination of the produced liner microstructure provided further insight on the behaviour of the laser sintered liners. This approach highlighted the influence of ductility and porosity on jet performance.

- **Chapter 5 – Evaluation of Filament Deposition Modelling Poly-lactic acid and Copper filled Polymer Composite Liners on shaped charge performance:** Chapter 5, focuses on the feasibility of employing a PLA liner doped with copper, produced via the filament deposition modelling technique as a liner. The objective was to investigate if the addition of

copper to the PLA matrix would improve the performance of polymer for use on electromagnetic targets, with this being one of the techniques for countering this warhead type.

- **Chapter 6 – Dynamic response of dense 3 dimensionally printed Polylactic acid:** This chapter is focused on derivation of the equation of state for PLA to gain further insight into its shock behaviour. Specifically, the Hugoniot equations of state and shear strength of the material are developed employing one dimensional shock in the target. The samples employed were produced using a commercially available Ultimaker 3D printer. Both lateral and longitudinal experimental plate-impact trials were conducted, with manganin gauges used to obtain the shock parameters; Shock velocity (U_s), particle velocity (U_p), and pressure required to develop the equations of state were obtained. Comparison of the shock behaviour with other polymers, such as polyethene, PMMA and polycarbonate, was also undertaken elucidating the chemistry underpinning the shock response of PLA.

  Published at: Agu HO, Hameed A, Appleby-Thomas GJ, Wood DC. The dynamic response of dense 3 dimensionally printed polylactic acid. Journal of Dynamic Behaviour of Materials. 2019. https://doi.org/10.1007/s40870-019-00198-8.

- **Chapter 7 – Comparison of the microstructure of laser sintered and traditional machined copper liner in the hydrodynamic regime:** Here, the mechanism underpinning the behaviour of laser sintered copper liners is investigated by examining the microstructure of the slug recovered from the experimental trials presented in chapter 4. Direct optical and scanning electron microscope comparison of variations between the starting (liner) and ending (slug) materials, along with comparison to works from Murr et al., 2009, and Guervitch et al., 2004 was undertaken. The effect of temperature on grain refinement is also investigated numerically by

recording temperature at various jet segments with the help of tracers or gauges in ANSYS Autodyn 2D.

Publication at: Agu HO, Hameed A, Appleby-Thomas GJ, Wood DC. Comparison of the microstructure of machined and laser sintered shaped charge liner in the hydrodynamic regime. Journal of Dynamic Behaviour of Materials. 2019. https://doi.org/10.1007/s40870-019-00213-y.

- **Chapter 8 – Application of shell jetting analysis to determine the location of the virtual origin in shaped charges:** In the final chapter comprising a stand-alone paper, a novel technique for determination of the virtual origin (VO) location using a unique modification of an ANSYS® Autodyn 2D shaped charge jetting technique postulated by Carleone and Chou; is explored. This approach was designed to enable effective VO location determination and to provide a technique to allow more accurate, economic and practical calculation of (resultant) penetration depths. The predicted VO Location was compared with literature results and verified using the analytical model put forward by Allison and Bryan for jets that particulate without breakup using 18 mm shaped charges.

  Published at: Agu HO, Hameed A, Appleby-Thomas GJ. Application of shell jetting analysis to determine the location of the virtual origin in shaped charges. International Journal of Impact Engineering. 2018; 122, pp. 175-181. https://doi.org/10.1016/j.ijimpeng.2018.04.014.

- **Chapters 9 (Discussion) and 10 (Conclusion and Future perspective):** The thesis is concluded with a general discussion in chapter 9 followed by conclusion, highlighting major contributions of each chapter / paper and recommendations for future study.

2 Literature Review

2.1 Overview

Shaped charges are designed to focus the energy from an explosive to produce an intense and localised force by creating a hollow or depression in the charge [1]. This phenomenon, also referred to as the Hollow Cavity Effect [2], allows the energy from a detonation to be directed in a single line against a target rather than being scattered in different directions as would be expected in a block of explosive. The shaped charge is a cylinder of explosive with a hollow cavity at one end and a detonator at the other, backed by an explosive all in a material casing. In simple terms, it is referred to as a hollow charge [3]. The charge case is employed to enhance the jet formation process before its shear strength is exceeded by the rapidly expanding detonation wave. The liner is a metallic or non-metallic conically (other shaped are available) shaped material that forms the jet. Detonators are a sensitive (primary) explosive placed centrally (other positions can be used) at the top end, in contact with the explosive to detonate the high explosive beneath. In some circumstances, an intermediate explosive or booster is employed to assist the detonation process. In addition, wave shapers are used occasionally to shape or contour the detonation wave such that it impacts the liner at a nearly normal or perpendicular angle [4], with potential for improved jet performance [5], [6]. A schematic of the various parts of a shaped charge is presented in Figure 2-1.

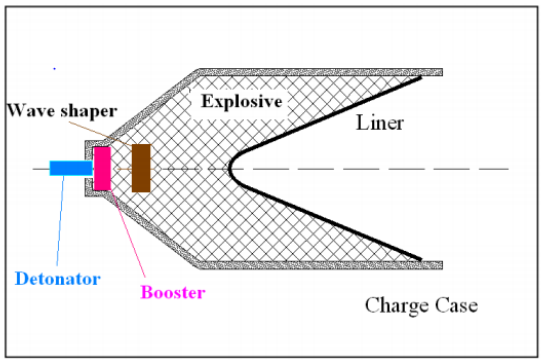

Figure 2-1. Schematic representation of a shaped charge [7].

Several materials including, concrete, metals, and air [8] have been explored as potential wave shapers. Recent work on wave shapers, conducted by William Walter [8], employed a hole volume which overlaps the apex of the liner to increase the jet tip velocity by about 2 km/s. Essentially, the intent is to contour the detonation wave to impact the liner at a favourable angle.

2.2 Mechanism of shaped charge jet formation

The principle underlying the formation of the shaped charge jet is the transfer of a detonation wave from the explosive to the liner, collapse of the liner (also known as liner collapse) and the formation of a stretching high velocity jet in a sequential but highly transient manner. When the explosive charge is detonated, the resultant detonation wave expands rapidly from the point of detonation, with a velocity typically around 6-9 km/s depending on the detonation velocity of the explosive. As the detonation wave propagates outwards, it engulfs the liner material and accelerates it rapidly to cause a very violent distortion over a very short time interval at extremely high pressure (peak pressures of around 200 GPa can be attained [2]). These extremely high pressures accelerate the liner rapidly with strains rates of around (10^4 -10^7/s) and collapses it inwardly. As the pressure generated far exceed the yield strength of the liner material, the liner flows hydrodynamically as an inviscid, incompressible fluid, in the form of a jet as shown in Figure 2-2. Jet tip velocities of 10 km/s are achievable [2], [3]. These high velocity jets are capable of forming a deep crater into any material placed along their path.

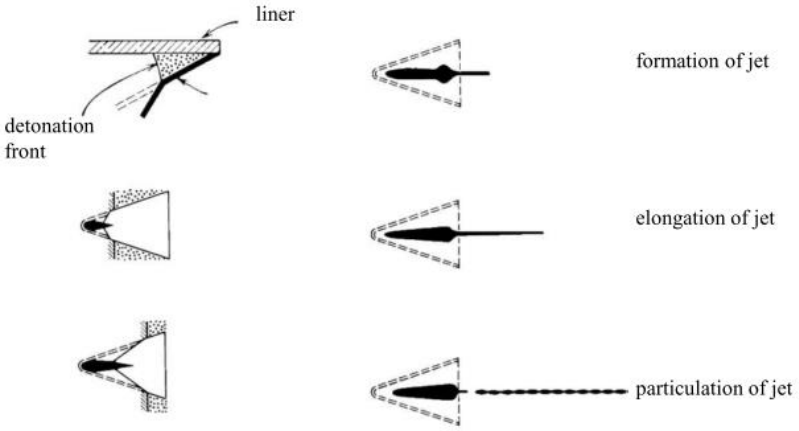

Figure 2-2. Schematics of the jet formation a conical shaped charge [2].

As the jet is forced out from its axis, it is accompanied by a heavier slug travelling at a lower velocity (2-3 km/s). By crude rule of the thumb [9], only about 20% of the inner surface of the liner cone goes into the jet while the remaining 80% that does not enter into the jet forms a slower, more massive portion known as the ‘slug’ (Figure 2-3). Further, the existence of variations in explosive-to-liner mass ratio along the jet length [8] cause a velocity gradient along the length of the jet, allowing it to stretch geometrically in a manner dependant on the liner characteristics. Jet elongations between 1000 and 2000 percent longer have been recorded for copper liners [10], illustrating the extreme nature for the conditions encountered within a deforming liner in a shaped charge system. After travelling a certain distance, the jet begins to fragment into particles, a process driven by elongation due to the velocity gradient along its length. The resultant particulate jets undergo radial acceleration and deviation from the axial direction, thus limiting the final depth of penetration.

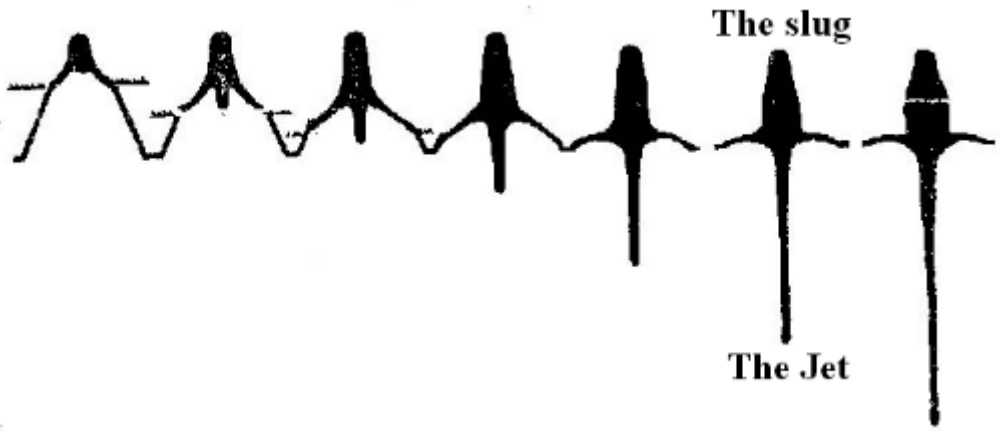

Figure 2-3. Jet and slug formation during liner collapse [2].

2.2.1 Jet particulation

In reality, the jet does not stretch indefinitely; at a sufficiently large standoff, the jet breaks up into small segments as shown in Figure 2-4. When this occurs the penetration depth is reduced as a result of the tumbling and deviation of the particles from its axis [11]. To produce deeper penetration, the stretching shaped charge jet must achieve a very long length before particulation. Hence an understanding of the time for the jet to particulate, also referred to as the breakup time, (t_b), is essential for developing methods to delay the onset of particulation. The mechanism underpinning this process of jet breakup (and the associated breakup time) have been investigated by numerous researchers, e.g. [12]–[14], using hydrocode simulations, empirical formulae and one-dimensional analytical models. For example, Karpp and Simon [15] investigated jet breakup using a numerical technique. They observed that prior to the jet breakup, the jet forms a series of necks during the stretching process attributed to instabilities arising majorly from the original material properties [13] such as material yield strength and density.

Figure 2-4. Shaped charge jet breakup of 81.2 mm [2].

When the jet stretches, tensile straining of the jet give rise to localised flow along different segments of the jet, thus some segments of the jet deform a little more than others. The cross-sectional area of the deformed section decreases forming necks. If the yield strength of the metal is high, the reduced section can still carry the force but if not, plastic flow will become localised at the neck and the specimen will fail. Essentially, the ratio of the flow stress to jet density (γ/ρ) controls the growth of the instability [13]. A lower value causes the jet to neck more slowly than a higher one. Hence, jets with high yield strength and low-density breakup earlier [13].

The effect of initial disturbances (material yield strength, wavelength of the disturbance, time of disturbance initiation, surface roughness and jet density) on jet stability was investigated by Carleone et al., [16], and a mild effect on the jet stability was observed. A similar observation undertaken by Walsh et al. [17] postulated that breakup time can be delayed by increasing homogeneity of the charge components and reducing manufacturing tolerances.

One of the earliest formula for estimating the jet breakup time, which is still applied to date, was presented by Hirsch [18]. The proposed formula is premised on the assumption that a liner material fractures into almost the same number of fragments irrespective of the velocity. As such, the velocity between neighbouring segments, also known as the plastic velocity, (V_{pl}) could be estimated by dividing the square root of the metal yield strength (σ_y) by the metal density (ρ) in Equation 2-1.

$$V_{pl} = \sqrt{\frac{\sigma_y}{\rho}} \qquad 2\text{-}1$$

However, determination of the yield stress for an elongating jet is difficult to measure accurately because of the highly transient jet phenomenon and also, whether the yield stress remains constant / at an empirical value for a metal. If this were the case, breakup time would be independent of factors such as temperature, quality of the liner material, manufacturing process and liner design

configuration [19], which have all been shown to affect the performance of the jet. As such via numerical methods, an estimated value of the plastic velocity could be obtained by dividing the differences in velocity between neighbouring particles by the number of particles.

A model for computing the number of jet segments from the jet during breakup was presented by Carleone [16], as well as an approach to identify the effect of varying shaped charge parameters such as cone angle and liner wall thickness on the number of segments.

By, employing the expansion theory of a metal pipe, Hirsch [18] posited that the breakup time is equal to the initial diameter (original liner thickness) of the elongating jet divided by the plastic velocity (V_{pl}), given in Equation 2-2.

$$t_b = \frac{2r_o}{V_{pl}} \qquad 2\text{-}2$$

This can also be expressed as:

$$t_b = \frac{1}{V_{pl}} \sqrt{8RT_L} \sin\frac{\beta}{2} \qquad 2\text{-}3$$

Where t_b is the breakup time measured from the arrival of the detonation wave at the liner element, R is the radius (when the jet elongation begins) of the element, T_L is its thickness and β is the collapse angle.

Although this formula gives a reasonable breakup time, it is independent of the stretching rate of the jet. As such, its application is limited particularly for highly ductile (liner) materials [20]. The effect of strain rate on breakup time was considered by Pfeiffer [21] in Equation 2-4. The formula was obtained by performing two-dimensional hydrocode simulations and fitting data.

$$t_b = \frac{1.4}{\eta_0} + 48.5\frac{r_0}{C_0} \qquad 2\text{-}4$$

Where η_0 is the initial strain rate of the jet material, r_0 is the initial jet radius, and C_0 is the sound speed in the jet material. Mostert et al., 1995 [22] related the jet breakup time with a change in mass and velocity. The authors suggested that the breakup time is proportional to the change in mass to velocity presented in Equation 2-5. This relation has been found to be closely related to the Walsh dimensionless parameter obtained from experimental and numerical simulation whose value correlates well with a large number of shaped charge devices. For a typical shaped charge, $\frac{\Delta m}{\Delta v}$ is invariant with time.

$$\left(\frac{\Delta m}{\Delta v}\right)^{\frac{1}{3}} \qquad 2\text{-}5$$

Subsequently, Baker [23] introduced a ductility parameter 'Q' to quantify the quality of various jets produced from the liner design presented in Equation 2-6.

$$t_b = Q \left(\frac{\Delta m^x}{\Delta v}\right)^{\frac{1}{3}} \qquad 2\text{-}6$$

Which can also be expressed as:

$$dv = dl_b \, Q \left(\frac{\Delta m^x}{\Delta v}\right)^{\frac{1}{3}} \qquad 2\text{-}7$$

where $m^x \; l_b$ is the length of a jet at breakup, Q is the material ductility parameter and dm* is given by:

$dm* = \frac{\Delta m^x}{\Delta v}$.

The larger the value of Q, then the more dynamically ductile the material being studied. This equation can be used to analyse a range of jets provided that the full jet kinematics are known.

2.2.2 Degradation of shaped charge jet

One of the main mechanisms of degradation of shaped charge jets over a long standoff distance is particulation. As mentioned previously, longer breakup times

are essential to achieve higher penetration. However, when the jet eventually breaks, the achievable penetration depth depends on a number of factors such as the particle shape, particle separation, velocity and collision of the particles. Cornish et al., 2001 investigated the effect of particle shapes on penetration depth using a DERA Eulerian hydrocode [24]. Three different particles shapes: cylindrical, lenticular and elliptical were considered and the highest penetration depth was recorded for the cylindrical particles in view of the higher mass in the cylindrical particles which drives the particle into the target. The lenticular particles were shown to penetrate less deeply because there is less mass at their extremities to drive hole formation. In the same work, the effect of particle collision, or inter-particle interference, was investigated by simulating the acceleration of 3 particles, front, middle and back, separated by a distance of 0.1 and 0.5 cm to which velocities of 2.1, 2.0 and 1.9 km/s were given. The results showed that particle collision is possible but unlikely as the middle particle has almost finished penetrating before the rear particle begins penetration into the target. However, the effect of clogging from the forward particles could affect the penetration of the particles behind reducing the overall penetration depth.

2.3 Factors that influence the performance of shaped charges

The objective of a shaped charge designer is (typically) to achieve as much depth into the target as possible. This requires a careful combination of all the various parameters that influence the performance of shaped charges. Some of the parameters are as follows:

- Explosive charge
- Standoff distance (SOD)
- Charge Diameter (CD)
- Liner material
- Charge design
    - Case shape, confinement, charge height, initiation method, precision and symmetry
- Head height
- Target Factor

2.3.1 Explosive charge

The collapse of a shaped charge liner and jet formation is dependent on the pressure exerted to the liner wall by the detonating explosive. One of the earlier works on the effect of explosive charge on jet performance was conducted by Julius Simon, in 1974 [25]. Ten explosives were investigated to determine the influence of the explosive on shaped charge warhead performance of BRL 81.3 mm precision shaped charges. The jet lengths, particle velocities and break-up times were measured using multiple flash radiography. The results showed that penetration increases monotonically with increasing explosive detonation velocity as well as the jet tip velocity while the breakup time remained fairly constant for all explosive charges (assuming that the jet breakup is simultaneous).

In a similar study, Elshenawy, 2012 [7], investigated the performance of six different types of high explosives numerically using the ANSYS Autodyn 2D hydrocode. The explosives include TNT, RDX, Cyclotol, HMX, LX-14 and PETN. The results showed a linear relationship between detonation and jet tip velocities as shown in Figure 2-5.

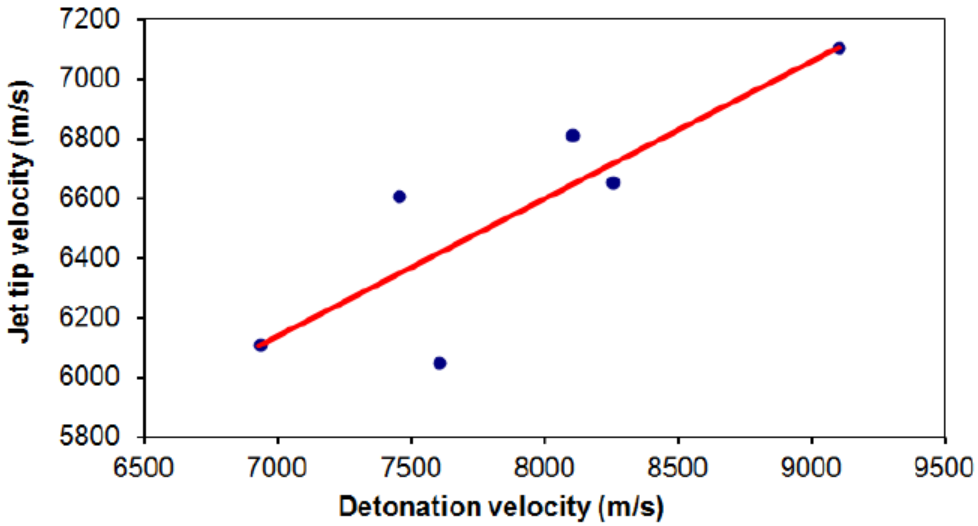

Figure 2-5. Relationship between jet tip velocity and detonation velocities of explosives [23].

From the experimental and numerical studies, it appears that performance increases with the detonation velocity of the explosive (e.g. with more energetic

explosives), with a greater amount of liner elements contributing to the jet resulting in longer, more massive and higher energy jets. The use of liquid explosives in shaped charges was explored by Cartwright et al., [26]. Sensitized gelled nitromethane containing 95% pure Nitromethane, polyethyene oxide and 5% diethylenediamine (for sensitization) were used in a 30 mm diameter, 60^0 cone angle, copper liner with 1.25 mm wall thickness shaped charges. The result showed outstanding consistent performance with a reduced velocity suitable for disposal of munitions.

2.3.2 Standoff distance

Studies have shown that average penetration depth varies greatly with standoff [27]. At first, penetration into a given target increases as the distance between the charge and the target increases (standoff) because more time is available for the jet to stretch [23], [59]. However, when the standoff is sufficiently long, the jet stretches adequately with greater length producing deeper penetration; as the jet length is proportional to the penetration depth. However, when the standoff is very large, the jet begins to particulate after stretching for a long distance. When this happens, the fragments drift away from their penetration axis in the crater [30], with a resultant decrease in penetration depth. Essentially, all the jet elements contribute to the penetration by arriving at the crater bottom to transform its KE into depth. However, in this circumstance, the deflection of the jet particles decreases the jet coherency and thus, not all of the jet element contribute to the crater leading to a reduction in the penetration performance [27]. There exists an optimum standoff for which the maximum penetration is achieved and this is typically between 2 and 8 times the cone diameter (Figure 2-8) but this depends on the characteristics of the liner. A high optimum standoff between 4 and 8 charge diameters can be obtained from precision liners compared with primitive liners as illustrated in Figure 2-6 [30].

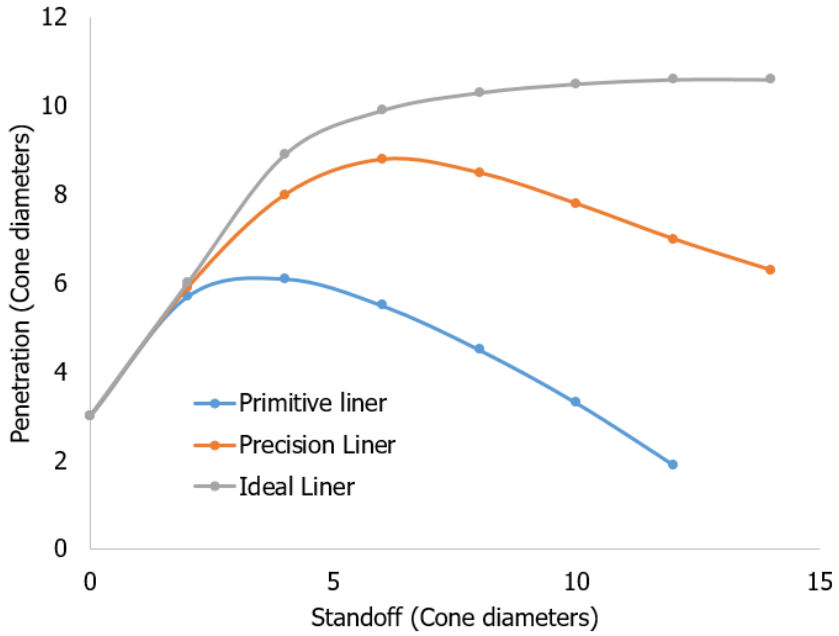

Figure 2-6. Optimum standoff for idealised, precision and primitive shaped charge liners modified from Reference [30].

2.3.3 Head height

Generally, it is necessary to allow enough room for the detonation wave to travel before contacting the liner. This is essential to allow a planer one-dimensional wave to impact the liner to obtain a symmetrical liner collapse. However, studies have shown that increasing the head height beyond a certain value is a waste as no improvement is derived. Walters postulated that only very little additional improvement is shown by increasing the head height beyond 1.5 CD, while a head height of 1 CD will show only slight improvements in jet velocity, penetration, and kinetic energy over a $\frac{5}{8}$ CD head height [2]. More so, increasing the quantity of explosive can cause further damage to surrounding equipment if done in the laboratory. Boat tailing is a technique which is currently employed to reduce the quantity of explosive without reducing the head height as shown in Figure 2-7.

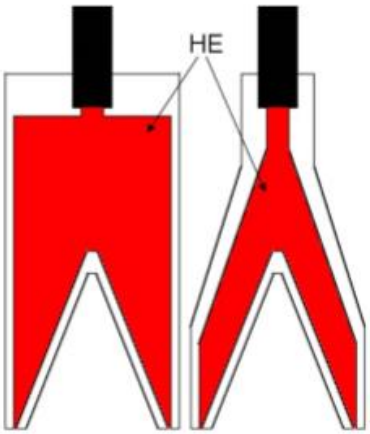

Figure 2-7. Schematics of boat-tailing in a shaped charge design (compared on the left-hand side to a conventional arrangement).

2.3.4 Charge casing or confinement

The charge casing is an important aspect of a shaped charge. The strength of the material casing as well as the thickness, has been shown to influence charge performance [7]. Numerically, confinement has been shown to increase the jet tip velocity by about 1.5% but this is at the expense of computational cost when compared to a bare charge. Aside from ensuring that all the ingredients of the charge are assembled in one place, the casing provides confinement to reduce energy loss during detonation.

2.4 Shaped charge liner

The liner is one of the most critical elements that determines the performance of the shaped charge. Therefore, careful liner design is crucial for optimum performance. In recent years, many researchers have studied the various aspects involved with liner design. In general, the key factors are classified into three broad areas: liner material type, liner geometry, and liner microstructure.

2.4.1 Liner material

For a material to be employed as a liner, it must possess dynamic high yield strength under severe pressure and high strain rate conditions, high melting temperature and sound velocity [2]. This explains why metallic materials such as

Aluminium, Copper, Zirconium, Tantalum and Molybdenum are used for shaped charge liners. However, the material should be readily available, inexpensive and nontoxic. For higher performance, the liner should be ductile (able to stretch continuously with a long breakup time) and must possess a relatively high density [10]. This explains why copper is the material of choice for the production of shaped charge liners. The properties are represented in the classical hydrodynamic theory put forward by Birkhoff [27] and explicitly by Held [10] who presented the theoretical penetration depth as a function of the jet length and the densities of the jet $'\rho_j'$ and target $'\rho_t'$, as shown in Equation 2-8. The jet length is represented by the differences in maximum $'V_j'$ and minimum jet velocities $'V_{min}'$, with breakup time $'t_p'$. The breakup time is a function of the ductility of the liner.

$$P = (V_j - V_{min}) t_b \sqrt{\rho_j / \rho_t} \qquad 2\text{-}8$$

M held, 2006 [10] investigated jets produced from different liner materials as shown in Table 2-1 and observed that aside from the commonly used Copper, Tungsten and Molybdenum have a good shaped charge properties while Aluminium has the lowest level of performance. Other materials such as Tantalum and Nickel produced coherent jets. Molybdenum, for instance, is an attractive material for shaped charge liners due to its high sound speed (4.9 km/s compared with 4.3 km/s for Cu), with a ductility close to that of high quality Copper [23] and a relatively high material density (10.0 g/cc compared with 8.93 for Cu), along with a high sound speed, gives it a high velocity coherent jet tips [31].

Table 2-1. Potential of different liner materials for shaped charge [10].

Material	**Al**	**Ni**	**Cu**	**Mo**	**Ta**	**U**	**W**
Density (g/cm^3)	2.7	8.8	8.9	10.0	16.6	18.5	19.4
C_0 (mm/μs)	5.4	4.4	4.3	4.9	2.4	2.5	4.0
$v_{jet\text{-}max}$ (mm/μs)	12.3	10.1	9.8	11.3	5.4	5.7	9.2
$v_{jet\text{-}max} \times \sqrt{\rho_{jet}}$	20.2	30.0	29.2	35.7	22.0	22.0	40.5
Ranking	7	3	4	2	6	5	1

Although Molybdenum and tantalum produce coherent jets with comparable performance with copper, the choice of liner material selection is a compromise between ductility of the selected materials, cost, ease of manufacture and target penetration capability. In terms of penetration capability, aluminium, for instance, is employed when a larger crater volume is required rather than deep penetration, or when the target is relatively soft compared to conventional armour-like targets [28]. Nonetheless, the basic irregularity in the selection of the liner material is density, which should be low for a high jet tip velocity for a given quantity of explosive, and at the same time high for better penetration [32]. These contradictory requirements need further exploration. In addition to this, liners made of ceramics and powdered materials have been explored and they are found to give penetration in different targets. These liner materials offset the ductility requirements of the liner and it is apparent that some new theory has to be developed for penetration of such brittle liner materials.

Bourne, et al., investigated the performance of liners with low melt energies (Table 2-2): Silver, Titanium, Zirconium, Depleted Uranium (DU) and Copper in a constant liner mass hemispherical warhead design [33]. The use of constant mass designs implies that the cumulative mass-velocity plots should be similar for all of the materials; another feature that makes a comparison between the

different materials easier. The Titanium liners had an average grain diameter of about 120 microns and the pure Zirconium had an average grain diameter of 80 microns. It was observed that Zirconium had the longest breakup time, the highest cumulative jet length and tip velocity. Further, it is apparent that the metals all have longer breakup times than copper. The low plastic particle velocity obtained from the silver, zirconium and DU jet indicate they are more ductile than Copper. However, the DU is toxic - preventing its usage as a shaped charge liner.

Table 2-2. Liner performance with low melt energies [33] .

Metal	**No of Particles**	**Jet length (mm)**	**V tip (km/s)**	**V tail Km/s**	**V_{pl} m/s**	**Breakup time (μs)**	**Material Ductility**
Ag	55	1456.0	6.48	3.01	64.26	419.6	181.90
Zr	54	2058.9	6.75	3.34	64.34	603.8	246.10
Ti	33	1327.4	6.34	2.99	104.69	396.2	175.70
DU	84	1700.0	6.4	3.30	37.35	548.4	217.67
Cu	38	1130.5	5.90	2.56	90.25	338.5	161.53

Alloy liners comprising of two or more materials have been investigated by several researchers. Wang et al., [34] investigated the use of Copper and Tungsten alloy (80-20%) employing infiltrating technology with a small quantity of nickel (0.5%) and observed an increase in the penetration performance by 30%, attributed to an increase in the density and jet breakup time. In a similar study, Bogdan and Zenon [35] investigated the performance of liners produced from a mix of electrolytic Copper and Tungsten; the resultant (ECu/W) liner produced through a powder metallurgical method made from a blend of Copper and Tungsten powder exhibited a lower jet tip velocity, but a deeper penetration than an otherwise similar copper liner due to a higher density (12.5g/cm^3). A similar observation was reported by Elshenawy [36], where a Copper-Tungsten liner manufactured using uniaxial pressing technique was compared with a baseline

shaped charge copper (Figure 2-8) liner produced by deep drawing technique. It was observed that the Copper-Tungsten liner (higher density powder) exhibited a higher penetration depth than the baseline copper liner obtained by deep drawing technique of uniform density in comparison with the baseline. In addition, the penetration crater which resulted from the powder liner showed a clean hole without clogging because there was no massive slug as in the case of the copper liners.

Figure 2-8. Pictures of the liners fabricated alloy; copper–tungsten liner powder (left) and the baseline copper (right) [36] .

In similar work, Z. Zhao et al., [37] showed that the addition of Zn and Ni to a W–Cu alloy liner reduced penetration depth and increased the lateral displacement of shaped charge liners. This was attributed to a reduction in penetration due to severe transverse dissipation of the jet's energy. The addition of Ni in the W–Cu alloy increased the melting point of the matrix phase, thereby decreasing the lubrication effect of the matrix during penetration. The reduced lubrication effect leads to severe interaction between the jet and the target, aggravating the aforementioned transverse dissipation of the jet's energy. On the other hand, the addition of Zn in the W–Cu decreases the melting point of the matrix, making the matrix easier to be melted and squeezed/extruded out. With the resultant reduced lubrication, there is a severe interaction between the jet and the target, causing high lateral energy dissipation and a lower resultant penetration depth. In addition, Zhao posited that the addition of Zn increases the bonding strength between the W particles and the matrix, thus during the penetration process, W particles within the W–Cu–Ni jet experience severe deformation compared with those within the W–Cu jets.

2.4.2 Liner angle

As a general principle, smaller liner (cone) angle gives higher penetration depth with high jet tip velocity [38]. Numerical studies using shell jetting analysis from ANSYS Autodyn 2D revealed that the amount of liner forming the jet is low with a small cone angle; thus the cumulative jet mass is reduced with a high jet tip velocity in contrast with large cone angles. However, when the cone angle is very large (90-120 degrees), the liner begins to form a hemisphere, dome-shaped, with characteristics similar to an explosively formed projectile (EFP). Such EFPs do not form a jet but produces a slug travelling about 2-3 km/s, but the massive slug carries a very large amount of momentum and they are generally consistent over long standoff ranges due to their higher stability in air travel. The relationship between liner cone angle and penetration depth is at Figure 2-9.

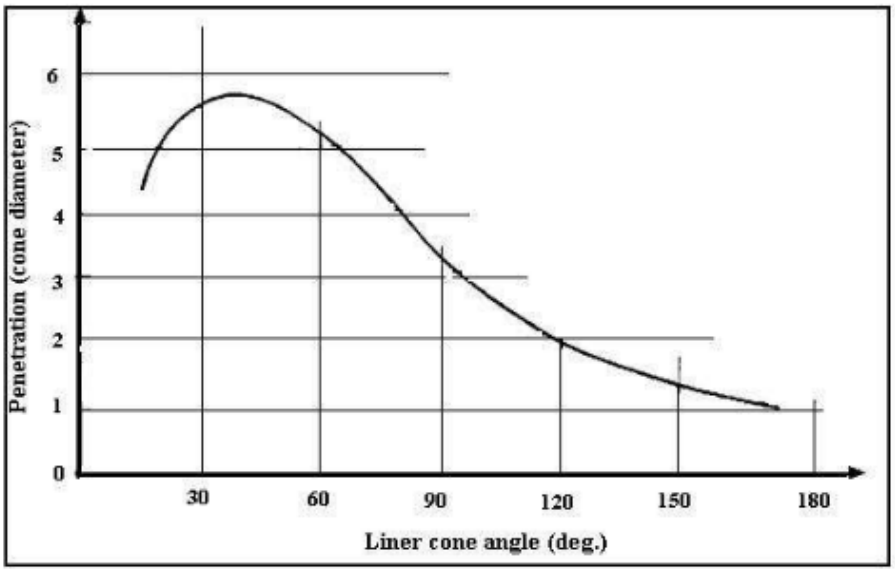

Figure 2-9. Relationship between liner cone angle and penetration [7].

2.4.3 Liner geometry

Since the discovery of shaped charge liners, various geometries have been investigated. The most popular are conical, hemispherical, Bell and trumpet, as shown in Figure 2-10 [21], [45]. and all have been found to produce coherent jets. However, the trumpet-shaped design was observed to produce better

performance [7], [29]. To illustrate the range of engineering solutions available, other shaped charge geometries available / which have been considered include:

- Tandem liners, comprising 2 distinct and separate liners designed to produce double penetration on a target.
- Fluted liners containing grooves in the inner surface of the liner which causes the jet to spin or rotate in flight, designed to counterbalance the missile spin for stability often called spin compensated liners.

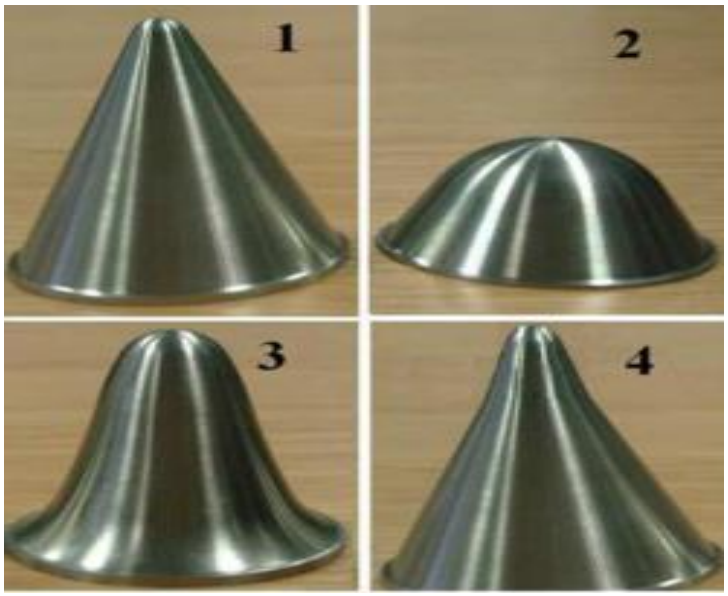

Figure 2-10. Picture showing different liner shapes. 1.conical 2. hemispherical 3. bell 4. trumpet or bi-conical [11].

2.4.3.1 Liner thickness

The effect of liner thickness has been investigated by several researchers. As expected, thinner liners are lighter in weight so the jets formed by them have higher velocities than thick liners with the same cone angles. Salih Saran et al., [29] investigated the effect of liner thickness on penetration performance of 100^{o} conical liners manufactured from AA6000 series aluminium at 15 CD standoff distance. It was observed that a decrease in liner thickness results in an increase in penetration depth, with a slight decrease in borehole diameter. For any liner design, a proper match between the mass of the explosive to the mass of the

liner is critical (charge-to-liner mass ratio). Large liner diameters could result in high energy losses from heating and internal friction during liner collapse [39]. Conversely, a thinner liner wall may damage the structural integrity of the wall leading to incoherent jetting.

2.4.4 Liner microstructure

There is a significant amount of work in the literature regarding the significance of grain size on the ductility of shaped charge jets. Duffy and Golaski (reported in Meyers et al.,1995) [40], observed that the break-up time, which is a direct measure of the jet ductility, increases as the grain size decreases with resultant depth in penetration (something highlighted in Figure 2-11). The variation in grain size was apparent for liner grain sizes below 30 μm [40]. In a similar study conducted by Lichtenberger et al., [41] on copper-shaped charge liners, two liner materials with different grain sizes of 20 and 90 microns, were fired into mild steel and higher penetration depths were recorded for smaller grain size liner materials. Flash X-ray images of the resultant shaped charge jets revealed considerably higher breakup time for the jets resulting from the 20-micron grain size specimens compared to the 90-micron cases. Essentially, fine, uniform recrystallized grain structures appeared to be advantageous in terms of prolonging jet integrity.

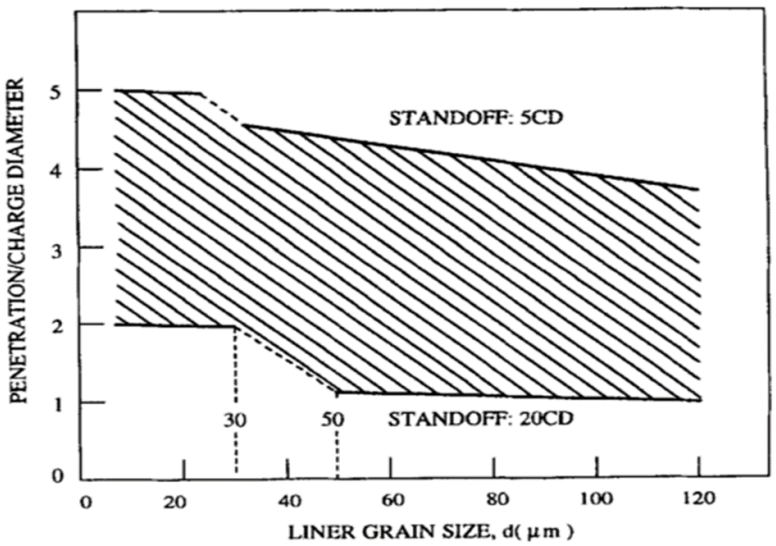

Figure 2-11. Normalised penetration as a function of grain size for copper shaped charge – original study by Golaski and Duffy; re-presented in Meyers et al., 1995 [40].

The influence of microstructure on jet performance was also reported by Petit J et al., 2006 [42]. However, while Petit et al. attributed the increased performance at reduced grain size to improved surface roughness, Lichtenberger et al., (as reported in Meyers 2005) [40], attributed the effect to an increase in ductility at reduced grain size. This is also contrary to the report by Meyers et al., 1994 where it was observed that enhanced (profuse) twinning occurred where higher grain size liners were employed compared to smaller grain sizes at 50 GPa, a pressure which is within the hydrodynamic range of shaped charges. Twinning is a highly favoured deformation mechanism in shocked loading that produces atomic displacement. At reduced grain sizes, the atoms are closely packed and hence there is a higher dislocation density which inhibits the incidence of twinning. In Ref. [43], Wongwiwat and Murr attributed the grain-size dependence of twinning in shock loading of Molybdenum to the possibility of a higher dislocation density associated with the smaller grained material.

The significant of microstructural effects on shaped charge liner collapse was brought to the fore when experimental observations revealed that shaped charge liners undergoes grain refinement after deformation [44]. Investigation on the

microstructural effects of the starting and ending grain size revealed smaller equiaxed grain size compared with the original liner material after deformation [45]–[47], [48] which suggests that the liner undergoes dynamic recrystallization during deformation at high strain rates [46]. G Schmidt et al., [42] observed small differences in grain size deformation at both high and quasi-static strain rates using rod impact and torsional Hopkinson bar test methods. Interestingly, a substantial reduction in surface irregularities was also observed at reduced grain size which suggests that applications with thin sections such as shaped charge liners could have great implication on grain size. This is an area that requires further exploration. Some early investigators also found that a decrease in the grain size resulted in an increase in ductility of a material [49], [50]. In a study conducted on magnesium alloy polycrystal, J A Delvalle, 2006 [49] observed that grain size and texture affects ductility by decreasing work hardening.

2.4.4.1 Recrystallization in shaped charges

When a material is subjected to strain, dislocation movements and generation within the crystal structure of the material cause the material to become stronger, harder and more brittle. The stresses are removed through heating and new crystals may begin to grow depending on the degree of annealing treatment as shown in Figure 2-12.

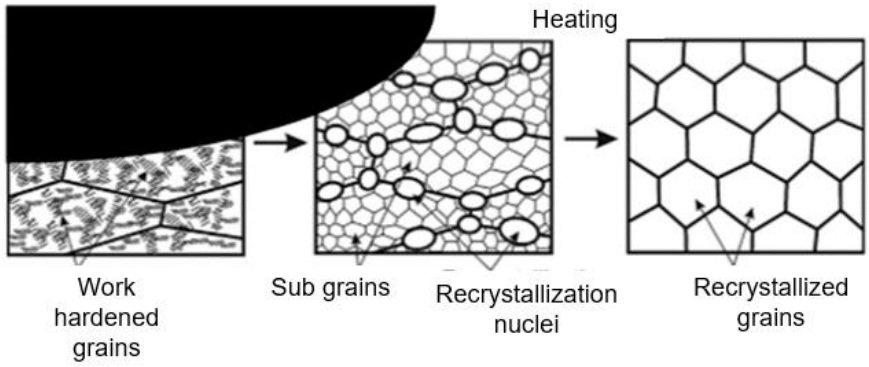

Figure 2-12. Schematic representation of recrystallization taking place during annealing of strain hardened material modified from reference [51].

Interestingly observation on the starting and ending grain sizes of liner material reveals a possible refinement of grain sizes during deformation [44]–[46], [52].

Murr et al. [46] made a systematic examination and comparison of two different Tantalum starting liner cones and corresponding recovered slugs and jet fragments for detonated shaped charges, using light and transmission electron microscopy. It was observed that the slug and jet grain sizes were lower than the initial liner grain size by nearly a factor of 100 (from roughly 35 to 0.3 μm). Further, the slug and jet cross sections exhibited different concentric zones of varying grain and substructures.

In a similar experiment, Gurevitch et al., [45] examined the microstructures of copper and tantalum shaped-charge liner as well as corresponding recovered jet fragments. Optical and scanning electron microscopes revealed a reduction in grain sizes in the recovered jet fragments. For Tantalum, the reduction factor was in some cases more than 10, while for Cu, only a factor of about 1.5 as illustrated in Figure 2-13. This shows that the grain size reduction is not constant for all materials, suggesting that other mechanisms may be at work during recrystallization. The grain size reduction was in fact about twice as much for an equiaxed, annealed Tantalum starting liner cone as compared with a deformed and irregular Tantalum starting cone that also contained a considerably heavier substructure, leading to the conclusion that this stored energy in the cone contributed to recrystallization in the elongating and particulating jet.

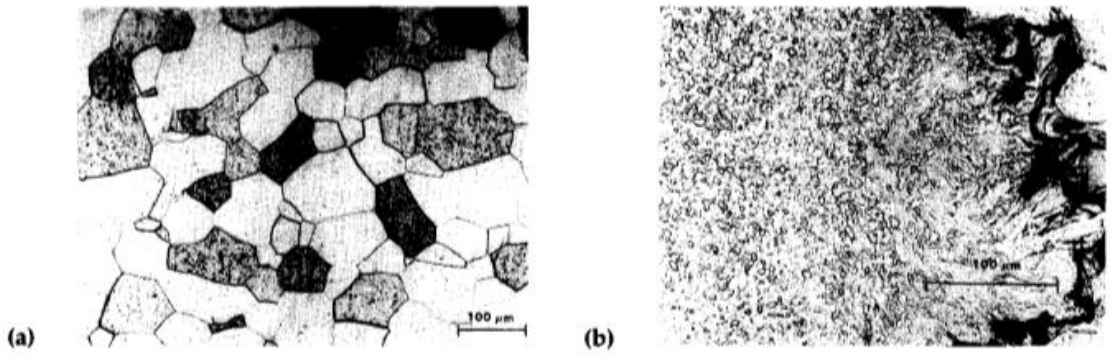

Figure 2-13. Light micrographs showing enlarged views of (a) the transverse "deformed" tantalum cone section and (b) the transverse, recovered jet fragment section [45].

2.4.4.2 Strain dependent

In an experiment conducted on Tungsten liners, similar observation in grain refinement was reported by Guo et al., [52]. The recovered grain size was proven to be dependent on the strain introduced as no twins or elongated sub-grains were observed in the slug but simply the generation of new crystals.

2.5 Liner production technique

It has been demonstrated that the microstructure especially, the grain size of the liner material, influences jet performance [53]. Liners employed for military applications require high precision and accuracy. Therefore, high precision flow turning manufacturing techniques and forging are employed. This is in contrast to liners employed for commercial applications where powder metallurgical technique and low-cost liner processing technique are used. There are several methods used for the production of shaped charge liners. These methods are described briefly in the following sections.

2.5.1 Machining

Machining involves the use of lathe or more advanced computer technology to cut metal blocks into the required shape and size [54]. Although this method has been used to produce some useful jets, the liners produced from it have poor microstructure. This is because of the typical large grain size and in-homogenous nature of the block or rod from which the liner is typically produced [10]. Also, the method is expensive, time-consuming, wasteful in materials and leaves residual stress in the liner microstructure. The technique is often preceded with annealing to remove residual stresses.

2.5.2 Powder metallurgical process

One of the commonly used methods where fine metal powders are pressed into their final form [16] in a matrix press mould. This method allows the production of small average grain size powder material liners from two or more different materials [35]. After compaction, the compact is ejected from the die and heated

under low temperature to convert compacted grains to a polycrystalline grain structure. This process comprises of four basic steps:

1. Producing the fine powder
2. Mixing and preparing the powder
3. Pressing the powder
4. Sintering at elevated temperature

For example, Elshenawy et al., [55] pressed Cu-W powder using a uni-axial hydraulic press as shown in Figure 2-14. The applied pressure was 100 MPa at a low strain rate (i.e. 1 MPa per second) using the hydraulic press to avoid trapping air voids inside the liner material. The result showed a good agreement with numerical and analytical simulations.

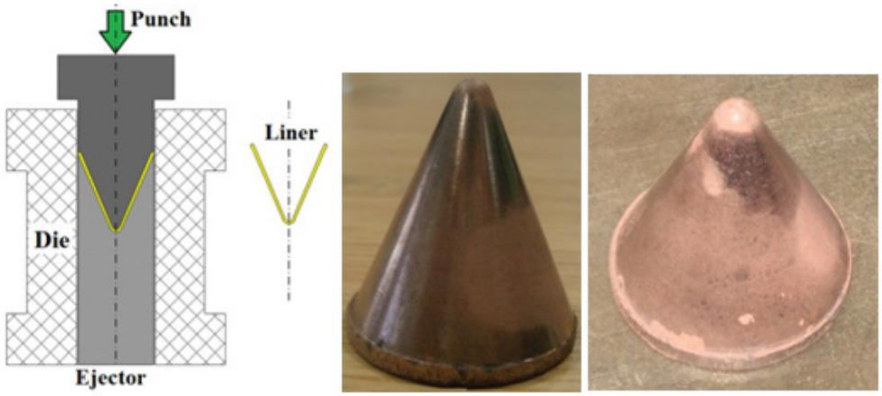

Figure 2-14. Schematic Illustration of the punch, die, ejector plus picture of the un-sintered powder liners produced [55].

This technique is usually followed with sintering to convert the compact powder into a solid polycrystalline material. Bogdan and Zenon also applied the powder metallurgical method to produce liners from electrolytic copper and tungsten powder [56]. The resultant liner was sintered at low temperature and machined to obtain the final dimensions (33.3 mm cone diameter at 45 degrees' cone angle). In spite of a comparative lower jet tip velocity, the Cu/W liner showed better penetration performance than a monolithic copper because of its higher density.

Essentially, the powder metal liners are inexpensive and show optimal performance at short standoff distance follows. However, they are susceptible to slight expansion (material creeping) under storage.

2.5.3 Deep drawing

This is one of the most commonly used liner [16] processing techniques due to its relatively low cost [10] when a large number of small liners are required. The liner is formed in several steps depending on the liner size. However, the liner retains the texture of the original plate but the crystal structure differs along the liner height due to variations in strains at different steps. As such, annealing is required at different steps for large cones which increases the production cost. The grain size of the final part depends on the grain size of the initial plate. Although the initial investment in a press is high and the tools required are expensive, the process is only suitable for the production of large quantities of liners [54]. The deep-drawing process gives a crystal structure of medium quality [10]. The steps involved in the production of a conical liner from sheet material are as shown in Figure 2-15.

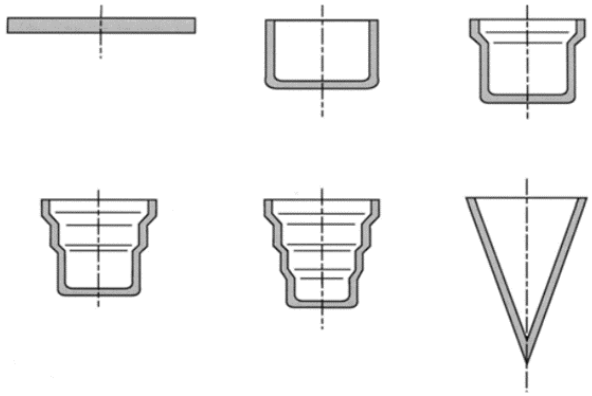

Figure 2-15. Liners produced from deep drawing technique [10].

2.5.4 Flow turning, spin forming or shear forming

In this process, the plate is deformed by the turning roller against a core as illustrated in Figure 2-16 [16]. The method introduces a spin texture on the surface of the liner by the rotational action of the rollers which could add spin to

the jet. The grain size and surfaces of the liner depend on the grain size and surface of the initial plates used.

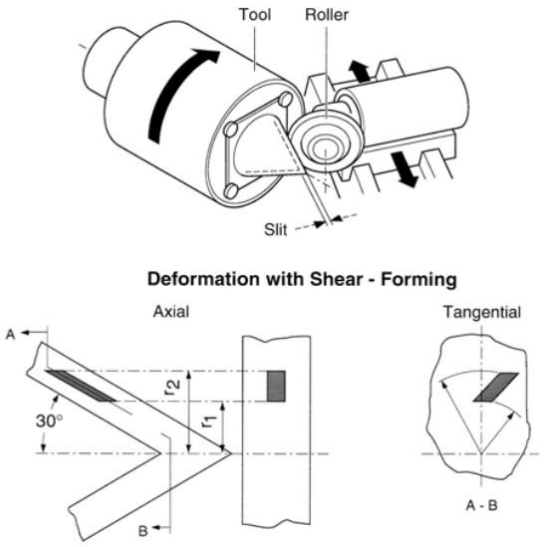

Figure 2-16. Schematic of a flow turning technique and the liner produced [10].

The advantages of the method are that the production is finished in one step with smooth internal and external surfaces; a small grain size / refined texture is also produced.

2.5.5 Cold forging

The cold forging method involves repeated pressing and annealing [10] at temperatures below the recrystallization temperature of the metal to reduce strain hardening until the liner is formed. Annealing is performed at intermediate stages to prevent rupture [16]. Unlike deep drawing, the texture of the internal surface takes the texture of the final press. Other advantages of the cold working process are [16]:

a. Improved strength properties
b. Better surface finish
c. Dimensions are better controlled
d. No heating required
e. Directional properties can be incorporated

The disadvantages of cold forging process are:

a. Requires higher forces for deformation
b. The forming equipment required is heavier
c. Involves strain hardening
d. Unwanted directional properties may evolve
e. Requires clean and scale free metal surfaces

Stages involved in the cold working technique are illustrated at Figure 2-17. This technique provides a very good surface finish.

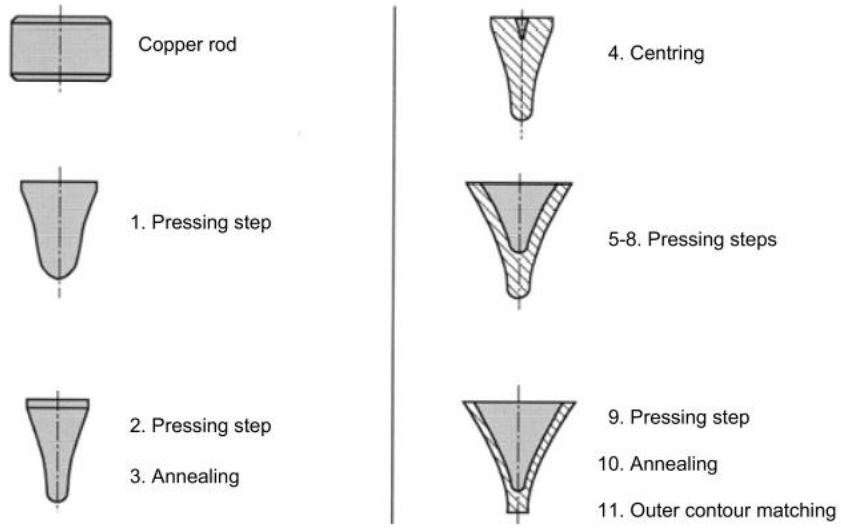

Figure 2-17. Liner formation employing the cold forging process [2].

2.5.6 Warm forging

Unlike the cold forging, the warm forging process requires small forges or presses and fewer steps than the cold forged process [10] at a temperature lower than the recrystallization temperature of the metal. This leads to the production of a very fine crystal structure. The hot forging method employs a single step under a forging press. Here, the liner material is heated to temperatures exceeding the recrystallization temperature. The resultant liner is machined to remove oxidised layers to obtain the required dimensions. Although the method is cheap, the crystal structure is poor making the method unsuitable for fabricating precision liners.

2.5.7 High energy rate fabrication (HERF) process

The HERF process involves a special impact machine (Figure 2-18) being used to press out the liner from a rod or billet with a velocity of around 20 m/s. The process results in liners which gives long jets with corresponding long breakup times arising from the resulting fine crystal structure [10] imparted by the manufacturing process.

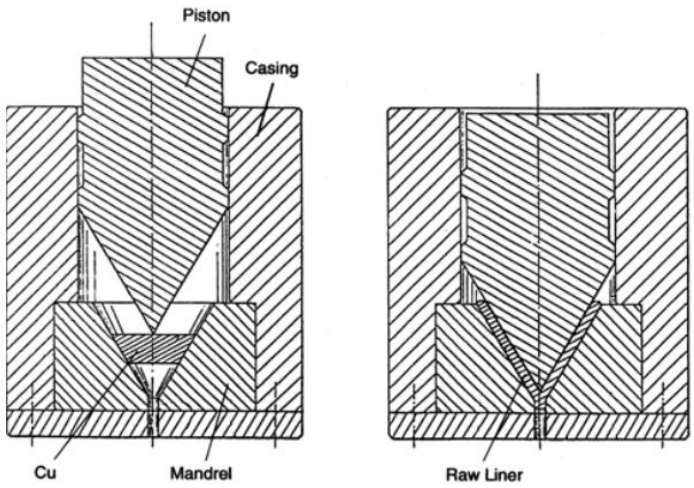

Figure 2-18. Warm forging process employed for liner production [7].

Complex shapes are made much more readily / easily, as compared to conventional forming and the required final shape / dimensions are obtained in one stroke, thus eliminating intermediate forming steps and preforming dies. Baker et al., [23] produced excellent Molybdenum jets from conical and hemispherical liner through high energy rate fabrication. Significant increases in jet ductility with high jet tip velocities of 12 km/s were achieved through the HERF technique, however, extremely brittle behaviour, with a large amount of radial particulate, was observed as shown in Figure 2-19 – limiting subsequent penetrability.

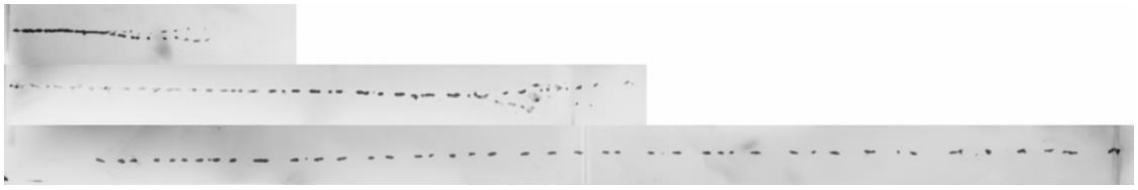

Figure 2-19. Long stand-off jet x-ray from monocrystal molybdenum lined shaped charge [23].

2.5.8 Summary of the various liner production process

Study of the various liner production process has illustrated that to obtain a fine and efficient liner for optimum performance, a combination of two or more processes are required. This is to say that no single method has all the characteristics. Machined liners, for instance, are relatively cheap but the microstructure of the liner is poor without any spin effect. Deep drawing on the other hand, though inexpensive, gives a medium quality crystal structure and is only suitable when large quantities of low cone diameter liners are produced. The process is, however, expensive when larger cone diameters are required as more annealing steps are undertaken. With controlled annealing, the approach of cold forging gives good crystal structure but without any spin. However, the cost of production is high due to the numerous steps required in the production process. Similarly, the approach of warm forging gives a fine crystal structure without any spin effect, while that of hot forging leads to a very poor crystal structure and is no longer used.

The flow turning process achieves a good crystal structure only with rods and the cost of production is relatively low as only one step is required for liner production. However, the technique cannot be employed for processing liners with dual material such as Cu/W liners. The HERF process appears promising. It produces liners with small grain size with a rotational symmetric structure. However, this process is expensive, time-consuming and produces jets with early breakup times.

2.6 Additive manufacturing process

While other liner production methods have been extensively investigated, that of Additive manufacturing, also known as the 3D printing process, which was introduced over three decades ago, has not been investigated for liner production. The concept of 3D printing or free-form fabrication is a broad term which covers all the processes involving the successive deposition of a solid by hardening from a liquid or gel state. Unlike the other liner production methods which are subtractive, the 3D printing processes build solid materials layer-upon-layer until the built part is completed [57]. The 3D printing process was developed in 1986 by Charles Hull [58] for the sole purpose of prototyping with polymers. However, tremendous advancement over the years has enabled not only the production of prototypic models, but also for readily customizable metal / working part [59]. Interestingly, 3D printing has enabled applications requiring both light weight and high strength in industries such as aerospace, [60]; medical industry, for production of surgical implants [61] and dental applications [59]; as well as in the automotive industry [62].

2.6.1 Advantages and disadvantages of additive manufacturing

Some of the benefits of additive manufacturing include:

a. Ability to fabricate complex design
b. Has a comparatively low production cycle time: only a few hours are required for the production of complex parts
c. Does not require tools as with other production methods which require removal tools and moulds
d. Ability to produce complex design in one step without the need for other operations such as welding or brazing (near-net shape manufacturing)
e. The use of lattice enables the production of light weight structures

The disadvantages are:

a. The built parts are often anisotropic in terms of material properties

b. Although high densities comparable with the original (feedstock) material are achievable, the presence of porosities make the built parts inherently weaker
c. The size of the built parts is limited to the 3D printer used

There are several processes used in 3D printing. For clarity, the processes are discussed under two broad categories: polymer additive manufacturing and metal additive manufacturing.

2.6.2 Employment of polymer in 3D printing

Polymers were the earliest material employed in 3D printing and they account for more than half of the printed parts currently produced [63]. This is partly because of their low melting temperatures which make them suitable for melt extrusion and their lower cost of production. Hence, thermoplastic polymers such as Acrylonitrile butadiene styrene (ABS), Poly Lactic Acid (PLA) and polycarbonates (PC) are commonly used as feedstock for parts production. However, pure polymer products built by 3D printing lack strength and functionality [57] to fully function as load-bearing parts. As such, particles, fibre or nanomaterial reinforcements are integrated in the polymers (composite polymers) to enhance the mechanical properties and functionality of the built parts [57].

There are several processes used for polymer printing such as ink jet printing, filament deposition modelling and the nano-composite deposition system. However, a comparative study of the compressive strength of the different processes suggests that parts made by the FDM had higher compressive strength. The Filament Deposition Modelling (FDM) process is one of the commonly used polymer processing techniques. A typical example is a study conducted by Caneiro et al., [64] on the performance of a glass fibre reinforced polypropylene (GFRP) and a neat non-reinforced polypropylene (PP). Printed samples were characterised mechanically and the results showed higher strength and modulus values of around 40 and 30% respectively for the GRFP.

2.6.2.1 Filament deposition modelling

The FDM process is a rapid prototyping technology which employs thermoplastic polymers to build parts sequentially using 3D printers. In this technique, the thermoplastics polymers are melted and extruded through a heated nozzle in a prescribed manner. The FDM is based on a material-melting technique otherwise known as extrusion additive manufacturing (AM) systems [65]. The extruded semi-molten polymer solidifies instantly onto the build platform, translating the sliced layers of digital data into an actual printed part. There are various open source printers but two of the most commonly employed are the Ultimaker 2 and 3 printers (available for this study) and which are comprised of several parts; print bed, drive wheel, filaments, extrusion nozzle and the fabrication platform. A schematic representation of the FDM set up is presented in Figure 2-20.

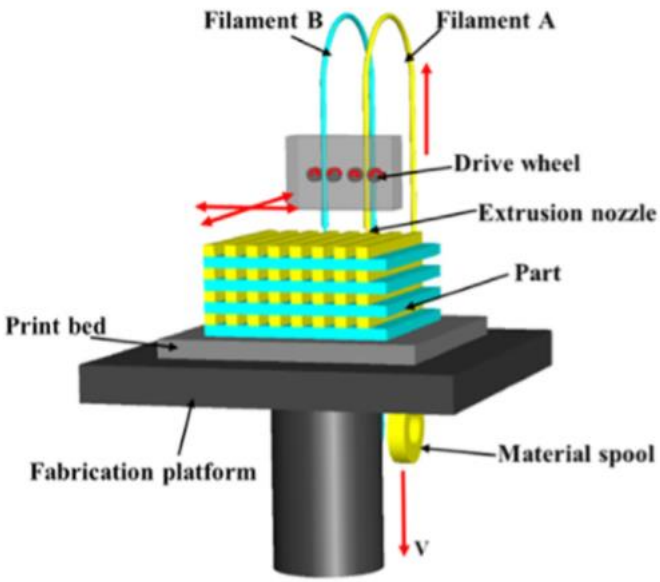

Figure 2-20. Schematic representation of FDM setup [65].

The advantage of the FDM process is the relatively low cost of the raw material and desktop 3D printers which also makes FDM the most popular 3D print process [66]. One major drawback of this technique is in the high-quality requirement of the filament to withstand stresses associated with the feeding (tension and compression) and melting (heating) action of FDM vis-a-vis its mechanical and thermal stability to be able to maintain high print quality. Also,

when supports are used, the surface finish is generally poor, requiring post-processing which may be time-consuming to improve surface aesthetics [67].

2.6.2.1.1 Mechanical properties of the FDM built parts

A number of investigators have studied the mechanical properties of built parts with regards to print parameters [68], [69], [70]. Major considerations in the build parameters include the air gap, which is the space between the beads of the FDM; build temperature - is the temperature at which the element is heated; raster orientation - which describes the direction of the beads relative to the loading of the parts (Figure 2-21); colour and layer thickness. Other parameters are nozzle diameter, bead width, feed rate. Highlighting such effects, Chacon et el., [71] used tensile tests to investigate the effect of layer thickness, build orientation, and feed rate on the mechanical performance of PLA samples manufactured with a low-cost 3D printer.

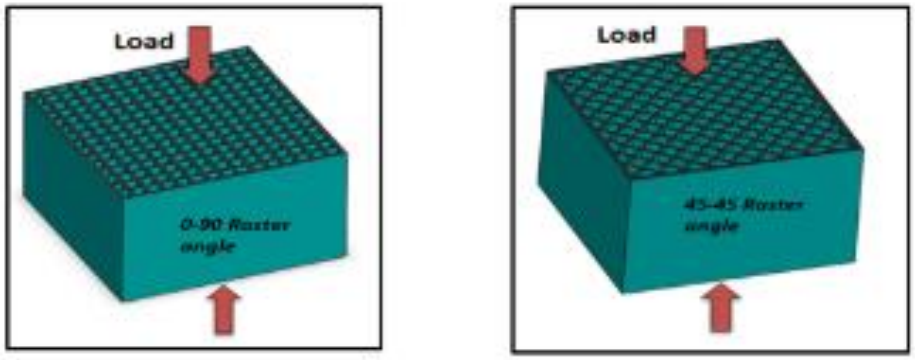

Figure 2-21. Physical models for horizontal-build specimens with (0^0, 90^0) and (45^0, -45^0) raster angles [72].

Ahn et al., [70] investigated the effect of process parameters (model temperature material colour, road/raster width air gap, and raster orientation) on the tensile and compressive properties of ABS parts. It was observed that the process parameters influence the mechanical properties of FDM-built parts and that parts built in the filament deposition direction show superior properties. Further, the effect of a negative air gap on tensile strength was studied and was shown to increase the tensile strength – an indication of a denser and stronger part. This

was shown, however, to be statistically insignificant in terms of effect on the compressive yield strength [72].

The effect of axial (horizontal) and transverse (vertical) build directions (Figure 2-22) on part compressive strength is highlighted in Figure 2-23, with the results indicating higher tensile strength for parts built in the axial direction. Although it is notable that the compressive strength of FDM material was shown to be higher than the tensile strength, this was not affected much by build direction [70].

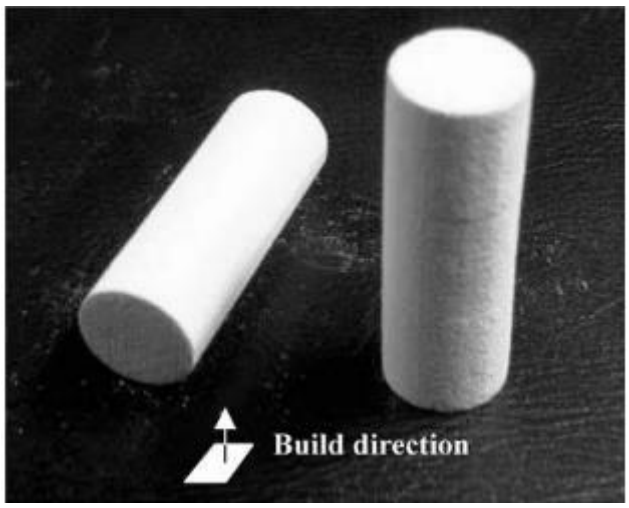

Figure 2-22. Axial and transverse build direction for an example part. [70].

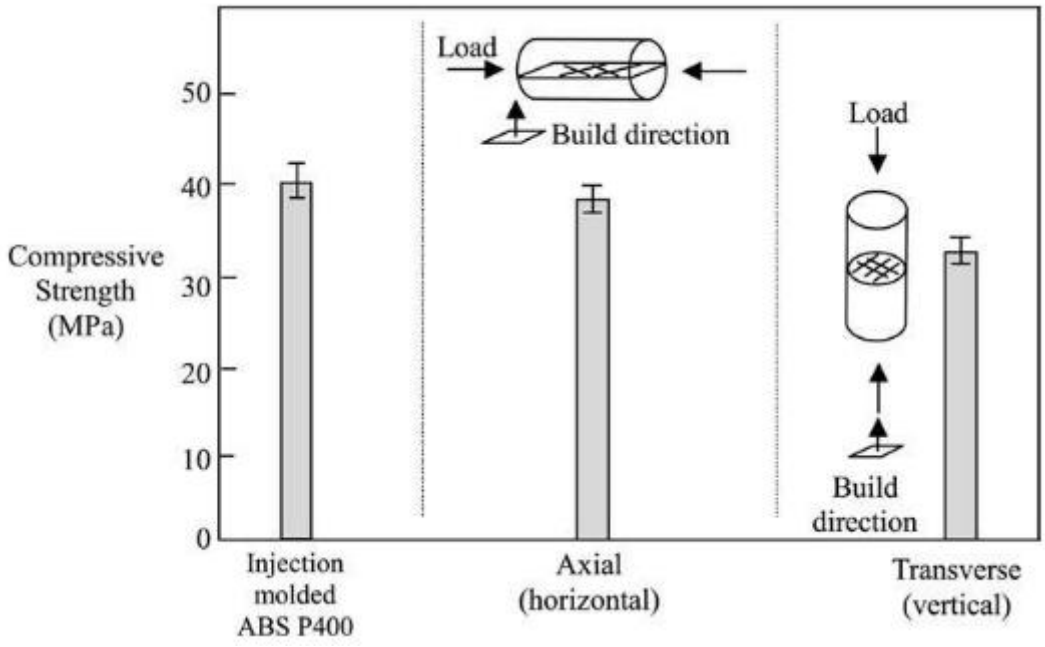

Figure 2-23. Compressive strength of specimens with different build direction [70].

Esi-Said et al., [73] investigated the effect of layer orientation on the mechanical properties of printed ABS samples by performing impact tests, tensile, and three-point bending. Five different layer orientations were studied: 0^0, 45^0, 90^0, $45/0^0$ (where one layer is deposited at 45° and a second layer is deposited along the sample length) and 45/-45° orientation (the two diagonals intersect at 45^0). The samples at 0° orientation where layers were deposited along the length showed superior strength and impact resistance over all the orientations [69]. A similar observation was recorded by Ahn [70] as shown in Figure 2-24. Es-said attributed anisotropic property of FDM printed parts to weak interlayer bonding and interlayer porosity [73].

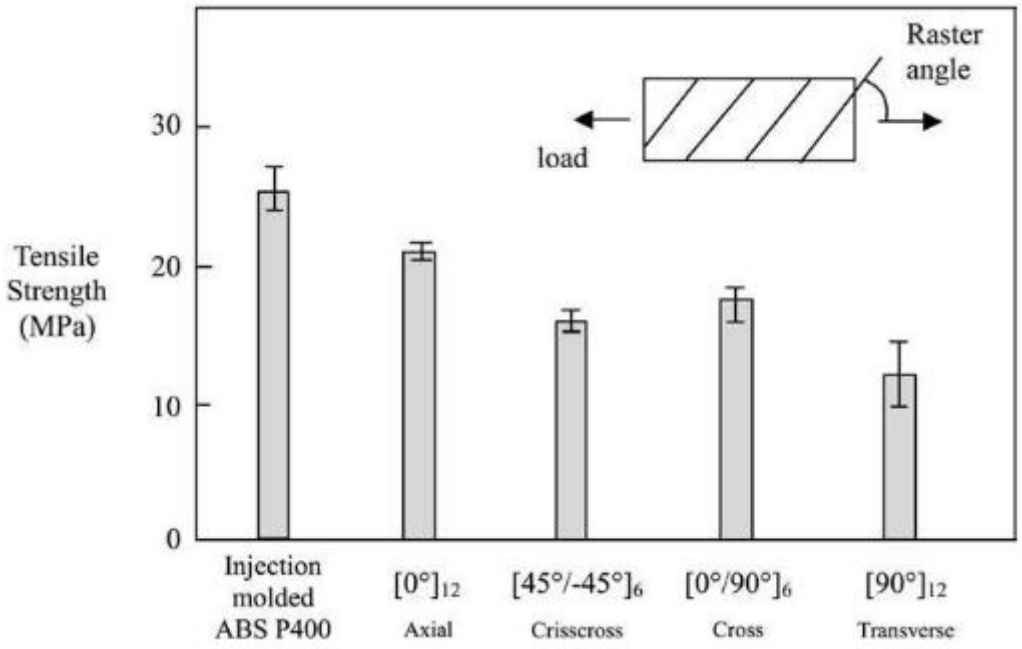

Figure 2-24. Tensile strength of specimens with various raster orientation [70].

2.6.3 Additive manufacture of metals

The 3D printing process has been used to construct metallic parts in a wide variety of industries, including antenna brackets for the aerospace industry, complex sand molds to case turbine wheel in a single piece for the energy industry, and for applications such as gas turbine burner tip repair and modification for the energy industries [74]. This approach simply involves building layers of material using techniques such as a computer-controlled laser which target pinpoint beams onto a bed to melt metal feedstock material into the desired liner shapes. Some of the processes employed in manufacturing metal is presented in Figure 2-25. These processes use less material than conventional techniques, reduces production costs and is faster because the machine can run around the clock. The possibility of using additive manufacturing techniques for the manufacture of a shaped charge liner is yet to be explored.

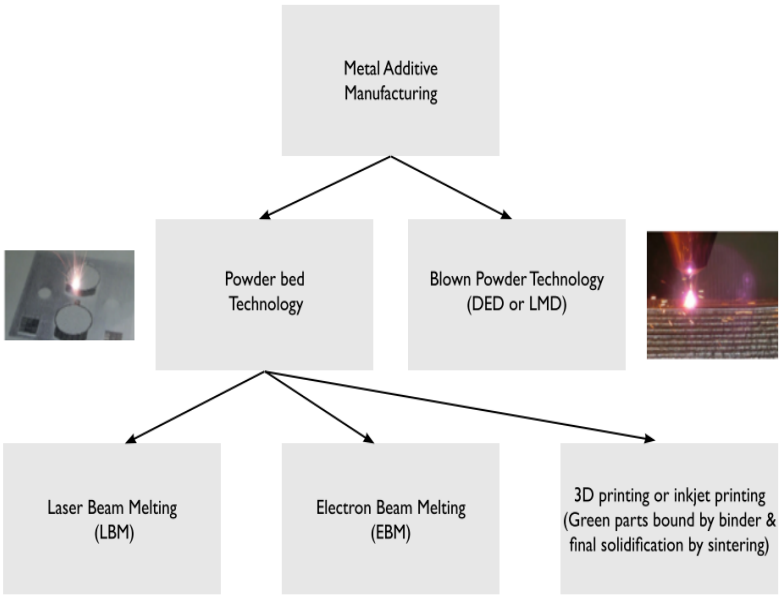

Figure 2-25. Overview of metal additive manufacturing technique.

During laser beam melting, the laser beam, typically with diameters of the order of 100 µm, will locally melt the upper powder layers on the powder bed. The laser will be partially absorbed by metal powder particles, creating a melt pool which solidifies rapidly. Laser power typically varies from 200 W up to 1000 W. This process is illustrated schematically in Figure 2-26.

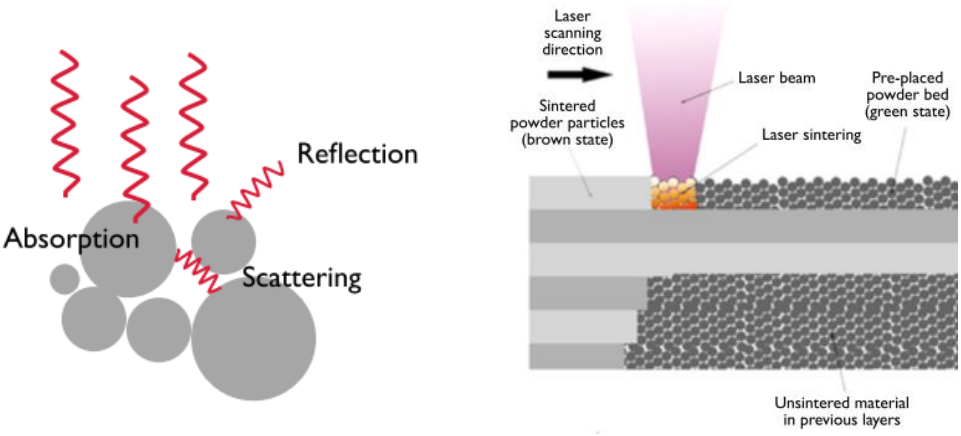

(a) (b)

Figure 2-26. laser melt process (a) laser melting process (b) interaction of laser with powder particles.

In the beam-based powder bed systems (such as LBM or EBM), a powder layer is first applied on a building platform. Then a laser or electron beam selectively melts the upper layer of powder. After melting, the platform is lowered and the cycle is repeated until the part is fully built, embedded in the powder bed. In selective laser melting, different scanning strategies are possible. The laser scanning patterns will influence porosity level, microstructure, surface roughness and heat build-up in the finished metal components. The stripe pattern is a band defined by the scan vector width (i.e. stripe width), the hatching space between adjacent tracks and the scan direction as well as the overlap with the neighbouring stripes.

2.6.3.1 Main process step

The AM process begins with the production of a 3D model of the parts using Computer Aided Design (CAD) software such as solid works which is then saved in an STL (Standard Tessellation Language) file [75]. These STL files tessellate the parts into a set of triangles. This allows the model to be sliced and imported into the 3D printer software. These STL format is widely employed because it is supported by most CAD systems and simplifies the geometry of the part to its most basic components. Although, some resolution is lost because true arcs and splines are lost in the triangles, errors arising from this are minimal and less than those occuring during the actual manufacturing process [70]. After part manufacturing, post-processing operations such as curing, annealing, and painting are conducted. Depending on the use, surface finishing and polishing are also conducted to produce a clean surface area. A block diagram of the main processes involved in 3D printing is highlighted in Figure 2-27.

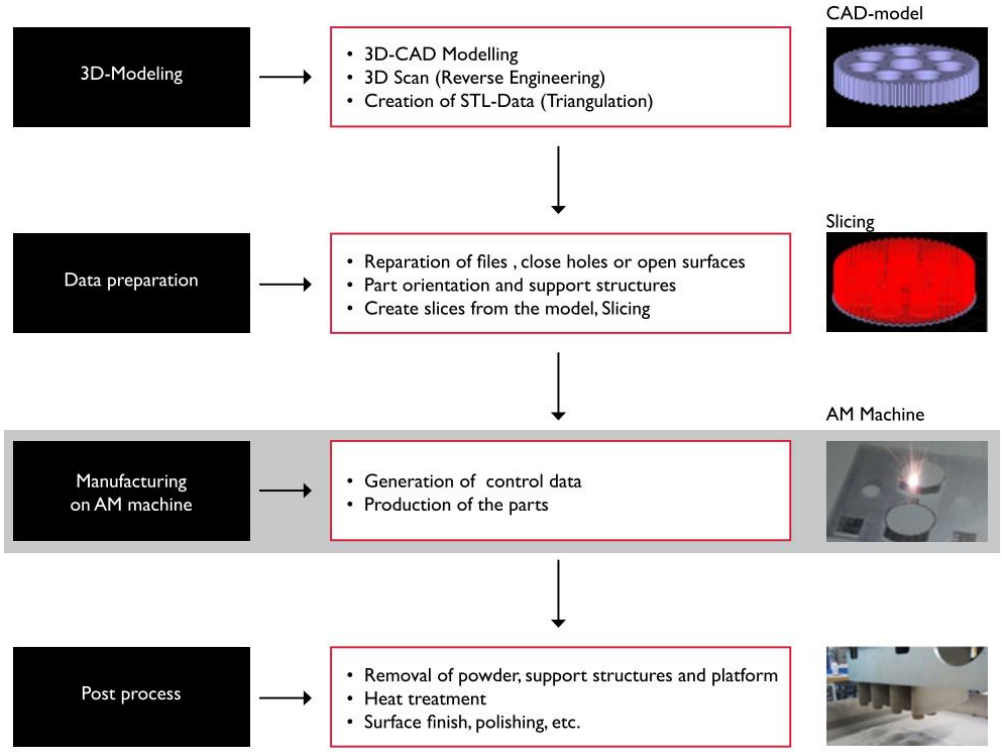

Figure 2-27. Summary of the main process steps of 3D printing.

2.6.3.2 Defects in materials obtained with additive manufacturing process

Despite the potential benefits of the AM process, some typical defects arising from wrong process parameters, part orientation, build strategy or poor powder quality can be observed. Some of these defects are:

- Un-molten powder particles
- Lack of fusion
- Pores
- Cracks
- Inclusions
- Residual Stresses
- Poor surface roughness
- Anisotropy

With regards to anisotropy, Es-said attributed the anisotropic property of FDM printed parts to weak interlayer bonding and interlayer porosity [75].

2.7 Shaped charge jet formation and penetration models

When a shaped charge is detonated, three different phases are observed, jet formation, breakup and penetration into the target. A mathematical model to describe the process of jet formation was first proposed by Birkhoff et al., [27]. The model was then developed by Pugh, Eichelberger and Rostoker, in what is known as the (PER) unsteady state theory [76]. Several modifications on the PER theory were proposed to account for deviations from the conical liner geometry, variations in the explosive initiation point among others. However, this section will simply describe the Birkhoff and PER jet formation model. The reader is referred to Reference [2] for detail derivations of the underlying equations. The PER theory is widely used and forms the basis on which calculation of the jetting parameters in numerical simulations are carried out.

2.7.1 Birkhoff steady state theory of jet formation

The Birkhoff theory is the fundamental analytical theory which models the velocity of the jet and slug, as well as their masses upon detonation [27]. The theory – which is referred to as the steady state theory was developed following some assumptions, namely:

- The pressure acting on all side of the liner is equal, thus the liner elements are accelerated instantaneously to their final collapse velocity
- The velocity of the jet is constant along the liner length of the
- The strength of the material is neglected
- The liner collapses inward at a constant velocity $'V_0'$ with an angle 'β' greater than the original cone angle 'α'

A schematic of the steady state collapse process in which the liner is modelled as a wedge is at Figure 2-28

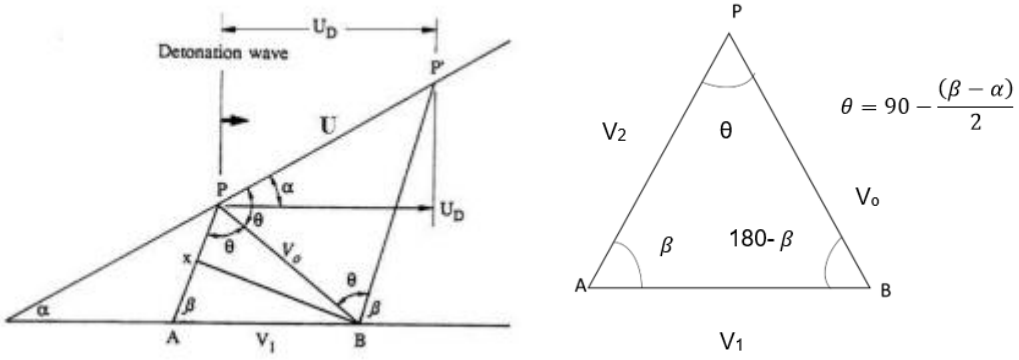

Figure 2-28. Schematic of the collapse process [27].

where, α represents one-half of the liner cone angle and β is the collapse angle, V_o is the velocity of the collapse element, V_1 is the moving coordinates velocity, V_2 is the flow velocity, U_D represents the wave speed of the detonation explosive.

At steady state conditions, element at point P collapses to line A at the same time P' will meet line B because the pressure is constant everywhere. Hence, the magnitude of the velocity is constant but the direction changes [27]. Line P'P and P'B represents the entry and emerging velocities, respectively. the line /PA/ represents the liner collapse at point P to the axis "A" as it sweeps across point A and B which is the velocity of the liner during collapse. From the schematic, PA/ is parallel to /P'B/ and /P'B/=/P'P/

Therefore, using basic trigonometric equations, Birkhoff derived the velocities of the elements. Employing sine rules, V_1 and V_2 can be estimated from Equations 2-9 and 2-10.

$$V_1 = \frac{V_0 \cos[(\beta - \alpha)/2]}{\sin \beta} \qquad 2\text{-}9$$

$$V_2 = \mathrm{V}_0 \left(\frac{cos\ [(\beta - \alpha)/2]}{\tan \beta} + \sin\left(\frac{(\beta - \alpha)}{2} \right) \right) \qquad 2\text{-}10$$

If the elements along A and B are represented schematically in Figure 2-29, then a moving observer positioned at point A would observe any point P in the upper plane (Figure 2-29) as approaching him with a velocity $V_1 Cos\ \beta + V_O\ Cos\ \theta$, the sum of the vector along Line /PA/.

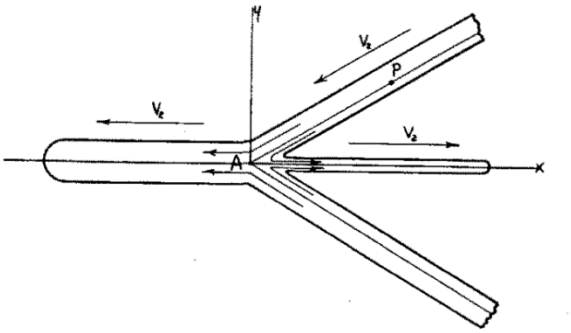

Figure 2-29. Formation of jet and slug [25].

From the stationary coordinates, we know that the jet moving to the right has a velocity:

$$V_{jet} = V_1 + V_2 \qquad 2\text{-}11$$

while the velocity of the slug in the opposite direction is given as:

$$V_{Slug} = V_1 - V_2 \qquad 2\text{-}12$$

Where V_1 and V_2 are the stagnation and flow velocities.

Hence the velocities of the jet and slug can be calculated from equation 2-13 and 2-14 to give:

$$V_{jet} = \frac{U_D}{\cos\alpha}\sin(\beta-\alpha)\left[csc\,\beta + ctn\,\beta + tan\left(\frac{\beta-\alpha}{2}\right)\right] \qquad 2\text{-}13$$

$$V_{slug} = \frac{U_D}{\cos\alpha}\sin(\beta-\alpha)\left[csc\,\beta - ctn\,\beta - tan\left(\frac{\beta-\alpha}{2}\right)\right] \qquad 2\text{-}14$$

From the moving coordinate system (Figure 2-29), using the conservation of momentum the masses of the jet and slug can be estimated from Equations 2-15 and 2-16 as:

$$m_j = \frac{1}{2m}(1 - cos\beta) \qquad 2\text{-}15$$

$$m_s = \frac{1}{2m}(1 + cos\beta) \qquad 2\text{-}16$$

The jet velocities are over predicted in this theory because:

- The velocity gradient in the jet was not accounted in the model.

- The length of the jet was assumed to be the length of the cone.

- The increase in the collapse angle as the wave velocity travels from the apex to the base of the liner was not accounted for. This model was modified in the PER theory as discussed in subsequent paragraph.

2.7.2 Non-steady state PER theory

Pugh et al., [27] developed the non-steady state theory which assumed a variable collapse velocity instead of constant collapse velocity of the liner. This implies that the collapse velocity decreases from the apex to the base of the cone. Thus, the collapse angle β in the unsteady state is greater than the collapse angle β^+ in the steady state model. As such, the liner element does not move perpendicular with the original surface but moves with a small deflection angle (δ) with the normal to the liner surface. A schematic drawing of the collapse process showing the different angles proposed by PER model is as shown in Figure 2-30.

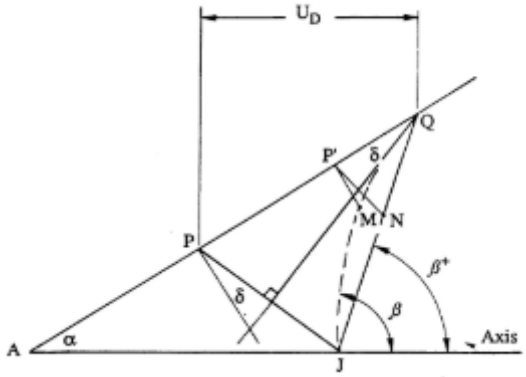

Figure 2-30. A schematic representation of the unsteady state collapse model (Pugh et al. [27]).

From the schematics, when the liner elements at point P collapses to point J, the element at position P' should have reached point 'm' if the collapse angle was constant as depicted by Birkhoff, but because the collapse velocity decreases from apex to base, the element at point P reached point M at the same time the liner at point P' reaches J. The liner collapse along a line that makes an angle δ with the normal. From Figure 2-30, the angle is defined as,

$$\mathrm{Sin}\,\delta = \frac{V_0}{2U} \qquad 2\text{-}17$$

if Vo is constant, then it reverts back to the Birkhoff theorem, then $\beta = \beta^+$

The relationship between the liner collapse velocity V_0 the collision point velocity V_1 and the collapse velocity relative to the collision point is shown in the schematic below.

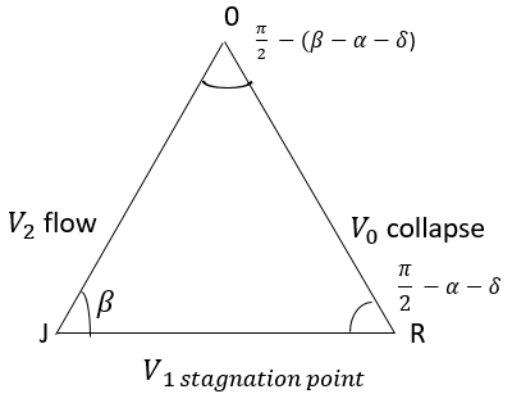

Using the sine laws relations, the velocity of the jet and slug can be estimated from flow velocity and velocity at the stagnation point, V_1 and V_2:

$$V_1 = \frac{V_0 \cos(\beta - \alpha - \delta)}{\sin \beta} \quad \text{2-18}$$

$$V_2 = \frac{V_0 \cos(\alpha + \delta)}{\sin \beta} \quad \text{2-19}$$

Thus, the velocity of the jet and slug can be estimated from:

$$V_j = V_o csc\left(\frac{\beta}{2}\right) cos\left(\alpha + \delta - \frac{\beta}{2}\right) \quad \text{2-20}$$

$$V_s = V_o sec\left(\frac{\beta}{2}\right) sin\left(\alpha + \delta - \frac{\beta}{2}\right) \quad \text{2-21}$$

Employing the principles of conservation of mass and momentum. The masses of the jet and slug are given in Equations 2-22 and 2-23 where m is the liner mass and m_j/m_s are the jet and slug masses, respectively.

$$\frac{dm_j}{dm} = sin^2 \frac{\beta}{2} \quad \text{2-22}$$

$$\frac{dm_s}{dm} = cos^2 \frac{\beta}{2} \quad \text{2-23}$$

2.7.3 Shaped charge jet penetration models

Birkhoff et al., [27] developed the first penetration model which was further improved based on the Bernoulli equation in 1948. The jet was modelled as a rod of length 'l', density ρ_j and velocity 'v' as shown in Figure 2-31. An inviscid and incompressible fluid flow was assumed because the pressure at the interphase exceed the yield strength of most materials.

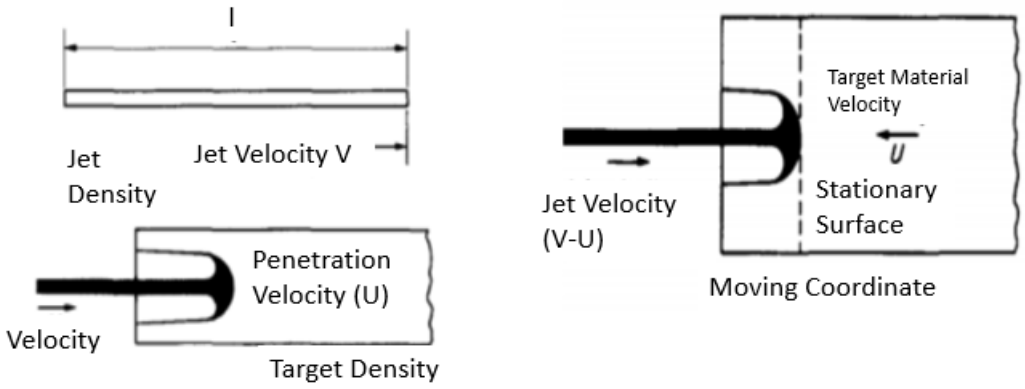

Figure 2-31. Jet penetration of a monolithic target in a coordinate system [26].

If a steady state condition is reached at the point where the whole length of jet penetrates the target, assuming constant jet length, then Bernoulli's equation may be applied along the axial jet stream.

From the law of conservation of momentum,

$$\frac{1}{2}\rho_j(V-U)^2 = \frac{1}{2}\rho_t(U)^2 \qquad 2\text{-}24$$

$$\rho_j(V-U)^2 = \rho_t(U)^2 \qquad 2\text{-}25$$

Assuming the steady state is reached instantaneously and that penetration ceases when the last jet element strikes the target. The total penetration P is the product of the penetration velocity and time.

$$P = U\frac{l}{V-U} = l\sqrt{\frac{\rho_j}{\rho_t}} \qquad 2\text{-}26$$

$$P = l\sqrt{\frac{\rho_j}{\rho_t}} \qquad 2\text{-}27$$

To a first approximation, this model predicts the penetration depth of the shaped charge jets. However, the simple equation indicates that the penetration is independent of jet velocity. However, the rate of jet penetration depends on the je velocity which is indicated by l [77]. Other factors not accounted for in the simple equations are:

- Standoff distance
- Secondary penetration
- Jet and target strength
- Jet tip velocity
- Jet-target interaction
- Target hardness
- Variable jet velocity
- Other factors such as aerodynamic drag, liner material properties, jet alignment and manufacturing error.

2.7.3.1 Effect of jet and target strength

At low velocities, Elchelberger et al., [78] observed that the strengths of the jet and target have a significant effect on penetration depth; particularly when the jet is broken. Thus the simple penetration equation was modified to account for the effect of yield strength of the jet and resistance of the target [27] by proposing a term to represent these variables.

$$Y_j + \frac{1}{2}\rho_j(V-U)^2 = \frac{1}{2}\rho_t(U)^2 + R_t \qquad 2\text{-}28$$

where, 'Y_j is the uniaxial yield strength of the jet and 'R_t is the resistance of the target to penetration.

Solving equation 2-28 above yields:

for $\rho_t \neq \rho_j$

$$U = \frac{1}{1-\frac{\rho_t}{\rho_j}} \left\{ V - \sqrt{\frac{\rho_t}{\rho_j}\left[V^2 + \frac{2(R_t + Y_j)}{\rho_t}\left(1 - \frac{\rho_t}{\rho_j}\right)\right]} \right\} \quad \text{2-29}$$

Similarly, Pugh and Klamer in Ref [2] verified the effect of strength by comparing the penetration of copper jet into Rolled Homogenous Armour (RHA) and mild steel. The penetration depth attained by the jet in mild steel was about 20% less than that in RHA. Pack and Evans [79] also noted the importance of target material strength on jet penetration. To account for the strength, a correction term, Equation 2-30 was introduced to the original model to obtain a modified penetration model:

$$\left(1 - \frac{\alpha Y}{p_{jV^2}}\right) \quad \text{2-30}$$

$$P = l_0 \sqrt{\frac{\rho_j}{\rho_t}} \left(1 - \frac{\alpha Y}{p_{jV^2}}\right) \quad \text{2-31}$$

Where α is a constant, Y is the dynamic yield strength, $\rho_j \; and \; \rho_t$ are densities of jet and target material respectively and V is the penetrator velocity.

Consistent with this, Pack and Evans showed that with the correction term, penetration is reduced by 30% due to the effect of the target strength.

2.7.3.2 Secondary penetration

William et al., [80] observed a residual inertial effect after the last jet particle strikes the target. Of more significance, is if the movement of the jet is toward the bottom of a crater. This was confirmed separately by Evans et al. [81] with the introduction of a factor ‘r’ to account for the secondary effect in Equation 2-33.

$$P = l_0 \sqrt{\frac{\lambda \rho_j}{\rho_t}} \left(1 - \frac{\alpha Y}{p_{jV^2}}\right) + r \qquad \text{2-32}$$

Where ‘r’ is the radius of the crater (measured near the bottom of the hole) and $'\lambda'$ is a parameter introduced to account for differences in the transfer of momentum to the target from a continuous and particulated jet. Where 1 is used for a continuous jet and 2 for a fully particulated jet.

2.7.3.3 Particulated jet

For a jet that particulates before impact with target, Carleone et al., 1982 in Ref. [2], posited that the actual penetration is reduced from the continuous jet penetration dp by the formula:

$$dp' = dP(1 - \tfrac{g}{go}) \qquad \text{2-33}$$

Where ‘g’ is the distance between jet particle, and go is an empirical constant, 6.5 for precision shaped charge and 4-6 for small charges. This model. However, the model did not account for the tumbling, dispersion angle and breakup time that characterised a jet. Smith 1981, undertook a more realistic approach by applying the Monte Carlo technique to the effect of tumbling, dispersion and breakup by following a prescribed probability distribution of each jet particle. By applying the Tate method [39] for a rod penetrator, excellent agreement was achieved with experimental results.

2.7.3.4 Stand-off distance

It is known from experiment that there is a significant effect of stand-off distance on penetration depth [79]. Allison and Bryan [82] introduced the concept of the virtual origin to account for the effect of stand-off distance. The virtual origin is a point on the distance-time plane where all the jet elements appears to originate from [39] (a projection). Allison and Vitalli studied the effect of stand-off distance and proposed a formula using the concept of virtual origin [83] for a continuous jet.

$$P = S\left[\left(\frac{V_0}{V_{min}}\right)^{\frac{1}{y}} - 1\right] \quad \text{2-34}$$

Where 'S' is the distance between the virtual origin and the target, V_0 is the velocity of the jet and 'y' represents $\sqrt{\rho_t/\rho_j}$.

In 2012, Elshenawy [84] linked the correction term $\frac{\alpha Y}{p_{jV^2}}$ in Equation 2-36 to a non-dimensionless number in impact dynamics [7].

$$\frac{\alpha Y}{p_{jV^2}} = \frac{\alpha}{J_D} \quad \text{2-35}$$

where $\mathrm{J_D} = \frac{p_{jV^2}}{Y}$ is the Johnsons damage number.

The Johnson's damage number was used to modify Allison-Vitali equation of jet penetration to obtain the depth of penetration of an oil well perforator.

$$P = z\left[\left(\frac{V_j}{V_c}\right)^{1/y} - 1\right]\left(1 - \frac{\alpha fc}{p_{jV^2}}\right) \quad \text{2-36}$$

where fc represents the compression strength of steel, p_j is the density of jet and V is the velocity of the jet.

While this theory was able to predict the depth of penetration, the model did not take account of secondary effects or after flow of the jet as pointed out by Evans et al., [81]. Additionally, the model also ignored target compressibility and did not take into account the various material density changes arising from different layers of the earth. It is consequently important to assess whether target compressibility during the jet penetration has a significant effect on the depth of penetration as well as secondary effect.

2.8 Summary

Overall, the performance of shaped charges depends largely on the liner, which is a function of both the characteristics of the original material and the liner microstructure. Essentially, the microstructure is controlled by the processing technique employed. As such, this chapter has outlined the main parameters governing the performance of shaped charges, with a particular emphasis on the liner and has reviewed relevant literature focused on the different liner manufacturing techniques. The feasibility of employing AM process for liner production was considered in view of its numerous benefits. This chapter has also highlighted the disadvantages of additive manufacturing techniques as well as the defects of parts produced from such processes. Some relevant shaped charge models including the steady state Birkhoff model (which assumed a constant collapse velocity) and the unsteady state PER model (where the velocity varies along the liner) have been presented alongside jet penetration models and their modifications in relation to standoff distance, material strength, jet breakup and secondary particulation. This provides a baseline for consideration of the performance of the shaped charges this thesis focuses upon.

3 Numerical Method and Parametric Study

3.1 Introduction

This chapter presents the Autodyn 2D numerical hydrocode used in this work. It describes the shaped charge set-up and penetration into a target and presents the mathematical and constitutive equations used to describe the materials employed in this work. Verification and validation of the numerical hydrocode was conducted and discussed. The chapter also evaluates the effect of some key parameters such as: the effect of confinement, liner material strength, surrounding medium and head height on charge performance, with a view to improve the accuracy and confidence in the hydrocode predictions in this project.

3.2 Numerical hydrocode

The non-linear dynamic hydrocode, Autodyn 2D was employed for all the numerical simulations carried out in this research. The hydrocode is designed to solve non-linear problems such as impact, blast, penetration and explosion [85] using inbuilt mathematical models based on conservation of mass, momentum and energy [86]. The use of Autodyn for modelling shaped charges has been investigated by multiple researchers and good agreement with experimental result [55], [87] has been obtained. In modelling shaped charges, the jet formation is modelled using the Euler processor based on continuum mechanics. The Eulerian grid is capable of large and rapid deformation in gases, fluids and where large distortions exist in solids because of its fixed grid through which the material in question flows, while the Lagrange processor is suitable for modelling solid continua where the grid distorts with the material. Other processors include: ALE (Arbitrary Lagrange Euler), the shell processor (for modelling thin structures) and Smooth Particle Hydrodynamics (SPH). These processors can be coupled between each other by remapping various regions to improve computational efficiency and accuracy.

In modelling shaped charges, the explosive, casing and liner are filled into the Euler multi-material part as shown in Figure 3-1. The jet output from the Euler solver will then be remapped to Lagrange moving grid before penetration into the

target. To avoid distortion of the mesh, an ‘erosion strain’ is applied to the jet and target materials. The erosion strain is not a physical phenomenon but a numerical algorithm to prevent mesh distortion [7].

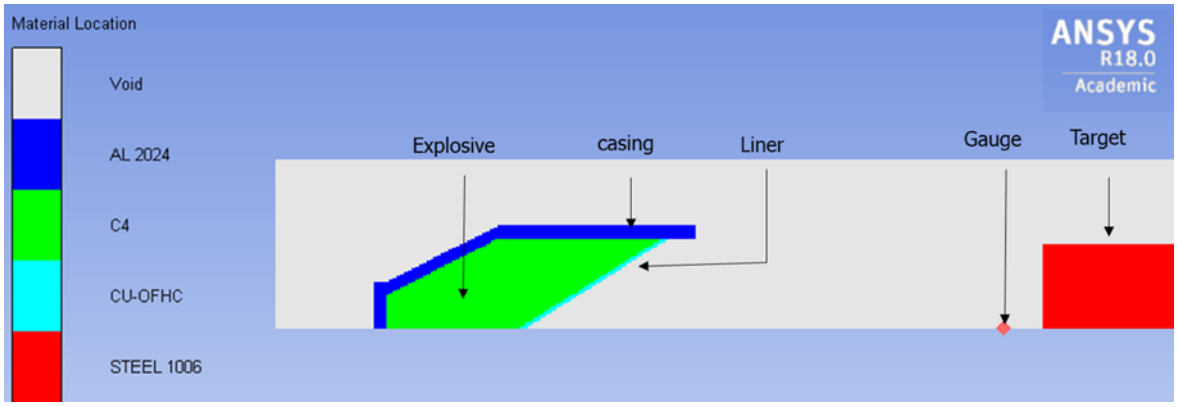

Figure 3-1 The Autodyn 2D set-up of a shaped charged and target in the multi-material Eulerian grid.

3.3 Standard shaped charge jetting analysis

The shaped charge jetting analysis employs the Euler, Lagrange and Shell processors in Autodyn to calculate the parameters of the liner and jet at different segments. This approach adopted is based on the unsteady state Pugh, Elchelberger and Rostoker theory [76], which assumes a variable instead of a constant collapse velocity to calculate the liner and jet parameters. By creating localised segments commonly referred to as nodal points or shell mass points [88], calculation of various shaped charge parameters such as mass of the liner and jet can be obtained using the formulae presented in Equations 3-1 and 3-2, where ‘j’ is a mass point assumed by PER to split into a slug and a jet [76]. Other parameters that can be obtained from the shell jetting analysis include (liner) collapse angles, jet momentum, jet kinetic energy, amongst others.

$$m_{jet}^{j} = m^{j}.\frac{1-cos\left(\beta_{0}^{j}\right)}{2} \qquad 3\text{-}1$$

$$m_{slug}^{j} = m^{j}.\frac{1 + cos(\beta_0^j)}{2} \qquad 3\text{-}2$$

To set up the jetting calculation, the liner is modelled as a shell, while the explosive and casing are modelled in the Eulerian grid. Although the liner thickness is considered during set up, it is not included in the geometric representation of the shell. The shell processor enables the creation of a string of jetting point shown in Figure 3-2 which are arranged in order in which they are expected to jet. [89]. Coupling is done between the Euler and shell sub-grid to allow deformation of the shell (liner) [88]. The liner apex point, which is usually node one, is fixed by a boundary condition to prevent its motion. This is done as this point is at the axis of symmetry and cannot jet while other jetting points are defined. After the simulation and jetting is completed, the jetting output can be read from the resultant history files and the following data can be obtained:

- Liner and jet mass
- Liner momentum
- Jet momentum
- Liner KE
- Jet KE
- Initial X coordinate
- Initial Y coordinate
- Liner thickness
- Liner collapse angle
- Jet velocity
- Cumulative jet mass and its KE
- Time of jet formation

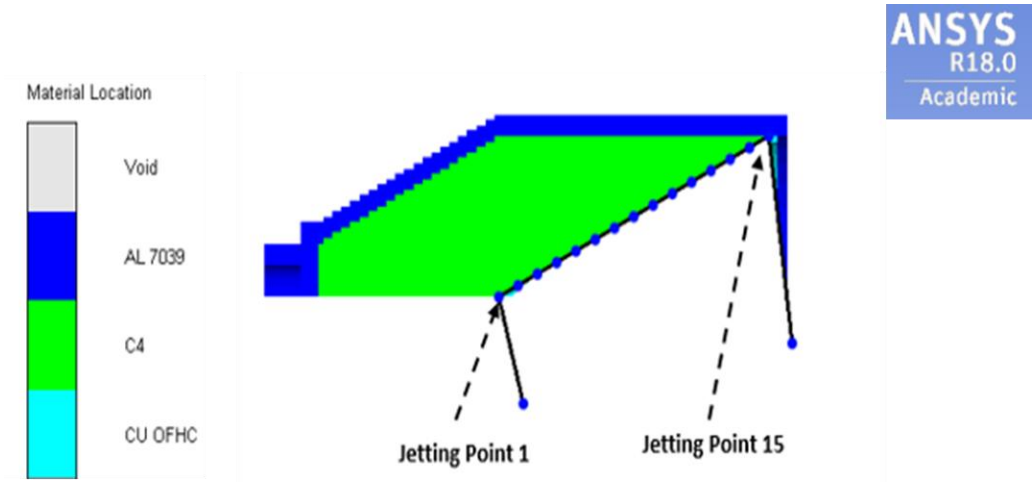

Figure 3-2. Jetting profile from Autodyn 2D with the nodal points**.**

3.4 Material description

The behaviour of a material in a numerical simulation depends largely on the mathematical and constitutive equations underpinning it; these which are represented in the form of Equations of state (EOS) and strength models. The EOS are derived from a range of experimental high strain rate impact loading conditions. To effectively model the shaped charge liner collapse, jet formation and penetration, the following equations of states detailed in the following sections were employed.

3.4.1 Description of the explosive

The Jones Wilkins-lee (JWL) equations of state, which describe the adiabatic expansion of explosive detonation in a simple pressure, volume and energy relationship [90], is presented in Equation 3-3 and was used to model the explosive fill for the shaped charges considered here.

$$P = A\left(1 - \frac{\omega}{r_1 v}\right)e^{-r_1 v} + B\left(1 - \frac{\omega}{r_2 v}\right)e^{-r_2 v} + \frac{\omega E}{v} \qquad 3\text{-}3$$

Where p is the pressure, v is the relative volume (1/ρ). A, B, r_1 r_2 and ω are constants which must be determined.

The linear coefficients A, and B, are determined from the change in internal energy 'E', the Chapman-Jouguet pressure and density [91]. In this project, the linear (A and B) and non-linear coefficients (r_1, r_2, and ω) in the Autodyn 2D (inbuilt parameters) hydrocode were employed. The explosive used for the shaped charges was PE 8, which is an advanced insensitive plastic explosive, manufactured by Chemring Energetics, UK. The explosive had a density of 1.57 g/cc and a velocity of detonation of 8,000 m/s (nominal), with improved mechanical properties to C4. Major ingredients are 86.5% RDX by weight, plasticisers / binder 12.5% and minimum 2,3 dimethyl-2,3-dinitrobutane (DMNB) taggant - 1%. However, the PE 8 explosive is not contained in the Autodyn library, thus, the C4 was employed but with a variation of the density and detonation energy to reflect the PE 8. Other mechanical properties employed for the PE 8 explosive in the numerical simulation are detailed in Table 3-1.

Table 3-1. Description of the PE 8 extracted from Autodyn 2D material data.

Equation of State	**JWL**
Reference Density (g/cm^3)	1.57
Parameter A (GPa)	609.0
Parameter B (GPa)	12.95
Parameter R1	4.5
Parameter R2	1.4
Parameter W	0.25
C-J Detonation Velocity (m/ms)	8.0
C-J Energy / unit Volume (J/mm^3)	9.0
C-J Pressure (GPa)	28.0
Erosion Strain	1.01000E+20
Type of Geometric Strain	Instantaneous
Maximum Expansion	0.1

3.4.2 Description of the liner materials

The liner materials used in this research programme were solid OFHC copper, aluminium, polylactic acid (PLA) and copperfill. The PLA and copperfill liners were produced through the additive manufacturing techniques of filament deposition modelling and direct metal selective laser sintering process. A commercially available Ultimaker 3D extended printer was used for the production of the PLA and copperfill liners. The EOS of PLA were derived and verified in this work as these were not covered in Autodyn (the approach adopted is presented in Chapter 6). For many solid materials which do not undergo phase transitions above the material's elastic limit, the shock Hugoniot data is linear in the shock velocity (U_s) and particle velocity (U_p) plane which is described by the linear Rankine-Hugoniot relationships in Equation 3-4 [92]. However non-linear behaviour have been observed with polymeric materials [93].

$$U_s = C_0 + Su_p, \qquad 3\text{-}4$$

Where C_0 and S are constants which are generally determined by experiment. However, C_0 has been shown to be equivalent to the bulk sound speed of the metal at ambient conditions while the second variable, S, reflects the rate of change of compressibility of the material with pressure [94].

Based on the above, extrapolation of a linear Rankine Hugoniot fit, is often equivalent to the bulk sound velocity. However, for polymers, the linear extrapolation of the linear Rankine Hugoniot fit to the y-intercept always overestimates the bulk sound velocity due to the nature of material collapse on compression (differing strengths of inter-atomic and chain bonds) [92]. Table 3-2 is the material description for OFHC copper employed in this research.

Table 3-2. Material description for OFHC copper extracted from Autodyn 2D material data.

Equation of State	Shock
Reference Density (g/cm^3)	8.93
Gruneissan coefficient	2.02 (none)
Parameter C1 (m/ms)	3.94
Parameter S1 (none)	1.48
Reference Temperature (K)	300
Specific Heat (kJ/gK)	3.83E-04
Erosion Strain	1.01000E+20
Type of Geometric Strain	Instantaneous

3.4.3 Description of the material casing

The shock EOS was employed for the liner material behaviour, while the Johnson-Cook (J-C) strength model was used. The J-C model describes the strength behaviour of a material when subjected to large strains, high strain-rates and high temperatures. It is grouped into three parts:

1. The relationship between strain and stress
2. The relationship between strain rate and stress, and
3. A section connecting the stress value with material temperature during plastic deformation (thermal material softening)

A version of the J-C material model [95] which expresses flow stress in terms of equivalent plastic strain, plastic strain rate and homologous temperature was used to model the aluminium and steel target materials. The flow stress, given in Equation 3-5 is:

$$\sigma_y = \left(A + B\varepsilon_p^n\right)(1 + CIn\,\varepsilon^*)\left((1 - \mathrm{T}^*)\right)^m. \qquad 3\text{-}5$$

Where ε_p is the plastic strain, ε^* is the strain rate, A is the yield stress constant, B is the strain hardening coefficient, n is the strain hardening exponent, C is the strain rate dependence coefficient, m is the temperature dependence exponent, and T^* is the homologous temperature which is described by the relation in Equation 3-6.

$$\mathrm{T}^{*} = \frac{\left(T - T_{ref}\right)}{\left(T_{melt} - T_{ref}\right)} \qquad 3\text{-}6$$

Where T_{ref} and T_{melt} are the reference and melting temperatures of the material.

The Johnson-Cook equation has five constants: A, B, C, n and m [95] used for calculating material dynamic response during plastic deformation. The inbuilt material models employing the Johnson cook strength model for al and steel (the casing materials employed here) are described in Table 3-3.

Table 3-3. Mechanical properties for the material casings extracted from Autodyn 2D material data.

Material	Al 2024	Steel 1006
Equations of state	Shock	Shock
Reference Density (g/cm^3)	2.78	7.8
Gruneissan Coefficient	2.0	2.170
Parameter C1 (m/ms)	5.32	4.56
Parameter S1	1.33	1.49
Parameter C2 (m/ms)		0.00
Parameter S2	0.00	0.00
Reference Temperature (K)	0.00	300.
Strength	Johnson cook	Johnson Cook
Shear Modulus (GPa)		81.8
Yield Stress (GPa)		0.35
Hardening Constant (GPa)		0.27
Hardening Exponent		0.36
Strain Rate Constant		2.2E-02
Failure	None	none
Erosion	Geometric Strain (Instantaneous)	Geometric Strain (Instantaneous)

3.5 Mesh sensitivity study

It is well known that the size and density of the mesh affects the accuracy of the numerical simulations as well as the time required to complete the simulation [96], [97]. Essentially, smaller mesh size (closer to reality) produces better agreement with experiments but at the cost of higher computational resources [84], [98] albeit the performance of the computer. A balance between accuracy and computational time resource is therefore required. In this study, a mesh

sensitivity study was conducted using 0.15, 0.2, 0.3, and 0.35 mm square mesh sizes as outlined in the following sections.

3.5.1 Shaped charge jet formation and penetration

As mentioned earlier, the shaped charge jet formation and penetration process employed the Eulerian and Lagrangian solvers in the Autodyn 2D. The Eulerian solver enabled the simulation of the fast-moving explosive detonation products, while the target (mild steel) was filled into the Lagrangian grid at a distance of 3 cone-diameters (CD). Monitoring gauges were placed at 2CD to obtain the jet tip velocity. A 50 mm conical shaped charge OFHC copper liner with a 40-degree cone angle in a 3 mm aluminium 2024 casing was designed. The charge is shown schematically in Figure 3-3.

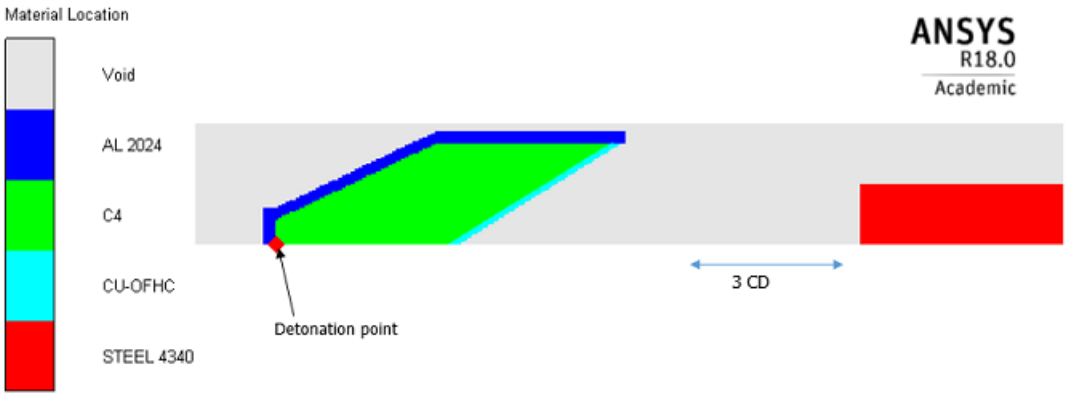

Figure 3-3. Autodyn 2D Layout of shaped charge penetration into mild steel at 3 charge diameter.

An erosion strain was applied to all the materials to avoid errors in the simulation process. The penetration was allowed to run until the jet was completely eroded in the target or until the tip velocity dropped below 1 km/s, at which point, no further penetration could be made [99]. The total time taken for the jet to penetrate the target and the resultant penetration depth obtained from each mesh size case is presented in Table 3-4.

Table 3-4. The penetration depth and jet tip velocity obtained for different mesh sizes.

Mesh size (mm)	Time (hrs)	Penetration Depth (mm)	Jet tip Velocity mm/μs
0.15 x 0.15	277	234	9.036
0.20 x 0.20	94	226	8.771
0.30 x 0.30	36	216	8.133
0.35 x 0.35	22	196	8.051

Note: The time consumed is based on a computer employing an intel (R) Core (TM) i7-6700HQ CPU@2.6GHz 2592 Mhz processor.

A non-linear trend in both jet tip velocity and final depth was apparent, with increasing convergence as the mesh size was reduced. This is illustrated in Figure 3-4. Which plots the key numerical data presented in Table 3-4.

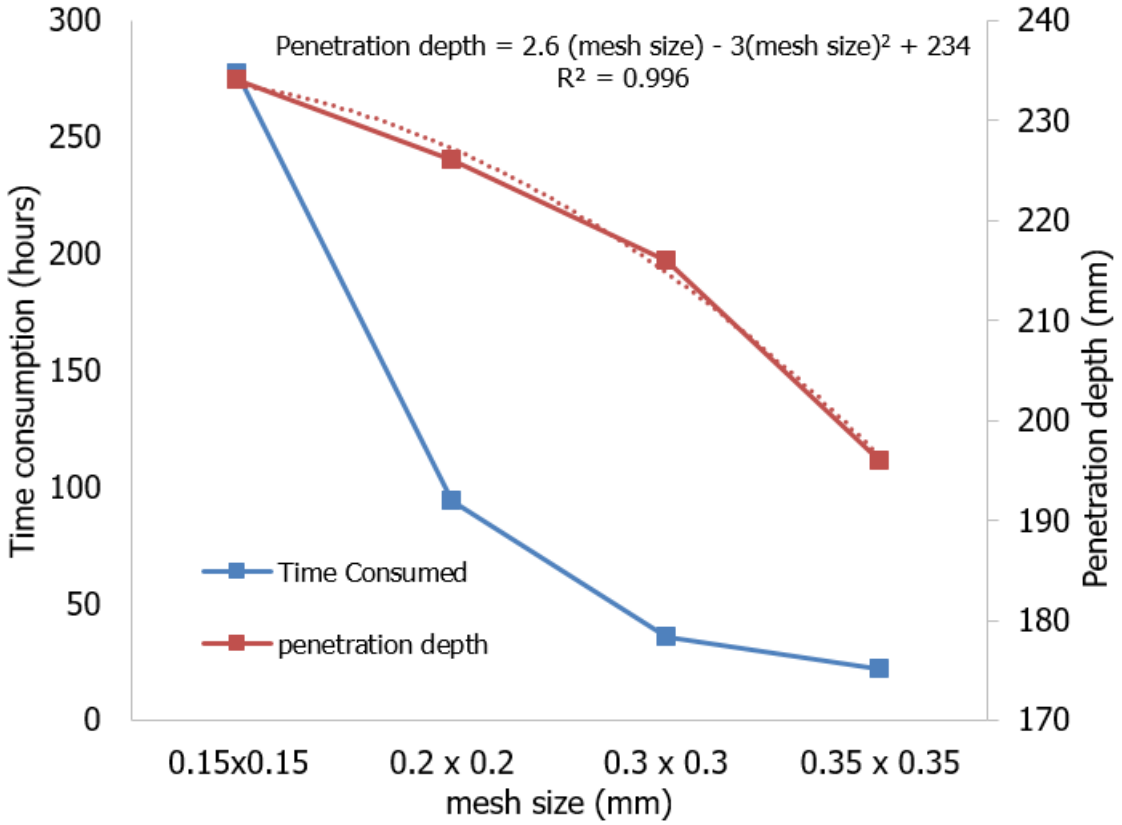

Figure 3-4. Relationship between penetration depth and time consumption for the various mesh sizes considered.

From Figure 3-4, it is immediately apparent that a polynomial relationship exists between the calculated penetration depth and the mesh size; extrapolating the corresponding best-fit curve to a theoretical mesh size of '0' mm provides a corresponding depth-of-penetration of 234 mm. This suggests that at a mesh size of 0.20 mm the error in calculated shaped charge performance is only around 3.4%. While a further reduction in mesh size would therefore, lead to a corresponding increase in accuracy, this would be minimal. Further, it can be observed from Table 3-4 that more time is consumed to run a smaller mesh size compared with a bigger mesh size. Further, the jet tip velocity increases with decreasing mesh size – something highlighted in Figure 3-5 below, with the highest jet tip velocity recorded for 0.15 x 0.15 mm mesh size. Essentially an additional 58 hours was required to run the model with a 0.2 mm rather than 0.3 mm mesh size, with an improvement in accuracy of only around 7.6% (relative to the nominal '0' mm mesh size baseline depth of 234 mm). Consequently, it was decided that, on balance, the computational cost to move beyond a 0.3 mm mesh was too great given the diminishing returns and this mesh size was therefore employed for all subsequent simulations.

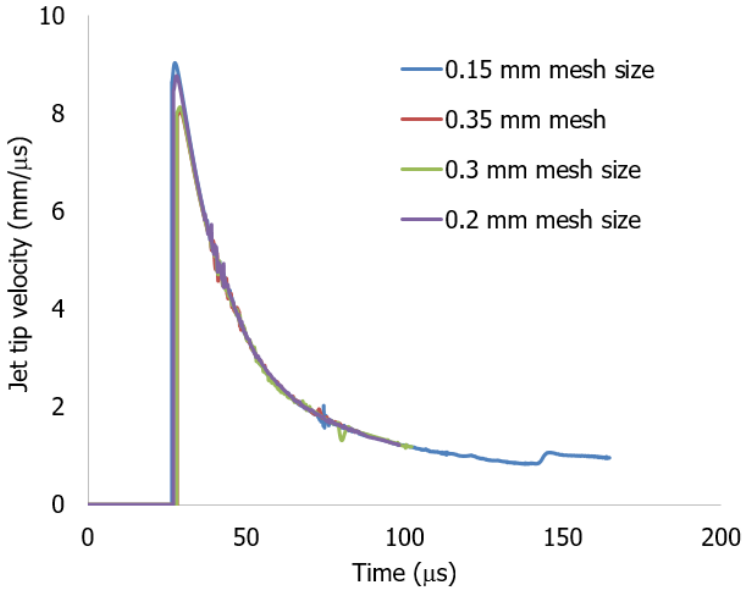

Figure 3-5. Recorded jet tip velocities of the gauge traces for the various mesh sizes considered at 2 CD SOD.

3.5.2 Standard shell jetting analysis

The standard shell jetting analysis employs the shell solver in Autodyn to compute the masses of jet and slug, collapse angle, jet kinetic energy and momentum based on the PER theory of continuum mechanics [100]. The explosive and liner were filled in the Eulerian multi-material grid while the liner was modelled as a thin element. Polygon points were created on the shell element during interaction and coupling between the Eulerian and shell element was done to enable the shell element to deform systematically with the Eulerian grid. With a fixed boundary inserted at the liner apex point, jet parameters during liner collapse and jet formation were obtained. Errors encountered during the jetting process were eliminated by deleting tangled polygons at the jetting points. Overall, a total of 25 jetting points were created, as shown in Figure 3-6.

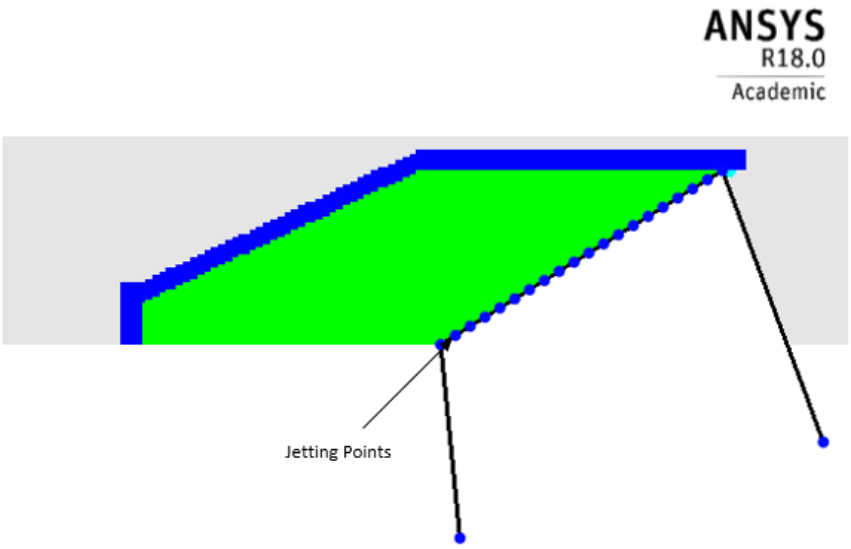

Figure 3-6. Representative layout of shell jetting points from Autodyn 2D.

The output data from the standard jetting analysis was obtained from the history files. The simulations were allowed to run until jetting was completed and a standard jetting analysis was obtained from the resultant history file which detailed key parameters. As an example, the jetting profile at different stages in the jet formation for the case of a 0.3 mm mesh at Figure 3-7 shows the gradual collapse of the liner with time as described by Pugh et al., 1952 which assumes a variable instead of a constant collapse velocity.

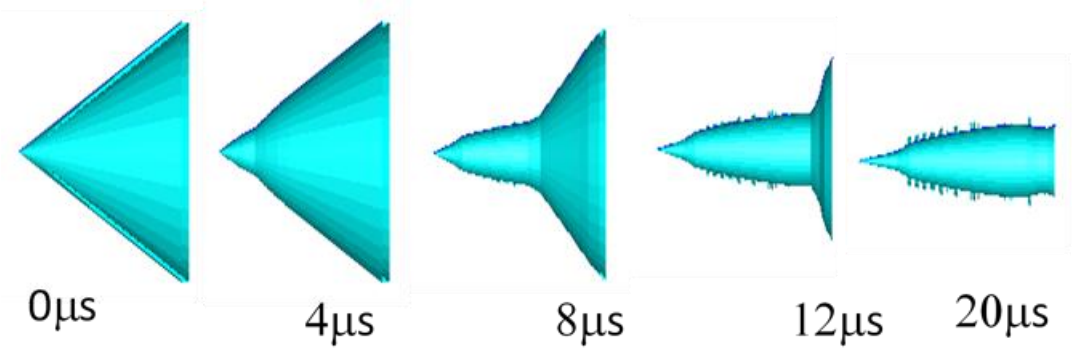

Figure 3-7. Shaped charge jetting profile of 0.3 mm mesh size liner collapse.

It was observed that the cumulative jet masses recorded in all mesh sizes were similar until a coordinate distance of nominally 140 mm on the X-axis. Beyond this point, a slight increase in cumulative jet mass was observed to occur at lower mesh sizes, indicating an increase in the amount of liner material forming the jet. This simply means that the use of a finer grid/mesh is leading to less erosion of material as distortion increases, with a seeming convergence towards the 0.35 mm mesh size. The relationship between cumulative jet mass and the on-axis 'X' jet is presented in Figure 3-8.

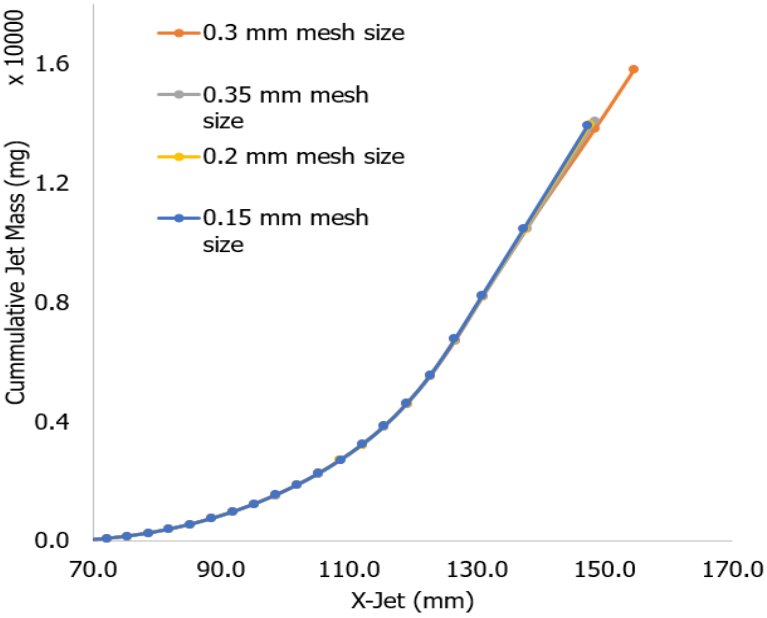

Figure 3-8. Mesh sensitivity study for standard jetting analysis.

3.6 Validation of the numerical model

Although the use of Autodyn has been validated severally, the decision to validate the numerical simulation employed here was to ensure an accurate comparison with the experimental results – thereby allowing for reduced experimental costs. The results obtained in terms of penetration depth for the experimental and numerical simulation are presented in Table 3-5, while the hole profiles are at Figure 3-9.

Table 3-5. Comparison of experimental and numerical simulation of 50 mm shaped charge penetration into mild steel at 3 charge diameters.

Liner material/ thickness (mm) / Cone angle (0^c)	**Penetration depth (mm)**		**Jet tip velocity (mm/μs)**	
	Cu /1.25/40	Cu /2.5 / 60	Cu/1.25/40	Cu/2.5/60
Experiment	215.0	165.0	7.28	5.59
Simulation	226.0	172.0	8.13	6.10
Difference %	4.8	4.1	10.45	8.36

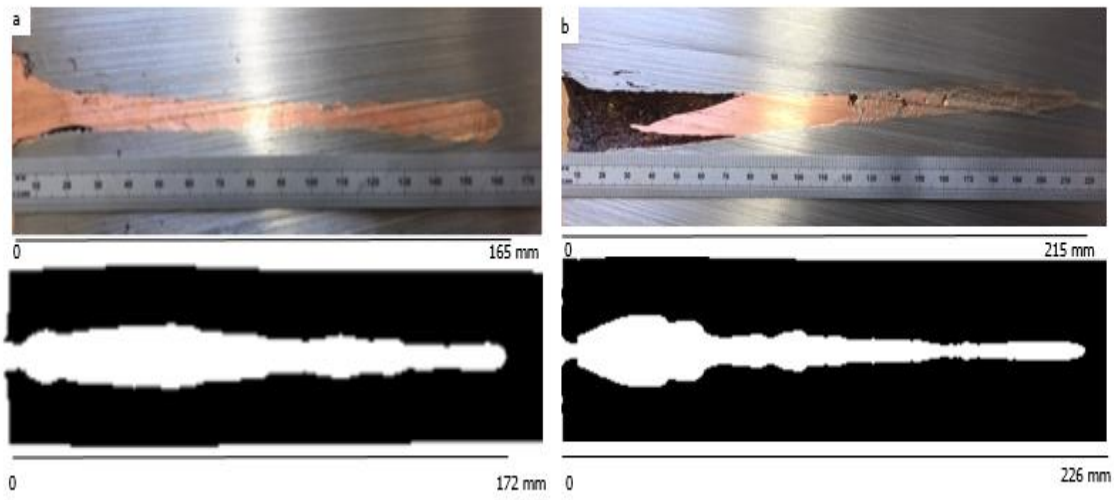

Figure 3-9. Numerical and experimental hole profiles of: a. 2.5 mm Cu liner thickness at 60^0 cone angle, and: b. 1.25 mm Cu liner thickness at 40^0 cone angle.

As indicated in Table 3-5, a lower penetration depth than predicted from the numerical simulations was recorded for the experimental trials. This is tentatively

attributed to the manual filling technique employed which may have led to the presence of pores in the explosive filling, as well as, possibly, liner manufacturing errors, such as material non-uniformity or the shaped charge axis ending up not exactly perpendicular to the target surface. A combination of these factors could alter the resultant jet characteristics (in contrast to the near perfect conditions in the numerical simulation). However, despite these error sources, only a small difference of <10.4% was observed between the numerical and experimental jet tip velocities, and <4.8% variation in penetration depths, providing satisfactory confirmation to the rigour of the experimental approach adopted.

3.7 Effect of confinement on predicted jet tip velocity

The effect of confinement and the degree of confinement on the predicted jet tip velocity was investigated. We evaluated the effect of bare charge and confined charge using aluminium 2024 casing. The advantage of the bare charge is that it reduces the charge set-up and time required to run the simulation as one material is absent. Table 3-6 is a summary of the bare charge, case thickness and predicted jet tip velocities calculated via the resultant simulations.

Table 3-6. Bare charge, case thickness and predicted jet tip velocity.

Case thickness (mm)	0 (bare charge)	1	2	3	4
Predicted Jet tip velocity (km/s)	8.004	8.047	8.087	8.136	8.137

The result of this study show that the bare charge produced the lowest jet tip velocity as expected. However, the difference between the predicted jet tip velocity of the bare charge and the 4 mm liner thickness is only 1.63%. This result therefore shows that the effect of whether a charge is confined or not on the jet tip velocity is very minimal. Hence, aside from the purpose of containment or securing the charge, the use of a casing appears to offer little effect on the performance of the charge.

3.8 Effect of liner material strength.

One of the simplifying assumptions employed in jet calculation is that the strength of the liner is negligible because the pressure at the stagnation point during liner collapse and jet formation far exceeds the yield strength of the liner material [16]. As such, the material is treated hydrodynamically as a fluid with a negligible yield strength. Evaluation of the stagnation pressured recorded from our base line shaped charge model indicates pressures within the range of 80 GPa giving credence to such assumptions. In this study, however, we conducted 4 calculations to investigate this assumption by examining the sensitivity of the yield stress of the liner material to the predicted jet tip velocity. The calculations were performed using the hydrodynamic assumption, no material strength and the Johnson-Cook equations of state with various yield strengths of 0.06, 0.075 and 0.090 GPa. A summary of the yield stresses used in the simulation and the resultant jet tip velocities is presented in Table 3-7 and represented in Figure 3-10.

Table 3-7. Strength model, yield stress and predicted jet tip velocity.

Strength Model	Yield stress (GPa)	Jet tip velocity (km/s)
Johnson-Cook	0.060	7.833
Johnson-Cook	0.075	7.786
Johnson-Cook	0.090	7.762
Hydrodynamic	0	8.136

From Table 3-7, it is apparent that increasing the yield stress produces lower jet tip velocities. Thus, neglecting the yield stress (hydrodynamic), over-predicts the jet tip velocity. Although this is a very small difference (4.59%) when compared to the baseline Autodyn 2D recorded yield stress of copper, this result shows that taking into account the yield strength of the liner material improves accuracy relatively.

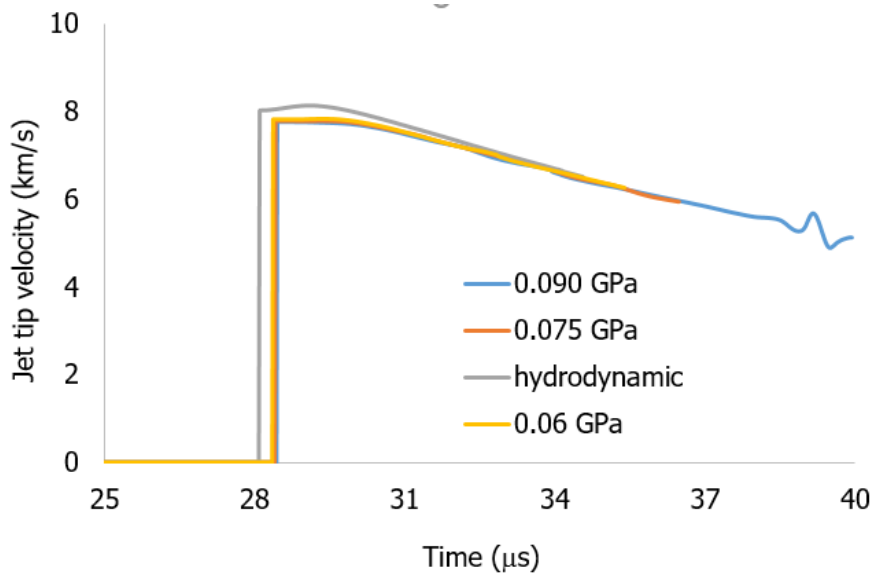

Figure 3-10. Relationship between material yield stress and jet tip velocity.

3.9 Effect of surrounding medium / environment on the predicted jet tip velocity

The effect of the surrounding medium was investigated by examining the influence of forming the jet in void and air. The use of void is common because of the simplicity in the EOS of void compared to that of air. Hence, by performing the simulation in a void rather than the air, the resultant simplification makes the simulation faster. More so, the presence of air drag in the air reduces the predicted jet tip velocity. In order to determine the effect of surrounding medium, effect of air drag and void on the performance of the jet was conducted. The result revealed that the predicted jet tip velocity for the void at 2CD is 8.136 km/s compared with a velocity for the jet formed in air media only of 8.104 km/s. Importantly, the difference is very small, only 0.30%, which indicates that it is not necessary to use the air medium in jet formation.

3.10 Effect of head height and charge length

As mentioned in section 2.3.3, it is desirable for the charge length to be large enough to allow a planar detonation wave to meet the liner for a point-initiated charge. However, too much a height will only be wasteful and increase the charge mass. According to Walters and Zukas, a head height of about 1.5 CD provides a value beyond which significant improvement in performance are no longer achieved. In this study, we investigated the effect of head height by examining

the predicted jet tip velocities of 5/8, ¾. 1 and 1.5 and 1.8 CD head heights, respectively. The results are presented in Table 3-8.

Table 3-8. Head heights and their corresponding jet tip velocities

Head height (CD)	5/8	¾	1	1.2	1.5	1.8
Distance between charge base and cone apex (mm)	31.25	37.50	50.00	60.00	75.00	90.00
Jet tip velocity (km/s)	8.136	8.141	8.187	8.224	8.226	8.227

From our calculation (Table 3-8), it is apparent that the predicted jet tip velocity increases as the head height increases. However, beyond a head height of 1.5 CD, the performance to the jet tip by a further increase in head height is negligible (0.001 km/s); The effect of head height on predicted jet tip velocity between the largest and smallest head height considered in this work is only 1.04% - an indication of the reduced sensitivity of charge length to predicted jet tip velocity.

3.11 Summary

In this chapter, the Autodyn 2D numerical hydrocode has been validated against static firings of copper liners into steel targets at 3CD with <4.8% variation in penetration depths between experimental and numerical simulation noted. This providing satisfactory confirmation with regards to the end use of Autodyn 2D to simulate shaped charge jet formation and penetration. The effects of variables such as the surrounding medium, casing or confinement, head height and liner material strength were studied. The results indicate that, while considering the yield strength of the liner material improves accuracy, the use of casing / confinement offers little effect on the performance of the charge. Also, an observed small difference of only 0.30% in terms of jet tip velocity between a (jet) medium of a vacuum (void) and air indicates that it is not necessary to model charge effects in this area (e.g. changes in atmospheric pressure, etc). In the same vein, the low variation in the different head heights considered is an

indication of the reduced sensitivity of charge length to predicted jet tip velocity. Collectively, these conclusions provide useful bounds for the subsequent study presented here.

4 Experimental Investigation of Shaped Charge Liners Produced from Selective Laser Sintering Process

H.O. Agu, A. Hameed and G.J. Appleby-Thomas
Centre for Defence Engineering, Cranfield University, Shrivenham
SN6 8LA, United Kingdom
Corresponding author: henry.agu@cranfield.ac.uk

This chapter / paper covers one of the key aim of this thesis focused on evaluating the performance of shaped charge liners produced from one of the most commercially used metal additive manufacturing process, that of selective laser sintering. The chapter is designed to stimulate a series of investigations on the feasibility of employing additive manufacturing processes for shaped charge liners by direct comparison with machined liners through experimental trials. Autodyn 2D numerical hydrocode models were employed to provide additional support on the results obtained. The study exploits the benefits, and prospects of employing 3D printing in the production of precision shaped charge liners.

This chapter / paper is adapted from: H. O. Agu*, A. Hameed, G. J. Appleby-Thomas. A research paper submitted to the International Journal of Impact Engineering for publication.

4.1 Abstract

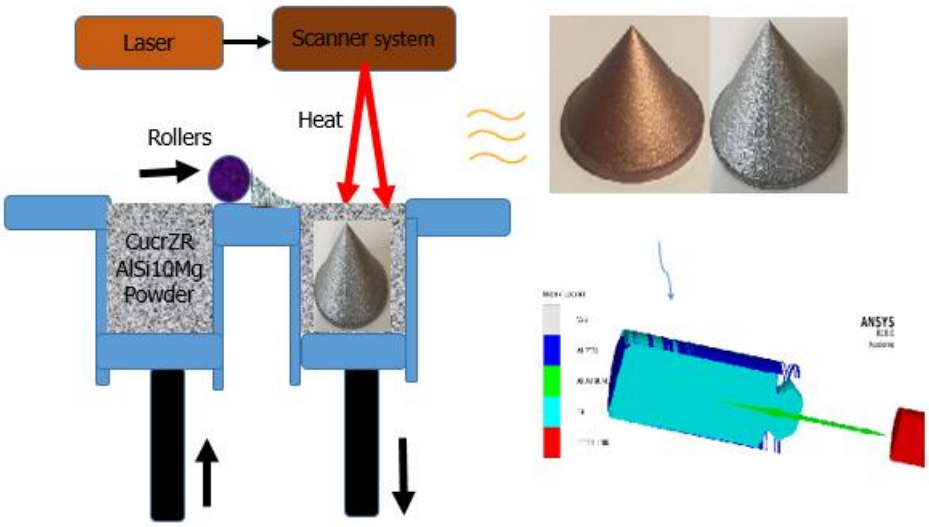

The performance of shaped charge liners produced via the selective laser sintering process has been studied with the aim of elucidating mechanisms underpinning their resultant behaviour. The performance was interrogated by comparing the variations in penetration depths for cones manufactured using both the laser-sintered additive process and conventional machining – in the latter case, liners from OFHC copper bar – with experiments backed by hydrocode simulations. Although performance in terms of penetration depth between the laser sintered and conventionally machined liners was comparable (with variation of less than 0.5 cone diameter), the laser sintered copper cones, however, showed a reduction in performance ($\leq$ 17.2%) attributable in part to relatively higher defects levels (porosity) compared to the sintered aluminium, which showed a higher performance with the corresponding machined liner ($\leq$ 11.8%). This approach highlighted the influence of porosity on the bulk sound velocity and ductility of the processed liner.

4.2 Introduction

When a shaped charge is initiated, the detonation wave accelerates the liner rapidly, (strain rates of $10^{4\text{-}7}$ /s are achievable), collapsing it inwardly [39]. The liner mass is deformed hydrodynamically under the resultant extremely high pressure to produce a jet typically travelling in the region of 9-12 km/s [101]. As such, any asymmetries, for example due to thickness variation, liner microstructure defects, or other flaws in the liner induced during production and assembly, are greatly amplified [102]. As an example, it has been shown that small deviations introduced in the liner (off-axis initiation) produce jet radial drift with a resultant reduction in penetration depth [10], a response attributed to a decrease in the number of jet particles impacting the target hole. In essence, the liner production technique is critical to the performance of shaped charges and several processes have been developed for liner production [10], key amongst which are: flow turning; deep drawing; cold forging, and; machining – as highlighted in section 2.5. However, employment of these techniques for high-density material such as tantalum, in spite of its excellent liner properties (ductility and density required for better performance [32]) is expensive because of difficulties associated with processing such high-density materials.

The ductility of the liner material is of key importance as it controls the breakup time or particulation time, which is critical for the determination of the jet length. In Equation 4-1 [103] the maximum achievable jet length is represented by the differences in maximum $'V_j'$ and minimum jet velocities $'V_{min}'$, with particulation time $'t_p'$.

$$P = (V_j - V_{min}) t_p \sqrt{\rho_j / \rho_t} \qquad 4\text{-}1$$

Increasing the particulation time reduces the number of particles and the extent of their tumbling and transverse motion [24], which in turn increases the jet length. Interestingly, particulation time has been shown to depend largely on the liner microstructure [10], [104]. Consequently, microstructural properties such as a large grain size [105], the presence of impurities and other defects, can reduce jet performance [10], [45], [106]. Some of these microstructural defects are influenced by the manufacturing or processing method. This explains why annealing is usually performed during or after liner production. For example, the conventional machining of liners generally results in a poor grain size distribution such that residual stress is locked in the material during production [10]. Therefore, these manufacturing processes are usually followed by annealing which helps to relieve residual stresses [41] as well as improving ductility [50], properties necessary to achieve longer jet length / higher break-up times. Although processes such as spin-forming has been shown to improve grain size distribution, such techniques are typically expensive (in time and resources). Hence, advanced liner manufacturing techniques such as powder metallurgy [35], [55], [56] and the high energy rate fabrication (HERF) process [23] have been developed to generate a more refined microstructure.

Even though the performance of liners produced using the techniques described above is well-controlled and understood, some of the techniques are also expensive, time-consuming and present difficulties for fabrication from high-density materials, especially when large quantities of small or medium-sized liners are required. Recently, 3D printing (also known as additive manufacturing) has been shown to offer many advantages for the fabrication of composites, including high precision, cost-effectiveness and customized geometry. Further, 3D-printed components can be manufactured quickly and easily, and complex geometries are possible. Additive manufacturing is a broad term for processes in which items are built up by the deposition of layers, which harden from a liquid or gel state. Examples include Direct Metal Laser Sintering (DMLS) – also referred to as Selective Laser Sintering (SLS), inkjet 3D printing, Fused Deposition Modelling (FDM), stereo-

lithography and 3D plotting. Such processes can also be used to fabricate complex composite structures without the typical waste generated by conventional manufacturing. The research reported here was inspired by the realisation that high density (98-99%) liner material can be produced from metal additive manufacturing techniques such as SLS.

The SLS technique employs high power laser beams to fuse metallic powders to form parts with the desired geometry [66]. During the process, any unbound powder is removed to get the final product [57]. Fine powders can also be employed to produce alternative microstructures with potentially interesting results. Although the technique has been known for over 3 decades, the employment of the SLS technique in parts involving high strain-rate events is limited. This is attributable to the lack of comprehensive high strain-rate data on the performance of such build parts. Instead, most research into SLS has focused on parts production, in particular, the effect of process parameters on build parts [107]. As such, even though a lot of progress has been made in building parts (98% metallic composition are achievable via the SLS technique), to the authors' knowledge, the application of the SLS technique in the production of shaped charge liners has not been investigated. Here, we have investigated the penetration performance of liners produced using the SLS technique, comparing their performance to that of machined liners – with experiments underpinned by numerical simulation (ANSYS® Autodyn 2D hydrocode models). Further, optical micrographs of the fabricated liners were evaluated to gain further insight into the liner performance.

4.3 Experimental method

The experimental methods employed here is divided into three sections: material selection, liner production and preparation of the shaped charges.

4.3.1 Material selection

Two extremes of material, Copper (CuCrZR) and Aluminium (AlSi10Mg), containing > 90 % w/w of the corresponding Copper and Aluminium were selected for the laser sintered cones. Copper exhibits extraordinarily high

dynamic ductility, which accounts for its high penetration performance [108], whereas aluminium does not elongate / stretch as extensively as copper during deformation , but rather – in the role of a shaped charge liner – forms a very large crater [98], particularly in concrete. The properties of the materials selected are detailed in Table 4-1. Densities of the initial and final products, measured using helium Pycnometry, were < 0.3g/cc; an indication of fully dense parts comparable to the theoretical density of the material. The machined liners were processed from bulk aluminium and oxygen free copper.

Table 4-1. Properties of materials selected for the SLS liners.

Properties	**SLS Copper Liner**	**SLS Aluminium Liner**
Material Alloy	CuCrZr	AlSi10Mg
% content	98-99% copper	92% aluminium
Theoretical density	8.90 g/cc	2.71 g/cc
Measured density	8.71 g/cc	2.62 g/cc
Variation	0.21 g/cc	0.09 g/cc

4.3.2 Production of the liners

Similar to many other 3D printing processes [62], the SLS process starts by drawing the design of an object in a computer aided design (CAD) file (in this case using the universal *.stl file format) which is then divided into cross-sectional slices that will be printed. The liners were commercially produced with typical achievable part accuracy of $\pm$100 μm (corresponding to the layer thickness). A 50 mm cone diameter (CD) shaped charge was selected for the study. To evaluate the performance of SLS liners, a comprehensive approach to cover the effect of liner thickness and cone angles was implemented.

Conical liners with varying thicknesses of 1.25 and 2.5 mm were considered, with varying cone angles of 40, 60 and 90 degrees as-required / as shown in Figure 4-1. A total of 16 conical liners were produced via both the laser sintering process (from aluminium and copper) and the traditional machining process from copper and aluminium bar; precise liner designs are outlined in Figure 4-1, with as-produced machined and LS liners shown in Figure 4-2. Table 4-2 details the various liners thickness and cone angles employed in this chapter.

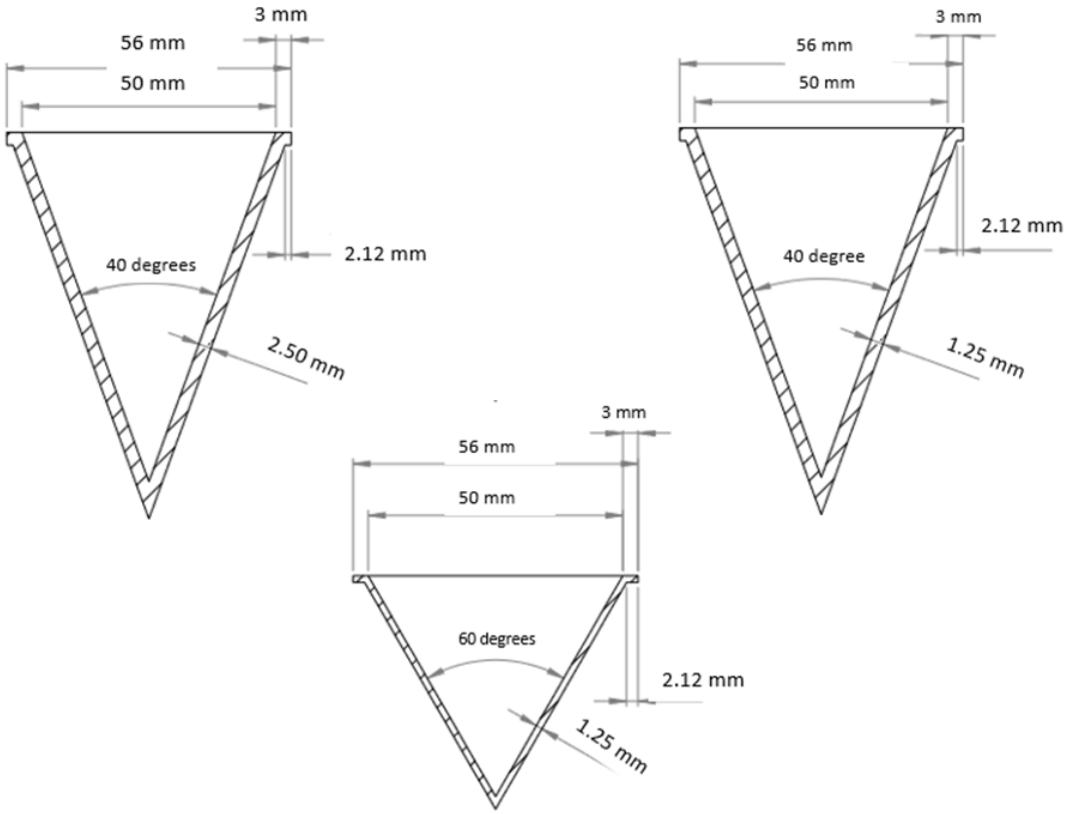

Figure 4-1. Liner design for production using the SLS process (dimensions in mm).

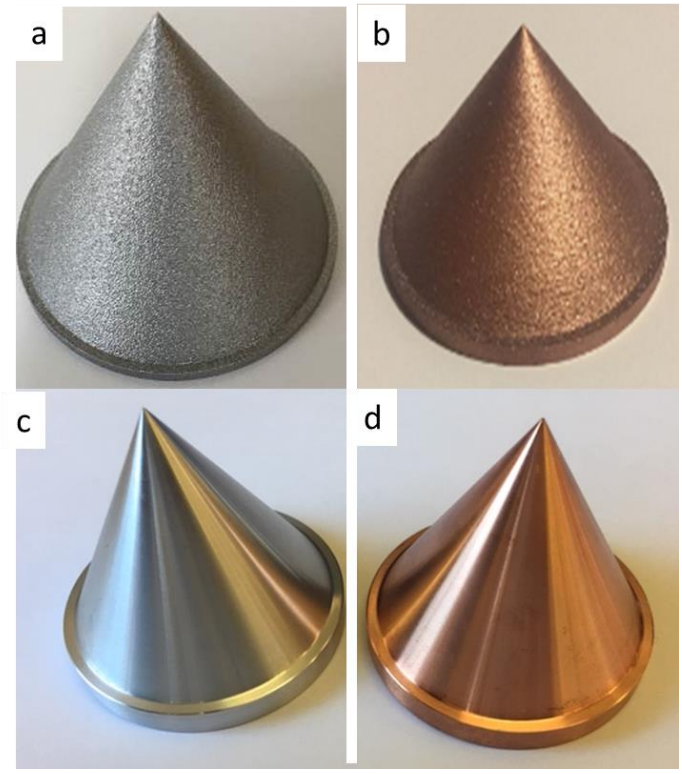

Figure 4-2. Produced Laser sintered aluminium and copper liners (a and b); machined aluminium and copper liners (c and d) in their as-manufactured forms.

Table 4-2. Liner thickness and cone angles employed for the liner production.

Aluminium Liners design	**Copper Liner design**
1.25 mm liner thickness at 40 degrees cone angle	1.25 mm liner thickness at 40 degrees cone angle
1.25 mm liner thickness at 60 degrees cone angle	1.25 mm liner thickness at 60 degrees cone angle
2.5 mm liner thickness at 60 degrees cone angle	2.5 mm liner thickness at 60 degrees cone angle
2.5 mm liner thickness at 90 degrees cone angle	2.5 mm liner thickness at 90 degrees cone angle

4.3.3 Preparation of the shaped charge

The shaped charges were assembled by inserting the printed cones into 3 mm thick aluminium casings and securing them in place with fast acting (5 minutes) 2-part Epoxy / 2K Epoxy, long-lasting adhesive. Hand-packed plastic Explosive No. 8, with a density of 1.57 g/cm^3 and a nominal detonation velocity of 8.0 km/s (nominal) was used in all trials. This explosive is composed of 88% 1,3,5-trinitrohydro-1,3,5-triazine (RDX) by weight, 12.5% plasticisers/binders and a minimum of 1% 2,3-dimethyl-2,3-dinitrobutane (DMNB) as a detection taggant [109]. The explosive fill was pressed slowly against the liner to avoid creating air gaps and to ensure good contact. Adequate care was taken to ensure consistent, concentric filling of the explosive charge across the width of the liners [102], with each filled casing measured to ensure consistency in charge weight. Finally, a plastic cap was used to cover the end of the explosive charge before placement at a distance of 3 CD from the target. The shaped charges were fired into steel (EN24) using L2A2 electric detonators and the result in terms of penetration depth were extracted for analysis.

4.4 Numerical method

The ANSYS Autodyn-2D hydrocode [25] described in chapter 3 was used to model and evaluate the performance of a bulk OFHC Copper and Aluminium shaped charged liners in terms of jet penetration into steel. Although several studies have verified the use of Autodyn in modelling shaped charges, [26], [27], [28], [29], re-validation was undertaken due to the critical role the results obtained here serve where simulations were employed to supplement the experimental trials, (specifically the traditionally machined liners) and to improve the accuracy of the result obtained. Representative design of machined OFHC copper and aluminium liners were employed for re-validation by firing 50 mm shaped charges into 60 mm diameter cylindrical heat treated EN 24 (4340) steel with a tensile strength of 850 N/mm^2 and yield stress of 700 N/mm^2 with Brinell hardness of 248 at 3 CD. Precisely, the 1.25 mm and 2.5 mm cone diameters with 40 and 60 degree' cone angles were employed to obtain multiple data points necessary for

good confidence in the hydrocode simulation. The plastic explosive described in section 2.2 was used with centre point detonation employing an L2A2 detonator. The penetration depth was obtained and reduced for subsequent analysis. A leveller was used to align the cone axis perpendicular to the target. The jet tip velocity was measured by employing 2 sensors placed in aluminium foil and separated by a distance of 50 mm as shown in Figure 4-3. A sensor was used to record the time at which the jet makes contact with the foils.

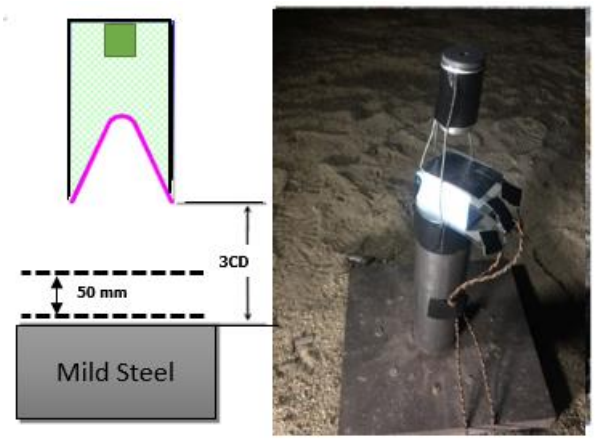

Figure 4-3. Schematic and experimental set up of the shaped charge.

The subsequent simulations were modelled in a void using the Eulerian and Lagrangian solvers coupled in a single analysis to provide an efficient solution [29]. The explosive, liner and casing were represented in the multi-material Eulerian grid while the target was modelled at 3 cone diameters standoff distance (SOD) in the Lagrangian grid. The jet output from the Eulerian solver were remapped to penetrate the target in the Langregian grid. Finally, the velocity gauge was monitored to obtain the jet tip velocity. The material models employed are described in subsequent sections.

4.4.1 Explosive model

The Jones Wilkins-lee (JWL) equations of state, which describes the adiabatic expansion of explosive detonation products, and which is presented in Equation 4-2 [91], was employed to model the plastic explosive.

$$P = A\left(1 - \frac{\omega}{r_1 v}\right)e^{-r_1 v} + B\left(1 - \frac{\omega}{r_2 v}\right)e^{-r_2 v} + \frac{\omega E}{v} \qquad 4\text{-}2$$

Where p is the pressure, v is the relative volume (1/ρ) and A, B, r_1 r_2 and ω are constants which are determined empirically. The Autodyn inbuilt parameters for the linear coefficients were employed because they have been well defined and reported in the previous work reported in Reference [97]. The properties of PE8 explosive used to model the explosive are detailed in Table 4-3.

Table 4-3. Properties of the explosive extracted from the Autodyne library.

Equation of State	**JWL**
Reference density (g/cm^3)	1.57
Parameter A (GPa)	609.77
Parameter B (GPa)	12.95
Parameter R1	4.50
Parameter R2	1.40
Parameter W	0.25
C-J Detonation velocity (m/μs)	8.00
Strength	None
Erosion	Geometric Strain

4.4.2 Liner material

Shock equations of state were employed for the liner and material casing. This was due to the high strain rate encountered on the liner and wall casing during explosive detonation – which led to the production of a shock wave. A linear relationship between the shock velocity and the particle velocity was employed to represent material behaviour in the form presented in Equation 4-3 [110].

$$\mathrm{U_s} = \mathrm{C_0} + \mathrm{SU_p} \qquad 4\text{-}3$$

Where the parameter C_0 is often related to the bulk sound speed of the material, while S is a material constant which corresponds to the first pressure derivative of the bulk modulus – an indication of materials' compressibility. U_s and U_p are shock and particle velocity derived empirically from high strain rate experiments [111]. No strength model was applied for the liner because of the high pressure generated at the explosive–liner interphase, which greatly exceeds the strength of the liner material leading to minimal shear strength effects. The casing and target were represented by the Steinberg–Guinan [112] and Johnson–Cook strength [95] models, respectively. An abridged set of the data of the properties employed for modelling the casing, liner and target, from the Autodyn library, are presented in Table 4-4.

Table 4-4. The mechanical properties of the liner, casing and target extracted from the Autodyn library.

Parameter	**Al 2024 (casing)**	**OFHC copper (Liner)**	**Aluminium (Liner)**	**Steel 4340 (Target)**
Equation of state	Shock	Linear	Shock	Linear
Reference density (g/cm^3)	2.78	8.93	2.71	7.83
Bulk Modulus (GPA)	-	123.0	-	159.0
Gruneissan coefficient – Γ	2.00	2.02	2.10	2.17
Parameter C_o (m/μs)	5.32	3.94	5.38	4.56
Parameter S	1.34	1.48	1.34	1.49
Reference temperature (k)	300	300	300	300
Strength model	none	none	none	Johnson Cook
Shear Modulus (GPa)	-	-	-	0.82
Yield stress (GPa)	-	-	-	0.79
Hardening Constant (GPa)	-	-	-	0.51

4.5 The Microstructure of SLS liners

To provide further insight into the performance of laser sintered liners, transverse sections were prepared (sectioned perpendicularly to the build-plane) with surfaces etched to reveal the underlying microstructure (Figure 4-4).

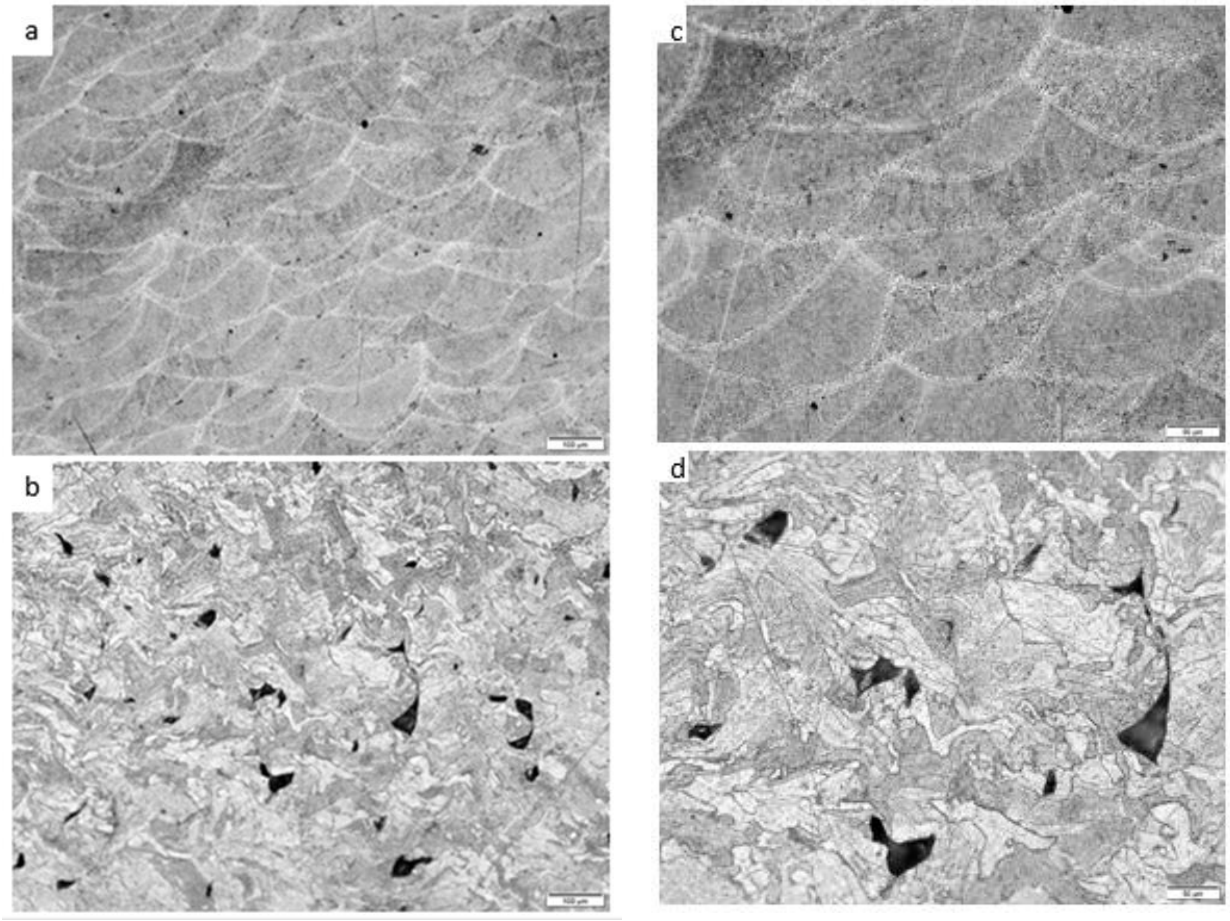

Figure 4-4. Optical micrographs of the transverse section of SLS liners a. Aluminium x10, b. Aluminium x 20 c. Copper x 10, d. Copper x 20.

Both the copper and aluminium liners featured a layered and refined microstructure. This is consistent with the particle size of the feedstock powder and hence the nature of the SLS layered-solidification process. Interestingly, the micrographs of the copper and aluminium liner revealed some dark regions, suggesting the presence of voids/pores at grain boundaries. The microstructure of the aluminium liner features segregated melt pools with more distinct (than the

copper) boundaries and a relatively low number of dark regions. Further investigation of the porosity using the open source image J software package revealed large and irregularly shaped pores in the copper microstructure. This is in contrast with the aluminium liner which possessed very small circular pores (<5 microns) and which had a lower density than their copper counterparts.

4.6 Result and discussion

A total of 16 conical shaped charge liners produced from traditional machining and laser sintering process (of copper and aluminium), with cone angles of 40°, 60° and 90° and having thicknesses of 1.25 and 2.5 mm (Table 4-2) were used in the trials. We compared the performance of the liners by impact testing on mild steel at a distance of 3 CD. The masses of the liners and explosive are presented in Table 4-5. The variation between copper and aluminium liners is immediately apparent. Copper liners, as expected, have the highest masses, owing to their initial high density (see Table 4-1), as compared with aluminium liners. In terms of the mass to charge ratio (M/C), efforts were made to reduce variations resulting from manually loading the explosive in the casings [14]. As such, only a slight variation (<0.8) between the highest and lowest mass to charge ratio was observed and this could be due to manufacturing tolerances. This variation could alter the performance of the charge but only slightly as the head height was constant in all charges. Increasing the quantity of explosive beyond a certain value adds little or no improvement to the performance of the shaped charge (with constant head height). This is because only about 10-20% of the total explosive chemical energy is converted to penetrator kinetic energy.

Table 4-5. Mass of explosive, casing and the mass to charge ratio.

Experiments	Cone angle (0^c) / liner thickness (mm)	Mass of explosive + casing (g)	Mass of explosive only (g)	M / C
SLS	40 / 1.25	466.4	286.1	1.6
Aluminium	60 / 1.25	354.1	221.6	1.6
	60 / 2.50	356.7	208.4	1.7
	90 / 2.50	269.6	159.0	1.7
SLS Copper	40 / 1.25	515.3	283.0	1.8
	60 / 1.25	380.3	211.2	1.8
	60 / 2.50	429.7	210.3	2.0
	90 / 2.50	325.8	174.3	1.9
	40 / 1.25	408.0	171.8	2.4
Machined	60 / 1.25	329.5	138.1	2.4
Aluminium	60 / 2.50	369.7	208.4	1.8
	90 / 2.50	271.4	160.0	1.7
Machined	40 / 1.25	492.2	241.3	2.0
Copper	60 / 1.25	387.6	220.1	1.8
	60 / 2.50	437.3	236.0	1.9
	90 / 2.50	330.5	177.4	1.9

After firing, the targets were sectioned to allow measurement of the resultant penetration depth. We found that generally, all the laser sintered liners produced small entry hole diameters as shown in Figure 4-5 – an indication of the formation of a coherent jet. This implies that the liner(s) apex were aligned perpendicular to the target with minimal drift arising majorly from off-axis initiation or dimensional inaccuracies [102]. Even though it is practically impossible to have a perfectly symmetric jet because of the limitations in manufacturing processes [102], considering the hole profiles shown in Figure 4-5 and the penetration depths achieved, it is very likely that only minimal particle drift existed with the SLS liners employed here.

(a) (b)

Figure 4-5. Entry hole surface of shaped charges with liners produced using the SLS method and the substrates (a) aluminium, and (b) copper.

In terms of performance, all of the different liner material / manufacturing techniques considered produced some form of penetration into the target. However, as expected, copper liners achieved greater penetration depth with narrow craters whereas aluminium liners produced larger crater volumes but shallower penetration in agreement with literature reports [98]. Representative hole profiles of shaped charges produced from the laser sintered liners and machined liners are presented in Figure 4-6.

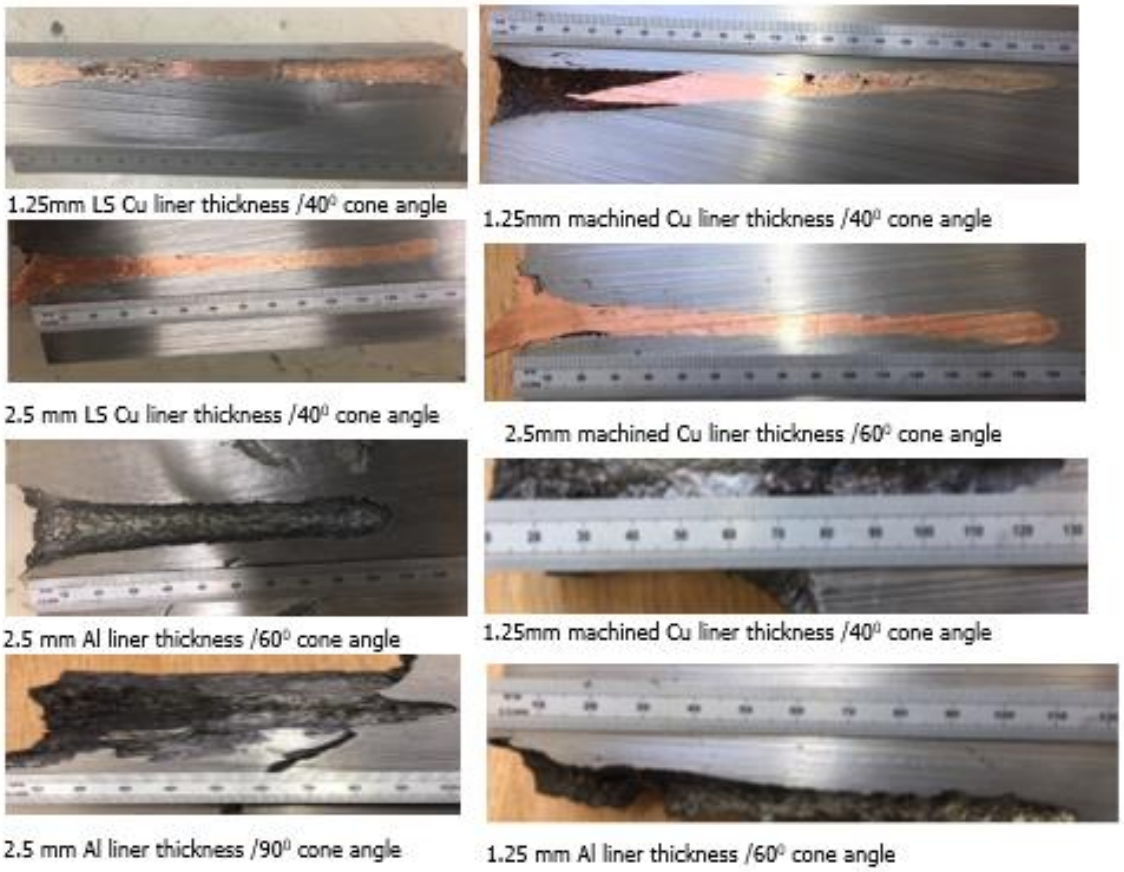

Figure 4-6. Representatives hole profiles made from shaped charges manufactured from the machined (right) and laser sintered liners (left) in steel targets.

From the numerical study, the maximum jet tip velocity of 9.94 km/s (without jet tip correction) was recorded for the aluminium liner with the lowest liner thickness (1.25 mm) and cone angle (40 degrees) considered, consistent with previous work [38]. The effect of cone angle on jet tip velocity was also apparent, with smaller angles producing higher jet tip velocities. A summary of the recorded jet tip velocities obtained from the Autodyn 2D history files, without jet tip correction, is presented in Table 4-6 with the recorded net traces in Figure 4-7.

Table 4-6. Recorded jet tip velocities of aluminium and copper liners (without jet tip correction).

Liner thickness (mm)	Cone angle (0^0)	Aluminium jet tip velocity (mm/μs)	Copper jet tip velocity (mm/μs)
1.25	40	9.94	8.14
1.25	60	8.66	6.86
1.25	90	6.84	5.48
2.5	40	9.85	7.96
2.5	60	8.20	6.10
2.5	90	6.29	4.20

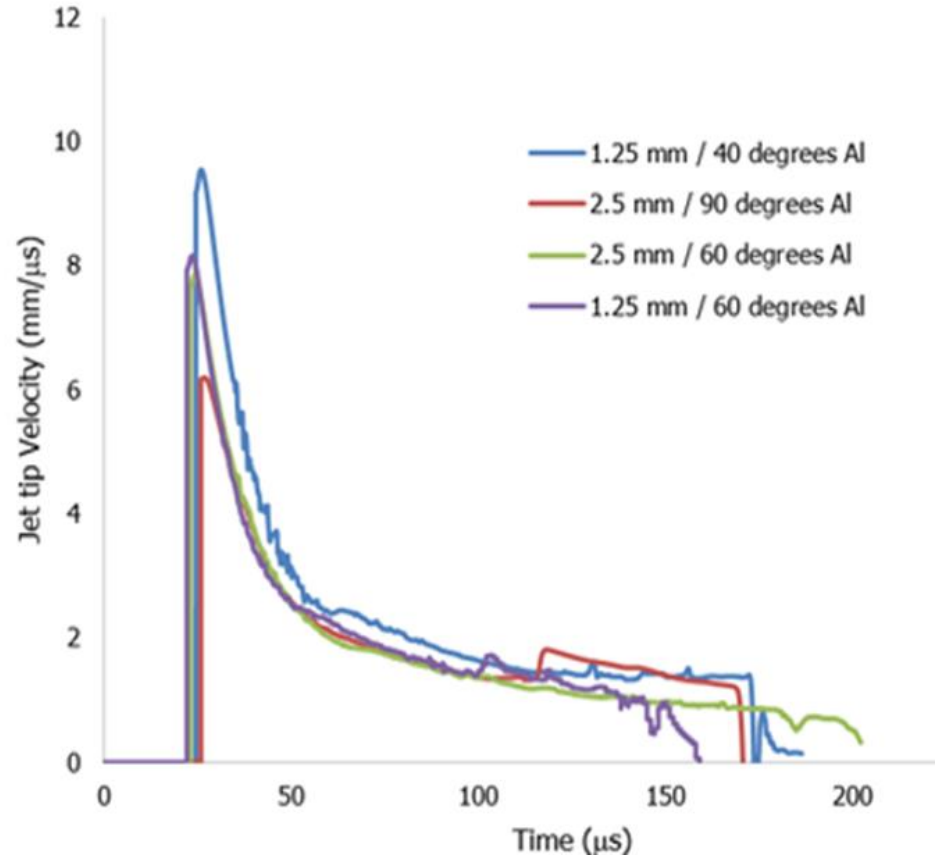

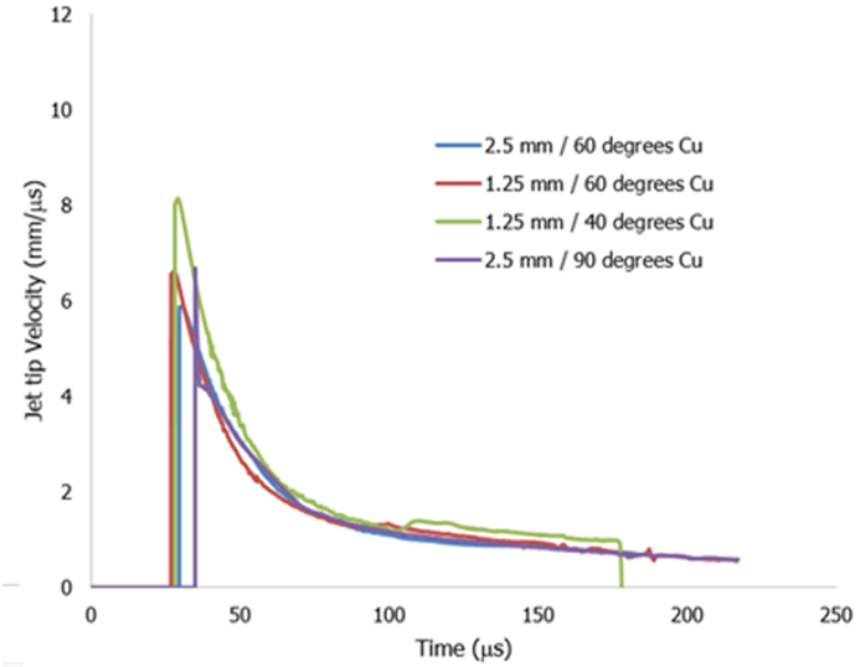

Figure 4-7. Jet tip velocity for 50 mm shaped charges from aluminium (top) and copper (bottom) cones.

The penetration depth obtained from the numerical simulations was then measured when the jet was completely eroded. The hole profiles from the numerical simulations are presented in Figure 4-8. We found that in agreement with the experiment, copper produced higher penetration than aluminium, reflecting the much higher density of copper (8.96 g/cm^3) compared to the aluminium liners (2.7 g/cm^3).

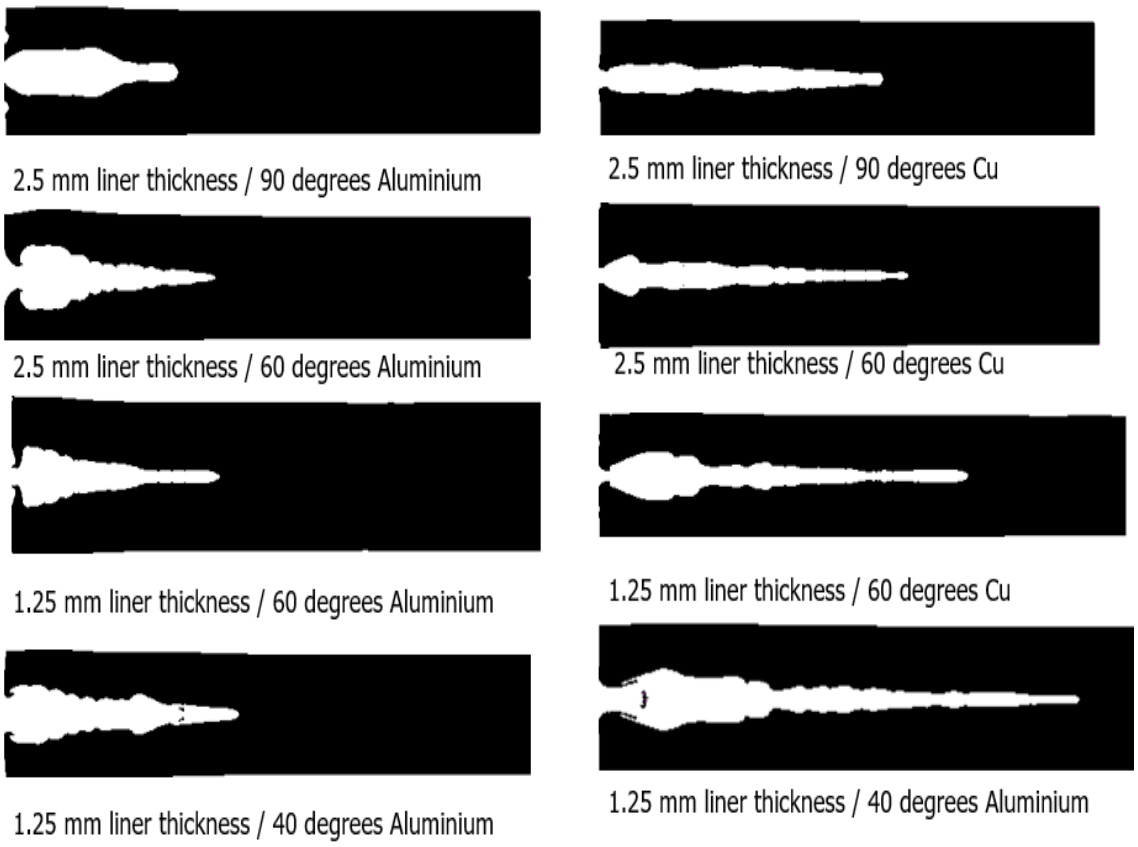

Figure 4-8. The penetration craters from Autodyn 2D numerical simulation.

4.6.1 Comparison of the performance of liners manufactured through machining and laser sintered process

The main objective of this study was to evaluate the performance of liners manufactured from the SLS technique by direct comparison with liners produced via conventional machining. An Autodyn 2D hydrocode which has been previously validated was also employed to predict penetration depths. As mentioned earlier, the hydrocode was revalidated using a machined 50 mm

OFHC copper liner fired at 3 CD SOD and the result showed good agreement with the experiment. Tables 4-7 and 4-8 present the penetration depths recorded for the SLS and machined liners, respectively.

Table 4-7. Measured penetration depth of aluminium liners manufactured from laser sintering process, machining and numerical simulations at 3 charge diameter SOD (mm).

Liner thickness (mm) / cone angle (degrees)	1.25 mm / 40^o	1.25 mm / 60^o	2.50 mm / 60^o	2.50 mm / 90^o
SLS Liners (mm)	144	116	106	75
Machined Liners (mm)	127	110	97	70
Numerical Sim (mm)	154	135	127	97
Difference between machined and Laser Sintered (%)	11.8	5.1	8.5	6.6

Table 4-8. Comparison of copper shaped charge liners manufactured using the SLS method (experiment), traditional machining (experiment) and numerical simulation.

Liner thickness (mm) / cone angle (^{0})	1.25 mm / 40^o	1.25 mm / 60^o	2.50 mm / 60^o	2.50 mm / 90^o
SLS Liners (mm)	199	138	134	83
Machined Liners (mm)	215	176	165	94
Numerical Sim (mm)	226	188	172	103
Difference between machined and Laser Sintered liner (%)	9.5	10.4	17.2	11.7

From Table 4-9 and 4-10, it is apparent that the variations between both liner processing techniques are minimal, with the highest variation of 17.2% (less than 0.5 CD) recorded for the copper liners. This implies that the performance of both processes is comparable. However, in spite of this comparable performance, there is a significant disparity between the performance of copper and aluminium material with respect to their processing technique. It was observed that even though higher penetration depths were recorded from the numerical simulations, the laser sintered aluminium liners performed better than the laser sintered copper liner. This is reflected by the relatively higher performance recorded from the laser sintered aluminium liners with its corresponding machined liner to the laser sintered copper liners. In other word, the laser sintered aluminium liners compare more favourably with the machined liners than the copper liners. In fact, a reduction of up to 17.2% in penetration depth was recorded for the laser sintered copper liner compared with its corresponding machined liner. This comparison, highlighted in Figure 4-9 and 4-10 indicates that the laser sintered copper liner is under-performing when compared with the equivalent SLS aluminium liner which has a higher penetration depth than its machined counterpart.

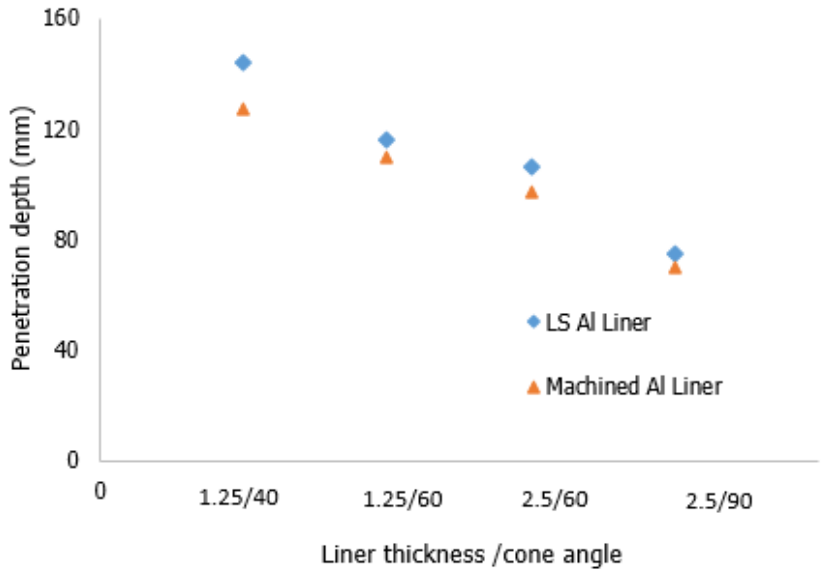

Figure 4-9. Relationship between machined and laser sintered liners on the penetration depth of aluminium liners.

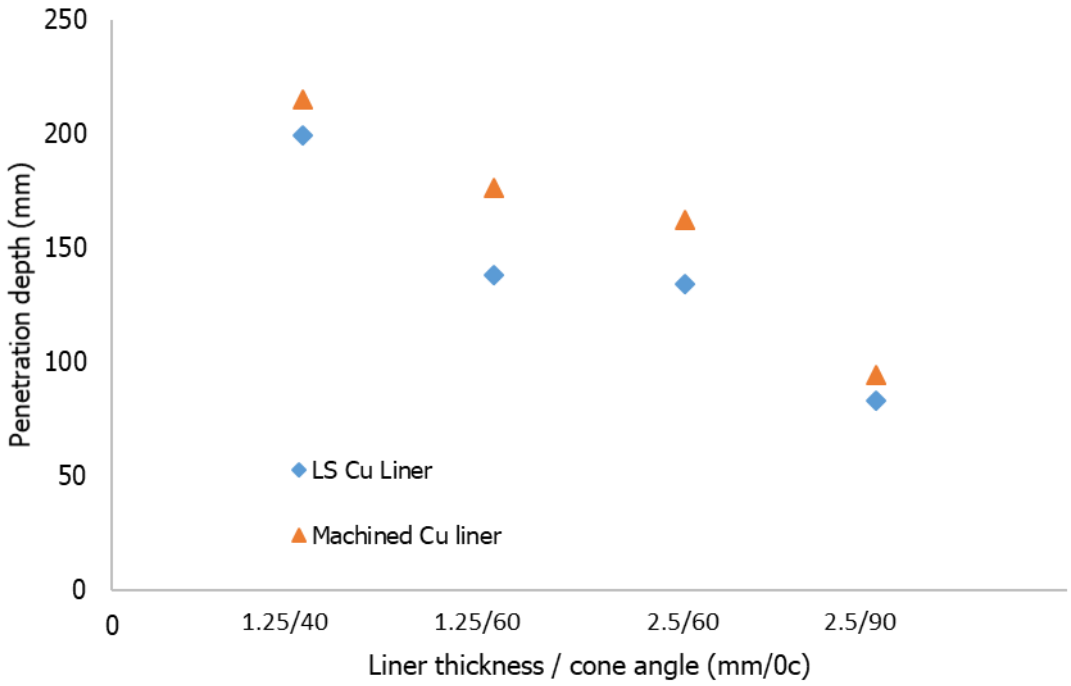

Figure 4-10. Relationship between machined and laser sintered liners on the penetration depth of OFHC copper.

The performance of liners produced by the selective laser sintering process is in the main affected by two factors.

1. A physical factor due to the interaction between the jet and the target owing to density.

2. The presence of pores in the sintered liners (as shown in Figure 4-6), which is one of the major drawbacks of the SLS technique [113]. These pores, which are microscopic in nature, are induced by entrapment of gas bubbles in-between layers during laser scanning [114].

However, these effects do not act in isolation, but rather in combination – with one of the core aims of this paper being to indicate how these factors affect the penetration depth. It has been established that the density of the sintered liners depends mainly upon the layer thickness, scan spacing and composition, whereas the porosity is influenced by layer thickness, scan spacing and laser

power [115]. Interestingly, aside from laser power, porosity and density of the liner are controlled by similar processing parameter. As might be expected, this suggests a clear interdependence between porosity and density.

In general, the maximum velocity attainable by a shaped charged, estimated by Chou and Carleone [2] in Equation 4-4 reveals the relationship between the bulk sound speed 'C' and the jet tip velocity $\boldsymbol{V_j}$ **.**

$$V_j \leq 2.41C_o \qquad 4\text{-}4$$

This implies that the maximum jet tip velocity of the liner is limited by a factor of the bulk sound velocity. Given that pores decrease the speed at which sound travels through a material – and therefore the inherent bulk sound speed – it is anticipated that the presence of numerous pores observed in the copper liner would reduce the penetrability relatively rapidly. Further, even though the presence of pore will result in local changes in liner density, which will influence jet-target interaction, the presence of pores has been shown to reduce the static and dynamic strength of a material [116] as they act as stress concentrators and effective crack initiation sites. When such cracks evolve the ductility of the liner is reduced, with a resultant propensity for earlier jet breakup time and consummate reduction in penetrability due to jet particles tumbling and moving transversely.

From the optical microscopic images of the laser sintered liners in Figure 4-6, it is apparent that a considerable level of grain refinement is observed in both copper and aluminium liners. Essentially, grain refinement leads to an increase in the material yield strength and ultimate tensile strength required for better liner performance. However, both liner materials contain certain quantity of voids. Examination of the liner material porosity reveals a higher percentage of pores per square metre with irregular shapes and sizes from the copper liners compared to the aluminium liners. It therefore, follows that the large number of pores present in the SLS copper liner would result in a higher percentage of porosity. Since high porosity leads to brittle failure modes with significantly reduced elongation [117], the SLS copper would breakup more quickly than the

equivalent SLS aluminium liners; as low levels of porosity (0.1%) have been shown to produce a ductile failure mode with higher elongation values [117].

It is important to note that crack initiation always starts from defects such as pores at the surface or subsurface arising from localised plastic deformation. Hence, even though a sintered built part may approach the density of the original material, the presence of residual microstructural porosity makes such materials inherently weaker than the original material.

Further, following the concept of material ductility factor and breakup time proposed by Baker [23], in Equation 4-5, the ductility of the liner depends mainly on the liner material and the processes employed in production.

$$t_b \cong \bar{Q}\left[\frac{\Delta m^*}{\Delta v}\right]^{1/3} \quad \text{and } L_b \cong \bar{Q}\Delta m^{*1/3}\Delta v^{2/3} \qquad 4\text{-}5$$

where t_b is jet break-up time, L_b is the jet length at break-up, Q is the material ductility parameter which differs with different liner design.

Consequently, the larger the value of Q, the more dynamically ductile the material [33]. Aside from the effect of pore size and volume on ductility, Grayson et al., 1990 [118] further established links between ductility to pore shape, spacing, size, and placement. While smooth pores are noted to be less detrimental than small, closely spaced pores, the overall effect of pore size on distribution is yet to be fully studied. However, it is apparent from this study that the density / volume of pores has a negative effect on jet performance. We consequently hypothesize that, aside from the density reduction, the percentage of porosity is critical to the performance of laser sintered liners.

5.0 Conclusions

This paper aimed at investigating the performance of copper and aluminium liners produced using 3D SLS printing technique employing both copper and aluminium materials. The study has established the mechanism by which

microscopic pores affects the penetration potential of a laser sintered shaped charge liner. In this regards, two approaches were established:

- Firstly, porosity affects the bulk-sound velocity of the liner with a consequent impact on the jet tip velocity
- Secondly, the pores act as crack initiation sites; decreasing the material ductility

Thus, even though laser sintered shaped charge liners present a range of benefits including lower production cost when large quantities are required as well as control of the liner microstructure, the resultant performance is comparable. Although a sintered sample may attain full density, nevertheless, it may possess inferior mechanical properties as a result of microstructural defects, primarily pores, inherent due to the SLS manufacturing technique. We therefore, conclude that porosity is an important factor which affects performance by reducing ductility and jet tip velocity – something which, as demonstrated in this study, is a particular issue for 3D printed copper shaped charge liners.

5 Evaluation of Filament Deposition Modelling Polylactic acid and Copper Filled Polymer Composite Liners on Shaped Charge Performance

H. O. Agu[1*], A. Hameed[1], G. J. Appleby-Thomas[1]
[1]Centre for Defence Engineering, Cranfield University, Defence Academy of the UK, Shrivenham, SN6 8LA, United Kingdom

This chapter/paper provides additional insight into the performance of 3D printed liners produced through an alternative 3D printing process, Filament Deposition Modelling (FDM). Unlike the Selective Laser Sintering (SLS) process discussed in Chapter 4, the FDM process employs polymers such as ABS, PLA etc, to produce finished parts which until recently, have been used only for the production of prototypes. As the laser sintered 3D printing process appears promising for liner manufacturing, it was necessary to investigate other additive manufacturing processes like FDM. Although polymers have been found to produce poor jets, this investigation was sparked by the fact that composite materials containing 40% copper in a PLA matrix (for example) have become available, providing improved mechanical properties. As such, it is unknown how use of such materials would influence the performance of the resultant jet produced from such composite liners. This chapter, therefore, fits into the core thesis objective of evaluating AM liners. The choice of selecting PLA over other thermoplastics in this study, is simply for the practical reason that this material worked best with the available Ultimaker 3D printer, allowing the production of parts with a relatively lower degree of porosity. In addition, the strength of PLA was approximately 20% higher than carbon fibre reinforced PLA and twice that of ABS [119]. This chapter/paper therefore investigates the performance of PLA liners produced via the FDM process and the influence of copper dopants on the performance of the PLA matrix (copper-fill material) as a shaped charge liner.

This chapter is adapted from: H. O. Agu* A. Hameed, G. J. Appleby-Thomas, “Evaluation of Filament Deposition Modelling Poly-lactic acid and Copper-filled Polymer Composite Liners on shaped charge performance. A technical paper submitted for the 2019 Cranfield Defence and Security Doctoral Symposium.

5.1 Abstract

This paper investigates the potential performance of a Filament Deposition Modelling (FDM)-based 3D printing process for the production of shaped charge liners employing both pure and composite matrix materials, comprising of:

- a homogenous material manufactured from polylactic acid, and
- a heterogeneous material made from copper-fill matrix (40% w/w copper in a polylactic acid)

In both cases shaped charge liners were manufactured using a commercially available 3D printer. We measured the depth of penetration into mild steel, and obtained further insight on the liner performance using both static post-impact (microscopic) and dynamic (flash X-ray) analysis, comparing behaviour to that of standard copper liners. The penetration depth of the copper-fill liners was significantly inferior to that of the conventional liners. The addition of copper to the wired PLA matrix reduced the performance of the liner compared to the PLA, reflecting the steric influence of the copper particles in the matrix. The liner heterogeneity introduced by copper in the matrix prevented the formation of a coherent jet, instead generating a stream of jet particles which produced multiple holes in the target as the liner diameter increased. Consequently, although the resultant penetration depth is limited, the copper-fill liners might however, be useful as a limited effective radius component in an active protection system, or as a frangible warhead forming a cone of copper pellets.

Key words: Shaped charge, liner, penetration depth, fused deposition modelling, selective laser sintering, flash X-ray.

5.2 Introduction

It is well known that the penetration potential of shaped charges is improved by the choice of liner material. Investigations into various materials including Copper [35], [120], Tungsten [55], Molybdenum [23] and zirconium [10], [33], [121], have attributed liner efficiency to high strength, high ductility, high density and high melting point [11], [122] – essentially functions of the original material. These properties make metals the preferred choice for shaped charge liners [108]. However, it has been widely reported that metallic jets can be disrupted by electromagnetic fields [123], [124]. When this occurs, the penetration potential of the jet is reduced [124]. One mechanism to counter this measure is the development of non-metallic liners. In contrast with metals, non-metallic materials such as glass and woods, amongst others [2], have been investigated but the jet produced was not satisfactory. In spite of the extreme brittleness of ceramic (silica glass cones 2.6 g/cc and alumina cones 3.8 g/cc), flash X-radiographs showed them to jet effectively into coherent particle streams, although while penetration into steel targets was significantly less effective than for equivalent copper liners [32], [125]. Thermo-softening polymers such as polyethylene can give tensile ductility of over 800% elongation to failure under ambient conditions. However, at the very high strains and temperatures encountered during jet formation ($0.7T_M$ for copper) [126], the resultant jet would be molten (truly hydrodynamic), unlike that for their metallic counterparts which retains their solid nature [127]. This would be the case due to the low melting point of such polymers (e.g., T_M of polyethylene is around 138^o C [128]). As such, to date, not much progress has been made on the use of polymer cones.

Interestingly, it has become possible to produce composite polymers by doping powder materials heterogeneously into a polymer matrix in order to produce parts of higher subsequent mechanical strength through Filament Deposition Modelling (FDM) 3D printing process. The FDM technique is capable of building parts of any complicated geometry in the least possible time [67], [71] without incurring extra cost due to the absence of tooling and with minimal material waste [6]. In the FDM process, heated thermoplastic materials such as Acrylonitrile Butadiene

Styrene (ABS) and Polylactic acid (PLA) are commonly used, with these materials extruded from the tip of a nozzle in a semi-molten state, fabricating parts on a heated bed (typically at around 60^0C). Recently, introduction of a glass-fibre reinforced polypropylene showed the potential of FDM to compete with conventional techniques, especially for the production of small series of parts/components with adequate mechanical performance [67], lifting the limitations of FDM from the production of mock-ups and prototypes [66] to actual parts/components production. Similarly, copper-filled filaments, 40% w/w of copper, embedded in a PLA matrix have been developed with improved mechanical properties expanding the range of FDM process-based. As copper is highly ductile, it is not known how this would contribute to the resultant jet performance in shaped charge devices. In this investigation, polylactic acid and copper-fill were processed into shaped-charge liners. The objective was to observe the behaviour of polylactic acid and the effect of the copper on the PLA matrix by observation of the behaviour of the resultant jet utilising both flash X-ray and monitoring of penetration into mild steel targets.

5.3 Liner production

The 3D printer used in this study was a Dual Extrusion Ultimaker 3D printer (extended) located at the Shrivenham site of Cranfield University. The printer is fully customizable just like any other 3D printer with an auto-nozzle lifting system and swappable print cores. Print cores of diameters 0.4 and 0.8 mm can be used on the print heads, allowing for the deposition of a wide range of materials including as PLA, ABS, Polycarbonate (PC) and Polypropylene (PP) [129]. The printer is also equipped with a material recognition system for material selection. Some of the key components in a typical FDM machine include the thermal housing, extrusion nozzle, plastic filament supply coil and the X-Y-Z stage system. Major components of the Ultimaker 3 Extended are: the build plates, dual extrusion print heads, control section comprising the display, USB slot (for data import / extraction) and push roll button, while other components are the feeder and the spool holder. A schematic of the Ultimaker 3D extended is presented in Figure 5 -1.

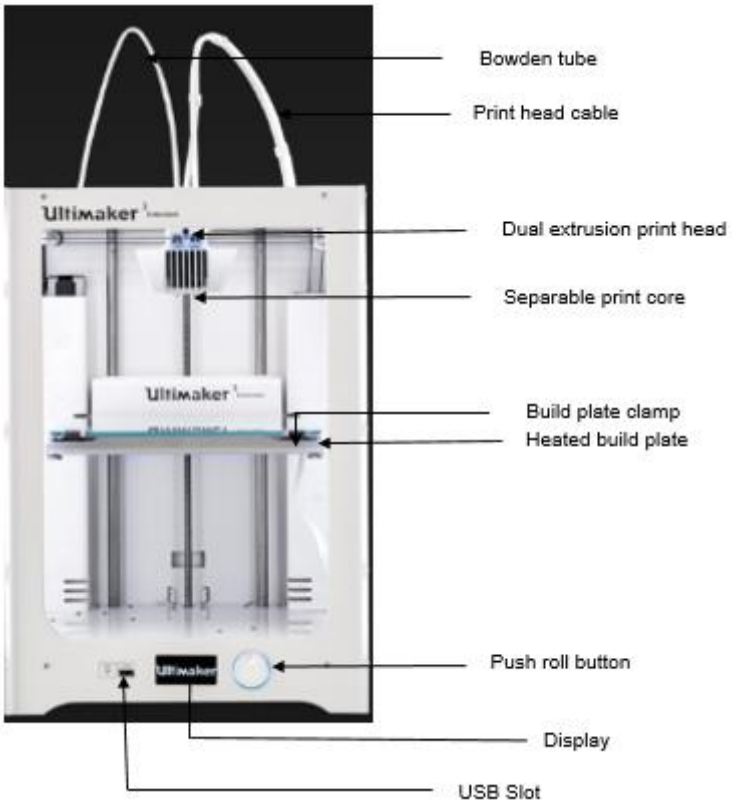

Figure 5-1. Annotated picture of the Ultimaker 3D Extended printer used in this work.

5.4 Material selection

Two rolls of commercially procured polylactic acid (PLA) and copper-filled filaments (which comprises 40% weight by weight copper) embedded in a wired PLA matrix were used for the production. The filaments were stored under vacuum to prevent absorption of moisture before use [69]. As with any 3D printing process, the liner design was first produced on computer-aided design (CAD) software as shown in Figure 5-2 and imported as. stl files into the Ultimaker 3D printer – in this case, with a 0.4 mm print core. While there are no standard input parameters to optimise the material properties available in the literature, previous investigations have determined the effect of print parameters such as orientation, layer thickness and air gaps on the quality of printed parts by studying their flexural, tensile, and impact strengths [20]. The effect of choosing between 0.20 and 0.35 mm layer thicknesses has also been compared, with the thicker layers achieving higher tensile strengths because there are fewer interfaces [67].

The infill density also affects the mechanical performance of printed samples, with the tensile strength and modulus increasing by more than 250 percent when the infill density is increased from 20 to 100% [67].

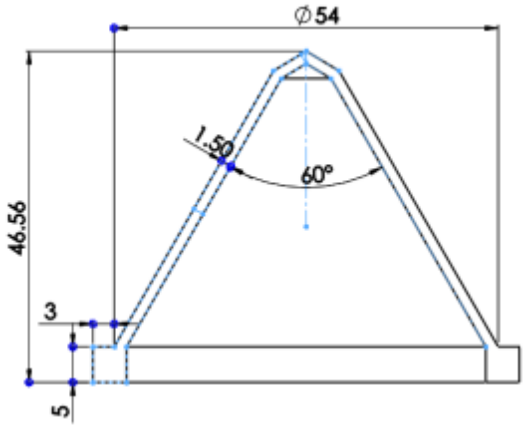

Figure 5-2. Liner design for manufacturing using the FDM method (dimensions in mm).

The decision was taken to select 100% infill density with a concentric infill pattern at a print speed of 70 mm/s in order to produce as higher density part as possible. Other print parameters are summarised in Table 5-1. The time taken to produce each liner increased with thickness (1.5 mm = 3 h 10 min, 3.5 mm = 5 h 20 min, 5.5 mm = 7 h 49 min and, 7.5 mm = 9 h 20 min).

Table 5-1. Print parameters for the production of liners by FDM.

Parameters	**Value**
Layer height / width	0.1 / 0.35 mm
Wall / top and bottom thickness	0.5 / 1.2 mm
Top / bottom pattern	concentric
Z seam alignment	random
Infill density / pattern	100 / concentric
Infill / print speed	50 / 70 mm/s

A total of 8 conical liners with thicknesses of 1.5, 3.5, 5.5 and 7.5 mm were produced from copper-fill and PLA filaments. Aluminium casings (of 3 mm wall thickness) were attached to the liners using 5 minute quick-setting Epoxy (Loctite Double-Bubble 2-Part Epoxy). All test specimens were printed under similar conditions to maintain consistency and were used without further modification (Figure 5-2). Before printing, the build plate was calibrated, cleaned and glue was applied on the surface to obtain good adhesion and better print quality. Further, a ‘brim setting which places a single-layer-thick flat area around the object was applied to create a larger adhesion surface, thereby minimizing warping on the first layer, as shown in Figure 5-3.

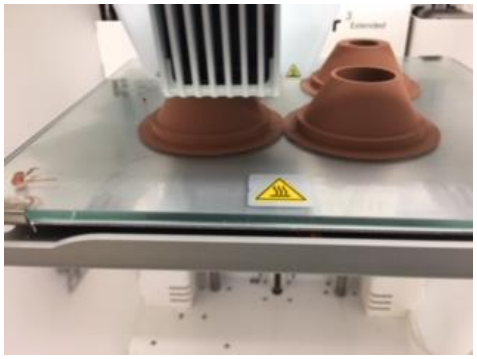

Figure 5-3. Build process of copper-fill liners using the Ultimaker 3D printer.

After printing, the build plate was allowed to cool to enable removal of the built cones before other support structures were removed. As a control experiment, standard OFHC copper shaped charge liners were produced from the same design. The resultant liners are shown in Figure 5-4 while the liner design is at Appendix 3.

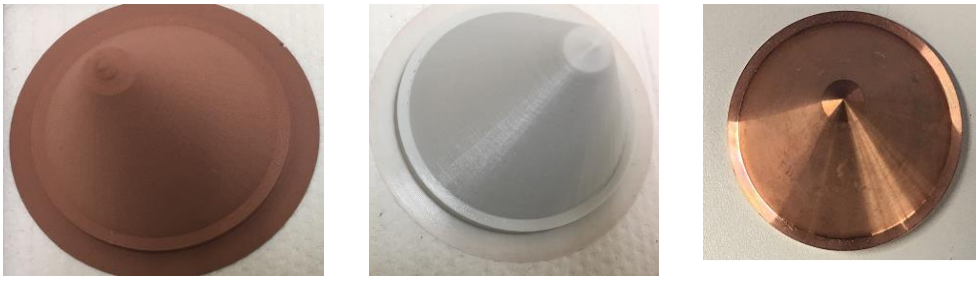

Figure 5-4. Liners produced from copper-fill (left) PLA (middle) and machined OFHC copper (right).

The measured density of the as-produced liners in comparison with the nominal material density is presented in Table 5-2.

Table 5-2. Density of manufactured liners as compared to the source material measured using an XS105 precision balance (Mettler Toledo Ltd. Leicester, UK), plus textbook values.

Liner manufacturing technique	Measured density (g/cm^3)	Nominal material density (g/cm^3)	Difference in material density (g/cm^3)
Machined copper	8.94 $\pm$ 0.1	8.96	0.02
FDM copper-fill liner	3.15 $\pm$ 0.1	3.90	0.75
FDM of PLA	1.18 $\pm$ 0.1	1.21	0.03

5.5 Preparation of the shaped charge and targets

The advanced insensitive plastic explosive (PE) No. 8, with a density of 1.57 g/cm^3 and detonation velocity of 8000 m/s (nominal), was used in all trials. The explosive was moulded and hand-filled into the aluminium casings by pressing slowly against the liner to avoid creating air gaps and to ensure good contact. Adequate care was taken to ensure consistent, concentric filling of the explosive

charge across the width of the liners [102]. Each filled casing was measured to ensure consistency in the mass/charge ratio. The shaped charges were fired into mild steel targets using L2A2 electric detonators at a standoff distance of three charge diameters (3 CD).

5.6 Results and discussion

Table 5-3 highlights the variation in liner masses. The machined OFHC copper liners had the greatest mass, owing to their high density, followed by the FDM liners produced from copper-fill material and then the PLA. The mass of explosive was kept as constant as possible to minimise experimental errors, given that differences in charge mass affect performance [14]. The slight variation (<2%) reflected the manual explosive filling technique.

Table 5-3. Performance of liners machined from copper or produced by FDM.

Manufacturing process	Liner diameter (mm)	Mass of explosive / Charge mass (g)	M/C	Penetration depths	Hole volume as a function of mass (g)
Machined OFHC Cu	1.5	199.4 / 437.5	2.19	165.00	-
	3.5	212.2 / 532.4	2.50	131.00	-
	5.5	210.2 / 598.0	2.84	70.00	-
	7.5	213.6 / 656.9	3.07	37.00	-
FDM with copper-fill	1.5	206.0 / 384.8	1.86	16.00	6.8
	3.5	212.5 / 417.7	1.96	11.88	4.0
	5.5	219.5 / 445.1	2.02	2.83	1.2
	7.5	202.9 / 439.6	2.16	1.50	0.5
FDM with PLA	1.5	-		18.10	12.2
	3.5	-		16.10	11.4
	5.5	-		9.90	6.6
	7.5	-		10.70	6.8

In terms of performance, as shown in Table 5-3, all liners achieved some form of penetration into mild steel. However, as expected, the machined OFHC liners penetrated more deeply, about 9 times the depth of the copper-fill liners produced by FDM (Figure 5-5). Among the liner materials we tested, copper is well suited for shaped charge liners because its relatively high ductility and density acts to delay the onset of particulation. Therefore, the jet from copper liners can stretch extensively before breaking; increasing the jet length. Although machined liners performed less well than those produced using techniques such as powder metallurgy, due to the presence of residual stress in the material during machining as well as poor grain size [125], our results showed that machined liners performed significantly better than FDM liners manufactured from copper-fill when the performance is compared vis-à-vis the percentage of copper in the matrix.

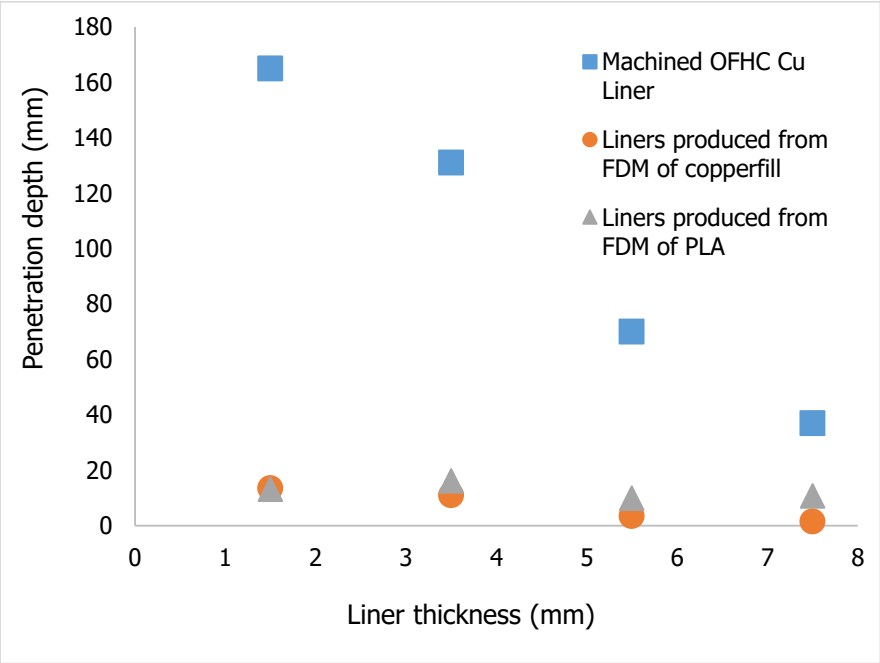

Figure 5-5. The effect of liner thickness on penetration depth for machined OFHC copper and copper-fill liners.

On the other hand, both PLA and copper-fill (copper in a PLA matrix) gave rise to poor-quality jets with erratic target penetration. The poor jet formation from PLA liners could be attributed to the characteristics of the jet formed. Essentially, PLA

has a low melting zone; at 60°C, PLA starts to soften and at 200°C, it would most-likely be flowing as a fluid. As such, it is very likely, that the temperature reached during the jet formation exceeds the melting zone of the plastic and therefore softens the jet such that, in contrast with its metallic counterparts that stays solid (although flowing in a nominally hydrodynamic manner, some residual strength will be retained), the thermoplastic jet flows as a liquid under such high strain /strain rate (e.g. no residual/shear strength). Under these conditions, and coupled with its lower density, the jet penetration is highly reduced. When this occurs, a large entry hole diameter is formed with a very short depth as shown in Figure 5-6.

Figure 5-6. Surface entry hole produced by PLA jet in steel.

However, until the temperature of the jet during formation and elongation is measured, this is only speculative. Further work on the liner temperature may need to be undertaken to clarify this aspect.

5.6.1 Performance of copper – filled composite liners

The copper-filled liners produced some interesting results. From Table 5-3, it is apparent that greater penetration depths were recorded for the pure PLA liners than the copper filled liners in spite of their lower density (Table 4-2). It was very much anticipated that the presence of copper in the copper-filled liners (40% w/w of copper) would result in higher performance, as is the case where powder metallurgical techniques are employed to manufacture liners [56]. On the contrary, the copper-filled liners recorded the poorest performance of those considered in this study, with the least penetration. Further analysis revealed the presence of multiple holes on the surface of the target impacted by the FDM

copper-fill liners. The number of holes was greater for the thicker liners. In particular, the 5.5 and 7.5 mm thick liners achieved limited penetration but produced multiple holes (Figure 5-7), suggesting the formation of a dispersing jet that ‘splatters’ across the surface of the target. It therefore, appears that no coherent jet is formed when using FDM copper-fill liners.

1.5 mm liner thickness	3.5 mm liner thickness

5.5 mm liner thickness	7.5 mm liner thickness

Figure 5-7. Target surface showing multiple holes from copper-fill liners manufactured using the FDM technique.

5.6.2 Flash x-ray analysis

To confirm the formation of a dispersing jet, a 150 kv Scandiflash X-ray system was used to record jet from the best-performing liner (a 1.5-mm thick copper-filled liner). The front face of the high-density polyethylene (HDPE) sits ~50 mm from the X-ray tube and the target was 3 m from the HDPE covering the X-ray heads, with the cassette a further 1 m beyond the target. The shaped charge device was

mounted vertically over the middle of a square metal plate and held in place with an adhesive mounting (Figure 5-8a).

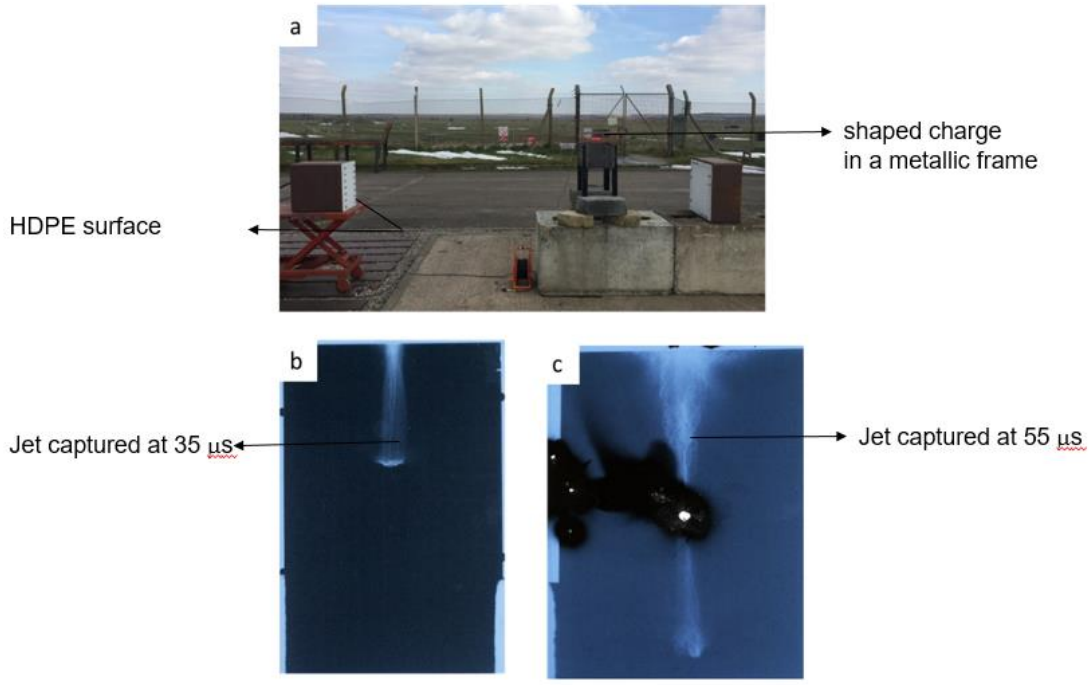

Figure 5-8. Flash X-ray of 1.5 mm copper-fill. (a). Experimental set up. (b) Jet X-rays at 35 μs. (c) Jet X-ray at 55 μs.

A flash X-ray taken after 35 μs revealed the formation of an expanding radial jet in the form of a stream (thin lines) of discontinuous (discrete) jet particles (Figures 5-8b and c). Essentially, the performance of liner materials has been linked to their microscopic crystal structure, which is a function of the original material properties [10]. To gain further insight, we compared the microstructure of a sectioned/polished piece of machined OFHC copper and the copper-fill liner produced by FDM (Figure 5-9). The micrograph of the copper-fill liner revealed the presence of inner voids, which confirms the porous nature of the liner, whereas voids were not apparent in the machined copper.

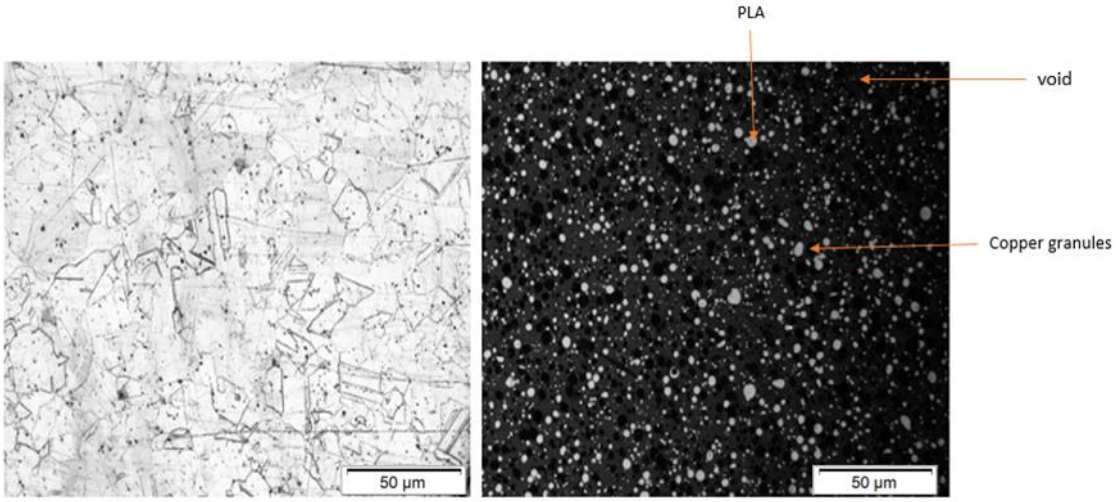

Figure 5-9. Optical images of machined OFHC copper liner (left) and copper-fill liner revealing voids (dark region) produced by FDM (right).

The effect of porosity on liner materials has been reported with similar results to those presented here, particularly the radial expansion of the jet as well as the production of multiple holes [130]–[132]. The response of a shaped charge with a porous liner was attributed to the inability of the liner to solidify during the collapse that occurs on impact [130]. As such, the jet maintains its porous nature during the stretching phase, and because the porous liner is heated more efficiently than a monolithic liner [130], the viscosity of the liner material decreases during acceleration [132] [133]. In contrast, the density and the radius of the porous jet change constantly, as confirmed by the change in jet radius recorded for the flash X-rays taken at 35 and 55 μs. The jet radius along its length first decreased and then expanded again, probably reflecting the lack of adhesion arising from the lower viscosity of the porous jets as it elongates (Figure 5-9). It is suggested that this behaviour may be attributed to the low melting point of PLA.

5.6.3 Effect of copper on the performance of PLA liners

The primary objective of this study was to determine the effect of the addition of copper particles (copper-fill) in the PLA polymer matrix on jet performance. We compared the performance of FDM liners manufactured from copper-fill and pure PLA. For the thinnest liner (1.5 mm) there was little difference between the two

materials, but with the thicker liners, we found that pure PLA achieved significantly higher penetration depths than the copper-fill liners (Figure 5- 10).

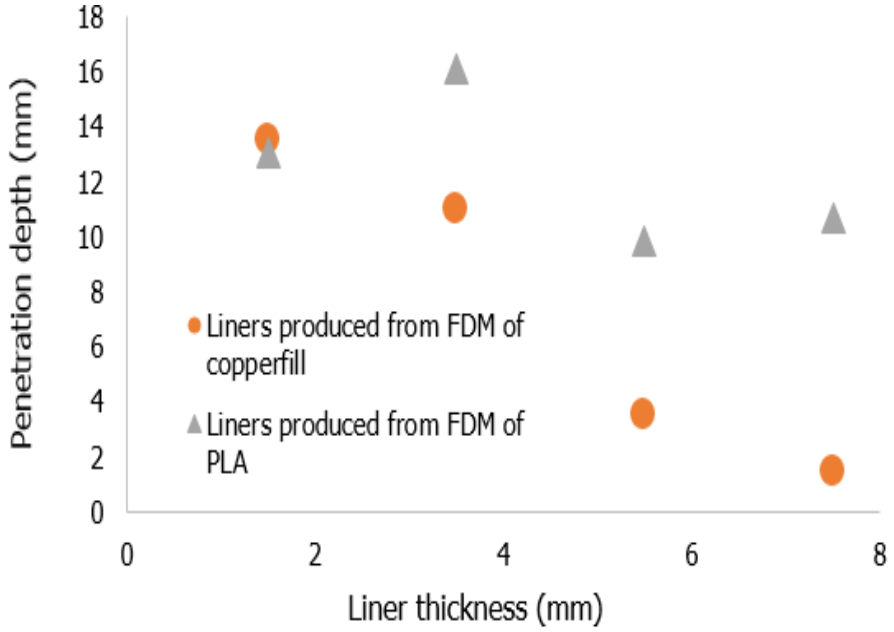

Figure 5-10. Comparative performance of pure PLA and copper-fill FDM liners differing in thickness.

The hole volumes formed from both liner types were measured by creating a replica cast using fast-curing two-part silicone rubber (Replifix-2). The mass of the replica cast was used as a proxy for the volume of the hole thickness. Further analysis of the penetration craters revealed that the hole volume, represented by the mass of a replica cast made from Replifix-2, decreased as the liners became thicker, and was greater for the liners manufactured from pure PLA compared to liners of the same thickness manufactured using copper-fill as highlighted in Figure 5-11.

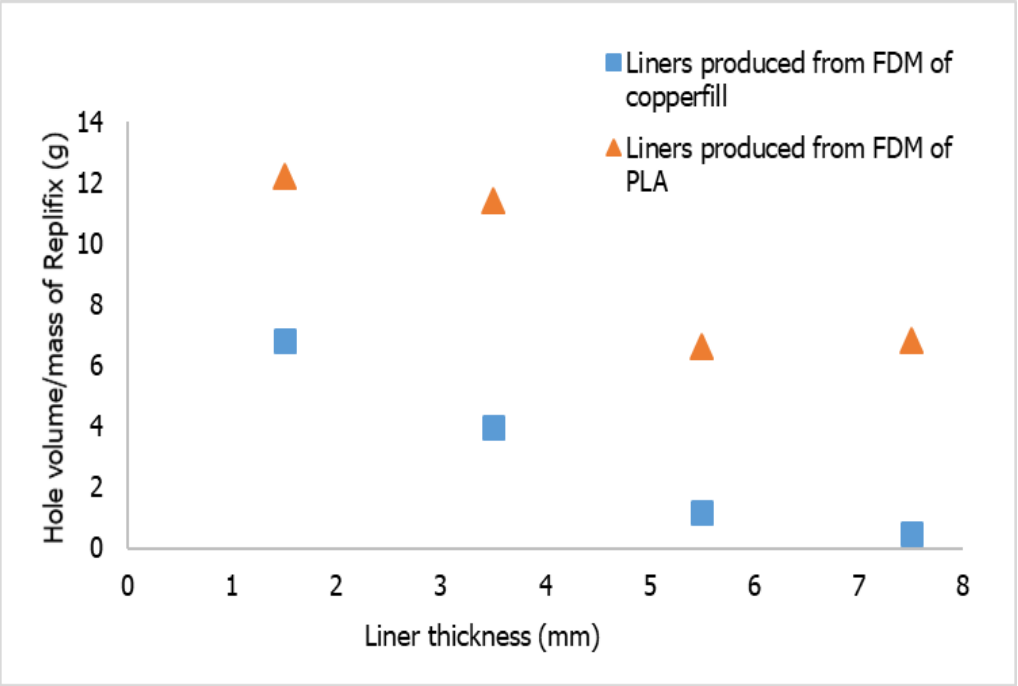

Figure 5-11. Volume of the penetration crater (represented by the mass of a replica cast) as a function of liner material and thickness.

From the preceding analysis, it is very likely that the jet produced during the impact of FDM liners is mainly contributed by the PLA, and that the addition of copper to make the copper-fill composite not only fails to augment the jet but actively interferes with it. We speculate that the heterogeneity of the copper-fill not only increases its porosity but also results in the particulation of the copper during impact, thus disrupting the PLA jet leading to the formation of a stream of discontinuous jet which generates multiple holes as the liner thickness increases. Such dispersed jets may not serve as a possible replacement for metallic liners to counter electromagnetic effect as is the primary objective of this work but has provided a framework which further research on the development of polymer composite liners. Despite their limited penetrative ability, the copper-fill liners might however, be useful as a limited effective radius component in an active protection system, or as a frangible warhead forming a cone of copper pellets or for the application of coatings [130]. It can also be employed for defeating fusing system and disposal of explosive munitions.

5.7 Conclusion

The use of 3D printing for the production of liners was investigated using the FDM technique. The performance of the manufactured liners was investigated in experimental trials in which penetration into mild steel barriers was evaluated at a standoff distance of 3 CD. The FDM liners were compared to conventional liners of machined copper. Our results showed that:

a. The effect of liner thickness in AM liners flowed in the same way as conventionally manufactured liners, with lower liner thicknesses producing deeper penetration.

b. The addition of copper to the PLA matrix (copper-fill) reduces the liner performance largely because of the heterogeneous nature of the matrix.

b. Liners manufactured from the copper-fill composite using the FDM technique produced multiple craters from the jet stream, reflecting the porosity and heterogeneity of the copper/PLA mixture.

c. The low (as opposed to conventional copper liners) performance of FDM liners was attributed to porosity and the low melting point of the PLA.

6 The Dynamic Response of Dense 3 Dimensionally Printed Polylactic Acid

H.O. Agu, A. Hameed and G.J. Appleby-Thomas
Centre for Defence Engineering, Cranfield University, Shrivenham, SN6 8LA, United Kingdom
*Corresponding author: henry.agu@cranfield.ac.uk

It was necessary to understand the shock behaviour of polylactic acid through numerical simulations. However, the absence of an Equations of state data from the literature makes this a daunting process. As such, this chapter investigates the shock behaviour of the polylactic acid used in Chapter 4. The paper fits into the thesis structure by providing Equations of state data of polylactic acid a means of representing the PLA cones in shaped charges for the employment of numerical simulations for prediction of the penetration depth. This paper has been accepted for publication in the journal of dynamic behaviour of material subject to minor changes (inserted in Appendix 2).

Adapted from: H. O. Agu* A. Hameed, G. J. Appleby-Thomas, “The Dynamic Response of Dense 3 Dimensionally Printed Polylactic Acid”, published in the Journal of Dynamic Behaviour of Materials.

6.1 Abstract

Polylactic acid (PLA) is commonly used as a feedstock material for commercial 3D printing. As components manufactured from such material become more commonplace, it is inevitable that some of the resultant systems will be exposed to high strain-rate / impact events during their design-life (for example, components being dropped or even involved in a high-speed crash). To this end, understanding the shock properties of polylactic acid, in its role as a major raw material for 3D printed components, is of particular importance. In this work, printed samples of PLA were deformed by one-dimensional shock waves generated via the plate impact technique, allowing determination of both the Hugoniot Equation of State (EOS) and shear strength of the material. Both linear and non-linear EOS forms were considered in the U_S-Up plane, with the best-fit found to take the general form $U_S = 1.28 + 3.06 - 1.09{U_p}^2$ in the $U_s - U_p$ plane, consistent with other polymers. Use of lateral Manganin gauges embedded in the material flow allowed consideration of lateral stress evolution at impact pressures ranging from 0.3 to 4.0 GPa. Shear strength was observed to increase with impact stress, however, with minimal strengthening behind the shock front. Deviation of the measured stress from the predicted elastic measurement (corresponding to the PLA's Hugoniot Elastic Limit) was observed at longitudinal stress of 0.90 $\pm$ 0.05 GPa, within range of polymeric materials of similar characteristics – the first time this important parameter has been measured for PLA. As a result, this material characterisation will allow numerical modellers to accurately predict the structural response of PLA-based components/structures against high strain rates such as impacts or drops.

6.2 Introduction

Polylactic acid is one of the major raw materials used in a filament deposition modelling (FDM) desktop 3D printer. The application of PLA has metamorphosed from the production of simple prototypes to manufacturing of finished / end-use products such as medical implants in the form of screws, plates and anchors [134], subject to a range of loading conditions. It is therefore important to understand the shock response of printed PLA. More importantly, understanding of the material's hydrodynamic and constitutive equations of state will enable the development of mathematical models for numerical simulations [135]. Although there are a number of studies on the response of printed PLA, [67], [119], [136] within the quasi-static loading regime, there is – to the author's knowledge – no existing study focused on the dynamic response of PLA under high strain rate conditions. However, usefully / as a potential point of comparison, a number of studies have already been conducted on the shock response of similar polymeric materials such as polyethylene (PE) [137], Polymethylmethacrylate (PMMA) [138], polyvinylchloride (PVC) [137] and polytetrafluoroethylene (PTFE) [137].

One of the earlier investigation conducted by Carter and Marsh [93] at the Los Alamos National Laboratory investigated the shock behaviour of over 20 polymers, showing certain similarities in the dynamic response of such materials. It was observed that at high pressure (20-30 GPa), there is a change in the slope of the shock velocity, $(\mathrm{U_s})$ and particle velocity, $(\mathrm{U_p})$, curve suggesting a phase transformation. This was attributed to the re-ordering of the polymer structure due to the nature of the compression at sufficiently high pressure [93]. More or less, a rearrangement of the chains at the molecular level resulting in a large volume change at high pressure was postulated. Another observable trend was the inability of the experimentally measured data in the $\mathrm{Us} - \mathrm{Up}$ plane to extrapolate to the zero-pressure ultrasonic sound speed measurement [93]. In contrast with metals, the bulk sound speed, C_B are usually below the abscissa Hugoniot intercept, giving polymers a non-linear Hugoniot. For example, J.C.F Millet et al., 2016 investigated the shock response of 4 common semi-crystalline thermoplastic polymers: PE,PTFE, PVC and PCTFE [137] and observed that all

four polymers had a linear response in the U_s and U_p, curve in common with other polymeric materials, represented in the form described in Equation 6-1. However, when interpolated from the measured bulk sound speed on the y-intercept, a non-linear equation presented in the form described in Equation 6-2 was obtained.

$$U_s = C_0 + Su_p, \qquad 6\text{-}1$$

$$U_s = C_0 + SU_p + RU_p^2 \qquad 6\text{-}2$$

The values of the C_0 and S in the Hugoniot equations are empirical constants, correlated to the bulk sound speed C_B and the first pressure derivative of the bulk modulus respectively [139].

This trend has been reported in a number of studies and has been attributed to variation between the forces in the C-C backbone (of higher magnitude) and the forces between the adjacent chains in the polymer altering the deformation pattern along the chains and backbone [93]. As such, in contrast with metals, the chemistry of polymer is key to understanding its dynamic response. Essentially, the carbon backbone in polymers (chain) forms a strong bond with itself compared with bonds between adjacent polymer chains [93]. Hence, as the shock propagates, smaller / weaker forces in the adjacent chain collapse even more rapidly than the forces in the C-C backbone. Usefully, the interaction between functional groups and or atoms (steric effect) plays a significant role in polymer response as well as the geometric arrangement (Tacticity) of these groups. As an example, polyethylene (PE), which is the simplest polymer only interact with hydrogen atoms on the adjacent chain has lower strength compared with PVC while PCTFE, with larger molecules in the side chains than PVC. This phenomenon is attributed in part to the increasing influence of electrostatic repulsion arising from increased electronegativity (9) resulting from the inclusion of chlorine (in PVC) and fluorine (in PCTFE) (6). Following on from this, it is likely that the presence of an oxygen atom in the side group chain of the PLA,

presented in Figure 6-1, would influence the shock response of PLA. As the slightly positive sections (carbon and hydrogen) are attracted to the negative sections of the chains, the stress required to break the bond increases with a consequent effect on the polymer strength.

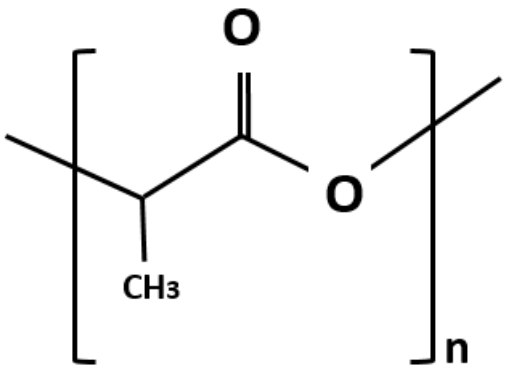

Figure 6-1. Representative monomer structure of Polylactic acid.

Further, as the polymer is compressed and the chains move closer together, physical interaction between the molecules (tangling or steric effect) due to the shape of the polymer increases the stress required to move the molecules together. Though reported particularly for polymers with open chain morphology such as PE [137] with dangling side groups, the addition of an electronegative atom to the chains increase the susceptibility for entanglement. Such an interplay between electronegative repulsion and tangling determines the polymer strength under dynamic (shock) loading. While the degree at which these factors influence polymer strength is yet to be fully established, it has been suggested that repulsive forces are more dominant in the fluorinated polymer such as PTFE and PCTFE, in contrast with hydrocarbon polymers controlled majorly by tangling. Interestingly, PLA has an open chain morphology similar to PE and the presence of a CH_3 side chain group should allow a greater degree of interaction (steric effect) between the adjacent polymer chains. In the same vein, the presence an electronegative atom (oxygen), while even not as strongly electronegative as the chlorine and fluorine atoms in PVC and PCTFE, means it is likely that the interaction of both factors could increase the strength of PLA. In this work, the dynamic shock behaviour of a 3D printed PLA was investigated using manganin

stress gauges. These gauges, of thickness, ca. 25 μm and embedded in the material flow, measure the longitudinal and lateral stresses induced in the samples. The data obtained were reduced to determine the Hugoniot Equations of state of the material and the shear strength – key data to allow for subsequent high strain-rate / pressure simulations.

6.3 Material production

The PLA filament, of diameter 2.85 mm, used in this study was obtained commercially and supplied in an airtight bag to prevent degradation from atmospheric humidity [69]. A 50 mm diameter, 10 mm thick disc was designed on Computer-Aided Design (CAD) software and imported as an STL file into an Ultimaker 3D printer with a 0.4 mm print core for printing via the Filament Deposition Modelling (FDM) desktop 3D printer (Ultimaker 3 extended). The 3D printing technique creates parts by heating filaments above its glass transition temperature before laying successive layers on the print bed based on input print parameters. Although, there are no standard parameter values for desired printing quality in the literature, the effect of certain parameters has been reported. As an example, Sood et al. [20] investigated the effect of printing parameters such as orientation, layer thickness, and air gaps on the quality of printed parts by studying their flexural, tensile, and impact strength. Schopper et al., [68] investigated the effect of build direction on the compression properties of FDM built parts and observed higher compressive modulus and yield strength of built parts in the horizontal direction in comparison to the specimens built in the vertical direction [140]. In turn, Caneiro et al., investigated the effect of the layer thickness by comparing samples produced with layer thicknesses of 0.20 and 0.35 mm and results have shown higher tensile stress with an increase layer thickness which was attributed to the lower number of interfaces between filaments. In the same work, the degree of infill (a printer setting which controls the density of the built parts) was reported to have a strong impact on the mechanical performance of printed samples. A difference in both modulus and tensile strength of more than 250% was reported when the infill density varied from 20 to 100% [67]. As such, for the investigations here / to ensure an optimum

print, a 100% infill density was used with a print speed of 70 mm/s employed. The target samples were finished with an impervious top and bottom layer to prevent percolation of epoxy used in the target preparation. Other print parameters are summarised in Table 6-1. A total of 8 samples were fabricated from a roll of 2.85 mm PLA from Spool Work. The samples were printed vertically with the layers oriented perpendicular to the shock direction. All test specimens were printed under identical conditions to maintain consistency in all samples.

Table 6-1. Print parameters for the production of 10 mm thick PLA on Ultimaker FDM printer.

Parameter	**Value**
Layer Height	0.1 mm
Line width	0.35 mm
Wall thickness	0.5 mm
Z Seam alignment	Random
Top/bottom pattern	Concentric
Top/bottom thickness	1 mm
Infill	100%
Print speed	70 mm/s
infill speed	40 mm/s
Wall speed	30mm/s
Travel speed	250 mm/s
Printing temp	200^0C
Build plate temperature	60^0C

In order to evaluate the consistency of the print quality, weight and diameter of each sample were obtained. The weight was found to be consistent with a tolerance of ± 0.2g while the average density was 1.14 $\pm$ 0.02 g/cc, slightly lower than the nominal bulk PLA density of 1.24 g/cc. This could be attributed to the

presence of voids [136] which are a function of the input parameters during the printing process. The diameter was consistent with a tolerance of ±0.01 mm.

6.4 Experimental method

One of the methods commonly used to produce a shock wave in materials is the plate-impact technique. The plate-impact technique involves accelerating a flat and parallel plate into a similar target (surfaces were polished to a tolerance of <10 μm) [141], [142], [143] using a single stage gas gun. Simultaneous impact of all elements of the flyer and target impact surfaces leads to inertial confinement over very short (micro-second) timescales and the establishment of a one-dimensional state-of-strain within the materials. The gas gun employed for these experiments has a 50-mm bore, with a 5-m barrel and is situated at the Defence Academy of the UK, Shrivenham. A schematic of the gun set-up is presented in Figure 6-2. Well characterised materials such as Copper alloy (C101) and Aluminium (1050A) flyers, whose equations of state are known were employed to impact PLA targets at impact velocities in the range 300 – 1000 m/s. The projectile impact velocity was recorded via a series of light gates at known separation immediately prior to impact. Further, target rings were employed to support the target and ensure alignment experimentally with respect to the flyer, on a sacrificial barrel extension to ensure good flyer - target alignment.

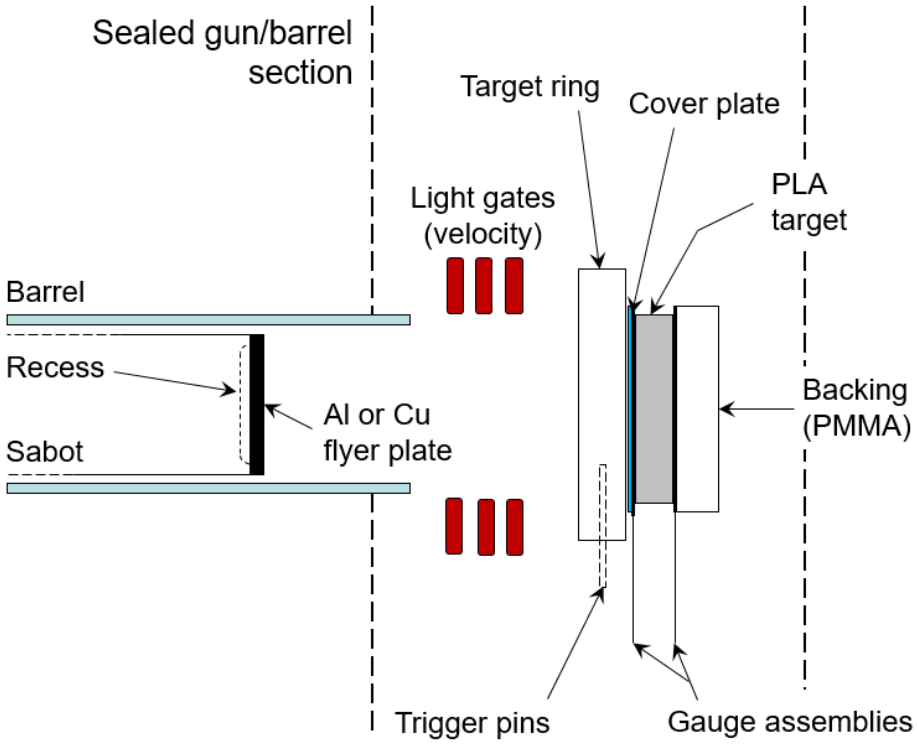

Figure 6-2. Schematic representation of the mounting configuration of longitudinal target arrangement in plate impact experiment.

Manganin longitudinal stress gauge (Vishay Micro-Measurement of Type LM-SS-125CH-048) of 48.0 $\pm$ 1.0% grid resistance in Ohms resistance were used to determine the stresses in the material. The gauges were placed at the front and rear of the target separated by a 50 micron Mylar (25 microns on each side) as illustrated in Figure 6-3 to protect and insulate the gauges. PMMA of 10 mm thickness were used at the rear gauge to trap reflection of the shock wave. All the components were held neatly together with a slow curing Loctite 0151 HYSOL epoxy-patch adhesive. Cover plate comprising 1 mm thick aluminium or copper, depending on the impactor material were employed at the target surface to protect the gauge from being damaged by the impactor.

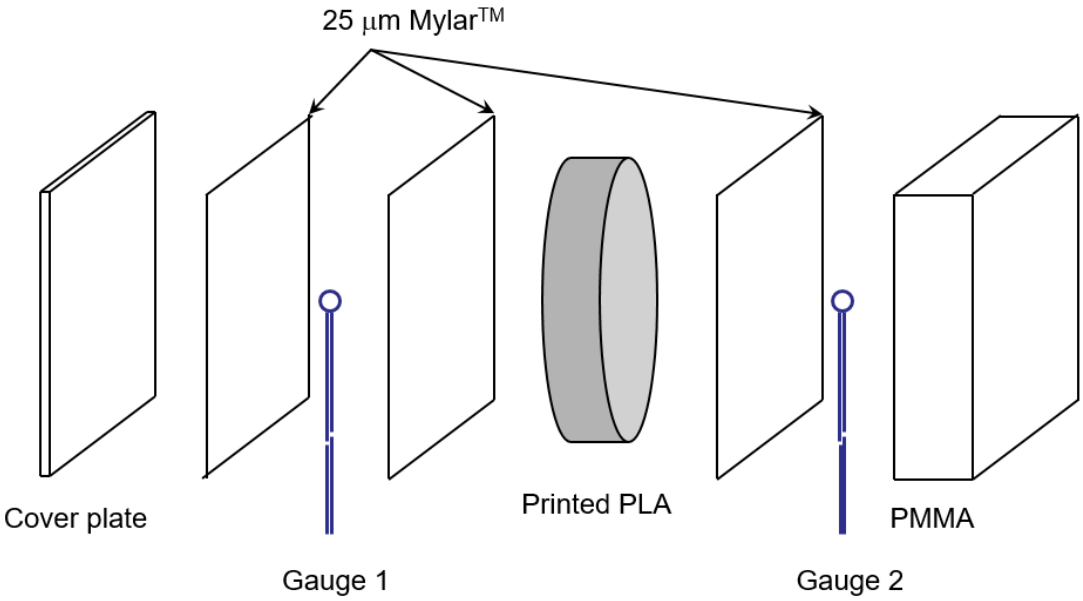

Figure 6-3. Schematic representation of target configuration in plate impact experiment showing expanded view.

The shear strength of the material was also measured by obtaining the lateral component of the stress (σ_y), from which the shear strength behind the shock front is calculated from the relationship in Equation 6-3.

$$2\tau = \sigma_x - \sigma_y \qquad 6\text{-}3$$

Embedded lateral Manganin gauges (Vishay Micro-Measurement of Type J2M-SS-580SF-025) were introduced into sectioned samples, 4 mm from the impact surface as shown in Figure 6-4. This depth was chosen to allow sufficient time for the shock to equilibrate / to resolve the elastic precursor (if any) before shock arrival. The samples were held firmly with a Locite 24-hour epoxy in a special jig for a minimum of 12 hours. In some experiments, longitudinal and lateral gauges were combined at impact velocities between 200 and 900 m/s to obtain additional $Us - Up$ data point on the Hugoniot. Errors were minimised by ensuring proper gauge alignment in the sectioned lateral halves of the target [144].

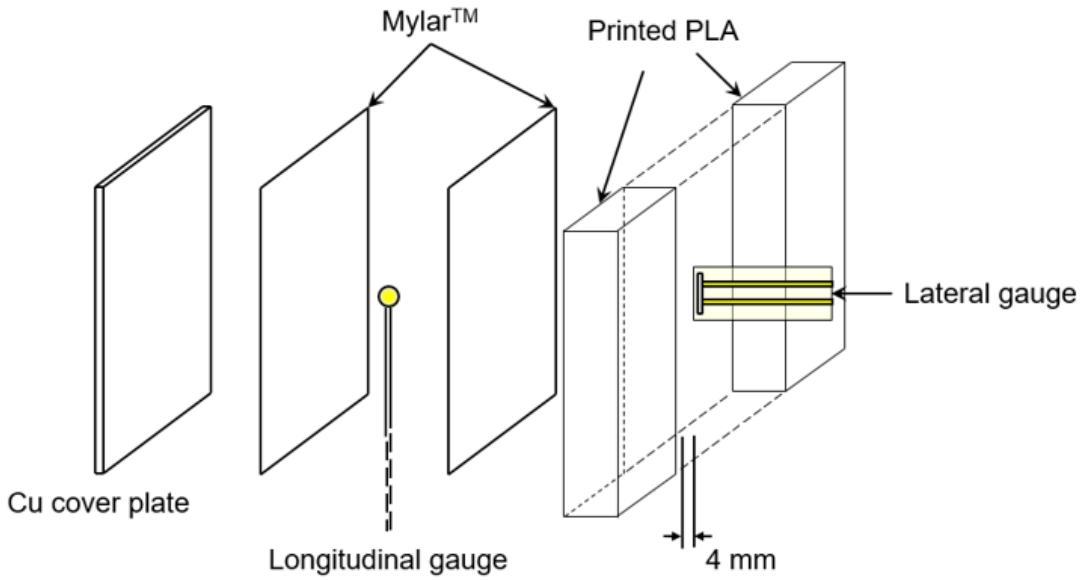

Figure 6-4. Schematic representation of target configurations with longitudinal and lateral gauge positions.

The densities of the printed PLA samples were measured using an XS 105 dual range excellence machine from Mettler Toledo. A density reduction relative to the initial material density (1.24 g/cc) was observed in all samples as a result of the pores generated between layers during the printing process. In addition, shear (C_S) and longitudinal (C_L) sound velocities were measured ultrasonically using 1 MH_Z quartz transducers with a Panemetrics 5077PR pulse receiver in the pulse-echo configuration. Employing the isotropic relation for wave speed in Equation 6-4 [145], the bulk sound c_B was obtained. Key elastic material properties of the printed PLA are summarised in Table 6-2.

$$\mathrm{C_B} = \sqrt{\mathrm{C_L^2} - \frac{4}{3}C_S^2} \qquad 6\text{-}4$$

Table 6-2. Relevant elastic material property for printed PLA measured perpendicular to the printing direction.

ρ_0	C_L	C_s	C_B
g/cm^3	(mm/μs)	(mm/μs)	(mm/μs)
1.14	1.86 ± 0.02	1.19	1.25

The FDM 3D printing technique has been shown to exhibit anisotropic behaviour dependant on print orientation[70]. As such, the wave speeds were measured perpendicular to the print direction and at different points on the surface to check that the resultant wave speed is consistent. The measured longitudinal sound speed for the printed PLA sample was 1,860 m/s – corresponding to a bulk sound speed of 1,250 m/s (Table 6-2). This appears to be below the result obtained by Parker et al., [146] who employed the pulse-echo technique to determine the bulk sound speed and acoustic impedance of PLA to be around 2,260 m/s. Variation between the measured sound speed measurements is consequently tentatively attributed to the presence of voids arising from the 3D printing manufacturing technique employed – e.g. FDM when compared with a cast PLA. Even though the pores are microscopic, small void contents can influence the sound speed in a mixture as the rate at which sound travels is lowered due to the need for waves to travel around the pores [147].

6.5 Results and discussion

A total of 6 experimental shots were undertaken at impact velocities between 200 – 1000 m/s using 5 and 10 mm thick aluminium and copper flyers against ~10 mm thick printed PLA targets. Figure 6-5 shows representative shock profiles of the printed PLA for 3 selected impact velocities ranging from 213 – 925 m/s corresponding to impact pressure between 0.3 and 4.0 GPa. Essentially, as touched on earlier by ensuring that all impact faces (target and projectile) are parallel and finished to a tolerance of <10 μm, planar shock waves are rapidly established in both the target and impactor due to the material being inertially

confined on impact. The resultant shocks are 1D in nature and are maintained until release arrival from free surfaces (interfaces). Key features can be interpreted from the shock profile obtained from the experiments. An initial pressure rise on shock arrival indicates the establishment of the shock wave into the target. The rapid rise in the front gauge indicates a good gauge alignment followed by a levelling of the shock front in the form of a plateau, the Hugoniot stress. An overshoot in longitudinal stress was observed after the initial rise with some ringing attributed to electrical effect.

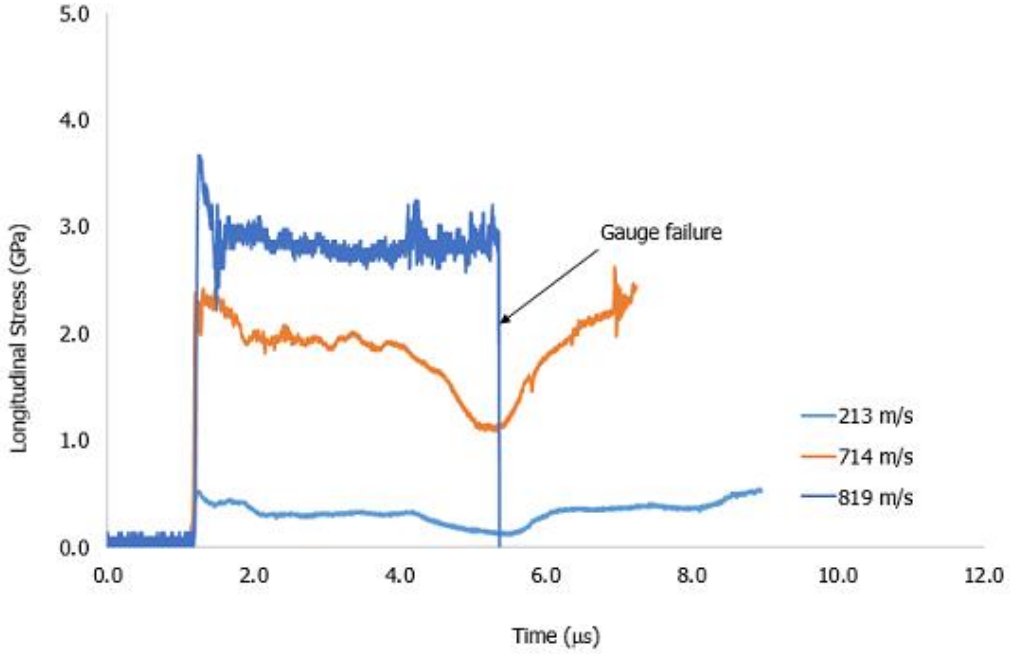

Figure 6-5. Representative wave traces of printed PLA shots at 213, 714 and 819 m/s (corresponding to impact pressures of 0.30, 1.93 and 2.88 GPa respectively)

The voltages were converted into stresses following a technique developed by Rosenberg et al., [148]. The front gauge measured the stress in the PLA while the rear gauge recorded that in the PMMA (backing material). To characterise a material mechanical shock response, five key parameters are required and these are: shock velocity U_s, particle velocity U_p, density ρ, pressure P, and internal energy E. By employing the principles of conservation of energy, mass and momentum, other parameters can also be obtained from just two parameters. In this study, the U_s and U_p values were obtained and employed to derive a shock

Hugoniot equation of state for the printed PLA. The shock velocity was obtained by calculating the time taken for the shock to travel between the front and rear gauge indicated by the rise in both gauges divided by the known gauge separation distance, with particle velocity determined via the impedance matching technique (requiring knowledge of impactor properties and velocity [149] and subsequently converted to volume as-required. In addition, the embedded gauges provided a direct measure of in-material stress. A Typical trace for the front and rear gauges of a printed 10 mm PLA with impact velocity of 714 m/s is presented in Figure 6-6.

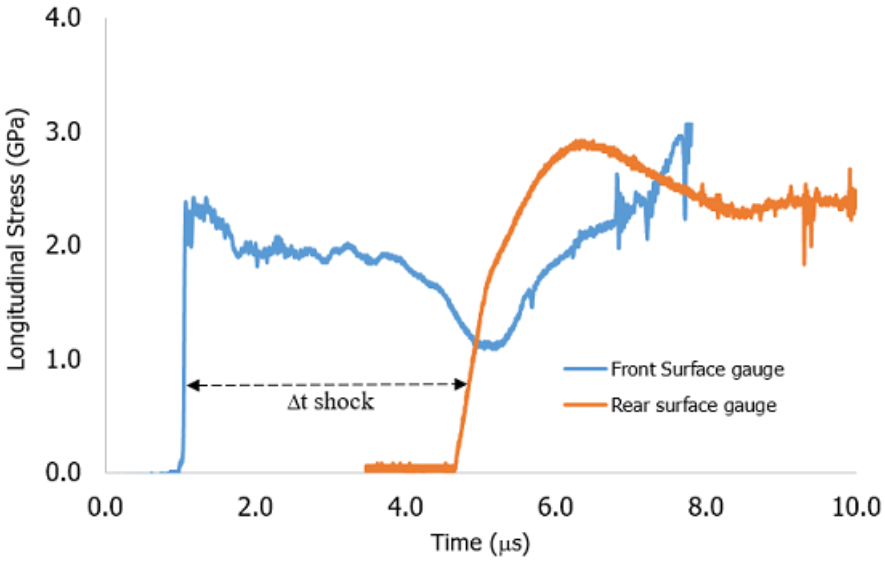

Figure 6-6. Typical gauge trace for 10 mm thick copper impacting a 10 mm thick printed PLA at 567 m/s.

By employing well-defined flyer materials with an established pressure – particle velocity ($P - U_p$), and known impact velocity, the $\mathrm{U_p}$ is obtained graphically via impedance matching technique described extensively by Meyers in Reference [149]. The $\mathrm{U_s} - \mathrm{U_p}$ Hugoniot relationship for the printed PLA was measured/calculated with data points obtained from shock states derived via experimental plate impact experiment. A summary of the experimental conditions and key results where $\mathrm{U_s} - \mathrm{U_p}$ data were extracted are presented in Table 6-3.

Table 6-3. Summary of plate impact experimental results.

Impact velocity (m/s)	Flyer thickness (mm) / material	U_p (mm/μs)	U_s (mm/μs)	Error (+)	Error (-)	P (GPa)	Error (+)	Error (-)
213	10 / Al	0.18	1.87	0.09	0.05	0.30	0.02	0.02
312	10 / Cu	0.30	2.04	0.15	0.13	0.70	0.1	0.69
490	10 / Al	0.41	2.37	0.14	0.12	1.45	0.05	0.05
714	10 / Al	0.58	2.74	0.24	0.21	1.93	0.14	0.12
819	10 / Cu	0.73	2.93	0.21	0.11	2.88	0.11	0.10
925	10 / Cu	0.84	3.17	0.22	0.14	3.59	0.13	0.18

Although the samples were observed to contain some degree of porosity, this is quite minimal (<8%). As such, the Mie-Gruneisen EOS relationship for porous materials, described in Reference [94] which predicts volume increases at all pressure for porosity of 50% cannot be employed here. Essentially, when the main bulk of the material contains a significant fraction of voids, such as solid foam (pg.64 of Reference [150]) with larger variations in impedance, the nature of the response is markedly difference. However, for the samples printed here, the void observed is in the quite small, much lower than the width of the pressure gauges employed. Hence, the authors consider that the effect of the voids on the resultant EOS is negligible. Moving forward, both linear and non-linear polynomial fits to the experimental data were considered. For the linear relationship, best-fit to the experimental data, C_o and S were found to equal 1.38 and 2.0 respectively, with a residual "R^2" value of 0.983. However, a 2nd order polynomial fit produced a higher $R^2 = 0.995$ which justified its use in Figure 6-7. In this case, the polynomial coefficient for the best fit were: C_o = 1.28 mm/μs, S = 3.06 and Q = -1.09 mm/us something highlighted in Table 6-4. Such non-linear response has been reported in the low pressure (below the 20-30 GPa transition)

regime for polymeric materials such as PMMA [151], polyethylene and PVC [92]. However, above the particle velocity of ca. 0.2 mm/μs, as recorded in this experiment, most polymeric materials give a linear response, of the form $U_s = C_o + SU_p$, along with other commercially available polymers and specially produced plastics [139]. The empirical constants C_0 and S in the linear and polymeric best-fit equations are related to the bulk sound speed (in metals such as copper) [152] and the rate of change of compressibility of the material with pressure [139], respectively. More striking, and in line with other polymeric materials such as PMMA, and polycarbonate [93], is the failure of the experimental data to extrapolate to the zero-pressure ultrasonic measurement as observed in metals. For the non-linear fit considered, the difference between the ultrasonic sound speed and the experimentally derived C_0 is only 0.02 mm/μs. As such, the bulk sound speed of the material lies only slightly below the zero vertical intercept of the $U_s - U_p$ plot giving a polynomial non-linear response of the form $U_s = C_o + SU_p + QU_p^2$ [153]. This accounts for the narrow variation in R^2 value between the linear and non-linear fits.

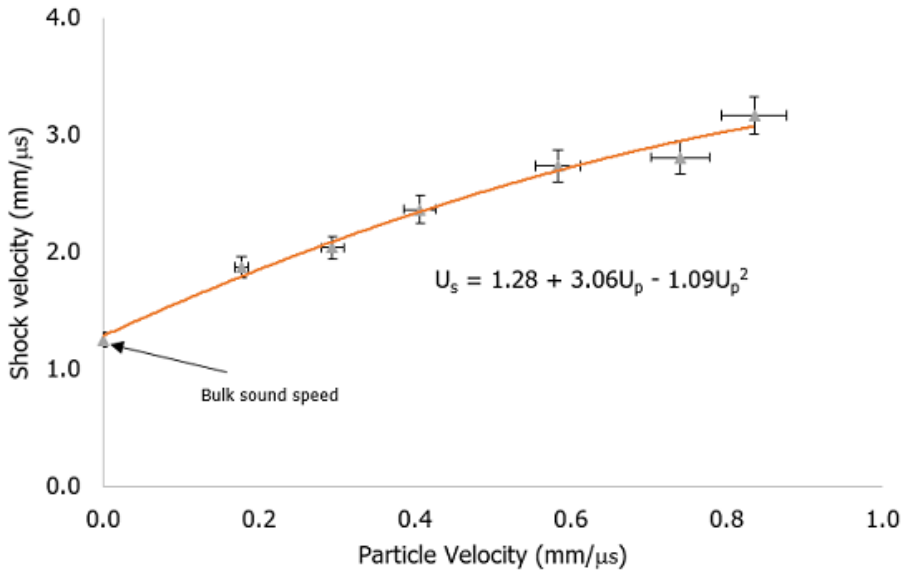

Figure 6-7. Non-linear Hugoniot response for printed PLA at low shock velocity range.

Table 6-4. Equations of state considered for PLA Hugoniot.

Type	Equation	R^2 value
Linear Form	$U_S = 1.4 + 2.02U_p$	0.983
Non-Linear form	$U_S = 1.28 + 3.06U_p - 1.09\ {U_p}^2$	0.995

Such non-linear response has been attributed elsewhere to the two-dimensional nature of polymer compression and to the form of the inter-chain interaction potential [93] owing to the substantial difference in magnitude between the backbone and inter-chain forces as described earlier. Fundamentally, weaker inter-chain forces are overcome during the initial stages of compression before the backbone covalent bonds, thereby resulting in a two-stage compression. A non-linear response occurs at low particle velocities, < 0.2 mm/μs; whereas a more conventional linear $Us - Up$ response is established. Comparison (low range data) of the measured $Us - Up$ plot with some selected polymers such as PE and PVC in Figure 6-8 revealed similarities in terms of lower bulk sound speed. Such changes have been linked to changes in the density and modulus due to molecular rearrangement of the chains [28].

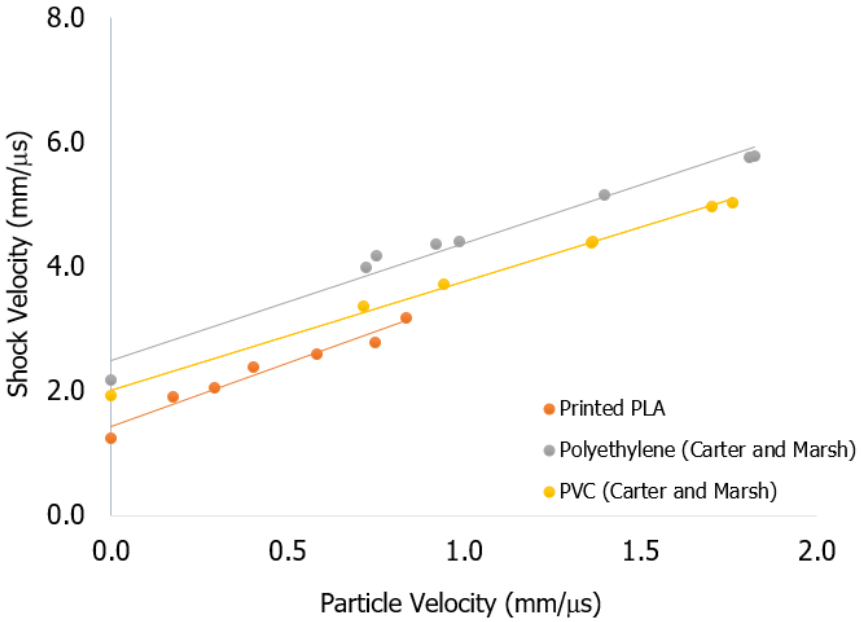

Figure 6-8. Comparison of U_s-U_p plot of printed PLA with Polyethylene and PVC.

As can be seen from Figure 8, PLA lies at the bottom of the plot followed closely by PE with a simple polymer structure. This response could be attributed to the presence of the methyl group on the carbon backbone of the PLA (in Figure 6-1) making the chain bulkier thus, providing a steric impediment to flow. Further, the presence of oxygen atom to the carbon chain increases the strength of the carbon-ligand bond and decreases Van-der-Waals forces between chains. Above the PE response are the highly electronegative polymers PCTFE and PVC with branch or side chains replaced by electronegative atoms such as fluorine or chlorine. Each of these polymers has other elements introduced onto the carbon backbone or into the side group chains increasing the density throughout the series. The PCTFE, for example, is higher up because of the presence of both chlorine and fluorine which increases the repulsion force as well as the density. As such, the combination of density and strength ensures that the Hugoniot lies above their hydrocarbon neighbours. By employing the non-linear equations of state from Figure 6-7, the hydrodynamic pressure can be calculated according to Equation 6-5. When plotted with the measured stresses in Figure 6-9, the strength of the material can be predicted.

$$P = \rho_o U_p U_s \qquad 6\text{-}5$$

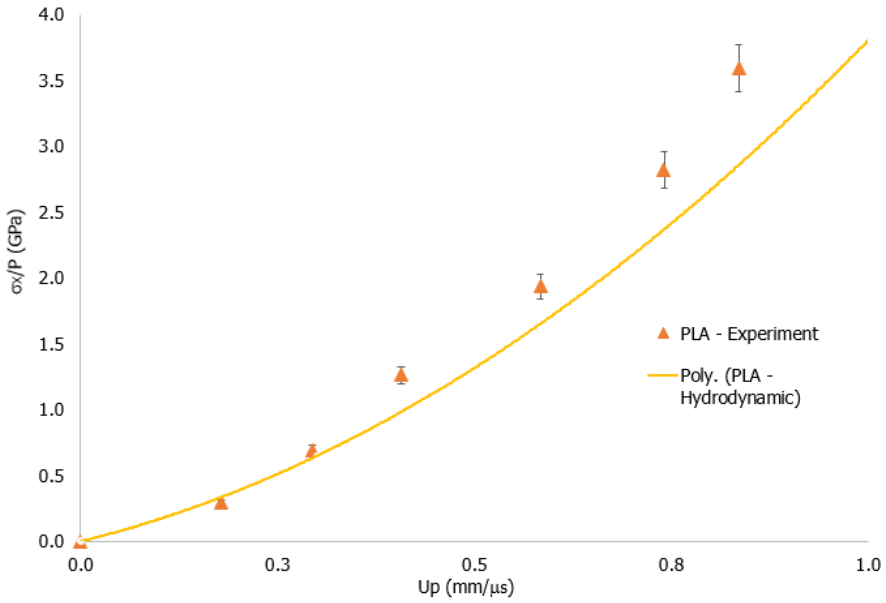

Figure 6-9. σ_X/P-U_p Hugoniot relationship for printed PLA plus hydrodynamic response based on Equation 6-5.

From Figure 6-9, there appears to be a deviation between pressure as particle velocity increases. This implies that, at least, within the shock pressure regime investigated, the printed PLA appears to strengthen behind the shock front suggesting material strengthening (τ) according to the relationship in Equation 6-6 [155], Similar response where divergence was observed between measured longitudinal stress and calculated hydrodynamic pressures has been recorded with other polymers such as PE, PCTFE and PVC [137] where large deviations were seen. Although, it's interesting to note that D. Wood et al., [141] observed no deviation between the hydrodynamic and experimental measured parameters for SC-1008 at pressures below 4.00 GPa, showing that such a response is not guaranteed – although, above 4 GPa, deviations from the hydrostat were observed suggesting potential material strengthening.

$$\sigma_x = P + \frac{4}{3}\tau \qquad 6\text{-}6$$

Recorded lateral gauge traces are presented in Figure 6-10 with the corresponding stresses noted on each trace. All traces reveal some similarities; a rapid rise to the Hugoniot stress signifying shock has been induced in the material and a subsequent decent in the trace due to interaction of the reflected waves with the incident. However, it appears that the response from the different gauge traces show some marked differences. The recorded gauge traces at 363 and 822 m/s reveals that the lateral stress is decreasing. This implies that the material hardens behind the shock front, following Equation 6-3. However, we have also observed increasing lateral stresses with the trace labelled 0.86 GPa and an undulating stress in the 0.41 GPa trace. The reason for the latter trace is not clear but the authors believe that, this is likely a result of the layers of air and material which the shock fronts meets as it travels (as it equilibrates) along the lateral halves of the target in view of the concentric pattern employed in the FDM built parts. This can only be verified by performing similar experiment using the bulk material. However, usefully, the decreasing lateral stresses recorded in the 1.09 and 0.18 GPa traces, reveals that the material is hardening behind the shock front, consistent with other polymeric material, such as PMMA [138] and Polycarbonate [156]. This has been attributed to an increase in the proximity of molecular components, arising from densification of molecules, with strong attractive bonding and steric [157] entangling which tends to resist further strain with time [150].

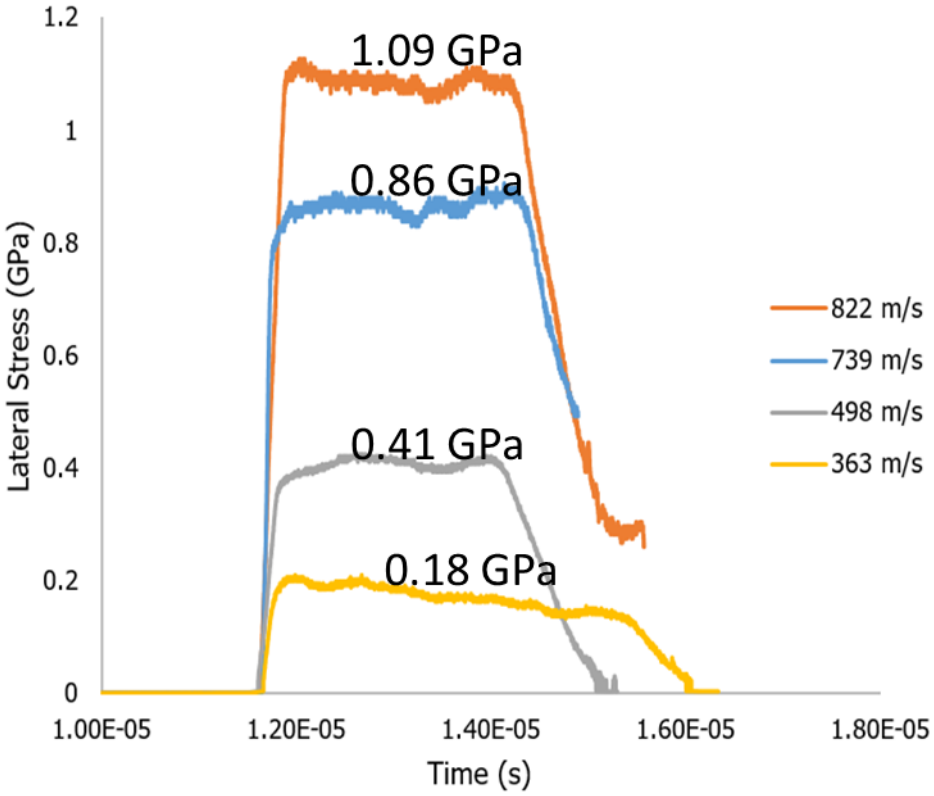

Figure 6-10. Lateral stress histories for printed PLA at varying impact velocities; gauges are 4 mm from the impact surface.

Another interesting feature is the gauge response time. It was observed that the time taken for the gauge to respond differs with impact velocity. It was expected that the higher impact velocities will produce lower response time but this is not completely seen here. The highest response time of 2.95E-7s was recorded for the highest impact velocity of 822 m/s followed closely by 2.56E-7 s recorded at 498 m/s and then 1.008E-7 s response time for 739 m/s impact velocity shot. Although differences between the response time are insignificant, the authors believe that the variation are due to possible misalignment of the gauges in the lateral half of the target. A slight misalignment of the gauge could increase the response time because of the time it takes for the shock to equilibrate across the gauge length. Although the initial rise in the gauge traces has been attributed elsewhere to gauge equilibrium [158], essentially, polymer densify to large strain against weaker inter-chain Van-der-Waals [150] forces before material begin to exhibit a steady state behind the shock front. This implies that the stress state

stability can only be achieved once the polymer has been loaded to compression at which the carbon atoms interact at a maximum density which suggests that rate of compression determines the amplitude and time to stable state. At lower stresses such as that observed in the 0.405 GPa, the printed PLA takes more time to equilibrate to the stable state. As such, the effect of densification, which also includes closure of the pores and rearrangement of the molecule to a fully dense state is more visible at lower stresses.

The shear strength data calculated from Equation 6-3, using lateral stress gauges at 4 mm from the impact surface is presented in Table 6-5.

Table 6-5. Experimental conditions and results of lateral stress gauges at 4 mm from the impact face.

Flyer thickness (mm) / material	**Impact velocity (m/s)**	$\boldsymbol{\sigma_x}$ **(GPa)**	$\boldsymbol{\sigma_y}$ **(GPa)**	$\boldsymbol{2\tau}$ **(GPa)**
10 / Cu	366	0.90	0.18	0.72
10 / Cu	478	1.32	0.41	0.91
10 / Cu	739	2.54	0.86	1.68
10 / Cu	822	2.99	1.09	1.90

From Table 6-5, it is apparent that shear strength increases with increasing impact stresses in agreement with similar polymeric materials [138]. The lateral stresses immediately behind the shock front have been used, along with the known longitudinal stresses to determine the shear strength of the printed PLA. Usefully, the shear strength can be employed to help define the elastic-plastic transition. Above the elastic limit, the material behaves plastically and vice-versa. By comparing the yield strength of the material to an elastic prediction given in Equation 6-7, the Hugoniot Elastic Limit (HEL) can be obtained. This technique has been previously validated in Reference [138] and employed to determine the HEL of PMMA. Employment of the technique in the determination of the shear

strength is presented in Figure 6-12. The elastic behaviour is represented by the solid line according to Equation 5-7 [150].

$$2\tau = \frac{1-2v}{1-v}\,\sigma_x \qquad 6\text{-}7$$

Where 'v' is the poisons ratio. A linear line of best-fit has been put through the measured stress which intercepts the elastic prediction at longitudinal stress of ~ 0.9 GPa. This can be taken as the Hugoniot Elastic Limit. In comparison with similar polymeric material like PMMA where the elastic limit has been placed in the range ~0.7 - 0.9 GPa. It is pertinent to note that the specimens employed here were fabricated with the build direction perpendicular to the shock direction and considering the fact that the mechanical properties of FDM built parts varies with built parameters[159] as well as the bulk material, the elastic limit obtained may vary with the different print settings and the bulk material; although this is only speculative.

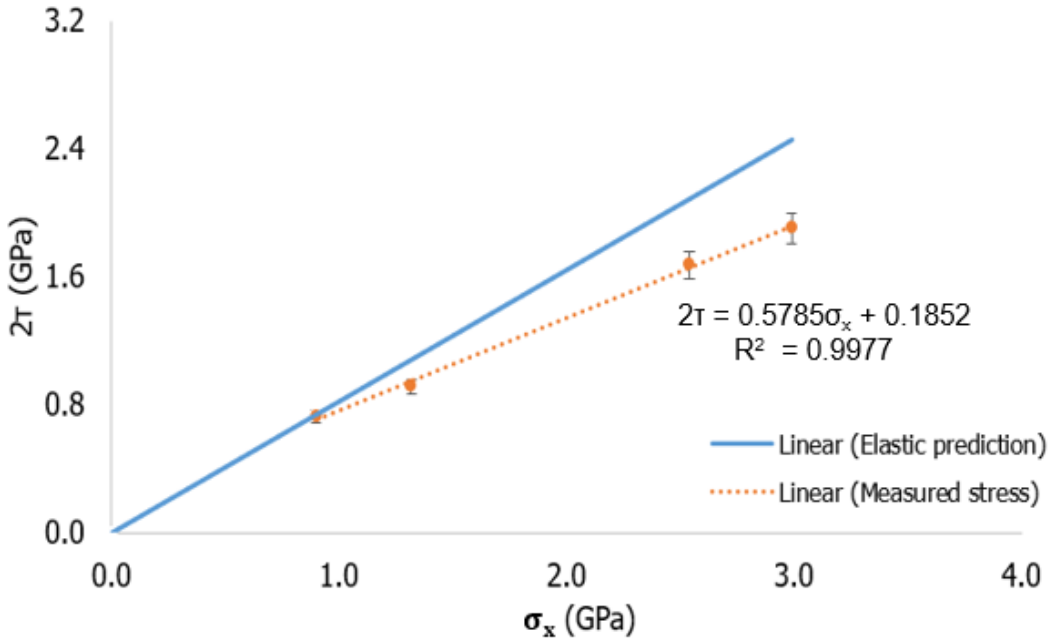

Figure 6-11. The shear strength vs longitudinal stress for printed PLA.

From Figure 6-11, it is apparent that shear strength increases with stress, as with other similar polymeric materials, PE and PVC. It is however interesting to note

that the measured HEL of PLA is within similar range with PMMA which has been shown to have higher strength than basic polymers (particularly PE and PVC). This could be attributed in some ways to steric effect, arising from large chain structure due to the presence of multiple side chains and the presence of electronegative atom in the side group chain. While the presence of oxygen increases the electronegativity, allowing polar attraction to increase the bond strength, it's very likely that the dynamic response is controlled majorly by the interaction between adjacent polymer chains emanating from the inclusion of Methyl group and oxygen to the polymer chain, causing further tangling of the polymer chain structure.

6.6 Conclusion

Using the plate impact experiments, the dynamic response of 3D printed polylactic acid has been investigated over the impact velocity range of 200 – 900 m/s (corresponding to impact stresses of 0.30 to 4.00 GPa, respectively). A total of six plate-impact experiments were undertaken to determine the Hugoniot of commercially produced 3D printed PLA via the filament deposition technique. Both linear and non-linear Hugoniot was considered with the non-linear R^2 value tending to 1, giving it a non – linear equation of the form $U_s = 1.28 + 3.05U_p - 1.09U_p^2$. This non-linearity appears indicative of the underlying material structure. A change in slope in the plot of shear strength against longitudinal stress at 0.90 $\pm$ 0.05 GPa within similar range with PMMA was observed, attributed to both the increase chain entanglement and electronegativity of the polymer chain structure via the addition of methyl and oxygen atom respectively to the polymer chain.

7 Comparison of the Microstructure of Laser Sintered and Traditional Machined Copper Liner in the Hydrodynamic Regime

H.O. Agu, A. Hameed and G.J. Appleby-Thomas

Centre for Defence Engineering, Cranfield University, Shrivenham, SN6 8LA, United Kingdom

*Corresponding author: henry.agu@cranfield.ac.uk

This chapter/paper is designed to provided additional insight into the key aim of this thesis which is the investigation of the performance of 3D printed shaped charge liners. While the performance of additive manufactured shaped charges liners has been elaborated in Chapter 4 and 5, it was necessary to investigate the microstructure of the as-manufactured and resultant (slug) to provide a complete study of the behaviour of laser sintered liners in the hydrodynamic regime. The investigation presents some interesting discoveries which shows that laser sintered liners undergoes dynamic recrystallization under explosive loading with the formation of precipitates. The work also explains the mechanism underpinning the presence of centre hole formation at the jet axis, wave pattern observed around the centre axis of the jet microstructure and more importantly, molten 10% of the jet diameter reported during soft recovery.

Adapted from: H. O. Agu* A. Hameed, G. J. Appleby-Thomas, Comparison of the Microstructure of Laser Sintered and Traditional Machined Copper Liner in the hydrodynamic regime, research paper published in the Journal of Dynamic Behaviour of Materials.

7.1 Abstract

To gain further insight into the mechanisms underlying jet formation and elongation of laser sintered parts under high strain rate deformation, Cu-Cr-Zr alloy liners fabricated by selective laser sintering process were deformed by explosive detonation. Their as-manufactured (liner) and resultant (slug) microstructures have been investigated in comparison with those of traditional machined liners, employing both optical and scanning electron microscopy. The resultant microstructure of both machined and laser sintered liners revealed a smaller refined equiaxed grain size consistent with traditionally fabricated liners, characteristic of dynamic recrystallization. Disappearance of the (originally present) pores in the post-shot / recovered material microstructure was observed for laser sintered liners. Comparison of the forward and rear region of the slug revealed variations in liner deformation, a result attributed to temperature variation across the slug. In contrast with the machined liner, a unique feature of precipitation, observed in the ending (slug) microstructure of the laser sintered liner was observed, something indicative of the associated extreme high strain and strain rate liner deformation which occurred during slug formation. The precipitates are likely compounds of Chromium and Zirconium which are constituents of the laser sintered copper alloy – importantly, this is the first time this observation has been reported and it therefore provides insight into potential additional effects when manufacturing shaped charge liners via such novel techniques. This study provides a link between post charge evolution microstructure and liner manufacturing processes, potentially providing a new route to help optimise jet formation and effectiveness.

Key words: Liner, sintering, shaped charge, copper, microstructure

7.2 Introduction

It has become widely accepted that shaped charge liners undergo dynamic recrystallization during liner collapse and jet formation to produce refined microstructures [44], [45], [160]. Under high strain / strain-rate conditions, severe plastic deformation of the liner gives rise to nucleation and growth of new grains by continuous accumulation of dislocations [51]. During this process, low angle boundaries are being transformed into high angle boundaries accompanied by subdivision of original grains into small, sometimes equiaxed grains with significant microstructural refinement [127]. Although the resultant microstructure is controlled by the degree of deformation [44], it is influenced majorly by the strain / strain rate as well as the deformation temperature (itself a function of the nature of load on the liner) which varies along the jet length [121], [127]. This variation, results in segments of the ending (slug) microstructure having higher deformation with apparently more refined microstructure than others [52]. Guo et al. observed that, in spite of the small equiaxed microstructure observed in recovered Tungsten slugs, significant variation in grain sizes were recorded at the centre, 0.5 and 1 mm away [52]. In short, the grain size of the slug appeared to change linearly outward with the smallest grains at the centre and the largest in the outer regions.

A similar observation was reported by Murr et al., [45], where different grain sizes were observed at three concentric rings, with the middle ring having the largest. Usefully, analysis of hydrocode simulations of a stretching shaped charge jet has revealed higher temperatures [121] and strain at the centre, indicative of a higher degree of deformation. A relationship between the starting liner grain size (D_0) and the ending grain size (D_s), revealed that smaller starting liner grain sizes produce correspondingly smaller grain size ratios [44] because lower starting grain sizes have dramatically high liner volumetric stored energy [53]. This implies that the ending grain size is influenced not only by the starting grain size but by the degree of deformation.

In addition to the starting liner microstructure, other factors such as the liner material properties, particularly; thermal conductivity and heat capacity as well as

processing route, have been reported to have a significant influence on the ending microstructure [52]. As an example, Murr et al., [46] observed that the grain size ratio between the starting and ending microstructure of Tantalum differs widely from that of copper (by a ratio of 10:1.5), something the authors attributed to inherent liner material properties. In a separate study, comparing differences in processing technique, it was observed that equiaxed and well-annealed Tantalum both showed similar slug microstructural features which were consistent with a forged Tantalum liner, but with variations in average grain size. While the forged liner showed a resultant grain size of 35 μm, the equiaxed and well-annealed liner averaged 5 μm.

With regards to the effects of processing routes, similar microstructural differences have been reported for several processing techniques [161]. A case in point is the difference observed between OFC copper and electrolytic tough pitched copper (ETP). In contrast to OFC copper, the ETP copper showed significant voids [162], suggesting an effect of processing technique on ending (slug) microstructure. Surprisingly, while several liner processing technique has been examined [161], liners fabricated by selective the laser sintered (SLS) process - which commenced several years ago have yet to be considered. This study consequently deals with the characterization and analysis of slug recovered from explosively deformed laser sintered liner. In the present work, liners fabricated by both conventional machining and the selective laser sintering process were deformed by explosive loading to form a jet and slug as shown in Figure 7-1. We examined the microstructures of the liners and resultant slugs in comparison with machined OFHC copper liner and slug employing both optical and scanning electron microscope (SEM).

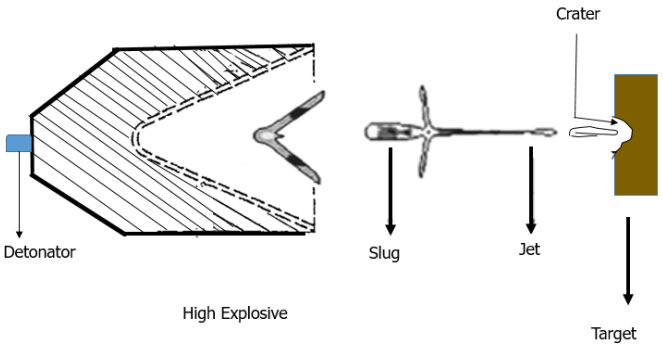

Figure 7-1. Schematics illustration of jet, slug and crater formation.

7.3 Experimental methods

Oxygen Free Copper (OFHC) and a CuCrZr alloy of grade C18150 were employed for the production of the machined and laser sintered liners, respectively. The chemical composition of CuCrZr alloy of grade C18150 employed is detailed at Table 7-1.

Table 7-1. The chemical composition of CuCrZr grade C18150.

Element	Content (%)
Copper (Cu)	98.12~99.27%
Chromium (Cr)	0.5~1.2%
Zirconium (Zr)	0.03~0.3%

The liner design used was of 50 mm charge diameter and, 1.5 mm liner wall thickness inclined at 42^{o} (cone angle). The SLS liner was solution annealed at 960^{o}C for 3 hours, water quenched and heat treated at 460^{o}C for 3 hours, while the machined liners were used as produced. The liners were deformed in the plastic and hydrodynamic regimes upon detonation with Plastic Explosive Number 8. The jet tip velocity produced by the machined liner was determined independently using ANSYS Autodyn 2D hydrocode to be 8.6 km/s. The jet was allowed to penetrate a mild steel target placed 3 charge diameters away. After firing, the resultant slugs were recovered, prepared and observed optically and in a scanning electron microscope (SEM). Metallographic preparation involved

successively finer (320 grit and then 800 grit) silicon carbide grinding followed by rough polishing using 3-micron diamond suspension and then a final polish using an alumina suspension. Ammonium hydroxide/hydrogen peroxide etch was then employed before both optical and scanning electron microscopic (SEM) analysis (using an Olympus BX53M optical and Scanning Electron Microscope, Hitachi type SU3500, respectively). The machined and laser sintered liners employed in this study are shown in Figure 7-2.

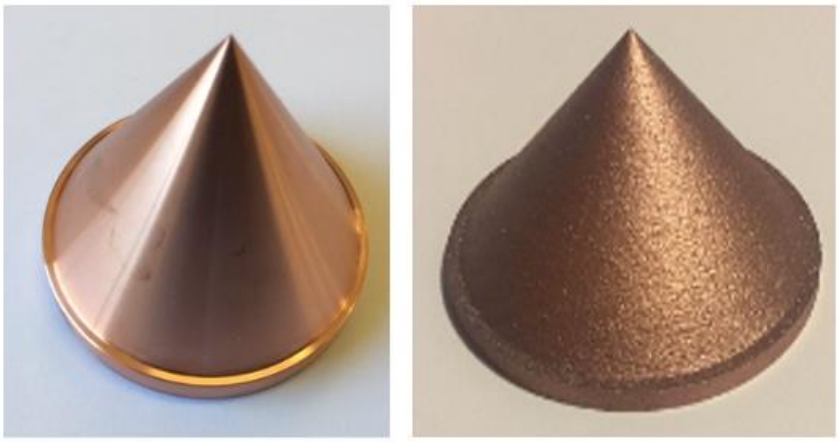

Figure 7-2. Images of machined OFHC liners (left) and laser sintered liner (right) in their as-produced state**.**

For grain size measurement, three standard ASTM approaches were considered. These were: a comparison procedure which involved a direct comparison of the grain structure to a series of the graded image superimposed over the microstructure; the planimetric (or Jeffries) procedure which requires actual counting of the number of grains within a known area and the Intercept procedure. These approaches have been summarized in Reference [163]. Of the three approaches, the intercept procedure which is faster and more convenient than the planimetric method was employed to determine the grain sizes of the starting (liners) and ending microstructure. Further, the intercept method has demonstrated reliability and efficiency for the determination of grain sizes and is particularly recommended for grains that depart from uniform equiaxed form [163]. The Heyn Lineal Intercept procedure, backed by Image J software which employs long straight lines, was used. To ensure precision, counting was done on three long lines with low magnification from which the average was taken.

7.4 Results and discussion

Figure 7-3 shows optical micrographs of the machined and laser sintered copper liner before deformation. The microstructure of the laser sintered liner consists of elongated grains along the build direction. The density of the machined liner was measured using an XS 105 dual range analytical balance from Mettler Toledo as 8.91 $\pm$ 0.02 g/cm^3 while the laser sintered liner was found to be 8.77 $\pm$ 0.02 g/cm^3, comprising approximately 98-99 % copper with 1-2 % Chromium and Zirconium. It is postulated that this difference in density may have arisen due to residual porosity in the laser sintered liner. The average measured grain size of the machined liner was ~54 $\pm$ 4 μm, while the laser sintered liner after being solution annealed at 960^{o}C for 3 hours, water quenched and heat treated at 460^{o}C for 3 hours, exhibited grain sizes ranging from circa 20 and 70 μm $\pm$ 6 μm along the horizontal and vertical axis respectively; an indication of a partially recrystallized structure arising from the sintering and post-production processes on the fabricated part.

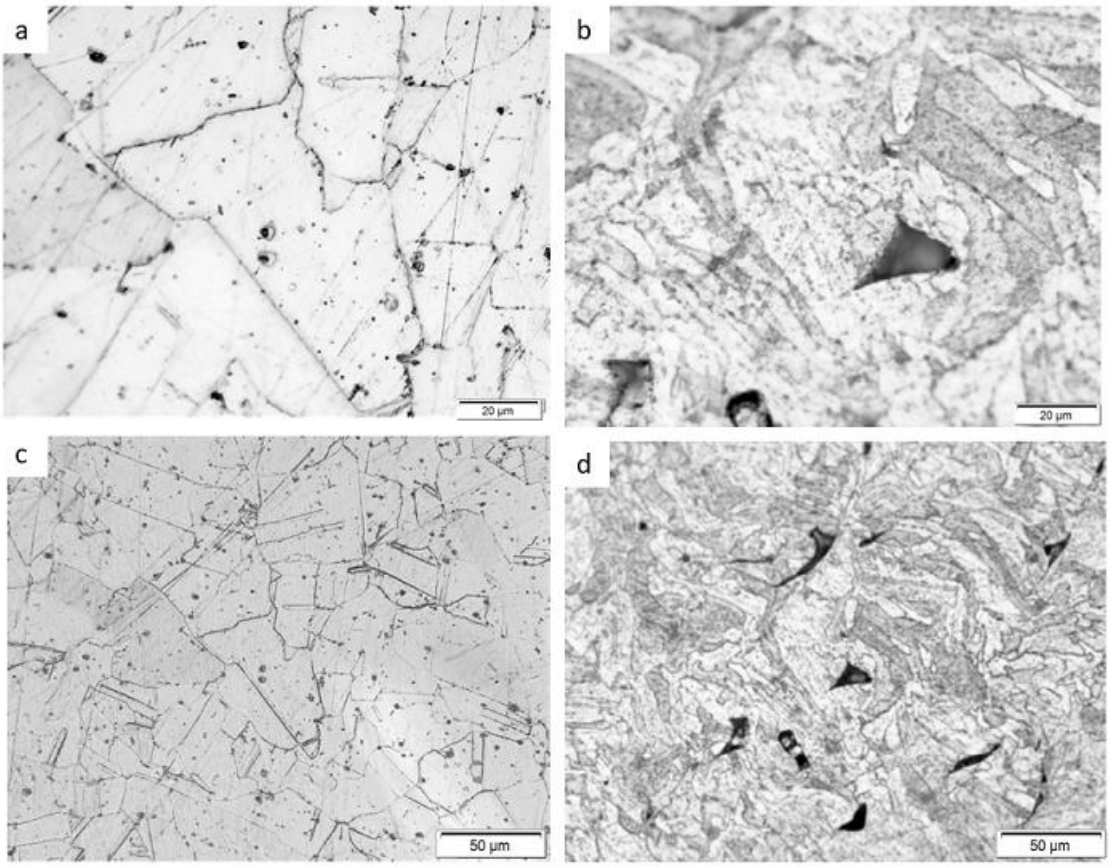

Figure 7-3. Optical images of polished and etched sections of the starting microstructure of machined OFHC Copper liner (a and c; x50 and x20, respectively); laser sintered liner (b and d; x50 and x20, respectively).

Essentially, fusion heat caused in-situ recrystallization during the building process [164], resulting in partial recrystallization of the microstructure. Of particular significance is the presence of pores which is one of the common defects in SLS liners [113] and which are observable in the SEM image in Figure 7-4. The pore sizes and shapes are irregular with no distinct pattern. In addition, there are characteristic lines running diagonally which likely correspond to the layers' boundaries in areas of their fusion during sintering ('scan tracks'); this supposition is backed by their separation which nominally corresponds to the SLS machines manufacturing tolerances of separation of ca. 100 mm per-sweep.

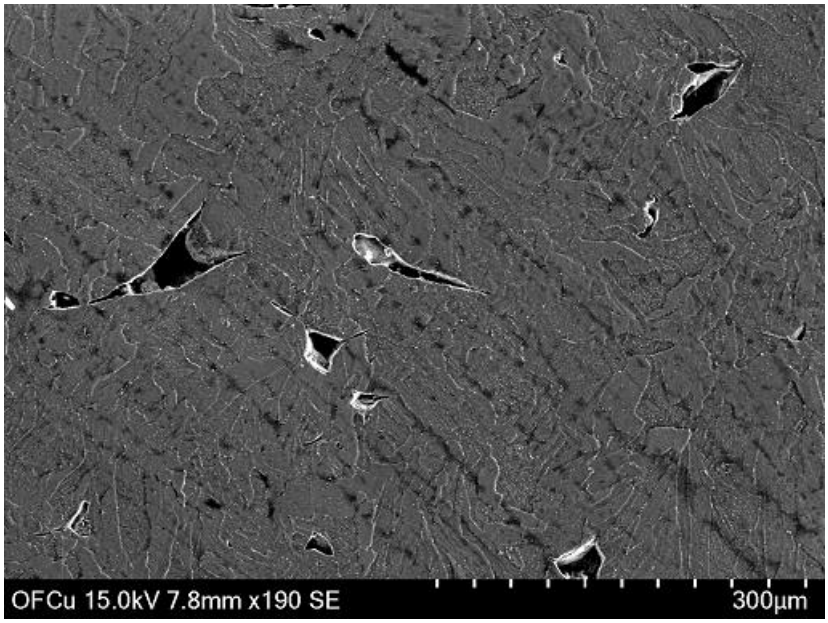

Figure 7-4. SEM observation of the laser sintered liner microstructure revealing scan tracks and irregularly shaped pores before deformation**.**

7.4.1 Optical metallography of slug recovered from machined copper liner

It is pertinent to note that unlike the soft recovery process where the jet/slug is recovered in flight, interaction between the jet and mild steel plate (as is the case here) could increase the strain and generate higher deformation temperature in the jet/slug, leading to higher grain refinement. Figure 7-5 shows optical metallographic observations of both the starting and ending microstructures of the machined copper liner and slug for comparison. It is very convincing that there is a significant reduction in the grain size of the recovered slug compared to the starting liner material. The measured grain size of the recovered slug averaged 6 μm $\pm$ 2 μm**.** This phenomenon (grain size reduction / refinement) has been reported extensively elsewhere [44], [53], consistent with the concept of dynamic recrystallization occurring at such high strain rates. In fact, Murr et al., observed a reduction in grain size by a factor or 10 for copper shaped charge liners. In this study, the measured recovered material grain sizes were equiaxed, consistent with previous work [45], [165] and varied from the initial liner grain size (an average of 54 μm) by a factor of 9. A similar study on Tungsten shaped charges liners revealed the role of dislocations in the refinement of the microstructure

during dynamic recrystallization suggesting a link between strain and grain size of the recovered slug [52].

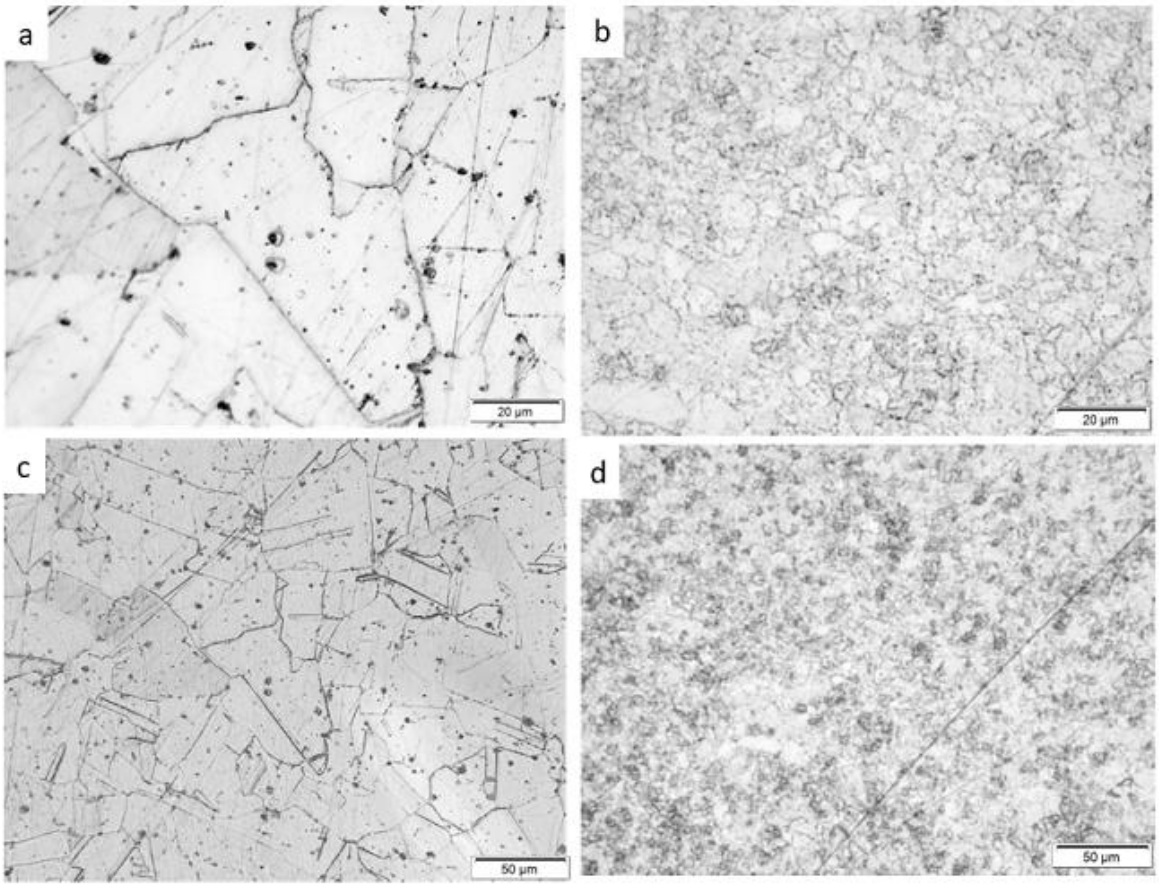

Figure 7-5. Comparison of the initial and final microstructure of machined copper liner and slug; a. Microstructure of starting copper liner x50 b. Microstructure of recovered copper slug revealing equiaxed microstructure and reduction in grain size x50. c. Microstructure of starting liner x20. d. Recovered copper slug x20.

We have also observed variations in grain size refinement in various sections of the recovered slug. As an example, the forward (tip region) and the rear sections of the recovered slug presented in Figure 7-6 shows some variation in the grain sizes. Although slightly, it is apparent that there is a more refined microstructure with smaller grain sizes in the rear (Figure 7-6a) of typical average grain size of 4 ± 2 μm averaged than the forward section (Figure 7-6b) of average grain size 7 ± 2 μm, (please note that no particular attention was placed on the distance/ depth from the centre axis at which the samples were extracted from both

positions) providing further proof of the variation in the degree of deformation in the microstructure across the resultant slug. This observed apparent variation in the grain size refinement at different sections of the slug has been reported severally elsewhere [45], [46], [166]. However, in all the recovered slug sections for the machined copper liner, no melt related phenomenon were observed on the samples analysed – strongly suggesting hydrodynamic behaviour (flow, rather than melt).

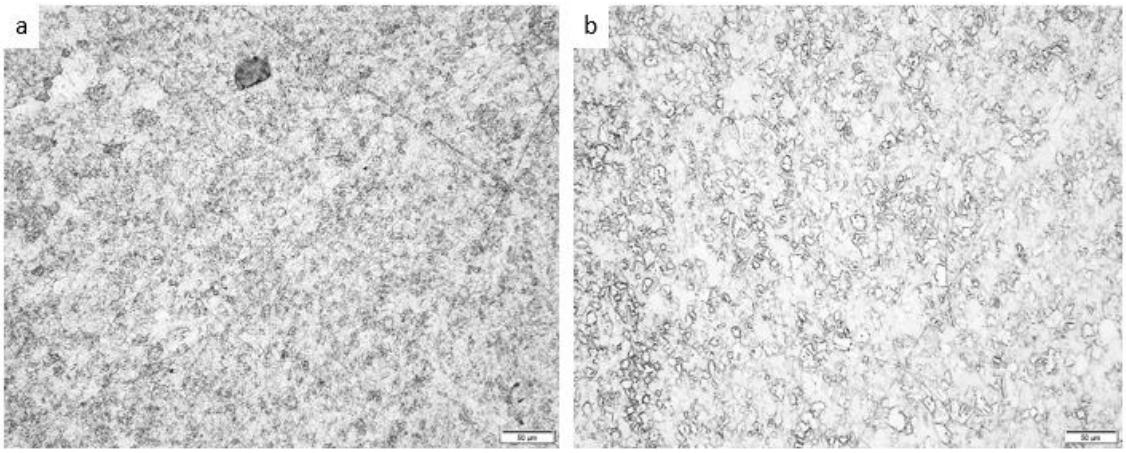

Figure 7-6. Optical micrograph of slug recovered from the machined copper liner experiment a. The rear region (x 20) b. The forward region (x 20).

7.4.2 Measurement of the jet temperature

The first attempt to measure the temperature of a shaped charge's jet was by Von Holle & Trimble [126]. Employing infrared radiometry technique, properties of 81.3 mm-diameter Copper shaped charge's jets loaded with Comp. B or Octol were determined. An average recorded jet temperature of 428 °C (701 K) was measured for Comp. B, while 537 °C (810 K) was recorded for Octol [167]. Subsequent measurement recorded by Lassila found an exterior jet temperature of 500^0c using CALE – an arbitrary Lagrange-Eulerian computer code [168]. Essentially, jet heating results from the interaction of the detonation waves with the liner (grazing detonation), plastic work during liner collapse, and jet elongation [169], [168]. In this study, an Autodyn 2D [96], [170], [171] numerical algorithm was used to study temperature variation in shaped charges. The use of Autodyn 2D to measure jet temperature was employed by Elshenawy et al., 2013 for a

Zirconium shaped charge jet for calculating the break-up time of a Zirconium liners [121]. Here, the temperature at different sections of the jet was calculated in the resultant jet and slug to proffer a possible explanation to the variation in grain refinement in various sections of the jet and slug. The hydrocode temperature calculations were first validated by modelling a BRL-81.3 mm shaped charge [16] in the multi-material Eulerian grid, employing the complete Mie-Gruneisen form of the equation of state which describes the heat capacity variations and thermodynamic properties with a reference temperature of 300K and heat capacity 3.83e-4 J/Kg.K [172]. We derived the temperature of the jet due to severe plastic work, during jet elongation (as this has been shown to produce higher temperature increase in the jet), rather than the grazing detonation wave (occurring during liner collapse) [169], for an 81.3 mm charge diameter shaped charge. The longitudinal section of Autodyn 2D shaped charge layout is presented at Figure 7-7.

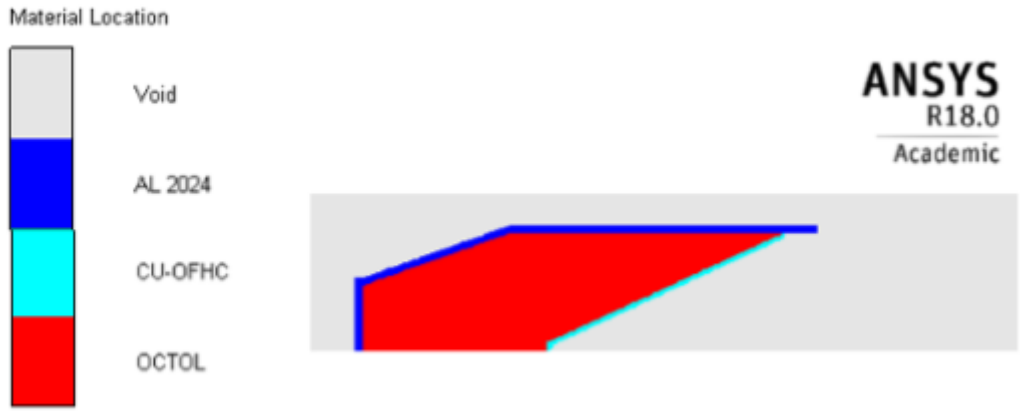

Figure 7-7. Autodyn 2D layout of 81.3 mm charge diameter in the multi-material Eulerian grid.

The jet temperature was recorded at three different times: 36μs, 45μs and 54μs respectively during the jet elongation regime. From the resultant jet profiles (Figure 7-8), it is apparent that temperature varies across the jet with the highest temperature found on the jet axis (up to 1500K), while the outer surface ranges from 795K (522^{o}c) to 905K (632^{o}c).

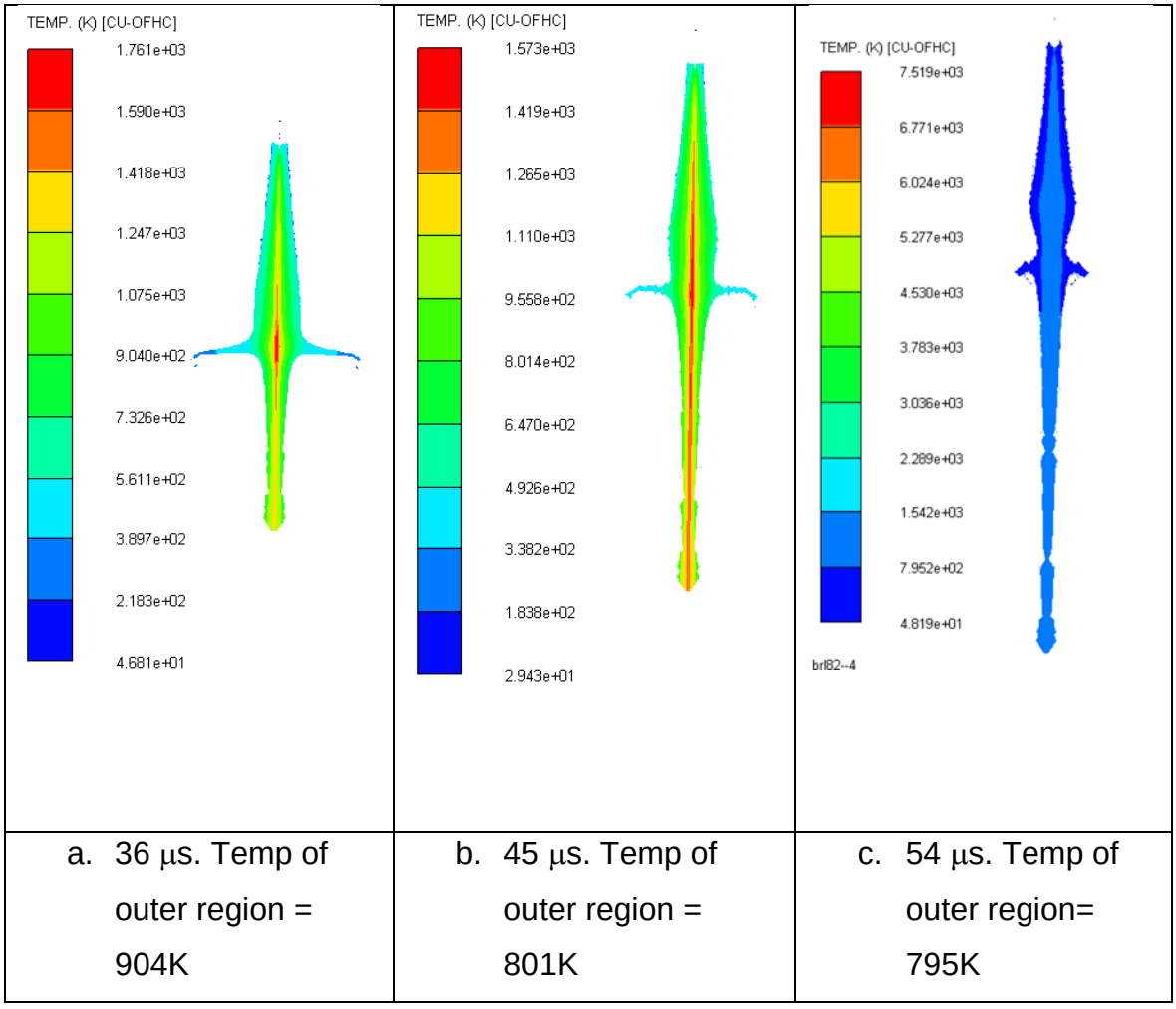

a. 36 μs. Temp of outer region = 904K	b. 45 μs. Temp of outer region = 801K	c. 54 μs. Temp of outer region= 795K

Figure 7-8. Jet temperature for BRL-81.3 mm shaped charge at various times and before jet particulation.

When the temperature and time are plotted (Figure 7-9), we observed that the jet temperature rises initially to a peak before equilibrating at a steady temperature of 710 K (437^{o}c). This recorded temperature agrees well with the temperature recorded by Von Holle and Trimble (720K) [126] and Lassila (500K). The high temperature recorded on the jet axis is likely a result of the high dynamic pressure at the collision point as the liners interact with each other. This extremely high-temperature phenomenon at the jet centre axis has presented a unique deformation pattern in the region around the jet axis. For instance, metallurgical examination by Lassila et el., of soft recovered copper jet particles and slug indicate that a central region of approximately 10% of the jet's diameter was molten [168]. Baoxiang et al., 2018 observed a wave pattern around the centre

axis of the jet microstructure, characteristic of fluid instability which he speculated, results to jet breakup [173] was noted. More interestingly, the presence of a central hole at the jet centre axis symmetry of the jet and slug [173] which was postulated to account for an unexplained 6.5% density deficit [174] in the stretching shaped charge jet [173]. While these phenomena were attributed to extremely high dynamic pressure (from 70 GPa recorded at a distance less than 1mm from the axis), which tends to resist further compression of the liner towards the centre axis and possibly alter the deformation pattern [173], from the findings reported here, giving the high temperature observed at the jet axis, it is very likely that the material in this central region of the jet and slug experience melting (lasting for only a short time) as the temperature's recorded are higher than the melting temperature of the copper – something observed by Lassila [168] to account for the 10% melt phenomenon recorded in her work. If this is true, and under such molten state, it is speculated that, the forward action of the travelling molten jet would invariably cause a corresponding backward motion of the fluid, leaving a space (centre hole in the jet and slug).

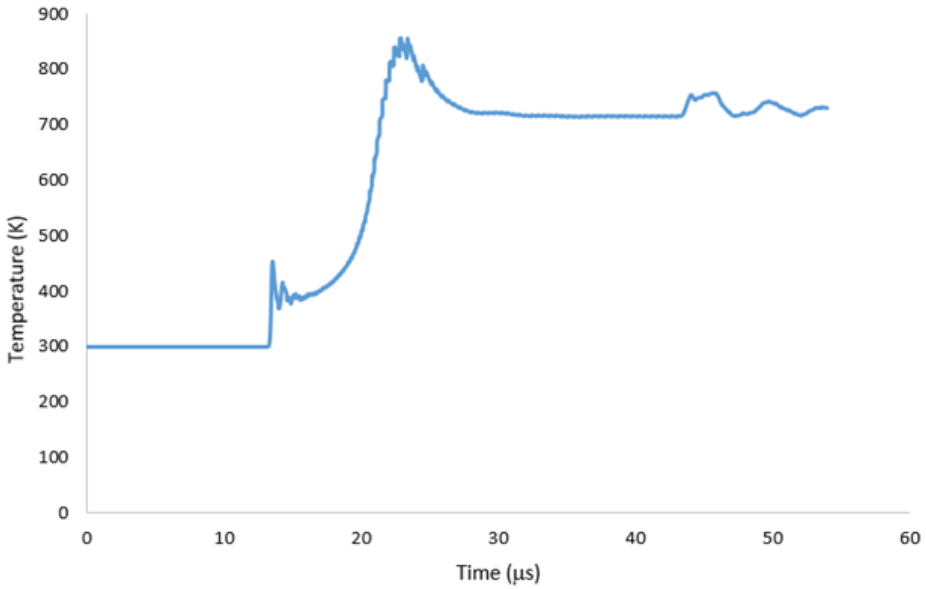

Figure 7-9. Jet temperature variation with time recorded from Autodyn 2D simulation.

To verify temperature distribution across the jet length, moving temperature gauges were placed at the outer, middle and inner surfaces of the liner. It is generally known that for conventional conical charges, the first 30-40 % of the liner from the theoretical apex forms the tip of the jet [2]. Employing a simple Lagrangian coordinate definition, postulated by Carleone and Chou (1976) [170] (Figure 7-10), we identified positions of various segments of the jet and on the liner where our gauges were placed [170]. The axial liner position is described by coordinate 'x' whereas the position of the jet is given by coordinate $'\xi'$ (Equation 7-1):

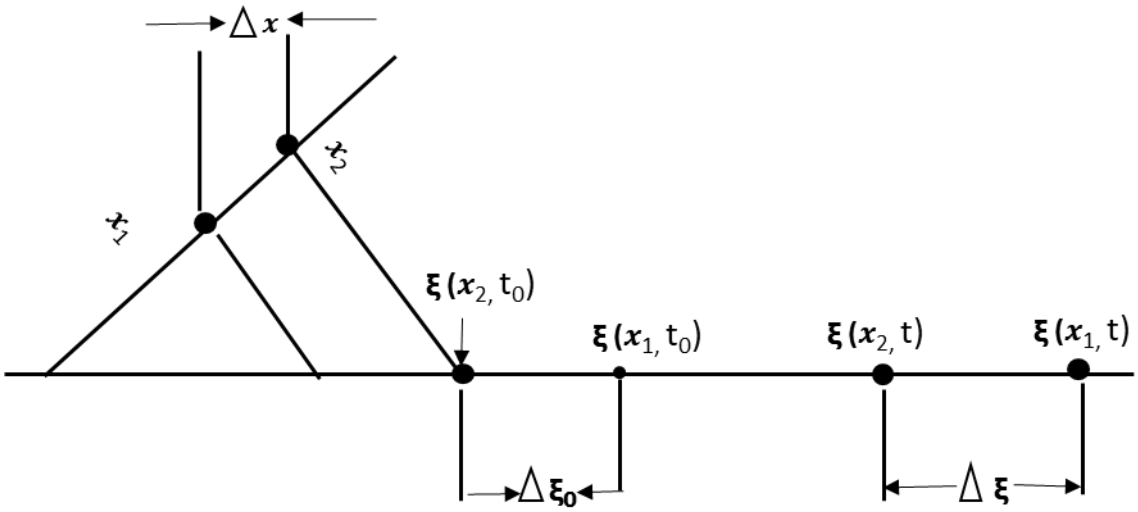

Figure 7-10. Relationship between the liner coordinate x and the jet coordinate ξ adapted from Reference [180].

$$\xi(x,t) = \mathrm{Z}(x) + (t - t_o)V_j\,(x) \qquad 7\text{-}1$$

where $\mathrm{Z}(x)$ is the location of the formation, t_o is the time at which the liner element first arrives at the axis, and $V_j\,(x)$ is the jet velocity, which is a function of the liner position and time. Accordingly, we measured the jet temperature at various positions of the jet including the outer surface, mid-radius and jet centre. The temperature across the jet length was also evaluated by placing temperature gauges on defined areas on the liner as shown in Figure 7-11 to obtain corresponding temperatures at the marked regions on the jet.

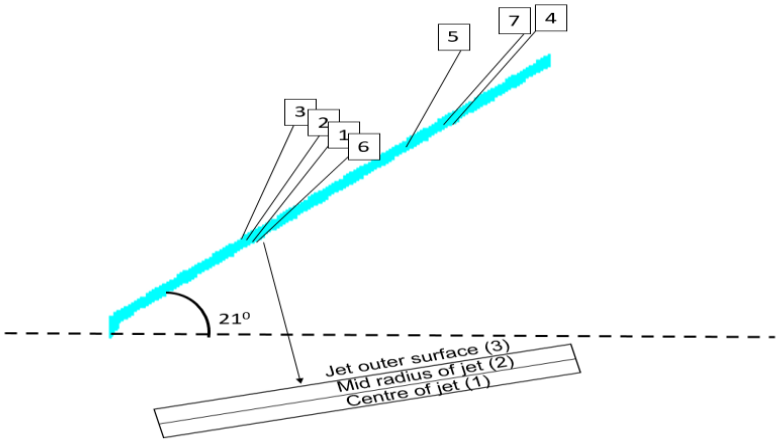

Figure 7-11. The cross section of the liner inclined at 21 degrees half cone angle showing gauge locations.

Figure 7-12. Corresponding gauge locations on the shaped charge jet during formation and elongation.

From Figure 7-13, it is apparent that the temperature across the jet width varies almost linearly outward. The highest temperature was recorded at the gauge trace closest to the inner centre axis (1100K), and this was observed to decrease outward towards the surface, consistent with the jet profile displayed previously (Figure 7-9,) suggesting that temperature decreases as the jet elongates. Hence the jet centre is heated higher than the outer surface, providing evidence of temperature variation along the entire jet width with resultant variation in grain refinement.

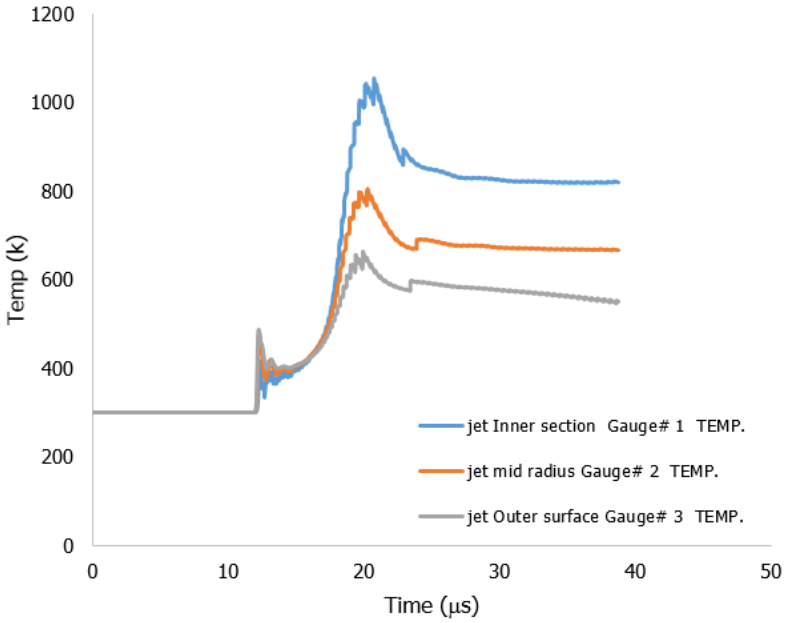

Figure 7-13. The recorded temperature histories of tracers positioned at the outer, middle and inner section of the liner.

To investigate how the temperature varies across the jet length, temperature gauges were placed at three different outer positions on the jet (gauges 4, 5 and 6, Figure 7-11). Adequate care was taken to ensure the gauges sat horizontally at the same depth on the outer surface. The highest temperature was found at the forward section of the jet and this decreases down to the rear as can be seen in Figure 7-14; an indication of the temperature variation across the jet length within the regions investigated. If this trend continues across the entire jet and slug length, it would therefore, suggest that temperature across the outer surface and slug length varies, with the jet tip recording higher temperatures.

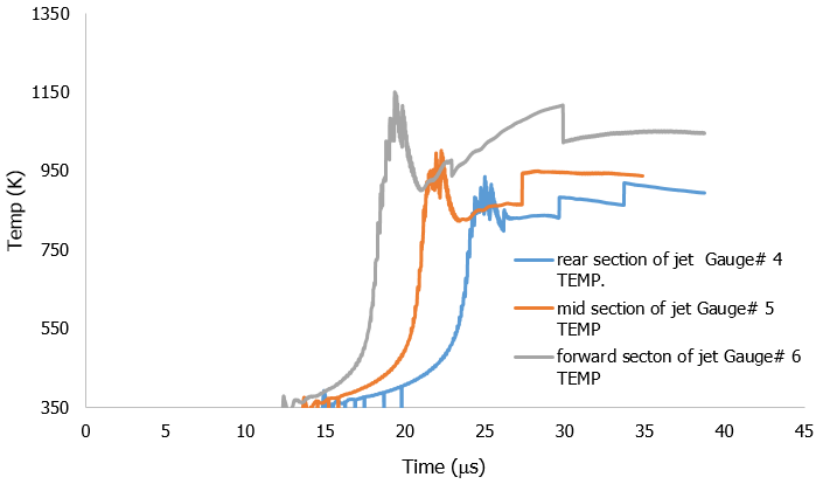

Figure 7-14. The recorded temperature histories at the forward, middle and rear sections of the jet.

7.4.3 Optical metallography of slug recovered from laser sintered liner

Figure 7-15 shows an image of a recovered laser sintered slug while Figure 7-16 shows optical metallographic observations of the starting and ending microstructures of the laser sintered copper liner and slug for comparison. In contrast with the elongated grains observed along the build direction of the starting liner microstructure, the recovered slug shows a more refined/ microstructure with a reduction in the average grain size. The grain size reduction was from 20 - 70 μm to an average grain size of around 14 μm. As the final grain size is dependent on the initial grain size, the low reduction in variation between the initial and ending microstructures is attributed to the already reduced starting grain size resulting from the post-processing of the sintered liner part. More importantly, the pores which were observed in the starting liner are completely absent in the slug. While it is difficult to rule out any form of melting or melt-related phenomenon as reported in previous shaped charges studies [127], several precipitates distributed randomly in the microstructure were visible and concentrated along the grain boundaries. A similar observation has been reported in Reference [164] of a sintered CuCrZr alloy during high-temperature annealing. X-ray diffraction analysis of the precipitate revealed a high content of Cr and Zr with dimensions ranging from the nm to μm scale without forming any intermetallic compounds. While Cu_8Zr_3 precipitates were formed at higher

temperatures, in contrast with $Cu_{10}Zr_7$, the variation in behaviour of the precipitates suggests the influence of temperature and annealing condition on the precipitation pattern. As a consequence, the apparent high temperature encountered during the jet formation process is a possible cause of the precipitation observed in this study. Whether the precipitate is a result of melt or melt related phenomenon is a subject of discourse. However, it is pertinent to point out that no melt or melt-related phenomenon has been reported in previous shaped charge studies [52], except for electroformed nano-sized nickel liners where melting was observed due to the high volumetric stored energy associated with small grains [53]. Hence, even though the liner flows hydrodynamically ('as fluid') under impact loading, it remains solid because the liner is not heated to its melting temperature [126]. In fact, at such extremely high strain / strain rate the liner deforms plastically and is drawn in the form of a wire with diameter much lower than the initial diameter. Under such conditions, it is very likely that the precipitates of Chromium and Zinc are evolved as Chromium is not soluble in Copper. Previous work on the heat treatment of CuCrZr at 450^{o}C indicates a high content of Cr and Zr located at the melt pool boundaries [164], something similar to the slug microstructure observed here which indicates that the particles have formed during the solidification of the melt pool. As such, we speculate that the formation of precipitates in the slug is an indication of adiabatic temperature rise during liner collapse and jet formation.

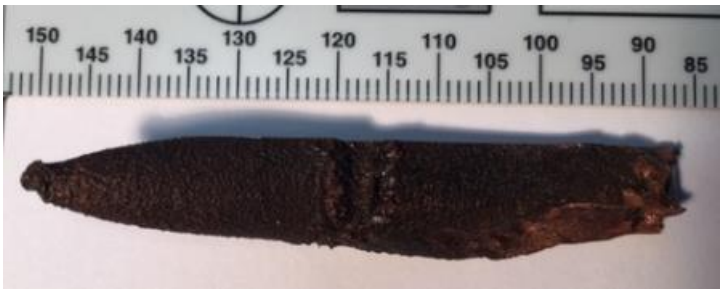

Figure 7-15. Recovered laser sintered slug.

A particularly interesting phenomenon is the further grain size reduction and enhanced presence of precipitates observed in the rear slug (Figure 7-16c) in comparison with the forward section; similar behavior observed in the ending microstructure of machined liners. Although the depth from which the samples

were collected were not considered (in both liner processing techniques), it is only an indication of the degree of deformation in various section of the slug – something that has already been shown numerically in the temperature variation across the entire slug. As the calculated temperature in the rear slug section is higher, the propensity for a higher degree of deformation is expected at the rear.

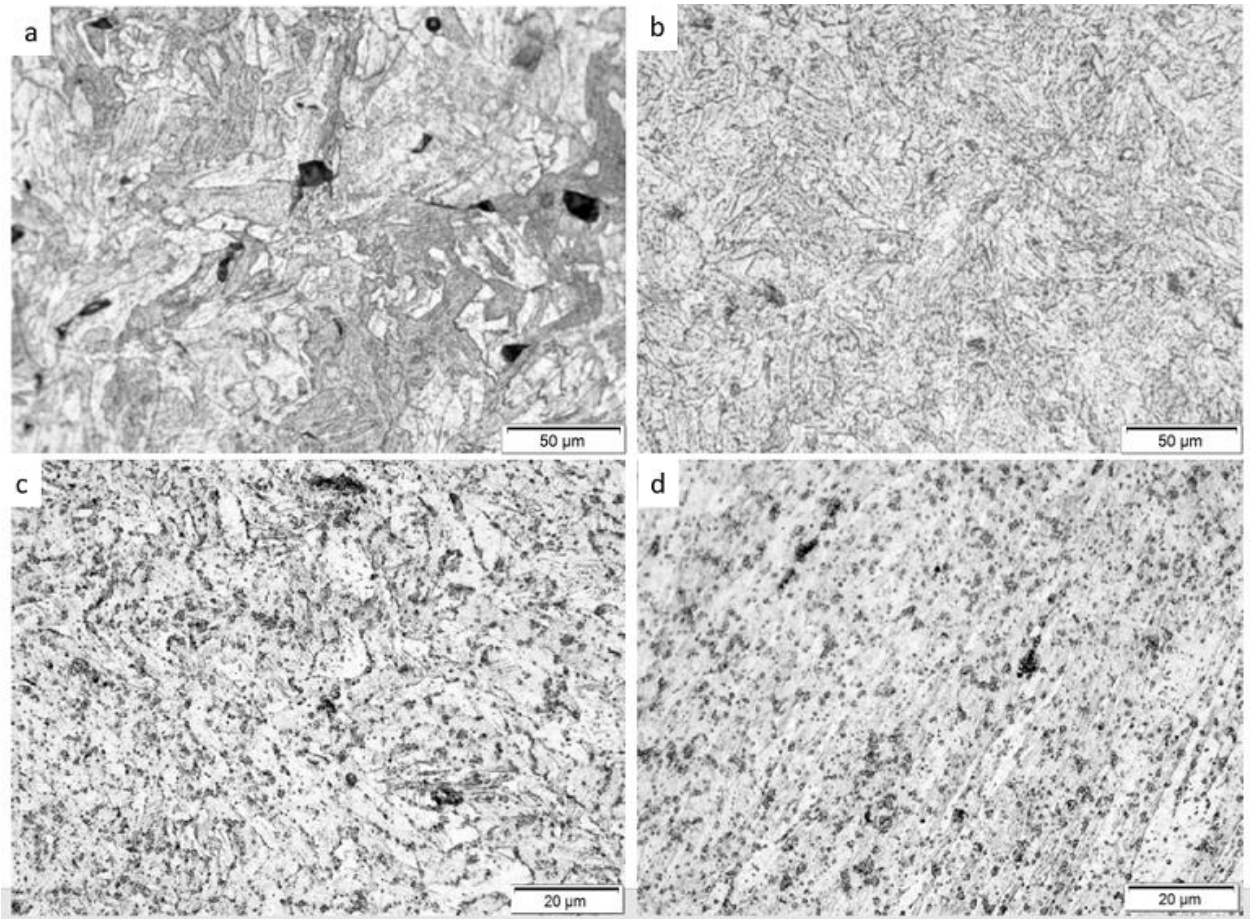

Figure 7-16. Comparison of the initial and final microstructure of laser sintered copper liner and slug; a. Starting laser sintered copper liner (b). recovered slug (c). forward region of recovered laser sintered copper slug, (d). Rear region of recovered laser sintered slug showing several precipitates. Magnifications are the same in all cases.

A comparison of the final / ending material of the machined and laser sintered liners in Figure 7-17 revealed two different ending microstructures. Firstly, as mentioned earlier, the laser sintered microstructure was observed to exhibit clear evidence of precipitates distributed randomly along the observed surface with a

microstructure showing something similar to a melt surface observed only in the rear region of the slug. With the variation between the forward and rear region of the slug, one can conclude that the microstructure observed in the slug is a temperature-related phenomenon which can result in the formation of higher precipitates indicative of a melting. Although, the precipitates formed are not investigated in this study, previous work has shown that because of the low solubility of chromium in Copper, the formation and growing of Cr precipitates especially at grain boundaries (apparent in the recovered slug here) is triggered by high temperatures and exposure times [164]. As such, higher quantities of precipitates would be expected in the shaped charge regime.

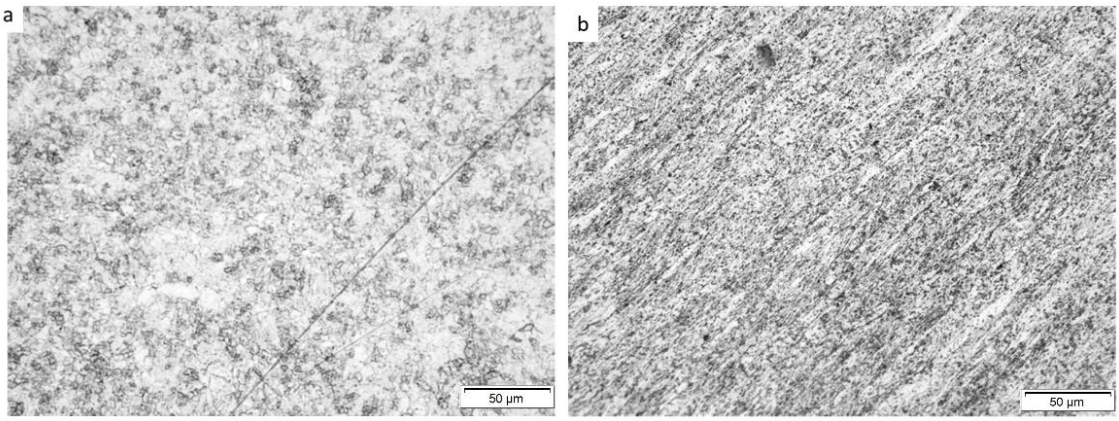

Figure 7-17. Comparison of the ending microstructure of machined and laser sintered liner.

7.5 Conclusion

The starting microstructures for machined and laser sintered copper shaped charge liners have been compared with corresponding recovered (ending) slugs – the first time the microstructure of recovered selective laser sintered slugs has been studied. It has been observed that:

a. Consistent with previous work [44]–[46], [127], a common feature of both processing techniques in terms of their ending / post-employment microstructures is reduction in grain size (slug), which is a classical feature of dynamic recrystallization.

b. Variation in grain refinement at different sections of the slug is an indication of differences in the degree of deformation at various sections of the slug.
c. The ratio of the starting and ending microstructure (in terms of extent of grain size reduction) is higher in the machined liner compared with the laser sintered liners, in correlation with the dependence of the initial grain size for predicting the final grain size.
d. According to jet temperature calculations, it has been shown that the center axis experiences an extremely high temperature exceeding the melting temperature of copper; this is speculated to accounts for the 10% melt reported by Lassila et al., [168], wave fluid like instability reported by Baoxiang et al., 2018 [173] and the observed hole in the center axis of soft recovered jets.
e. The formation of precipitates in the ending microstructure of deformed laser sintered liner are likely compounds of Chromium and Zirconium formed from an adiabatic temperature rise during liner deformation.

8 Application of Shell Jetting Analysis to Determine the Location of the Virtual Origin in Shaped Charges

H.O. Agu, A. Hameed and G.J. Appleby-Thomas
Centre for Defence Engineering, Cranfield University, Shrivenham
SN6 8LA, United Kingdom
*Corresponding author: henry.agu@cranfield.ac.uk

This chapter / paper covers the second key aims of this thesis as outlined in Chapter 1, namely those focused on development of a reliable / novel technique for determination of the virtual origin of a shaped charge to facilitate shaped charge optimisation in a more economic manner. In this study we developed a novel technique for determination of the VO location using a unique modification of an ANSYS® Autodyn 2D shaped charge jetting technique. The paper fits into the thesis structure by exemplifying the process of VO location determination and thereby providing a technique to allow more accurate, economic and practical calculation of theoretical penetration depths. This paper has already been accepted and published in the International Journal of Impact Engineering. The paper is included in its published form in its entirety in Appendix 3.

Adapted from: H.O. Agu, A. Hameed, G.J. Appleby-Thomas, Application of shell jetting analysis to determine the location of the virtual origin in shaped charges, International Journal of Impact Engineering, 122 (2018), pp. 175-181.

https://doi.org/10.1016/j.ijimpeng.2018.04.014.

8.1 Abstract

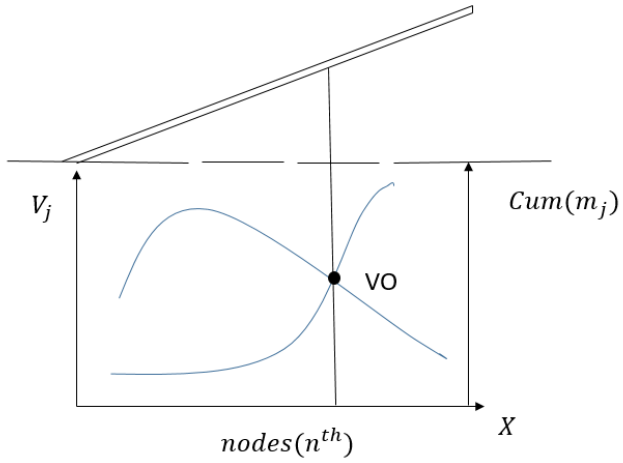

$Cum(m_j)$
$= cumulative\ jet\ mass$

Shaped charges are designed to produce high-velocity jets for penetration. During jet formation, the liner collapses and converges at a point source, also known as the virtual origin (VO), along the distance–time plane. The location of the VO must be known to allow the development of penetration analytical models. Here, we determined the location of the VO using the ANSYS® Autodyn 2D shaped charge jetting technique. Jetting analysis was conducted for two shaped charges of 18 and 32 mm diameter. The explosive and casing were represented by Eulerian two-dimensional finite difference grids, whereas the liner was modelled using a shell formulation. The summary/history of the jetting analysis was used to determine the VO position in the shaped charges. Interpolating the point of intersection on the liner between the jet velocity (U-Jet) and the cumulative jet mass revealed the location of the VO at a distance equivalent to approximately two-thirds of the inner cone diameter of the shaped charges, in agreement with earlier studies based on different methods. Validation of this technique using the DiPersio, Simon and Merendino (DSM) model based on the Allison-Vitalli equation also showed good agreement with the numerical results.

Key Words: Virtual origin, cumulative jet mass, jet velocity, jetting analysis, numerical simulation.

8.2 Introduction

Shaped charges are used extensively against armoured vehicles and structures. Enhancing the performance of shaped charges by optimizing their parameters in experimental trials is expensive, so analytical formulae have been developed to predict their performance. DiPersio and Simon' [175] introduced explicit formulae taking into account the concept of a virtual origin (VO) [2] as proposed by Allison and Bryan [82] and developed by Allison and Vitalli [83] for continuous and particulate jets with a non-uniform jet velocity distribution [176]. In particular, given target density (ρ_t) and jet density (ρ_j), jet tip velocity (V_0), and cut-off velocity (V_c), DiPersio and Simon [175] applied Equations 8-1 to 8-3 to calculate the depth of penetration before, during, and after jet breakup [175].

Equation 8-1 is used when the jet breaks before penetration:

$$P = Z_0\left[\left(\frac{V_0}{V_c}\right)^{1/\gamma} - 1\right] \text{ for } \quad 0 \leq Z_0 < V_c\ t_b\left(\frac{V_c}{V_0}\right)^{1/\gamma} \tag{8-1}$$

Equation 8-2 is used when the jet breaks during penetration:

$$P = \frac{(1+\gamma)(V_0\ t_b)^{\frac{1}{(1+\gamma)}} Z_0^{\frac{\gamma}{1+\gamma}} - V_c\ t_b}{\gamma} - Z_0 \text{ for } \quad V_c\ t_b\left(\frac{V_c}{V_0}\right)^{1/\gamma} \leq Z_0 < V_0\ t_b \tag{8-2}$$

Finally, Equation 8-3 is used when the jet breaks before reaching the target:

$$P = \left(\frac{(V_0 - V_c)}{\gamma}\right) t_b \quad \text{for} \quad V_0\ t_b \leq Z_0 < \infty \tag{8-3}$$

Although these formulae agree reasonably well with experimental results [179], one of their limitations is the a priori determination of Z_o, which is effectively the distance between the VO and the target surface *b* [180], also known as the effective jet length (Equation 8-4).

$$Z_o = VO - b \tag{8-4}$$

One of the methods established to locate the VO is that of back-projection of the jet particles by X-ray radiography [181]. Although accurate, this technique is very expensive and requires specialised equipment such as an X-ray source, coolers, capacitors and isolated fibre optics. Even so, such techniques have been used to determine the VO of shaped charges [96]. For example, in a previous study, the VO for a large (150-mm calibre) shaped charge was located at a distance from the liner base equivalent to 64% of the charge diameter [182]. Several qualitative estimates have also been used for the computation of penetration depths, e.g. by assuming the VO is located about one-third of the distance from the apex to the base of the cone [182] or by estimating the position of the VO based on past experience (rule of thumb) as three-quarters of the liner height [183]. Also, Held [103] found that the VO was located at a distance of about two-thirds of the internal diameter of the liner. In a recent study, the back-projection technique was applied numerically using the Euler solver method in ANSYS® Autodyn 2D to determine the locations of both the jet tip and the stagnation point at different times [96]. This technique requires the back-projection of the jet to be calculated at a defined time during jet motion.

Here, we developed a simple Lagrangian coordinate technique as postulated by Carleone and Chou [184] to map the position of the jet element on the liner, and thus to pinpoint the VO of shaped charges. By obtaining shaped charge parameters such as the cumulative jet mass and U-Jet (jet velocity) from a standard shell jetting analysis, the point where the jet velocity just overcomes the cumulative jet mass was marked as the VO, and this was related back to the exact position on the charge. A mesh sensitivity study was carried out first to determine the effect of mesh size and the density of shaped charges before the technique was tested on the 18-mm and 32-mm shaped charges.

8.3 Mesh sensitivity study

The ability of ANSYS® Autodyn 2D to simulate shaped charges has been verified in several studies [76], [185], particularly the representation of jet velocity as a function of cumulative jet mass. A mesh sensitivity study was conducted with four uniform square mesh sizes of 0.2, 0.3, 0.5 and 0.7 mm to determine the effect of

mesh size on jet tip velocity, penetration depth and the cumulative jet mass via a standard jetting analysis. A 32-mm cone-diameter shaped charge with a 1.2-mm OFHC copper liner at a half-cone angle of 26.84° was tested, incorporating a C4 explosive charge with a 2-mm thick aluminium 7039 casing. Material models for the OFHC copper liner and aluminium casing were taken from the Autodyn standard library, with the inbuilt Jones-Wilkins-Lee equation of state applied for the C4 explosive.

8.3.1 Effect of mesh size on jet tip velocity

The explosive, liner and casing were modelled in a Euler sub-grid. Nodal monitoring points (velocity gauges) were placed at intervals of 1–3 cone diameters (CDs) to obtain the jet velocity (Figure 8-1).

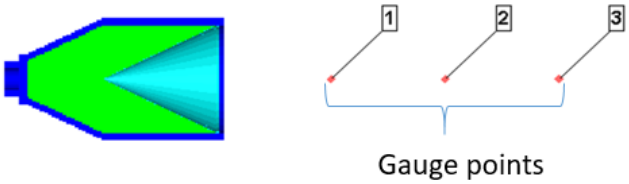

Figure 8-1. Gauge points at 1, 2 and 3 cone diameters.

The result of the simulations is summarized in Figure 8-2, which clearly shows that the coarse mesh size (0.7 x 0.7 mm) produced the lowest jet tip velocity of 4.11 km/s, compared to a velocity of 5.9 km/s produced by the finest mesh size (0.2 x 0.2 mm). A gradual decrease in the tip velocity was observed for all mesh sizes, in agreement with experimental results described by Walters and Jonas [2]. The finest mesh size produced the most accurate result but required nearly three times longer than the 0.3 x 0.3 mm mesh to complete the simulation, and the difference between the 0.3 and the 0.5 mm mesh in terms of the jet tip velocity was only 0.36 km/s (5.9%). The 0.3 x 0.3 mm mesh size was therefore selected for all simulations because the computational cost of the finer mesh was not justified by the diminishing returns in terms of accuracy.

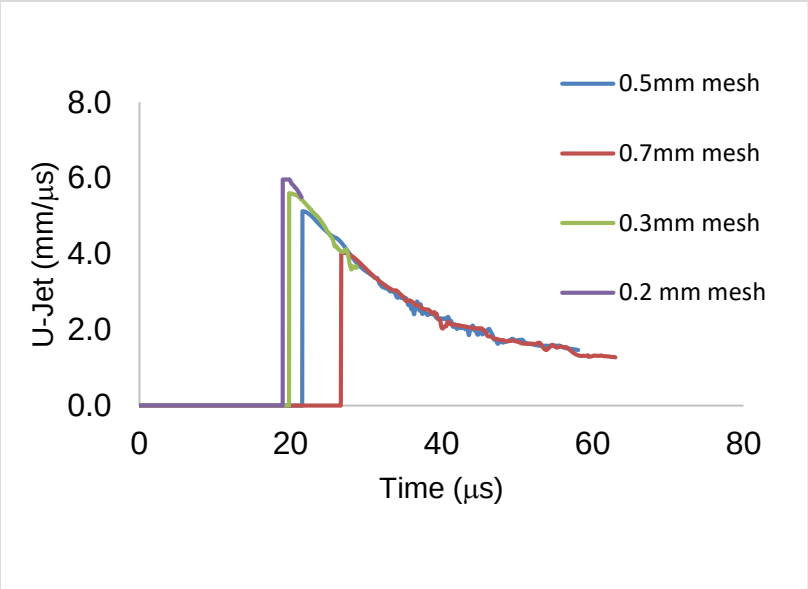

Figure 8-2. Velocity–time histories for the jet at the gauge points defined in Figure 8-1 for different mesh sizes.

8.3.2 Effect of mesh size on penetration depth

The jet formed from the Euler sub-grid was remapped for penetration into 1006 steel with a standard fixed mesh size of 0.5 x 0.5 mm producing results that compared favourably with previous experiments [186]. The simulation was allowed to run until the jet was eroded in the target. The resultant calculated penetration depths for the different mesh sizes are summarised in Table 8-1. The finest mesh size achieved the greatest penetration depth, reflecting the higher tip velocity.

Table 8-1. The effect of mesh size on penetration depth.

Mesh Size (mm)	**0.2**	**0.3**	**0.5**	**0.7**
Penetration depth (mm)	141	136	116	90
Time required (h)	32	13	5	2

The time required is based on a computer with an Intel® Core™ i7-6700HQ processor CPU at 2.6 GHz (2,592 MHz).

Overall, a non-linear trend in mesh size and penetration depth was apparent, with increasing convergence as the mesh size was reduced. This is shown in Figure 8-3, which plots the key numerical data from Table 8-1.

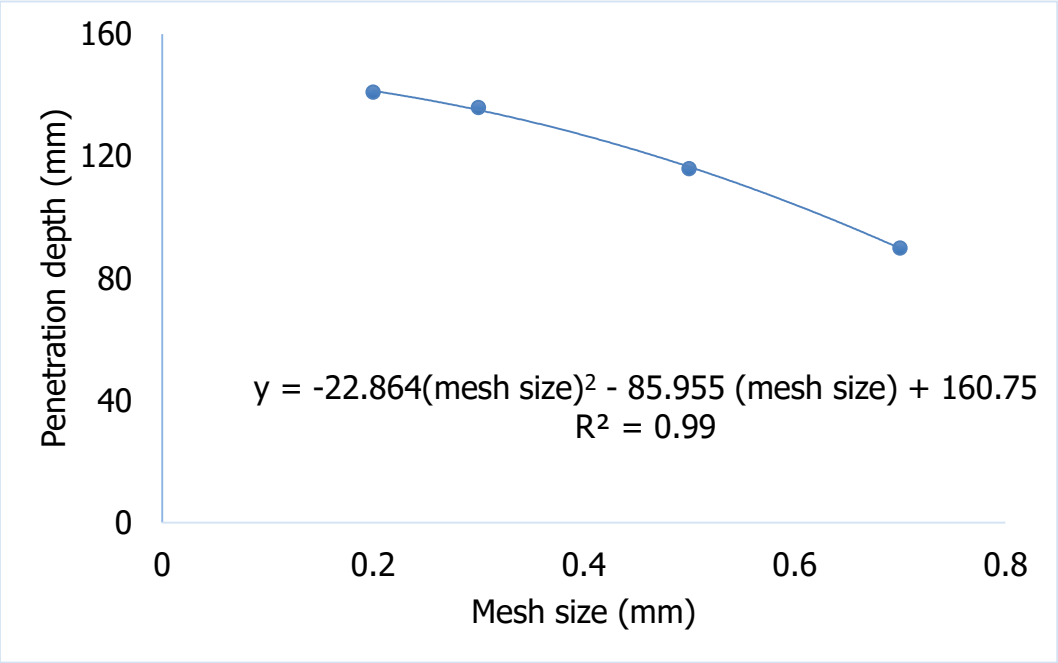

Figure 8-3. Variation of penetration depth with mesh size.

Figure 8-3 clearly reveals a polynomial relationship between the calculated penetration depths and the mesh size. Extrapolating the corresponding best-fit curve to a theoretical mesh size of 0 mm provides a corresponding penetration depth of 160.75 mm. This suggests that, given a mesh size of 0.2 mm, the error in the calculated shaped charge performance is only ~12%. While a further reduction in mesh size would therefore increase the accuracy, the advantage would be minimal. Table 8-1 indicates that more time is required to run simulations with smaller mesh sizes, as highlighted in Figure 8-4. Essentially, an additional 19 hours (h) were required to run the model using a 0.2 x 0.2 mm mesh rather than a 0.3 x 0.3 mm mesh with only a 3.54% increase in accuracy (relative to the nominal 0-mm mesh size baseline depth of 160.75mm). The computational cost of simulations with mesh sizes of less than 0.3 x 0.3 mm is again unjustifiable given the diminishing returns, and the 0.3 x 0.3 mm mesh size was selected.

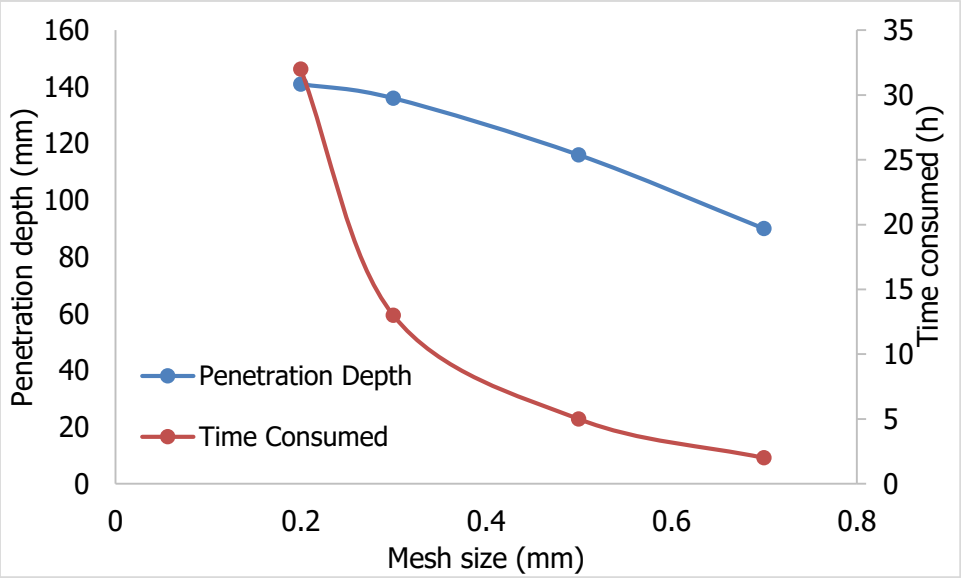

Figure 8-4. Penetration depth and computation time for various mesh sizes**.**

8.3.3 Mesh sensitivity for standard jetting analysis

Shaped charge jetting analysis is based on the use of continuum mechanics to estimate the non-uniform collapse velocity [187], and is applied to calculate other jetting parameters based on the Pugh, Eichelberger and Rostoker (PER) theory [88]. In the jetting setup, the explosive is modelled in the Euler sub-grid, whereas the liner is modelled in the shell formulation with the generation of jetting points, as shown in Figure 8-5.

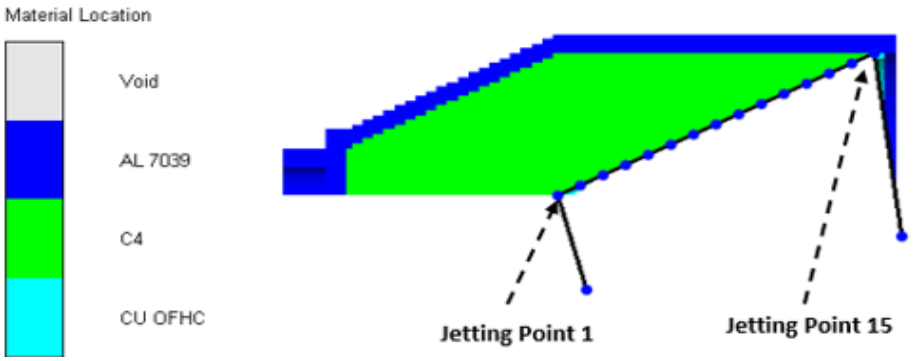

Figure 8-5. Jetting points on the shell copper liner.

Jetting calculations were conducted for four mesh sizes: 0.2, 0.3, 0.5 and 0.7 mm. The detonation wave travelled along the liner surface with a decreasing collapse velocity from the apex to the base, with more liner material forming the jet. A summary of the jetting analysis, in which the cumulative jet mass is plotted against the axial *x* position (X-jet) for all four mesh sizes, is provided in Figure 8-6. The relationship between the cumulative jet mass and the X-jet for all mesh sizes was similar, bearing the same shape at the beginning, up to a nominal coordinate distance of 55 mm from the apex of the cone. Beyond this point, variations in the curve were observed with a general convergence of the solution towards the 70 mm position for a mesh size of 0.3 mm x 0.3 mm. The accuracy and computational time of the 0.3 mm square mesh makes it suitable for the simulation and it was therefore used for the entire jetting analysis.

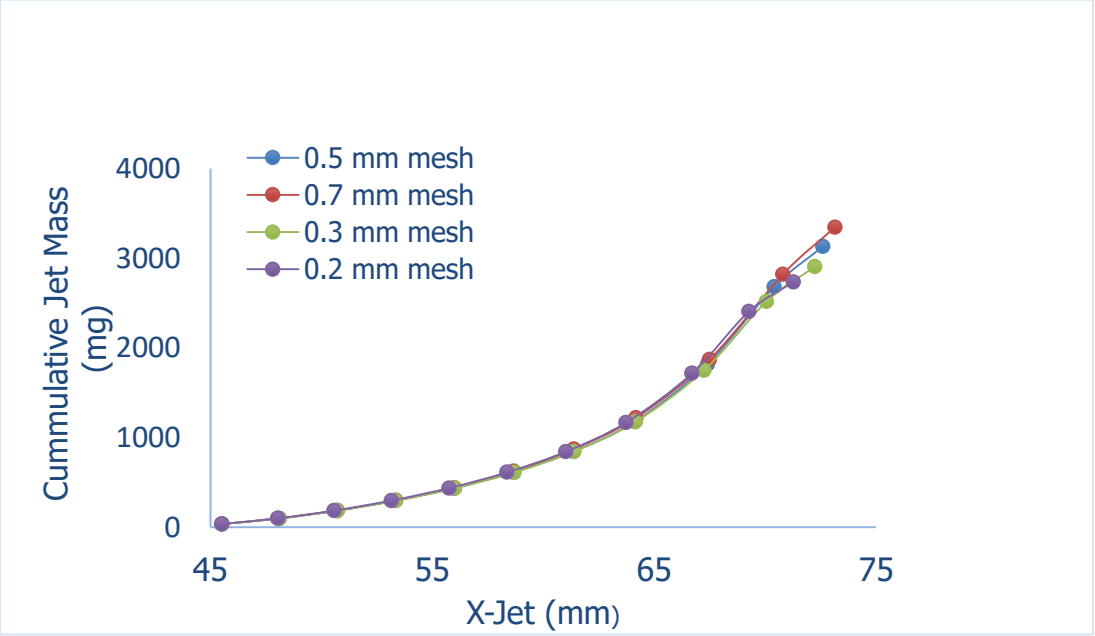

Figure 8-6. Mesh sensitivity study for standard jetting analysis.

8.3.4 Effect of varying the number of nodes on the cumulative jet mass

Because this technique involves locating the VO using shell jetting analysis, it is necessary to investigate the effect of varying the number of nodal points on the U-Jet and cumulative jet mass. Four jetting calculations were conducted with similar charge configurations but a different number of nodes (J Max): 10, 15, 20 and 25. The effect of node variations on the U-Jet and cumulative jet masses are

plotted in Figures 8-7 and 8-8, respectively. From the jetting calculation, the maximum jet velocity remains the same in all four jetting calculations but the cumulative jet mass increases as the number of nodal points increases. This is because more liner material is added in the calculation, as shown in Figure 8-8.

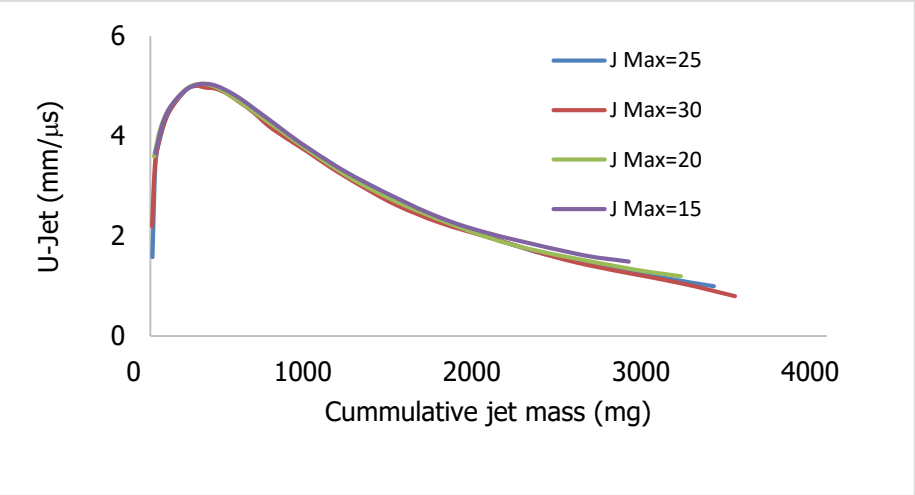

Figure 8-7. Relationship between jet velocity and cumulative jet mass according to the number of nodes.

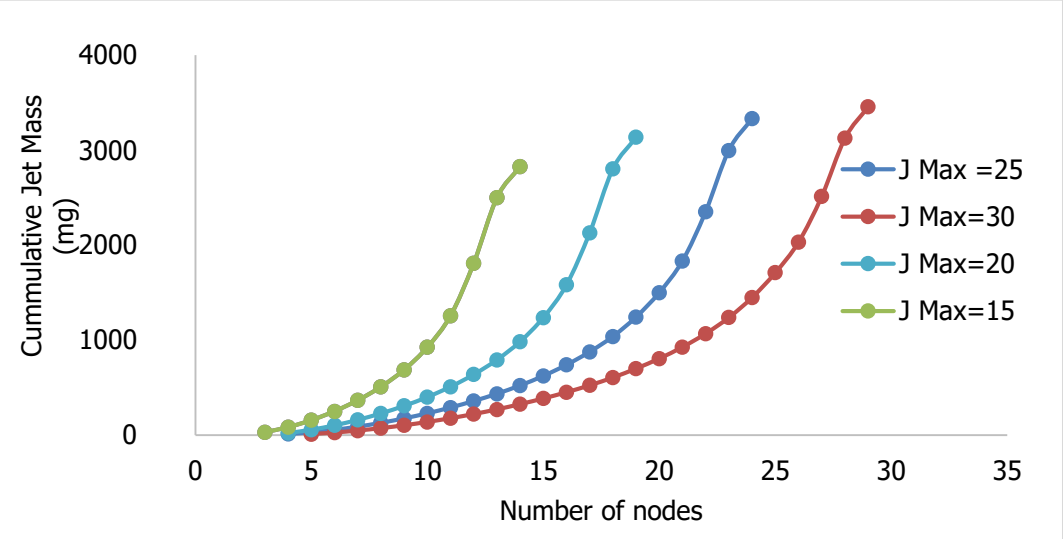

Figure 8-8. Relationship between cumulative jet mass according to the number of nodes.

8.4 Method to determine the VO position

This technique applies a single Lagrangian coordinate to relate the position of the jet element back to its original position on the liner. The technique was first developed by Chou and Flis [31] and applied by Carleone and Chou [184] to calculate the strain, jet length and jet radius. The axial liner position is described by coordinate *x* whereas the position of the jet is given by coordinate ξ (Equation 8-5):

$$\xi(x,t) = \mathrm{Z}(x) + (t - t_o)V_j\,(x) \qquad 8\text{-}5$$

where t_o is the time at which the liner element first arrives at the axis, $\mathrm{Z}(x)$ is the location of the formation, and $V_j\,(x)$ is the jet velocity, which is a function of the liner position and time. The relationship is shown in Figure 8-9.

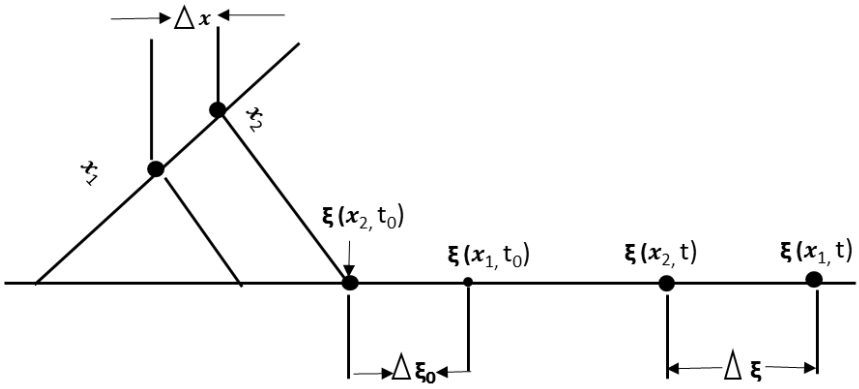

Figure 8-9. Relationship between the liner coordinate x and the jet coordinate $\boldsymbol{\xi}$ [184]**.**

In turn, Equation 8.5 can be rearranged to derive Equation 8-6:

$$\mathrm{Z}(x) = \xi(x,t) - (t - t_o)V_j\,(x) \qquad 8\text{-}6$$

Applying the inverse velocity gradient based on the principle of conservation of momentum, with respect to *x* when *x* is the VO, yields Equation 8-7:

$$V_j\,(x) = V_j\,(VO) = \frac{\int_0^{X_{VO}} V_j \left(dm_j/dX\right) dX}{\int_0^{X_{VO}} V_j \left(dm_j/dX\right) dX} \qquad 8\text{-}7$$

By integrating the mass piled up along the jet velocity of the jet particles, a one-dimensional jet is observed when the U-Jet just overcomes the cumulative mass effect created by the pilling up. The point that the jet begins to protrude from the collapse matrix is the VO, and this is shown in Figure 8-10 as the intercept point between the U-Jet and cumulative jet mass. An example of the technique was applied to 18 and 32-mm shaped charges with C4 explosive in a 2-mm thick aluminium 7039 casing. Copper (OFHC) liners of constant thickness (0.5 and 1.2 mm) were used for the 18 and 32-mm shaped charges, respectively, with a half cone angle of 26.5° in both cases. Point initiation at the rear of the charge was assumed. The output jetting data, comprising the U-Jet, cumulative jet mass and nodal points/jetting points, were then extracted and reduced for subsequent analysis.

8.5 Results and discussion

The liner collapse data revealed that the amount of liner mass entering the jet increases towards the base of the liner while the jet velocity (U-Jet) declines. The point at which the U-Jet intercepts the cummulative jet mass lies between the tenth and eleventh nodes on the 32-mm charge. To obtain this position on the *x*–*y* plane, the jetting points were numbered in ascending order and the position (between the tenth and eleventh nodes) was interpolated on the charge as shown in Figure 8-10.

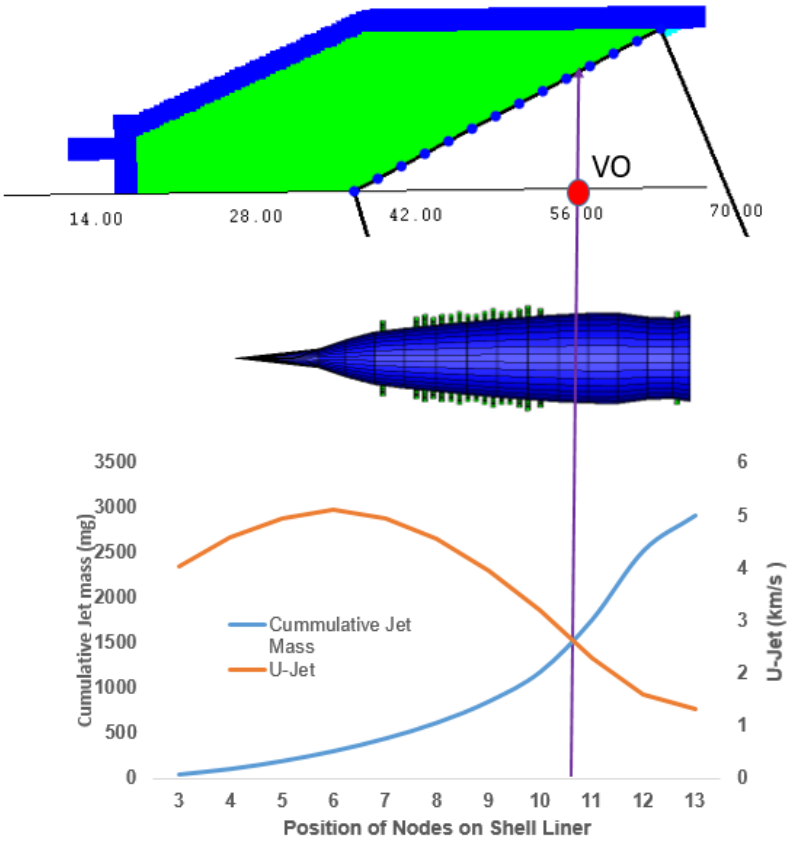

Figure 8-10. Determination of the VO for the 32-mm shaped charge.

The VO was found to be at the 61.00 mm mark, which is 24.13 mm from the cone apex and 7 mm from the charge base. This position is 75.86% of the liner height (about three-quarters of the liner height from the conical apex and about one-quarter from the base), which is also two-thirds of the shaped charge liner base diameter. The same technique was applied to the 18-mm shaped charge and the VO appeared to flow in the same way. Importantly, our results were in agreement with the VO position reported by Held [14] who located the VO at about two-thirds of the inside diameter of the liner, and also DiPersio et al., [13] who located the VO at a distance equivalent to about three-quarters of the liner height from the cone apex.

8.5.1 Verification of the technique

To confirm the suitability of this technique, an experimental study is ideal but prohibitively expensive as stated earlier. Instead, verification can be achieved via other methods, one of which involves investigating the effect of the number of

nodes on the VO position. Four additional jetting calculations were conducted, with 5, 10, 14 and 20 nodes on the shell liner. As the number of nodes increased, we observed issues associated with tangled polygons and these were deleted from the simulations. Analysis of the results showed that when the maximum number of nodes is low (e.g. J Max = 5), the jet formation is distorted as shown in Figure 8-11, pushing the VO position towards the apex (55% from the charge base). A decrease in the proposed VO position was observed for an increase in the number of nodes. At higher values of J Max, the distance between the charge base and the VO decreased to the point at which a further increase in the number of nodes gave no change in the VO position. This point was regarded as the true VO location.

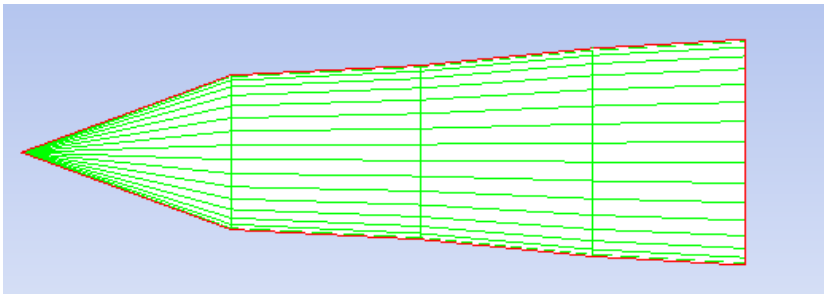

Figure 8-11. Distorted liner collapse resulting from a low number of nodes (J Max = 5).

8.5.2 Verification of the VO position

The technique was also verified by computing the penetration depth of the effective and traditional stand-off distance using the DSM formula described in Equations 8-1 to 8-3. The jet tip velocity was determined at two cone diameters (2CD) with a nodal monitoring point/gauge as shown in Figure 8-1. By applying the jet tip correction, when the U-Jet was plotted against the cumulative jet mass, the modified jet velocity was 5.096 km/s.

The resultant depth of penetration was determined numerically using Autodyn 2D. The explosive, liner and casing were modelled in the Euler sub-grid whereas the target was modelled with the Langregian sub-grid. The jet from the Euler solver was remapped to the Langregian solver for penetration into 1006 steel until

the jet element was completely eroded. Figure 8-12 shows the depth of penetration for the 32-mm shaped charge.

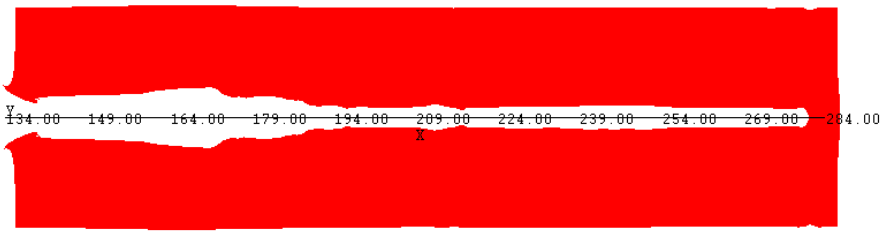

Figure 8-12. The depth of penetration for 32-mm shaped charges was 141 mm.

According to Hirsch [99], the penetration of an ideal jet into steel becomes mostly ineffective below ~1.8 km/s, when the rate of target penetration becomes less than half the jet velocity. However, deviations from perfect symmetry and jet particulation accounts for the loss of penetration efficiency below 3 km/s. The cut-off velocities were determined from the penetration–time history (Figure 8-13) of the shaped charge jet as described by Held [186], [188].

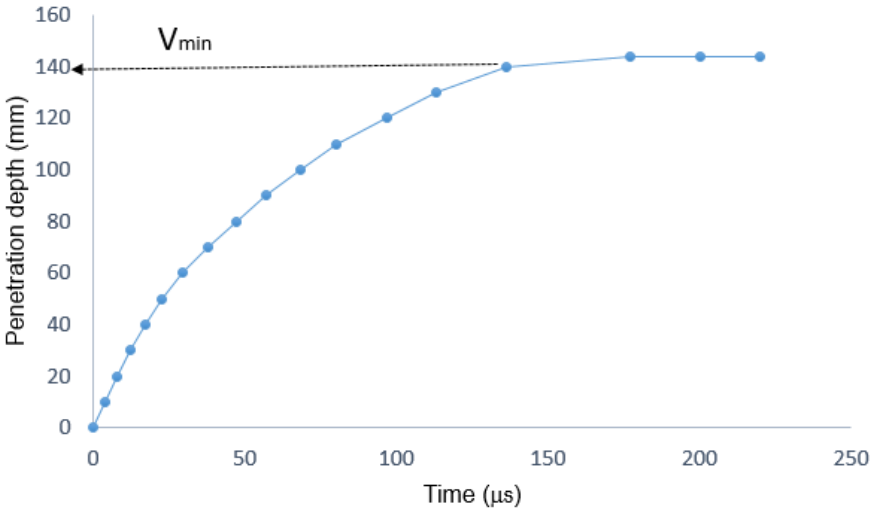

Figure 8-13. Jet penetration–time history for the 32 mm shaped charge.

Having satisfied the conditions for a continuous jet, Equation 8-1 was applied. The parameters used to determine the penetration depth are in Table 8-2.

Table 8-2. Parameters used to determine the depth of penetration. SOD = stand-off distance.

V tip (m/s) corrected	~$V_{(min)}$ (m/s)	SOD (mm)	Effective SOD (mm)	Solid jet density (g/cm^3)	Target density (g/cm^3)	$y = \sqrt{\rho_t/\rho_j}$
5096	1787	64.00	71.00	8.96	7.85	0.93

The resultant depth of penetration for the numerical simulations and analytical equations using the derived and traditional SOD are summarized in Table 8-3. Higher penetration depths were observed for the effective SOD compared to the numerical simulations. The proposed VO technique shows only a 4.5% difference in penetration depth from the numerical simulation, whereas the traditional SOD underestimates the VO by 5.6% compared to the numerical simulation. The ability of this technique to determine the location of the VO as well the improved predictions compared to the traditional SOD makes it valid for specifying the position of the VO.

Table 8-3. Comparison of the depth of penetration (DOP) determined by numerical simulations, SOD and derived SOD positions.

Numerical simulation at 0.3 mm mesh (mm	Using the traditional SOD (mm)	Using the Effective SOD (mm)	Difference in DOP between traditional SOD and numerical simulation.	Difference in DOP between effective SOD and numerical simulation.	Difference in DOP between traditional SOD and Effective SOP
141.00	133.43	148.02	7.67 (~5.4%)	6.92 (~4.5%)	14.59 mm

8.6 Conclusions

In conclusion, we carried out a series of numerical simulations to investigate the ability of ANSYS® Autodyn 2D to predict the VO of shaped charges. The technique applies a simple Lagrangian coordinate for relating the position of the jet element on the liner. We found that:

a. Ignoring the distance between the charge base and the VO underestimates the depth of penetration
b. The VO position can be reasonably estimated by shaped charge jetting analysis using ANSYS® Autodyn 2D
c. The jet tip velocity remains the same irrespective of the number of nodes or J Max in the shell jetting analysis
d. When the number of nodes is low, the jet formation is distorted therefore moving the VO towards the apex
e. The depth of penetration estimated using the derived VO deviates by only 4.5% from the numerical simulation, while the traditional SOD results in a 5.6% deviation
f. The proposed technique agrees well with earlier works [180, 181]

9 Summary and Discussion

This chapter present a general discussion of the work in this thesis, as outlined in Figure 9-1. It begins with a comprehensive summary of each chapter and outlines the important contributions of this PhD work in the field of shaped charges. This Chapter then ends with a recommendation on future work / directions.

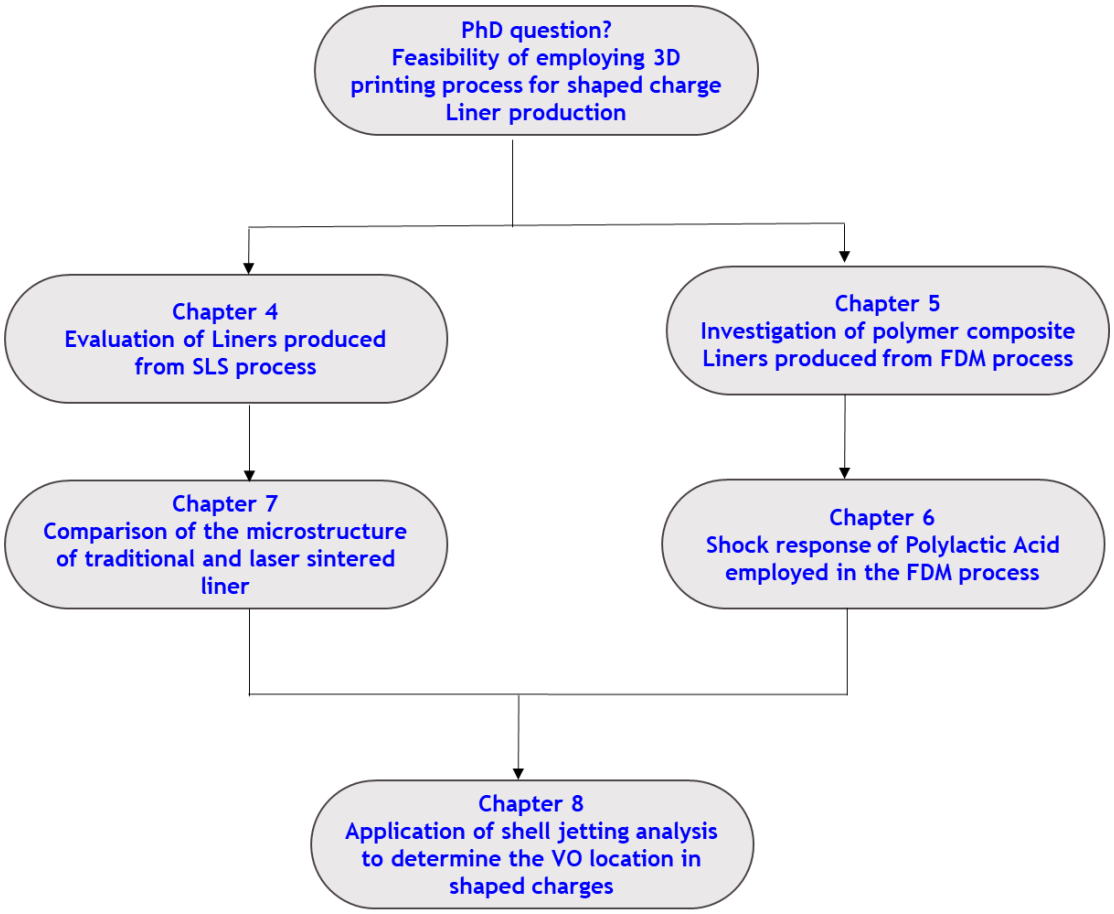

Figure 9-1. Schematic representation of the contribution of this thesis.

Fundamentally, the work presented in this thesis can be said to be in two parts. The first deals with the use of 3D printing processes for the production of shaped charge liners, while the second part involves a novel technique for determination of the virtual origin of shaped charges.

The first part of this thesis, essentially Chapters 4 to 7, investigates the feasibility of employing additive manufacturing processes for the production of shaped charge liners. As mentioned in Chapter 2, the liner is a very critical element of shaped charges which requires careful processing both in its micro and macro elements for optimum performance, with due consideration also being given to the associated production costs. As development into 3D printed parts becomes more commonplace – particularly with built parts being of comparable density to their bulk material – it is not known how this process would serve when employed for liner production. As such, the first part of this thesis was designed primarily to investigate liners produced utilising two significant, commercially available, 3D printing processes. These were Selective Laser Sintering (SLS) and the Filament Deposition Modelling (FDM) processes, described in Chapters 4 and 5, respectively.

Chapter 4 of this thesis was a detailed study of liners produced by sintering copper and aluminium substrates. The performance of the liners produced was compared with traditionally machined liners and was backed-up by validated hydrocode simulations, employing Autodyne 2D and using the software's' inbuilt material properties. The use of both experiment and numerical simulations was necessary to enhance the accuracy of the findings. Specific attention was given to the effect of liner density and liner microstructure of the laser sintered liners with some interesting results. The effect of liner thickness and cone angles for the laser sintered liners using 40^{o}, 60^{o} and 90^{o} cone angles as well as 1.25- and 2.5-mm liner thicknesses was found to be in agreement with the literature. The results in terms of (resultant) penetration depth between the machined and laser sintered liners (experimentally) was less than 0.5 CD, suggesting a comparable performance between both liner processes. From the numerical simulations, it was clear that the laser sintered liners perform less effectively lower than the copper and aluminium shaped charge liners simulated using the bulk inbuilt material processes. However, the numerical simulation is a near perfect condition compared to the experimental process where errors due to liner dimensional inaccuracies, manual handling and filling of explosives and asymmetries could be present. More specifically, we have observed a variation between the

performance of copper and aluminium liners linking the overall performance of the laser sintered liners to porosity. Examination of the microstructure of the laser sintered liners reveals large, irregular and dark brown pores of a large magnitude than the aluminium. Following the theory and knowledge of porosity, bulk sound speed as well as ductility, it is suggested that the poor performance recorded by the laser sintered copper liners is likely linked to their less isotropic microstructure as compared to the aluminium liners. Although, this variation is only small, it is a pointer that different sintered materials would have different performance depending on the material used and the printing conditions – with one of the key factors governing subsequent response the degree of porosity in the liner. Overall, given the benefit of 3D printing process in terms of its capability of producing complex design, different shaped charge liner designs could be explored with potential for developing novel liner shapes as well as optimisation of the process for efficient jet performance. This would require a series of liner design and experimental trials to optimise performance of 3D printed shaped charge liners.

The second aspect of the 3D printed shaped charge liners (Chapter 5) evaluated the performance of liners produced from the filament deposition modelling process using a desktop 3D printer, the Ultimaker 3. The printer is designed to print polymers such as PLA, ABS etc. Generally, polymers – when employed as the liner of a shaped charge warhead – do not give a good jet because of their lower density, poor ductility and low melting temperature range. However, this research was motivated by the fact that composite materials with increased mechanical properties such as copperfill, comprising 40% w/w of copper in a PLA matrix are now available and it was postulated that these could possibly enhance the performance of printed polymers as is the case for composite metallic liners such as Cu/W. Analysis of liner microstructure and flash X-ray images of the jet was conducted to provide insight into the performance of the composite polymer liners and the result showed that, contrary to our expectation, the addition of copper to make the PLA composite not only reduced the performance of the liner but generated a stream of jet particles which produced multiple holes in subsequent targets. This implies that the addition of copper heterogeneously

introduces a steric influence on the matrix which prevented the formation of a coherent jet. Although the resultant penetration depth is limited, the copper-fill liners might however, be useful as a limited effective radius component in an active protection system, or as a frangible warhead forming a cone of copper pellets. Clearly, the investigation on FDM printed liners is not finished yet and a more detailed numerical study would be required to understand the behaviour of the material. However, to model the material, the equations-of-state which described the material behaviour are required – something not currently available in the existing literature. To this end, derivation of such material properties is essential to allow for such simulations to be carried out.

Consequently, Chapter 6 was focused on the derivation of a (shock) equation-of-state for (PLA). This is because PLA is not contained in the Autodyn library and, to the authors knowledge, there has not been any study on the EOS data for this important class of material in the literature. The core material properties in the high strain-rate regime were derived through a series of one-dimensional plate-impact experiments employing a single stage gas gun within the Cranfield University Survivability and Advanced Materials group for a range of impact velocities (200-1,000m/s). Embedded longitudinal (one-axis) and lateral Manganin gauges were employed to monitor shock propagation. In this work, printed samples of PLA were deformed by one-dimensional shock waves generated via the plate impact technique, allowing determination of both the Hugoniot Equation-of-State (EOS) and shear strength of the material. Both linear and non-linear EOS forms were considered, with the best-fit found to take the general form $U_S = 1.28 + 3.06 - 1.09U_p{}^2$ in the $U_s - U_p$ plane, consistent with other polymers. Use of lateral Manganin gauges embedded in the material flow allowed consideration of lateral stress evolution at impact pressures ranging from 0.3 to 4.0 GPa. Shear strength was observed to increase with impact stress, however, minimal strengthening behind the shock front was apparent. Deviation of the measured stress from the predicted elastic response (with the intercept at which this occurred corresponding to the PLA's Hugoniot Elastic Limit) was observed at a longitudinal stress of 0.90 $\pm$ 0.05 GPa, within range of polymeric

materials of similar characteristics – the first time this important parameter has been measured for PLA.

In Chapter 7, further study on the behaviour of laser sintered liners was performed by examining the microstructure of the resultant material (the 'slug') in comparison with the as-manufactured material (e.g. the liner itself pre-deformation). The objective of this study was to elucidate the deformation pattern of laser sintered liners. Optical and scanning electron microscopy was employed to interrogate the as-manufactured and recovered material as-required. The effect of temperature on the deformation patterns was evaluated using a well validated ANSYS Autodyn 2D hydrocode. The resultant microstructure of both machined and laser sintered liners on recovery revealed a small / refined and equiaxed grain size consistent with traditionally fabricated liners, characteristic of dynamic recrystallization. While the grain size was to found to vary at different section of the jet and slug, this was attributed to variation in temperature across these regions. The chapter also attributed the centre hole and other unexplained phenomenon (wave fluid like instability) found around the collapsed axis, reported recently, to the high temperature deformation due to the high stagnation pressure at the stagnation point during the liner collapse. In addition, interestingly, the formation of precipitates in the resultant (recovered) microstructure of deformed laser sintered liners were shown to comprise of compounds of Chromium and Zirconium likely evolving from the adiabatic temperature rise during liner deformation.

The final parts of this thesis were focused on approach to enable determination of the Virtual Origin (VO) point for shaped charges. The development of an analytical model – something vital to predict the penetration performance of shaped charges – was presented in Chapter 8. Aside from saving time and cost in conducting field trials, such a model is an invaluable tool for planning experimental design. However, the development of these formulas requires accurate determination of one or two parameters. For example, in the basic hydrodynamic equation, the length of jet, which is the distance between the point at which the jet originates (the Virtual Origin position) and the target surface, is

required to predict the penetration depth. While there are some research papers which describe methods for determination of the VO point, most researchers employ the ‘rule-of-thumb’ approach – with associated inaccuracies. In the first part of this work, a novel technique was developed to predict the location of the Virtual Origin in shaped charges. The technique was developed from a simple Lagrangian coordinate postulated by Carleone and Chloe to map out the position of the jet element during its formation and elongation process. The technique was dependent on core shaped charge parameters such as cumulative jet mass and the U-Jet (jet velocity) obtained from a standard shell jetting analysis employing an Autodyn 2D simulation. The point at which the jet begins to protrude from the collapse liner matrix is observed when the U-Jet just overcomes the cumulative mass effect created by the pilling up, and this is shown in Figure 8-10 as the intercept point between the U-Jet and cumulative jet mass to be around three-quarters of the liner height from the conical apex. The technique was validated against data obtained from 18 and 32 mm cone diameter shaped charge and the result obtained was in agreement with the VO position reported by M. Held [182].

10 Conclusion and Recommendations

This thesis considered the feasibility of employing 3D printing for the production of shaped charge liners using 2 major 3D printing processes; selective laser sintering and filament deposition modelling process using Aluminium, Copper and Polylactic acid baseline materials. The results revealed that liners produced from the SLS produces coherent jet comparable with traditional machining suggesting the applicability of the process for liner production. Variations between copper and aluminium liners revealed the effect of defects associated with laser sintered liners including the presence of porosity in the produced liner microstructure. Optimisation of the laser sintered process would be required for improved jet performance. Further investigation of the resultant slugs reveals the formation of precipitates of the alloying elements Cr and Zr - something different from machined liners. Extensive numerical simulation of the jet temperature provides explanation to the unusual occurrence at the jet centre axis during liner collapse such as centre hole formation.

The liners produced from filament deposition modelling using PLA produced incoherent jet. The addition of copper to the PLA failed to augment the jet formed by the PLA but produces a stream of discontinuous jet when view through X-ray. Attributed to a series of factors including low melting point of PLA, the jet could be employed for applications requiring reduced jet tip velocity such as explosive demolition and fusing defeat. To provide additional understanding on the deformation of PLA, it was necessary to model the liner deformation and this require an understanding of the material behaviour. As such, employing the plate impact experiment, the Equations of state of printed PLA which was hitherto not available was derived to provide data for modelling. This was accompanied by a determination of the material shear strength. While it is unclear how this will vary from a cast PLA, it would be necessary to investigate the behaviour of cast PLA under high strain rate condition.

In the last part of this work, a novel technique for predicting the virtual origin position of shaped charges was developed using shell jetting analysis from ANSYS Autodyn 2D by relating the position of the jet element on the liner. This

was necessary to improve the accuracy of prediction of penetration depth using the Allison and Vitalli equations.

In particular, the important contributions of each chapter and directions for future research work to the overall thesis is presented in a concise manner as follows:

- In **Chapter 4**, we have observed the following:

  a. Variation of less than 0.5 charge diameters (in resultant penetration depth) between machined and laser sintered liners indicating a broadly comparable performance.

  b. In terms of differences in response, the laser sintered copper liner showed a reduction in performance (of about 17.2%), attributable in part to a relatively higher rate of material bulk defects compared to the laser sintered aluminium.

  c. Aside from a reduction in the %Theoretical Maximum Density, the presence of pores in laser sintered material reduced the resultant bulk sound velocity and was postulated to act as concentration points for stresses which in turn reduced the jet tip velocity.

- In **Chapter 5**, we have observed that:

  a. The jet formed from explosively loading Filament Deposition Modelling liners is mainly contributed by the PLA.

  b. The addition of copper to make the copper-fill composite not only fails to augment the jet, but actively interferes with it, preventing full jet formation.

  c. This action is likely to be a steric effect, with the copper particles interacting with each other and thus leading to the formation of a stream

of discontinuous jet-like material which was observed to generate multiple holes as the liner thickness increased.

d. Such dispersed jets may be useful for the application of coatings or as a limited effective radius component in an active protection system, or as a frangible warhead forming a cone of copper pellets.

- In **Chapter 6**, we have derived the EOS for polylactic acid – something not found elsewhere in the literature, and of critical importance for numerical simulation of the dynamic response of such 3D printed systems – and have successfully determined the elastic limit of PLA to be around 0.9GPa, close to that of similar polymers such as PMMA.

- In **Chapter 7**, the starting microstructures for machined and laser sintered copper shaped charge liners have been compared with corresponding, recovered (ending) slugs and we have observed that:

  a. Consistent with previous work [44]–[46], [127], a common feature of both processing techniques in terms of their end / post-employment microstructures is a reduction in grain size (slug), which is a classical feature of dynamic recrystallization.

  b. Variation in grain refinement at different sections of the slug is an indication of differences in the degree of deformation at various sections of the slug.

  c. The ratio of the starting and ending microstructure (in terms of the degree of refinement) is higher in the machined liner compared with the laser sintered liners, in correlation with the dependence of the initial grain size for predicting the final grain size.

d. According to the jet temperature calculation, it has been shown that the center axis experiences an extremely high temperature exceeding the melting temperature of copper. Consequently, it is speculated to accounts for the 10% melt - as reported by Lassila et al., [168], wave fluid like instability reported by Baoxiang et al., 2018 [173] and the center hole axis phenomenon.

e. Precipitates observed in the ending microstructure of recovered laser sintered slug(s) are likely compounds of Chromium and Zirconium formed due to the adiabatic temperature rise which occurs during liner deformation.

- In **Chapter 8** we developed a novel technique for determination of the VO location using a novel modification of an ANSYS® Autodyn 2D shaped charge jetting technique. Other findings are:

  a. Ignoring the distance between the charge base and the VO underestimates the depth of penetration.
  b. The VO position can be reasonably estimated by shaped charge jetting analysis using ANSYS® Autodyn 2D.
  c. The jet tip velocity remains the same irrespective of the number of nodes or J Max in the shell jetting analysis.

10.1 Future perspective

The work that has been presented in the previous section clearly shows that this PhD has taken a significant first step towards enhancing understanding of the feasibility of employing additive manufacturing process in the production of shaped charge liners. However, given the criticality of such systems (not least in terms of the fact that they employ energetic materials), there are still many numerical and experimental challenges that are yet to be addressed before the potential of this additive manufacture approach can be practically exploited. Therefore, in this section these challenges will be discussed under the areas of

numerical simulations and experimental work in detail in order to identify areas where future work could potentially be focused.

10.1.1 Numerical simulations

In Chapter 3, we have modelled only the bulk copper and aluminium liners using ANSYS Autodyn 2D employing the bulk material properties. We have made no attempt to model the laser sintered liners because of the lack of equation-of-state data to accurately describe their behaviour. Further, even though the proportion of alloying elements are quite small, it is unclear how this percentage will influence the EOS data from the bulk material. Hence it would be worth investigating the shock response of the sintered parts in order to enable accurate numerical modelling.

10.1.2 Experiments

While useful and novel insights into the potential of additive manufactured components for shaped charge applications have been identified, it is important to note that more repeats (experimental trials) would be required to strengthen the findings of this thesis as only limited trials were conducted on each of the shaped charge design. Furthermore, additional investigation would be useful; in particular, work focused on determining the feasibility of employing 3D printing process as part of decision-making process when different liner production processes are being considered would be advantageous. Moreover, the additive manufacturing process is improving constantly and new products are being developed. However, as detailed above, the ability to conduct thorough numerical simulation is often still missing due to the absence of an equations-of-state data to model the behaviour of the laser sintered part. Hence, extension of the work in this thesis focused on derivation of such equations-of-state to other potential additive manufacturing materials would be advantageous.

In Chapter 3, we examined the performance of laser sintered Aluminium and copper shaped charge liners and discussed the effect of porosity, density and ductility on the resultant jet. However, it is suggested that a further investigation focused on the effect of process parameters such as orientation, print speed etc

would be useful. Furthermore, the influence of surface roughness on the jet would be useful as the layer-by-layer deposition of material in 3D printing leads to an increase in the surface roughness. For example, Rz values of ~ 100 microns observed in laser beam melting [189] have been shown to increase concentration and early failure of 3D built parts under fatigue loading. However, it is not known how the surface roughness affects the performance of laser sintered liners. Therefore, while it was beyond the scope of the study herein, it would be important to understand how surface roughness influence the performance of laser sintered liners such as those considered here.

In Chapter 4, we evaluated the performance of liners manufactured through PLA and copper-filled composites. It has been reported in the literature that pure polymer products built by 3D printing lack strength and functionality which are essential requirement for a shaped charge liner. However, it is known that these properties can be improved by combining the matrix with other particles, fibre and reinforcements to achieve a system with more useful structural or functional properties. However, we have only considered the copper-fill containing copper w/w 40% composite. We have not considered other composite or structural reinforcements on the polymer matrix. It would therefore be interesting to investigate polymer incorporated with composites such as particles or fibres of nanomaterial reinforcement.

Further, if possible to extend this work it would be useful to measure the temperature of the resultant jet formed from the stretching or elongating polymer. Von and Thimble [126] measured the temperature of a stretching shaped charge copper jet and observed the temperature is around half the melting temperature of copper, demonstrating the feasibility of such an investigation. In this study, we speculate that the reason for the poor performance amongst other is melting occurring as the polymer begins to soften at 60 degrees. However, until the temperature of the jet during formation is measured, this is only speculative. To this end, further work on the liner temperature may need to be undertaken to clarify this aspect.

In Chapter 5, accurate determination of the shock response of PLA requires the sampled material to be isotropic. However, 3D printed parts are highly anisotropic and this present a challenge, particularly when taking the bulk sound speed of the material. In this work, we have taken the bulk sound speed along the impact direction but this would still require verification with a bulk PLA. As such, it would be worth investigating the material response of the bulk PLA and making comparison with this result before it can be employed for numerical subsequent simulations. In addition, FDM parts have shown variations with the mechanical parts depending on the orientation, raster angle and print direction. In this study, we have only considered the shock response on a defined parameter and direction. As such, we do not know how the direction (either at the macro-scale or microstructural level where textural effects might have an effect) would influence the shock behaviour of PLA.

In Chapter 6, we have observed a unique phenomenon of precipitates in the recovered slug of the laser sintered liner. The precipitates are likely a product of Chromium and Zirconium, However, we made no attempt to investigate the compound formed. Consequently, additional work in this area for example employing Energy Dispersive Spectroscopy (EDX) would be advantageous.

References

[1] Walters WP. AD-A240-999: Shock waves in the study of shaped charges. Technical Report BRL-TR-3258; 1991.

[2] Walters WP, Zukas JA. Fundamentals of shaped charges. A Wiley-Interscience Publication. New york, USA. 1989.

[3] Molinari J. Finite element simulation of shaped charges. Finite Element in Analysis and Design. 2002; 38(10): 921–936.

[4] Xu-dong ZU, Zheng-xiang H, Zhu C, Xiao Q. Study of detonation wave contours in EFP warhead. Defence Technology. 2016; 12(2): 129–133.

[5] Weimann K. Research and development in the area of explosively formed projectiles charge technology. Propellants, Explosive Pyrotechnics. 1993; 18(5): 294–298.

[6] Murphy M, Weimann K, Speck J. The effect of explosive detonation wave shaping on EFP shape and performance. 13th International Symposium on Ballistics. 1992, pp. 449.

[7] Elshenawy T. Criteria of design improvement of shaped charges used as oil well perforators. PhD Thesis. University of Manchester. 2012.

[8] Walters WP, Scheffler R. A method to increase the tip velocity of a shaped charge jet. 23rd International Symposium on Ballistics Terragona, Spain. 2007.

[9] Evans WM. The hollow charge effect. Bulletin of the Institution of Mining and Metallurgy. 1950; pp. 520.

[10] Held M. Liners for shaped charges. Journal of Battlefield Technology. 2001; 4(3):1–7.

[11] Hirsch E. The natural spread and tumbling of the shaped charge jet segment. Propellants, Explosive, Pyrotechnics. 1981; 6: 104–111.

[12] Hirsch E, Mordehai D. Shaped charge jet breakup time formula confirmed.

19th International Symposium on Ballistics. 2001. pp. 7–11.

[13] Chou P, Carleone J, Tanzio CA, Cicarelli R. Shaped charge jet breakup studies using radiograph measurement and surface instability calculations. BRL contract report No. 337. USA Armament Research and Development Command. 1977.

[14] Bourne B, Cowan KG, Golesworthy RC, Townsend I. The efficiency of shaped charges. 17th International Symposium on Ballistics. 1998: *2*, pp. 431–438.

[15] Karpp R, Simon J. An estimate of the strength of a copper shaped charge jet and the effect of strength on the breakup of a stretching jet. US Army Ballistic Research Laboratory Report No. 1893, June 1976. (AD BO12141L).

[16] Carleone J, Chou P. The stability of shaped charge jets. Journal of Applied Physics. 1977; 48(10), p 4187.

[17] Walsh J. Plastic instability and particulation in streching metal jets. Journal of Applied Physics. 1984; 56(7): 1997–2006.

[18] Hirsch E. A formula for the shaped charge jet breakup time. Propellants, Explosive, Pyrotechics. 1979; 4(5): 89–94.

[19] Hirsch E. The mott fragmentation model and the Vpl break-up parameter. Propellants, Explosive, Pyrotechics. 1989; 14, pp. 31–38.

[20] Haugstad B. On the breakup of shaped charge jets. Propellants, Explosive. Pyrotechics. 1983; 8(4): 119–120.

[21] Pfeffer G. Determination par simulations numtriques de L'etat et des lois de fragmentation des jets de charges Creusses. 5th International Symposium on Ballistics, Toulouse, France. 1980.

[22] Smith GJ, Mostert W. Analysis of jet properties of different liner materials manufactured under various conditions. 15th International Symposium on Ballistics. 1995.

[23] Baker E, Daniel A, Pham J, Vuong T, Defisher S. Jet Break-up characterization of molybdenum shaped charge liners. U.S Army Armament Research, Development and Engineering Center, Picatinny Arsenal. NJ 07806-5000. 2003.

[24] Cornish R, Mills JT, Curtis JP, Finch D. Degradation mechanisms in shaped charge jet penetration. International Journal of Impact Engineering. 2001; 26(1): 105–114.

[25] Simon J. The effect of explosive detonation characteristics on shaped charge performance. Ballistic Research Laboratories, Aberdeen Proving Ground, Maryland. 1974. AD-785680.

[26] Cartwright M, Simpson PJ. Non-solid explosives for shaped charges. Part II. Target penetration with metal liner devices used in explosive ordnance disposal operations. Journal of Energetic Materials. 2009; 27(3): 166–185.

[27] Birkhoff G, MacDougall DP, Pugh EM, Taylor G. Explosives with lined cavities, Journal of Applied Physics. 1948; 19(6).

[28] Murphy M, Kuklo R. Fundamentals of shaped charge penetration in concrete. 18th International Symposium on Ballistics. 1999.

[29] Saran S, Ayisia O, Yavuz MS. Experimental investigations on aluminum shaped charge liners. Procedia Engineering. 2013; 58, pp. 479–486.

[30] Held M. Characterizing shaped charge performance by stand off behavior. 7th International Symposium on Ballistics. 1983.

[31] Chou PC, Flis WJ. Recent developments in shaped charge technology. Propellants, Explosive, Pyrotechechnics. 1986; 11(4): 99–114.

[32] Shekhar H. Theoretical modelling of shaped charges in the last two decades (1990-2010): A review. Central European Journal of Energetic Material. 2012; 9(2): 155–185.

[33] Bourne B, Cowan KG, Curtis JP. Shaped charge warheads containing low melt energy metal liners. 19th International symposium on Ballistics. 2001.

pp. 583–590.

[34] Wang T, Zhu H. Copper-Tungsten shaped charge liner and its jet. Propellants, Explosive, Pyrotechnics. 21(4); 193–195.

[35] Zygmunt B, Wilk Z. Formation of jets by shaped charges with metal powder liners. Propellants, Explosive, Pyrotechnics. 2008; 33(6): 482–487.

[36] Elshenawy T, Abdo G, Elbeih A. High penetration performance of powder metallurgy copper-tungsten shaped charge liners. Central European Journal of Energetic Materials. 2018; 15, pp. 610-628.

[37] Zhao Z, Liu J, Guo W, Li S, Wang G. Effect of Zn and Ni added in W-Cu alloy on penetration performance and penetration mechanism of shaped charge liner. International Journal of Refractory Metals and Hard Materials. 2015; 54, pp. 90–97.

[38] Gokhan Aksoy I, Sen S. Effect of the variation of conical liner apex angle and explosive ignition point on shaped charge jet formation. Indian Journal of Engineering & Materials Sciences. 2003; 10(5): 381–389.

[39] Zukas JA, Walters WP. Explosive effect and application. Wiley Interscience Publication. New York, USA. 1998.

[40] Meyers MA, Andrade UR, Chokshi AH. The effect of grain size on the high-strain high-strain-rate behavior of copper. Metallurgical and Materials Transactions A. 1995; 26, pp. 2881-2893.

[41] Lichtenberger AB, Scharf M. Influence of the structural and metallurgical state of a liner on the performance of a shaped charge. Rapport-Bericht Co. 1981; 218 (81).

[42] Schmidt CG, Caliguri RD, Jacques H, Erlich DC. Effect of grain size on high strain rate deformation of copper. 1991; Metallurgical Transaction A. 1991; 22(10): 2349–2357.

[43] Wongwiwat LE, Murr K. Effect of shock pressure, pulse duration, and grain size on shock-deformation twinning in molybdenum. Material Science

Engineering. 1978; 35(2): 273–285.

[44] Murr LE, Niou CS, Sanchez JC, Shih HK, Duplesis L, Pappu S. Comparison of beginning and ending microstructures in metal shaped charges as a means to explore mechanisms for plastic deformation at high rates. Journal of Materials Science. 1995; 30(11): 2747–2758.

[45] Gurevitch A, Murr L, Shih H. Characterization and comparison of microstructures in the shaped-charge regime: copper and tantalum. Materials Characterization. 1993; 30(3): 201–216.

[46] Murr LE, Shih HK, Niou CS. Dynamic recrystallization in detonating tantalum shaped charges: A mechanism for extreme plastic deformation. Materials Characterization. 1994; 33(1): 65–74.

[47] Murr LE, Niou CS, Sanchez JC, Zernow L. A comparison of shaped charge liner cone and recovered jet fragment microstructures to elucidate dynamic recrystallization phenomena. Scripta Metallurgica et Materiala. 1995; 32(1): 31–36.

[48] Fan AL, Wang Z, Tian WH, Hu SL. Microstructural change in electroformed copper liners of shaped charges upon plastic deformation at ultra-high strain rate. Radiation Effect and defects in solids incorporating Plasma Science and Plasma Technology. 2002; 157(1): 145–156.

[49] Del Valle JA, Carreno F, Ruano OA. Influence of texture and grain size on work hardening and ductility in magnesium-based alloys processed by ECAP and rolling. Acta Materialia. 2006; 54(16): 4247–4259.

[50] Ahmad E, Karim F, Saeed K, Manzoor T, Zahid GH. Effect of cold rolling and annealing on the grain refinement of low alloy steel. IOP Conference Series: Materials Science and Engineering. 2014; 60(1): 12-29.

[51] Sakai T, Belyakov A, Kaibyshev R, Miura H, Jonas JJ. Dynamic and post-dynamic recrystallization under hot, cold and severe plastic deformation conditions. Progress in Material Science. 2014; 60, pp. 130–207.

[52] Guo W, Li SK, Wang FC, Wang M. Dynamic recrystallization of tungsten in a shaped charge liner. Scripta Materiala. 2009; 60(5): 329–332.

[53] Yang F, Li C, Cheng S, Wang L. Deformation behavior of explosive detonation in electroformed nickel liner of shaped charge with nano-sized grains. *T*rans. Nonferrous Met. Soc. China. 2010; 20(8): 1397–1402.

[54] Vernon John, Introduction to engineering materials. Palgrave Macmillan, London. 1992.

[55] Elshenawy T, Elbeih A, Li Q. A Modified penetration model for copper-tungsten shaped charge jet with non-uniform density distribution. Central European Journal of Energetic Materials. 2016: 13(4): 927–943.

[56] Borkowski J. Wilk Z, Koslik P, Szymanczyk L, Zygmunt B. Application of sintered liners for explosively formed projectile charges. International Journal of Impact Engineering. 2018; 118, pp.91-97.

[57] Wang X, Jiang M, Zhou Z, Gou J, Hui D. 3D printing of polymer matrix composites: A review and prospective. Compos. Part B Engineering. 2017; 110, pp. 442–458.

[58] Hull C. Apparatus for producing 3 dimensional objects by stereolithography. US Patent, 475330 A, 1986.

[59] Stansbury JW, Idacavage MJ. 3D printing with polymers: Challenges among expanding options and opportunities. Dental Materials. 2016; 32(1): 54–64.

[60] Kroll E, Artzi D. Enhancing aerospace engineering students' learning with 3D printing wind-tunnel models. Rapid Prototyping Journal. 2011; 17(5): 393–402.

[61] Wu GH, Hsu SH. Review: Polymeric-based 3D printing for tissue engineering. Journal of Medical Biological Engineering. 2015; 35(3): 285–292.

[62] Lee JY, An J, Chua CK. Fundamentals and applications of 3D printing for

novel materials. Applied Materials Today. 2017; 7, pp. 120–133.

[63] Wohlers T, Caffrey I, Campbell I. Wohlers Report 2016: 3D printing and additive manufacturing state of the industry annual worldwide progress report. Fort Collins, Colarado. 2016.

[64] Caneiro OS, Gomes R, Silva S. Fused deposition modelling with polypropylene. Materials and Design. 2015; 83, pp. 768–776.

[65] Sood AK, Ohdar RK, Mahapatra SS. Parametric appraisal of mechanical property of fused deposition modelling processed parts. Materials and Design. 2010; 31(1): 287–295.

[66] Dizon JR, Espera AH, Chen Q, Advincula RC. Mechanical characterization of 3D-printed polymers. Additive Manufacturing. 2018; 20, pp. 44–67.

[67] Caneiro OS, Gomes R, Silva S. Fused deposition modelling with polypropylene. Materials and Design. 2015; 83, pp. 768–776.

[68] Gebisa AW, Lemu HG. Effect of process parameters on compressive properties of ULTEM 9085 produced by FDM Process. Proceeding of the ASME 2018, Pittsburgh, USA. IMECA2018-87523.

[69] Kim E, Shin YJ, Ahn SH. The effects of moisture and temperature on the mechanical properties of additive manufacturing components: fused deposition modeling. Rapid Prototyping Journal. 2016; 22(6); 887–894.

[70] Ahn SH, Montero M, Odell D, Roundy S. Wright PK. Anisotropic material properties of fused deposition modeling ABS. Rapid Prototyping Journal. 2001; 8(4): 248-257.

[71] Chacón JM, Caminero MA, García-Plaza E,. Núñez PJ. Additive manufacturing of PLA structures using fused deposition modelling: Effect of process parameters on mechanical properties and their optimal selection. Materials and Design. 2017; 124, pp. 143–157.

[72] Motaparti KP, Tayloy G, Chandrashekhara K, Castle J. Effect of build parameters on mechanical properties of Ultem 9085 parts by fused

deposition modeling. Solid free form fabrication 2016: Proceedings of the 27th Annual Conference, USA. 2016, pp. 964–977.

[73] Es-Said OS, Foyos J, Noorani R, Mendelson M, Marloth R, Pregger BA. Effect of layer orientation on mechanical properties of rapid prototyped samples. Materials and Manufacturing Processes. 2000; 15(1):107–122.

[74] Delgado D, Camacho L. Applications of additive manufacturing in the construction industry – A forward looking review. Automobile Construction Journal. 2018; 89, pp. 110–119.

[75] Melnikova R, Ehrmann A, Finsterbusch K. 3D printing of textile-based structures by Fused Deposition Modelling (FDM) with different polymer materials. Material Science Engineering. 2014; 62.

[76] Rostoker N, Pugh EM, Eichelberger RJ. Theory of jet formation by charges with lined conical cavities. Journal of Applied Physics. 1952; 23, p. 532.

[77] Walters WP, Flis WJ, Chou PC. A survey of shaped-charge jet penetration models. International Journal of Impact Engineering. 1988; 7(3): 307–325.

[78] Jian-ping FU, Zhi-Gang CH, Xiu-Cheng HOU, Shu-Qiang LI. Simulation and experimental investigation of jetting penetrator charge at large stand-off distance. Defence Technology. 2013: (2)9 :91–97.

[79] Pack DC, Evans WM. Penetration by High-Velocity (Munroe) Jets: I. Armament Research Establishment, Fort Halstead, Kent. 1950

[80] Allen WA, Rogers JW. Penetration of a rod into a semi-infinite target. Journal of Franklin Institutue. 1961; 272(4): 275–284.

[81] Pack DC, Evans W M. Penetration by High-Velocity (`Munroe') Jets: II. Armament Research Establishment, Fort Halstead, Kent. 1950

[82] Allison FE, Brian GM. Cratering by a train of hypervelocity fragment. Proceedings, 2nd Hypervelocity Impact Effect Symposium. 1957; 1, p. 81.

[83] Allison FE, Vitali R. A new method of computing penetration variables for shaped charge jets. Ballistic Research Laboratory, Aberdeen Proving

Ground, Maryland. 1963, Report No 1184.

[84] Elshenawy T, Li Q. Influences of target strength and confinement on the penetration depth of an oil well perforator. International Journal of Impact Engineering. 2013: 54, pp. 130–137.

[85] Fairlie GE. The numerical simulation of high explosives using AUTODYN-2D & 3D. Institute of Explosive Engineering. 4th Biannual Symposium. 1998, p.13.

[86] Leslie MC, Federick G, Hulton RE. Sub surface barriers for ground shock attenuation: numerical techniques to model Experimental results. Recent Autodyne Publication. 1993, p. 89.

[87] Davidson D. Predicting the Initiation of Explosives in warheads subjected to Fragment Impact. ADPA. 1992.

[88] Autodyn Team. Jetting tutorial revision 3.0. Century dynamics. 2005.

[89] Cowler M, Century Dynamics, USA. Autodyn interaction tutorial. 1997.

[90] Lee CW, Finger EL. JWL equation of state for high explosives. Lawrence Livermore laboratories, 1973.

[91] Lee EL, Hornig HC, Kury JW. Adiabatic expansion of high explosive detonation products. Lawrence Livermore Radiation Laboratory. Livermore, CA, USA. 1968; p. 37.

[92] Dattelbaum DM, Coe J. The dynamic loading response of carbon-fiber-filled polymer composites. Dynamic Deformation, Damage and Fracture in Composite Materials and Structures. 2016; pp.225-277.

[93] Carter WJ, Marsh SP. Hugoniot equation of state of Polymers. Los Alamos National laboratory. 1995. LA-13006-MS

[94] Meyers MA. Shock waves - Measuring the dynamic response of materials. John Wiley and Sons inc. New York, USA. 2005.

[95] Johnson GR, Cook WH. A constitutive model and data for metals subjected

to large strains, high strain rates and high temperatures. 7th International Symposium on Ballistics. 1983; pp. 541–547.

[96] T. Elshenawy, Elbeih A, Klapötke TM. A numerical method for the determination of the virtual origin point of shaped charge jets instead of using flash x-ray radiography. Journal of Energetic Materials. 2017; pp. 1–14.

[97] T. Elshenawy, Elbeih A, Li QM. Influence of target strength on the penetration depth of shaped charge jets into RHA targets. International Journal of Mechanical Sciences. 2018; 136, pp. 234–242.

[98] Wang C, Xu W, Chung Kim S. Penetration of shaped charge into layered and spaced concrete targets. International Journal of Impact Engineering. 2018; 112, pp. 193–206.

[99] Hirsch E. The penetration cut-off velocity of ideal Jets. Rafael Ballistics Center, Haifa, Isreal.

[100] Malcoln .S. Autodyn jetting analysis Tutorial."

[101] Walters WP. Shock waves in the study of shaped charges. Ballistic Research Laboratory, Aberdeen proving Ground, Maryland. 1991. Technical Report No. BRL-TR-3258.

[102] Ayisit O. The influence of asymmetries in shaped charge performance. International Journal of Impact Engineering. 2008; 35(12): 1399–1404.

[103] Held M. Hydrodynamic theory of shaped charge jet penetration. Journal of Explosives and Propellants. R.O.C Taiwan. 1991; 7, pp. 9–24.

[104] Petit J, Jeanclaude V, Fressengeas C. Effect of liner grain size on shaped-charge jet performance: a combined experimental/numerical and analytical approach. J.Phys.IV Fr. 2006; 134, pp. 379–384.

[105] Duffy ML, Golaski SK. Effect of liner grain size on shaped charge jet performance and characteristics. 1987; Aberdeen, Tech. Report BRL-TR-2800.

[106] Held M. Spinning jets from shaped charges with flow turned liners. 12th International Symposium on Ballistics. 1990; pp. 1–7.

[107] Enzi A, Mynderse JA. Optimization of process parameters applied to a prototype selective laser sintering system. Proceedings of the ASME 2017 Internationa/ Mechanical Engineering Congress and Exposition IMECE2017. 2017; pp. 1–8.

[108] Zernow L, Chapyak E. Experimental and analytical study of early time material processing in a collapsing shaped charge liner, using softly - recovered partially - collapsed liners. International Journal of Impact Engineering. 1993; 14, pp. 863–875.

[109] Chemring Energetics, PE8 Plastic Explosive.

[110] Rice M, Mcqueen R, Walsh J. Compression of solids by strong shock waves. Solid State Phys. 1958; 6, pp. 1–63.

[111] Marsh S. LASL Shock Hugoniot Data. University of California Press. 1980.

[112] Guinan MW, Steingberg D, Cochran S. A constitutive model for metals applicable at high-strain rate. Journal of Applied Physics. 1980; 51(3): 1498–1504.

[113] Olakanmi E, Cochrane R, Dalgamo K. A review on selective laser sintering/melting (SLS/SLM) of aluminium alloy powders: processing, microstructure and properties. Progress in Material Science. 2015; 74, pp. 401–477.

[114] Liverani E, Toschi S, Ceschini L, Fortunato A. Effect of selective laser melting process parameter on microstructure and mechanical properties of 316L austenitic stainless steel. Journal of Material Process Technology. 2017; 249, pp. 255–263.

[115] Ghosh SK, Bandyopadhyay K, Saha P. Development of an in-situ multi-component reinforced Al-based metal matrix composite by direct metal laser sintering technique - Optimization of process parameters. Material

Characterization. 2014; 93, pp. 68–78.

[116] Tang Y, Loh H, Wong Y, Fuh J. Direct laser sintering of a copper based alloy for creating three-dimensional metal parts. Journal of Material Process Technology. 2003; 140, pp. 368–372.

[117] Carlton H, Haboub A, Gallegos G, Parkinson D. Damage evolution and failure mechanisms in additively manufactured stainless steel. Material Science Engineering A. 2016; 651, p. 414.

[118] Grayson G, Griffiths J, Schaffer G. On the fatigue of sintered aluminium alloys. Material Forum. 2004; 28, pp. 981–985.

[119] Song Y, Li Y, Song W, Tagarielli VL. Measurements of the mechanical response of unidirectional 3D-printed PLA. Material Destruction. 2017; 123, pp. 154–164.

[120] Held M. Determination of the material quality of copper shaped charge liners. Propellants, Explosive Pyrotechics. 1985*;* 10(5): 125–128.

[121] Elshenawy T, Ming Q. Breakup time of zirconium shaped charge jet. Propellants, Explosives and Pyrotechics. 2013; pp. 703–708.

[122] Liu J, Long Y, Zhong M, Liu Q. The influence of liner material on the dynamic response of the finite steel target subjected to high velocity impact by explosively formed projectile. International Journal of Impact Engineering*.* 2017;109, pp. 264–275.

[123] Shvetsov GA, Matrosov AD, Pavlovskii AI. Current instability of shaped charge jets. Proceeding of the 10th Pulsed Power Conference, Albuquerque, July 3-6. 1995; pp. 1136-1141.

[124] Shvetsov GA, Matrosov AD. Disruption of shaped charge jets by a pulsed current. 2004; 45.

[125] Doig A. Some metallurgical aspects of shaped charge liners. Journal of Battlefield Technology. 1998; 1, pp. 1–3.

[126] VonHolle W, Trimble J. Measurement of jet temperature. Sixth International

Symposium on Detonation, Colorado, San Diego. 1976, pp. 691–699.

[127] Murr L, Niou C, Garcia E. Comparison of jetting-related microstructures associated with hypervelocity impact crater formation in copper targets and copper shaped charges. Material Science Engineering. 1997; 222, pp. 118–132.

[128] Mohammadi H, Vincent M, Marand H. Investigating the equilibrium melting temperature of linear polyethylene using the non-linear Hoffman-Weeks approach. Polymer (Guild forum). 2018; 146, pp. 344–360.

[129] Epos D, Cell A. Ultimaker 3 specification sheet.

[130] Trishin YA, Kinelovskii SA. Effect of porosity on shaped-charge flow. Combustion, Explosion and Shock Waves. 2000; 36(2).

[131] Voitenko Y. I, Goshovskii SV, Drachuk AG, Bugaets VP. Mechanical effect of shaped charges with porous liners. Combustion, Explosion and Shock Waves. 2013; 49, pp.109–116.

[132] Hirsch E, Mayseless M. Penetration of porous jets. Journal of Applied Mechanics. 2010; 77(5).

[133] Agu HO, Hameed A, Appleby-Thomas GJ, Wood DC. The dynamic response of dense 3 dimensionally printed polylactic acid. Dynamic Behaviour of Material. 2019. https://doi.org/10.1007/s40870-019-00198-8.

[134] Lasprilla AJR,. Martinez GAR, Lunelli BH, Jardini AL, Filho RM. Poly-lactic acid synthesis for application in biomedical devices — A review. Biotechnology Advance. 2012; 30(1); 321–328.

[135] Field JE, Walley SM, Proud WG, Goldrein HT, Siviour CR. Review of experimental techniques for high rate deformation and shock studies. International Journal of Impact Engineering. 2004; 30(7): 725-775.

[136] Giordano RA, Wu BM, Borland SW, Cima LG, Sachs EM. Mechanical properties of dense polylactic acid structures fabricated by three dimensional printing. Journal of Biomaterial Science. Polymer Edition.

1997; 8, pp. 63–75.

[137] Millett JCF, Brown EN, Gray GT, Bourne NK, Wood DC, Appleby-Thomas G. The effects of changing chemistry on the shock response of basic polymers. Dynamic Behaviour of Materials. 2016; 2(3): 326–336.

[138] Millett JCF, Bourne NK. The deviatoric response of polymethylmethacrylate to one-dimensional shock loading. Journal of Applied Physics. 2000; 88(12): 7037–7040.

[139] Bourne NK. On the shock response of polymers to extreme loading. Journal of Dynamic Behaviour of Material. 2016; 2(1), pp. 33–42.

[140] Popovich A, Sufiiarov V, Polozov I, Borisov E, Masaylo D, Orlov A. Microstructure and mechanical properties of additive manufactured copper alloy. Material Letter. 2016; 179, pp. 38–41.

[141] Wood DC, Hazell PJ, Appleby-Thomas GJ, Barnes NR. Shock behaviour of a phenolic resin. Journal of Material Science. 2011; 46(18): 5991–5999.

[142] Hazell PJ, Appleby-Thomas GJ, Trinquant X, Chapman DJ. In-fiber shock propagation in Dyneema®. Journal of Applied Physics. 2011;110 (4).

[143] Appleby-Thomas G, Hazell PJ, Stennett C, Cooper G, Helaar K, Diederen AM. Shock propagation in a cemented tungsten carbide. Journal of Applied Physics. 2009;105(6).

[144] Appleby-Thomas GJ, Hazell PJ, Sheldon RP, Stennett C, Hameed A, Wilgeroth JM. The high strain-rate behaviour of selected tissue analogues. Journal of the Mechanical Behavior of Biomedical Materials. 2014; 33(1): 124–135.

[145] Millett JCF, Lowe MR, G. Appleby-Thomas, Roberts A. The mechanical and optical response of polychlorotrifluoroethylene to one-dimensional shock loading. Metallurgical Materials Science. 2016; 47(2): pp. 697–705.

[146] Parker NG, Mather ML, Morgan SP, Povey JW. Longitudinal acoustic properties of poly(lactic acid) and poly(lactic-co-glycolic acid). Biomedical

Material. 2010; 5.

[147] Wood A. A textbook of sound : being an account of the physics of vibrations with special reference to recent theoretical and technical developments by Wood, A. B. (Albert Beaumont). New York : Macmillan. 1930.

[148] Rosenberg Z, Yaziv D, Partom Y. Calibration of foil-like manganin gauges in planar shock wave experiments. J. Appl. Phys. 1980; 51, p. 3702.

[149] Meyers MA, Dynamic behavior of Material. John Wiley and Sons inc. 2014.

[150] Milne A, Logbottom A, Bourne N. On the unreacted hugoniots of three plastic bonded explosives. 2007; Propellants, Explosives and Pyrotechnics. 2013.

[151] Barker M, Hollenbach LE. Shock-wave studies of PMMA, fused Silica, and Sapphire. 1970;41, pp. 4208–4226.

[152] Davison L, Graham RA, Davison L. Shock compression of solids. Sandia Laboratories, Albuquerque, New Mexico 87185, U.S.A.

[153] Hazell PJ, Shock loading of polymer composites. School of Engineering and Information Technology. Elsevier, 2016.

[154] Bourne Neil. Materials in Mechanical Extremes. Cambridge University Press, 2013.

[155] Rosenberg Z, Bourne NK, Millett JCF. On the effect of manganin gauge geometries upon their response to lateral stress. Meas. Sci. Technol. 2007; 18(7): 1843–1847.

[156] Millett JCF, Bourne NK. Shock and release of polycarbonate under one-dimensional strain. Journal of Material Science. 2006; 41(6): 1683–1690.

[157] Shepherd CJ, Appleby-Thomas GJ, Wilgeroth JM, Hazell PJ, Allsop DF. On the response of ballistic soap to one-dimensional shock loading. International Journal of Impact Engineering. 2011; 38(12): 981–988.

[158] Painter JD, Appleby-Thomas GJ, Hazell P, Winter R, Wood DC. On the

importance of encapsulation environment for lateral gauges. AIP Conf. Proc. 2012; 1426, pp. 454–457.

[159] Alharbi N, Osman R, Wismeijer D. Effects of build direction on the mechanical properties of 3D-printed complete coverage interim dental restorations. Journal of Prosthetic Denture. 2016; 115(6): 760–767.

[160] Gurevitch AC, Murr LE, Shih HK, Nioul C. Zernow L. Materials Characterization. 1993; 30, p. 201.

[161] Guo W, Li SK, Wang FC, Wang M. Dynamic recrystallization of tungsten in a shaped charge liner. Scripta Materiala. 2009; 60(5): 329–332.

[162] Zernow L. Lowry L. High strain rate deformation of copper in shaped charge jets, in shockwave and high-strain-rate phenomena in materials.

[163] E 112-96. Standard test methods for determining average grain size 1. ASTM International. 2009; 96.

[164] Wallis C, Buchmayr B. Effect of heat treatments on microstructure and properties of CuCrZr produced by laser-powder bed fusion. Material Science Eng. A. 2019; 744, pp. 215–223.

[165] Murr LE, Esquivel EV. Observations of common microstructural issues associated with dynamic deformation phenomena: Twins, microbands, grain size effects, shear bands, and dynamic recrystallization. Journal of Material Science. 2004; 39(4): 1153–1168.

[166] Guo W, Li SK, Wang FC, Wang M. Dynamic recrystallization of tungsten in a shaped charge liner. Scripta Materiala. 2009; 60(5): 329–332.

[167] Flis WJ. On temperatures in shaped-charge jet penetration. 30th Internationational Symposium of Ballistics, Long beach, California. 2017.

[168] Lassila DH, Walters WP, Nikkel DJ, Kershaw RP. Analysis of soft recovered shaped charge jet particles. This paper was prepared for submittal to the Symposium Structures Under Extreme Loading Conditions at the 1996 American Society of Mechanical Engineers Pressure Vessels

and Piping Conference. 1996.

[169] Racah E. Shaped charge jet heating. Propellants, Explosive and Pyrotechnic.1988; 13, pp. 176–182.

[170] Agu HO, Hameed A, Appleby-Thomas GJ. Application of shell jetting analysis to determine the location of the virtual origin in shaped charges. International Journal of Impact Engineering. 2017; 122, pp. 175–181.

[171] Malcolm C. Autodyn® Jetting Tutorial, 3rd Revision, Century Dynamics, USA. 1997.

[172] Heuzé O. General form of the Mie-Grüneisen equation of state. Comptes Rendus - Mec. 2012; 340(10), pp. 679–687.

[173] Baoxiang R, Gang T, Peng W, Changxing D, Chunqiao P, Hongbo M. Analysis of the formation mechanism of the slug and jet center hole of axisymmetric shaped charges. Results in Physics. 2018; 9, pp. 135–141.

[174] Zernow L. The density deficit in stretching shaped charge jets. International Journal of Impact Engineering. 1997; 20, pp. 849–859.

[175] DiPersio J, Simon R. The penetration standoff relation for idealized shaped charge jets. Ballistic Research Laboratory. 1964.

[176] Abrahamson GR, Goodier JN. Penetration of shaped charge jet with non-uniform velocity. J. Appl. Phys. 1963; 34(1), p. 195.

[177] Dipersio R, Simon J, Merendino. Penetration of shaped-charge jets into metallic targets. Ballistic Research Laboratory; Aberdeen Proving Ground; Maryland. 1965. Report No 1296.

[178] Chou WP, Hirsch PC, Walters W. The virtual origin approximation of shaped charge jets. 6th International Symposium On Ballistic, Orlando, Flourida. 1981.

[179] Hsu CY, Liang CC, Teng TL, Nguyen AT. A numerical study on high-speed water jet impact. Ocean Engineering. 2013; 72, pp. 98–106.

[180] Shear RE, Brundick FS, John T. A link between shaped charge performance and design. Aberdeeen proving Ground, Maryland. 1981.

[181] Robinson A. SCAP-A shaped charge analysis program: User's manual for SCAP 1. Albuquerque, NM. 1985.

[182] Held M. Penetration cutoff velocities of shaped charge Jets. Propellants, Explos. Pyrotechnics.1987; 13(4), pp. 111–119.

[183] DiPersio R, Jones W, Merendino A, Simon J. Characteristics of jet from small caliber shaped charges with copper and aluminium liners. Ballistic Research Laboratory, Aberdeen Proving Ground, Maryland. 1967, Report No .1866.

[184] Carleone J, Chou PC. A One-Dimensional theory to predict the strain and radius of shaped charge jets. 1st international Symposium on Ballistic. 1974.

[185] Naury C, Birnbaum K, Malcolm S. A combined numerical/ analytics approach for shaped charge design. Century Dynamics, USA. pp 7-1.

[186] Held M. Assessment of measurement of the cratering velocities of shaped charge jet. International Journal of Impact Engineering. 1997; 20, pp. 349–361.

[187] Abrahamson GR, Goodier JN. Penetration by shaped charge jets of non-uniform velocity. J. Appl. Phys. 1963; 34(1), p. 195.

[188] Held M. Penetration of shaped charges in concrete and in sand in comparism to steel - target. Journal of Explosive and propellant, R.O.C Taiwan. 1992; 8, pp. 1–15.

[189] Herzog D, Seyda V, Wycisk E, Emmelmann C. Additive manufacturing of metals. Acta Materiala. 2016; 117, pp. 371–392.

Appendixes

Appendix 1

The Dynamic Response of 3 Dimensionally printed polylactic acid

Journal of Dynamic Behavior of Materials
https://doi.org/10.1007/s40870-019-00198-8

The Dynamic Response of Dense 3 Dimensionally Printed Polylactic Acid

H. O. Agu[1] · A. Hameed[1] · G. J. Appleby-Thomas[1] · D. C. Wood[1]

Received: 28 January 2019 / Accepted: 14 May 2019

Abstract
Polylactic acid (PLA) is commonly used as a feedstock material for commercial 3D printing. As components manufactured from such material become more commonplace, it is inevitable that some of the resultant systems will be exposed to high strain-rate/impact events during their design-life (for example, components being dropped or even involved in a high-speed crash). To this end, understanding the shock properties of polylactic acid, in its role as a major raw material for 3D printed components, is of particular importance. In this work, printed samples of PLA were deformed by one-dimensional shock waves generated via the plate impact technique, allowing determination of both the Hugoniot Equation of State (EOS) and shear strength of the material. Both linear and non-linear EOS forms were considered in the U_S-Up plane, with the best-fit found to take the general form $U_S = 1.28 + 3.06 - 1.09U_p^2$ in the $U_s - U_p$ plane, consistent with other polymers. Use of lateral Manganin gauges embedded in the material flow allowed consideration of lateral stress evolution at impact pressures ranging from 0.3 to 4.0 GPa. Shear strength was observed to increase with impact stress, however, with minimal strengthening behind the shock front. Deviation of the measured stress from the predicted elastic measurement (corresponding to the PLA's Hugoniot Elastic Limit) was observed at longitudinal stress of 0.90 ± 0.05 GPa, within range of polymeric materials of similar characteristics—the first time this important parameter has been measured for PLA. As a result, this material characterisation will allow numerical modellers to accurately predict the structural response of PLA-based components/structures against high strain rates such as impacts or drops.

Keywords Polylactic acid · Hugoniot elastic limit · Equations of state · Polymer

Introduction

Polylactic acid is one of the major raw materials used in a filament deposition modelling (FDM) desktop 3D printer. The application of PLA has metamorphosed from the production of simple prototypes to manufacturing of finished/end-use products such as medical implants in the form of screws, plates and anchors [1], subject to a range of loading conditions. It is therefore important to understand the shock response of printed PLA. More importantly, understanding of the material's hydrodynamic and constitutive equations of state will enable the development of mathematical models for numerical simulations [2]. Although there are a number of studies on the response of printed PLA, [3–5] within the quasi-static loading regime, there is—to the author's knowledge—no existing study focused on the dynamic response of PLA under high strain rate conditions. However, usefully/as a potential point of comparison, a number of studies have already been conducted on the shock response of similar polymeric materials such as polyethylene (PE) [6], Polymethylmethacrylate (PMMA) [7], polyvinylchloride (PVC) [6] and polytetrafluoroethylene (PTFE) [6].

One of the earlier investigation conducted by Carter and Marsh [8] at the Los Alamos National Laboratory investigated the shock behaviour of over 20 polymers, showing certain similarities in the dynamic response of such materials. It was observed that at high pressure (20–30 GPa), there is a change in the slope of the shock velocity, ($U_{s)}$ and particle velocity, (U_p), curve suggesting a phase transformation. This was attributed to the re-ordering of the polymer structure due to the nature of the compression at sufficiently high pressure [8]. More or less, a rearrangement of the chains at the molecular level resulting in a large volume change at high

✉ H. O. Agu
henry.agu@cranfield.ac.uk

[1] Centre for Defence Engineering, Cranfield University, Shrivenham SN6 8LA, UK

Published online: 22 May 2019

pressure was postulated. Another observable trend was the inability of the experimentally measured data in the $U_s - U_p$ plane to extrapolate to the zero-pressure ultrasonic sound speed measurement [8]. In contrast with metals, the bulk sound speed, C_B is usually below the y-intercept, giving polymers a non-linear Hugoniot. For example, Millet et al. [6] investigated the shock response of 4 common semi-crystalline thermoplastic polymers: PE,PTFE, PVC and PCTFE [6] and observed that all four polymers had a linear response in the U_s and U_p, curve in common with other polymeric materials, represented in the form described in Eq. 1. However, when interpolated from the measured bulk sound speed on the y-intercept, a non-linear equation presented in the form described in Eq. 2 was obtained.

$$U_s = c_0 + Su_p, \tag{1}$$

$$U_s = c_0 + SU_p + RU_p^2. \tag{2}$$

The values of the c_0 and S in the Hugoniot equations are empirical constants, correlated to the bulk sound speed c_B and the first pressure derivative of the bulk modulus respectively [9].

This trend has been reported in a number of studies and has been attributed to variation between the forces in the C–C backbone (of higher magnitude) and the forces between the adjacent chains in the polymer altering the deformation pattern along the chains and backbone [8]. As such, in contrast with metals, the chemistry of polymer is key to understanding its dynamic response. Essentially, the carbon backbone in polymers (chain) forms a strong bond with itself compared with bonds between adjacent polymer chains [8]. Hence, as the shock propagates, smaller/weaker forces in the adjacent chain collapse even more rapidly than the forces in the C–C backbone. Usefully, the interaction between functional groups and or atoms (steric effect) plays a significant role in polymer response as well as the geometric arrangement (Tacticity) of these groups. As an example, greater physical interaction between adjacent polymer chains is required in PE molecule due to its relatively open nature. Similarly, the addition of a single chlorine atom in PVC to the basic polyethylene monomer reduces the stress required for the atoms to slide past each other during shock loading. This is because of the sheathing effect of the large chlorine atoms (compared to hydrogen) upon the polymer chain, resulting in an over-all smoother shape that allows easier passage of the polymer chains [6]. However, the presence of chlorine (in PVC) and fluorine atoms (in PCTFE) also increases the influence of electrostatic repulsion arising from increased electronegativity. Following on from this, it is likely that the presence of an oxygen atom in the side group chain of the PLA, presented in Fig. 1, would influence the shock response of PLA. As the slightly positive sections

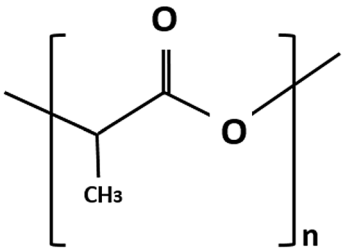

Fig. 1 Representative monomer structure of Polylactic acid

(carbon and hydrogen) are attracted to the negative sections of the chains, the stress required to break the bond increases with a consequent effect on the polymer strength.

Further, as the polymer is compressed and the chains move closer together, physical interaction between the molecules (tangling or steric effect) due to the shape of the polymer increases the stress required to move the molecules together. Though reported particularly for polymers with open chain morphology such as PE [6] with dangling side groups, the addition of an electronegative atom to the chains increase the susceptibility for entanglement. Such an interplay between electronegative repulsion and tangling determines the polymer strength under dynamic (shock) loading. While the degree at which these factors influence polymer strength is yet to be fully established, it has been suggested that repulsive forces are more dominant in the fluorinated polymer such as PTFE and PCTFE, in contrast with hydrocarbon polymers controlled majorly by tangling. Interestingly, PLA has an open chain morphology similar to PE and the presence of a CH_3 side chain group should allow a greater degree of interaction (steric effect) between the adjacent polymer chains. In the same vein, the presence an electronegative atom (oxygen), while even not as strongly electronegative as the chlorine and fluorine atoms in PVC and PCTFE, means it is likely that the interaction of both factors could increase the strength of PLA. In this work, the dynamic shock behaviour of a 3D printed PLA was investigated using manganin stress gauges. These gauges, of thickness, ca. 25 μm and embedded in the material flow, measure the longitudinal and lateral stresses induced in the samples. The data obtained were reduced to determine the Hugoniot Equations of state of the material and the shear strength—key data to allow for subsequent high strain-rate/pressure simulations.

Material Production

The PLA filament, of diameter 2.85 mm, used in this study was obtained commercially and supplied in an airtight bag to prevent degradation from atmospheric humidity [10]. A 50 mm diameter, 10 mm thick disc was designed on

Computer-aided Design (CAD) software and imported as an STL file into an Ultimaker 3D printer with a 0.4 mm print core for printing via the Filament Deposition Modelling (FDM) desktop 3D printer (Ultimaker 3 extended). The 3D printing technique creates parts by heating filaments above its glass transition temperature before laying successive layers on the print bed based on input print parameters. Although, there are no standard parameter values for desired printing quality in the literature, the effect of certain parameters has been reported. As an example, Sood et al. [11] investigated the effect of printing parameters such as orientation, layer thickness, and air gaps on the quality of printed parts by studying their flexural, tensile, and impact strength. Schopper et al. [12] investigated the effect of build direction on the compression properties of FDM built parts and observed higher compressive modulus and yield strength of built parts in the horizontal direction in comparison to the specimens built in the vertical direction [13]. In turn, Caneiro et al. [5] investigated the effect of the layer thickness by comparing samples produced with layer thicknesses of 0.20 and 0.35 mm and results have shown higher tensile stress with an increasing layer thickness which was attributed to the lower number of interfaces between filaments. In the same work, the degree of infill (a printer setting which controls the density of the built parts) was reported to have a strong impact on the mechanical performance of printed samples. A difference in both modulus and tensile strength of more than 250% was reported when the infill density varied from 20 to 100% [5]. As such, for the investigations here/to ensure an optimum print, a 100% infill density was used with a print speed of 70 mm/s employed. The target samples were finished with an impervious top and bottom layer to prevent percolation of epoxy used in the target preparation. Other print parameters are summarised in Table 1. A total of eight samples were fabricated from a roll of 2.85 mm PLA from Spool Work. The samples were printed vertically with the layers oriented perpendicular to the shock direction. All test specimens were printed under identical conditions to maintain consistency in all samples.

In order to evaluate the consistency of the print quality, weight and diameter of each sample were obtained. The weight was found to be consistent with a tolerance of ± 0.2 g while the average density was 1.14 ± 0.02 g/cc, slightly lower than the nominal bulk PLA density of 1.24 g/cc. This could be attributed to the presence of voids [3] which are a function of the input parameters during the printing process. The diameter was consistent with a tolerance of ± 0.01 mm.

Table 1 Print parameters for the production of 10 mm thick PLA on Ultimaker FDM printer

Parameter	Value
Layer height	0.1 mm
Line width	0.35 mm
Wall thickness	0.5 mm
Z Seam alignment	Random
Top/bottom pattern	Concentric
Top/bottom thickness	1 mm
Infill	100%
Print speed	70 mm/s
infill speed	40 mm/s
Wall speed	30 mm/s
Travel speed	250 mm/s
Printing temp	200 °C
Build plate temperature	60 °C

Experimental Method

One of the methods commonly used to produce a shock wave in materials is the plate-impact technique. The plate-impact technique involves accelerating a flat and parallel plate into a similar target (surfaces were polished to a tolerance of < 10 µm) [14–16] using a single stage gas gun. Simultaneous impact of all elements of the flyer and target impact surfaces leads to inertial confinement over very short (micro-second) timescales and the establishment of a one-dimensional state-of-strain within the materials. The gas gun employed for these experiments has a 50-mm bore, with a 5-m barrel and is situated at the Defence Academy of the UK, Shrivenham. A schematic of the gun set-up is presented in Fig. 2. Well characterised materials such as Copper alloy (C101) and Aluminium (1050A) flyers, whose equations of state are known were employed to impact PLA targets at impact velocities in

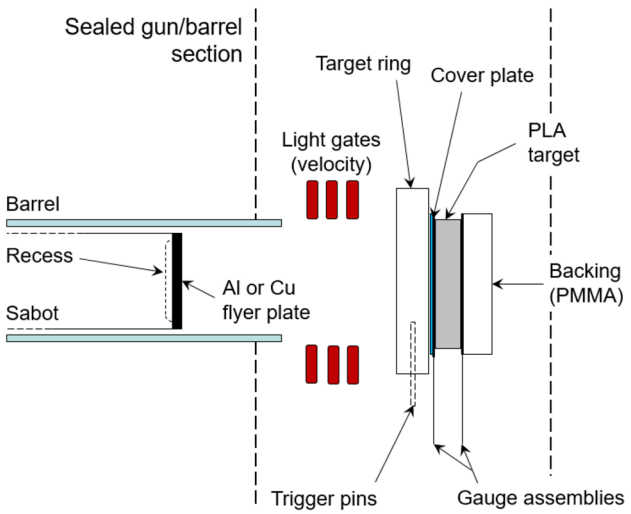

Fig. 2 Schematic representation of the mounting configuration of longitudinal target arrangement in a plate impact experiment

the range 300–1000 m/s. The projectile impact velocity was recorded via a series of light gates at known separation immediately prior to impact. Further, target rings were employed to support the target and ensure alignment experimentally with respect to the flyer, on a sacrificial barrel extension to ensure good flyer–target alignment.

Manganin longitudinal stress gauge (Vishay Micro-Measurement of Type LM-SS-125CH-048) of 48.0 ± 1.0% grid resistance in Ohms resistance were used to determine the stresses in the material. The gauges were placed at the front and rear of the target separated by a 50 micron Mylar (25 microns on each side) as illustrated in Fig. 2 to protect and insulate the gauges. 10 mm thick PMMA was used at the rear gauge to trap reflection of the shock wave. All the components were held neatly together with a slow curing Locite 0151 HYSOL epoxy-patch adhesive. 1 mm thick aluminium and copper cover plates (depending on the impactor material) were employed at the target surface to protect the gauge from being damaged by the impactor.

The shear strength of the material was also measured by obtaining the lateral component of the stress (σ_y), from which the shear strength behind the shock front is calculated from the relationship in Eq. 3,

$$2\tau = \sigma_x - \sigma_y. \tag{3}$$

Embedded lateral Manganin gauges (Vishay Micro-Measurement of Type J2M-SS-580SF-025) were introduced into sectioned samples, 4 mm from the impact surface as shown in Figs. 3 and 4. This depth was chosen to allow sufficient time for the shock to equilibrate/to resolve the elastic precursor (if any) before shock arrival. The samples were held firmly with a Locite 24-h epoxy in a special jig for a minimum of 12 h. In some experiments, longitudinal and lateral gauges were combined at impact velocities between 200 and 900 m/s to obtain additional U_s–U_p data point on the Hugoniot. Errors were minimised by ensuring proper gauge alignment in the sectioned lateral halves of the target [17].

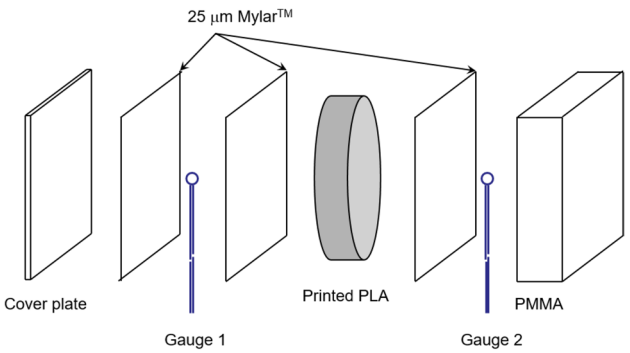

Fig. 3 Schematic representation of target configuration in plate impact experiment showing expanded view

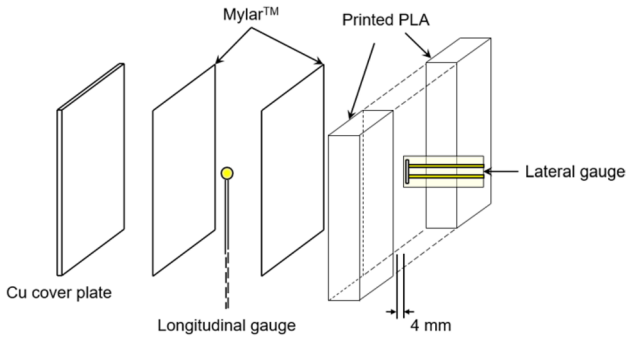

Fig. 4 Schematic representation of target configurations with longitudinal and lateral gauge positions

The densities of the printed PLA samples were measured using an XS 105 dual range excellence machine from Mettler Toledo. A density reduction relative to the initial material density (1.24 g/cc) was observed in all samples as a result of the pores generated between layers during the printing process. In addition, shear (C_S) and longitudinal (C_L) sound velocities were measured ultrasonically using 1 MH_Z quartz transducers with a Panemetrics 5077PR pulse receiver in the pulse-echo configuration. Employing the isotropic relation for wave speed in Eq. 4 [18], the bulk sound c_B was obtained. Key elastic material properties of the printed PLA are summarised in Table 2.

$$C_B = \sqrt{C_L^2 - \frac{4}{3}C_S^2}. \tag{4}$$

The FDM 3D printing technique has been shown to exhibit anisotropic behaviour dependant on print orientation [19]. As such, the wave speeds were measured perpendicular to the print direction and at different points on the surface to check that the resultant wave speed is consistent. The measured longitudinal sound speed for the printed PLA sample was 1860 m/s—corresponding to a bulk sound speed of 1250 m/s (Table 2). This appears to be below the result obtained by Parker et al. [20] who employed the pulse-echo technique to determine the bulk sound speed and the acoustic impedance of PLA to be around 2260 m/s. Variations between the measured sound speed measurements is consequently tentatively attributed to the presence of voids arising from the 3D printing manufacturing technique employed—e.g. FDM when compared with a cast PLA. Even though the

Table 2 Relevant elastic material property for printed PLA measured perpendicular to the printing direction

ρ_0 g/cm^3	C_L (mm/μs)	C_s (mm/μs)	C_B (mm/μs)
1.14	1.86 ± 0.02	1.19	1.25

pores are microscopic, small void contents can influence the sound speed in a mixture as the rate at which sound travels is lowered due to the need for waves to travel around the pores [21].

Results and Discussion

A total of 6 experimental shots were undertaken at impact velocities between 200 and 1000 m/s using 5 and 10 mm thick aluminium and copper flyers against ~ 10 mm thick printed PLA targets. Figure 5 shows representative shock profiles of the printed PLA for 3 selected impact velocities ranging from 213–925 m/s corresponding to impact pressure between 0.3 and 4.0 GPa. Essentially, as touched on earlier by ensuring that all impact faces (target and projectile) are parallel and finished to a tolerance of < 10 µm, planar shock waves are rapidly established in both the target and impactor due to the material being inertially confined on impact. The resultant shocks are 1D in nature and are maintained until release arrival from free surfaces (interfaces). Key features can be interpreted from the shock profile obtained from the experiments. An initial pressure rise on shock arrival indicates the establishment of the shock wave into the target. The rapid rise in the front gauge indicates a good gauge alignment followed by a levelling of the shock front in the form of a plateau, the Hugoniot stress. An overshoot in longitudinal stress was observed after the initial rise with some ringing attributed to electrical effect.

The voltages were converted into stresses following a technique developed by Rosenberg et al. [22]. The front gauge measured the stress in the PLA while the rear gauge recorded that in the PMMA (backing material). To characterise a material mechanical shock response, five key parameters are required and these are: shock velocity U_s, particle velocity U_p, density ρ, pressure P, and internal energy E. By employing the principles of conservation of energy, mass and momentum, other parameters can also be obtained from just two parameters. In this study, the U_s and U_p values were obtained and employed to derive a shock Hugoniot equation of state for the printed PLA. The shock velocity was obtained by calculating the time taken for the shock to travel between the front and rear gauge indicated by the rise in both gauges divided by the known gauge separation distance, with particle velocity determined via the impedance matching technique (requiring knowledge of impactor properties and velocity [23] and subsequently converted to volume as-required. In addition, the embedded gauges provided a direct measure of in-material stress. A Typical trace for the front and rear gauges of a printed 10 mm PLA with impact velocity of 714 m/s is presented in Fig. 6.

By employing well-defined flyer materials with an established pressure—particle velocity $\left(P - U_p\right)$, and known impact velocity, the U_p is obtained graphically via impedance matching technique described extensively by Meyers in Ref. [23]. The $U_s - U_p$ Hugoniot relationship for the printed PLA was measured/calculated with data points obtained from shock states derived via experimental plate impact experiment. A summary of the experimental conditions and key results where $U_s - U_p$ data were extracted are presented in Table 3.

Although the samples were observed to contain some degree of porosity, this is quite minimal (< 8%). As such, the Mie-Gruneisen EOS relationship for porous materials, described in Ref. [23] which predicts volume increases at all pressure for a porosity of 50% cannot be employed here. Essentially, when the main bulk of the material contains a significant fraction of voids, such as solid foam (pg. 64 of Ref. [24]) with larger variations in impedance, the nature of the response is different. However, for the samples printed here, the void observed is in the quite small, much lower

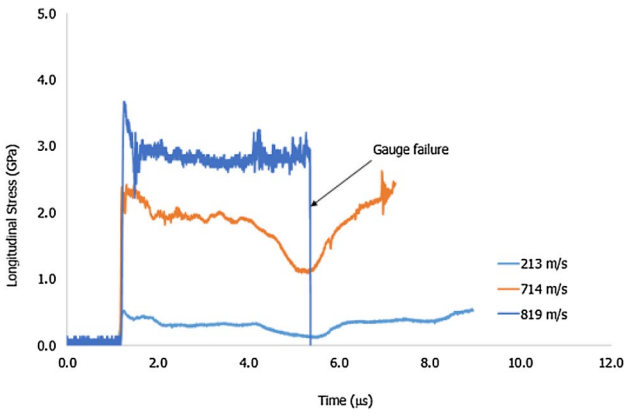

Fig. 5 Representative wave traces of printed PLA shots at 213, 714 and 819 m/s (corresponding to impact pressures of 0.30, 1.93 and 2.88 GPa respectively)

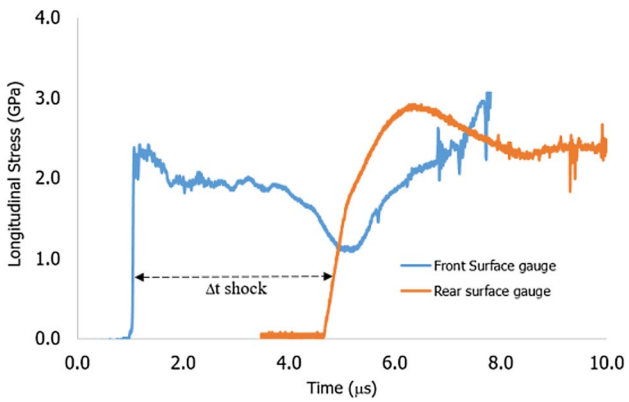

Fig. 6 Typical gauge trace for 10 mm thick copper impacting a 10.12-mm thick printed PLA at 567 m/s

Table 3 Summary of plate impact experimental result

Impact velocity (m/s)	Flyer thickness (mm)/material	U_p (mm/μs)	U_s (mm/μs)	Error (+)	Error (−)	P (GPa)	Error (+)	Error (−)
213	10/Al	0.18	1.87	0.09	0.05	0.30	0.02	0.02
312	10/Cu	0.30	2.04	0.15	0.13	0.70	0.1	0.69
490	10/Al	0.41	2.37	0.14	0.12	1.45	0.05	0.05
714	10/Al	0.58	2.74	0.24	0.21	1.93	0.14	0.12
819	10/Cu	0.73	2.93	0.21	0.11	2.88	0.11	0.10
925	10/Cu	0.84	3.17	0.22	0.14	3.59	0.13	0.18

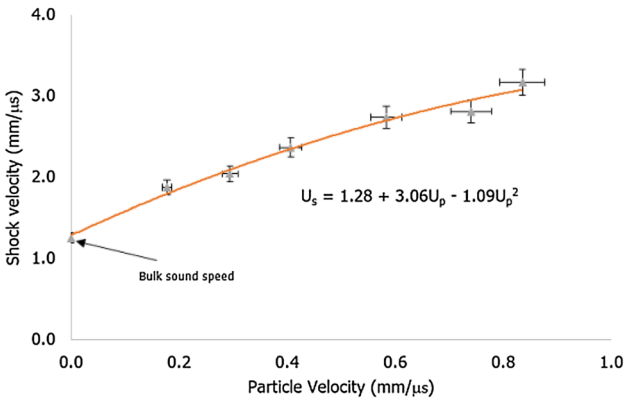

Fig. 7 Non-linear Hugoniot response for printed PLA at low shock velocity ranges

Table 4 Equations of State considered for PLA Hugoniot

Type	Equation	R^2 value
Linear form	$U_S = 1.4 + 2.02U_p$	0.983
Non-linear form	$U_S = 1.28 + 3.06U_p - 1.09\,U_p^2$	0.995

than the width of the pressure gauges employed. Hence, the authors consider that the effect of the voids on the resultant EOS is negligible. Moving forward, both linear and non-linear polynomial fits to the experimental data were considered. For the linear relationship, best-fit to the experimental data, C_o and S were found to equal 1.38 and 2.0 respectively, with a residual "R^2" value of 0.983. However, a 2nd order polynomial fit produced a higher $R^2 = 0.995$ which justified its use in Fig. 7. In this case, the polynomial coefficient for the best fit were: $C_o = 1.28$ mm/us, S = 3.06 and Q = − 1.09 mm/us something highlighted in Table 4. Such non-linear response has been reported in the low pressure (below the 20–30 GPa transition) regime for polymeric materials such as PMMA [25], polyethylene and PVC [26]. However, above the particle velocity of ca. 0.2 mm/μs, as recorded in this experiment, most polymeric materials give a linear response, of the form $U_s = C_o + SU_p$, along with other commercially available polymers and specially produced plastics [9]. The empirical constants C_0 and S in the linear and polymeric best-fit equations are related to the bulk sound speed (in metals such as copper) [27] and the rate of change of compressibility of the material with pressure [9], respectively. More striking, and in line with other polymeric materials such as PMMA, and polycarbonate [8], is the failure of the experimental data to extrapolate to the zero-pressure ultrasonic measurement as observed in metals. For the non-linear fit considered, the difference between the ultrasonic sound speed and the experimentally derived C_0 is only 0.02 mm/μs. As such, the bulk sound speed of the material lies only slightly below the zero vertical intercept of the $U_s - U_p$ plot giving a polynomial non-linear response of the form $U_s = C_o + SU_p + QU_p^2$ [28]. This accounts for the narrow variation in R^2 value between the linear and non-linear fits.

Such non-linear response has been attributed elsewhere to the two-dimensional nature of polymer compression and to the form of the inter-chain interaction potential [8] owing to the substantial difference in magnitude between the backbone and inter-chain forces as described earlier. Fundamentally, weaker inter-chain forces are overcome during the initial stages of compression before the backbone covalent bonds, thereby resulting in a two-stage compression. A non-linear response occurs at low particle velocities, < 0.2 mm/μs; whereas a more conventional linear $U_s - U_p$ response is established above 0.2 mm/μs as described earlier. Comparison (low range data) of the measured $U_s - U_p$ plot with some selected polymers such as PE and PVC in Fig. 8 revealed similarities in terms of lower bulk sound speed. Such changes have been linked to changes in the density and modulus due to molecular rearrangement of the chains [27].

As can be seen from Fig. 8, PLA lies at the bottom of the plot followed closely by PE with a simple polymer structure. This response could be attributed to the presence of the methyl group on the carbon backbone of the PLA (in Fig. 1) making the chain bulkier thus, providing a steric impediment to flow. Further, the presence of oxygen atom to the carbon chain increases the strength of the carbon-ligand bond and decreases Van-der-Waals forces between chains. Above the PE response are the highly electronegative polymers PCTFE

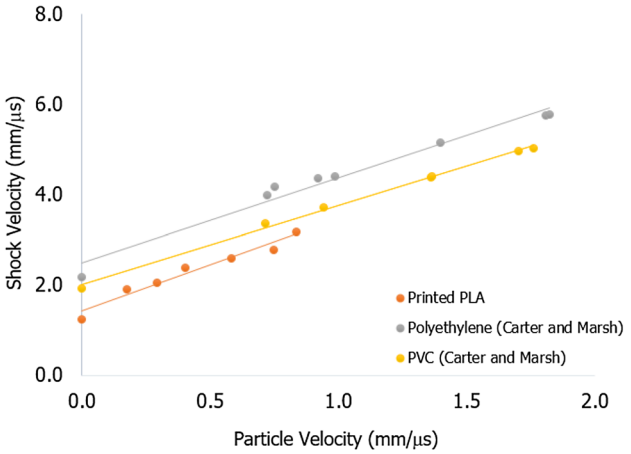

Fig. 8 Comparison of U_s–U_p plot of printed PLA with Polyethylene and PVC

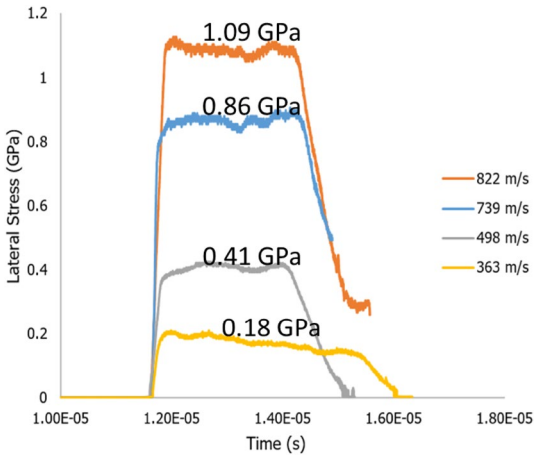

Fig. 10 Lateral stress histories for printed PLA at varying impact velocities; gauges are 4 mm from the impact surface

and PVC with branch or side chains replaced by electronegative atoms such as fluorine or chlorine. Each of these polymers has other elements introduced onto the carbon backbone or into the side group chains increasing the density throughout the series. The PCTFE, for example, is higher up because of the presence of both chlorine and fluorine which increases the repulsion force as well as the density. As such, the combination of density and strength ensures that the Hugoniot lies above their hydrocarbon neighbours. By employing the non-linear equations of state from Fig. 7, the hydrodynamic pressure can be calculated according to Eq. 5. When plotted with the measured stresses in Fig. 10, the strength of the material can be predicted.

$$P = \rho_o U_p U_s \tag{5}$$

From Fig. 9, there appears to be a deviation between pressure as particle velocity increases. This implies that, at least, within the shock pressure regime investigated, the printed

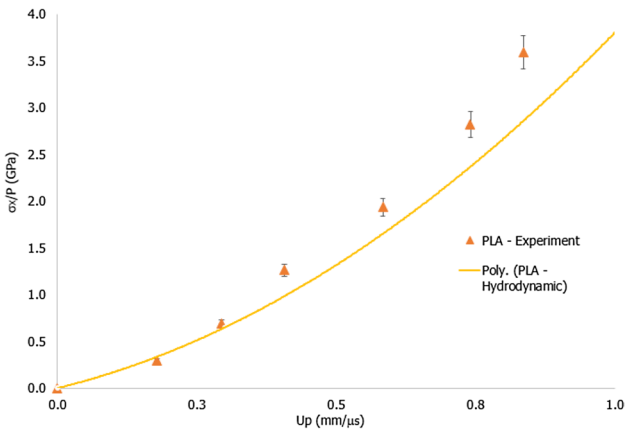

Fig. 9 σ_X/P–U_p Hugoniot relationship for printed PLA plus hydrodynamic response based on Eq. 5

PLA appears to strengthen behind the shock front suggesting material strengthening (τ) according to the relationship in Eq. 6 [29], Similar response where divergence was observed between measured longitudinal stress and calculated hydrodynamic pressures has been recorded with other polymers such as PE, PCTFE and PVC [6] where large deviations were seen. Although, it's interesting to note that Wood et al. [14] observed no deviation between the hydrodynamic and experimental measured parameters for SC-1008 at pressures below 4.00 GPa, showing that such a response is not guaranteed—although, above 4 GPa, deviations from the hydrostat were observed suggesting potential material strengthening.

$$\sigma_x = P + \frac{4}{3}\tau. \tag{6}$$

Recorded lateral gauge traces are presented in Fig. 10 with the corresponding stresses noted on each trace. All traces reveal some similarities; a rapid rise to the Hugoniot stress signifying shock has been induced in the material and a subsequent descent in the trace due to the interaction of the reflected waves with the incident. However, it appears that the response from the different gauge traces shows some marked differences. The recorded gauge traces at 363 and 822 m/s reveals that the lateral stress is decreasing. This implies that the material hardens behind the shock front, following Eq. 3. However, we have also observed increasing lateral stresses with the trace labelled 0.86 GPa and undulating stress in the 0.41 GPa trace. The reason for the latter trace is not clear but the authors believe that this is likely a result of the layers of air and material which the shock fronts meet as it travels (as it equilibrates) along the lateral halves of the target in view of the concentric pattern employed in the FDM built parts. This can be verified by performing a similar experiment using the bulk material. However, usefully, the decreasing lateral stresses recorded

in the 1.09 and 0.18 GPa traces, reveals that the material is hardening behind the shock front, consistent with other polymeric material, such as PMMA [7] and Polycarbonate [30]. This has been attributed to an increase in the proximity of molecular components, arising from the densification of molecules, with strong attractive bonding and steric [31] entangling which tends to resist further strain with time [24].

Another interesting feature is the gauge response time. It was observed that the time taken for the gauge to respond differs with impact velocity. It was expected that the higher impact velocities will produce lower response time but this is not completely seen here. The highest response time of 2.95E−7s was recorded for the highest impact velocity of 822 m/s followed closely by 2.56E−7s recorded at 498 m/s and 1.008E−7s response time for the 739 m/s impact velocity shot. Although differences between response time are insignificant, the authors believe the variations are due to possibly misalignment of the gauges in the lateral half of the target. A slight misalignment of the gauge could increase the response time because of the time it takes for the shock to equilibrate across the gauge length. Although the initial rise in the gauge traces has been attributed elsewhere to gauge equilibrium [32], essentially, polymer densify to large strain against weaker inter-chain Van-der-Waals [24] forces before material begin to exhibit a steady state behind the shock front. This implies that the stress state stability can only be achieved once the polymer has been loaded to compression at which the carbon atoms interact at a maximum density which suggests that rate of compression determines the amplitude and time to stable state. At lower stresses such as that observed in the 0.405 GPa, the printed PLA takes more time to equilibrate to the stable state. As such, the effect of densification, which also includes closure of the pores and rearrangement of the molecule to a fully dense state is more visible at lower stresses.

The shear strength data calculated from Eq. 3, using lateral stress gauges at 4 mm from the impact surface is presented in Table 5.

From Table 5, it is apparent that shear strength increases with increasing impact stresses in agreement with similar polymeric materials [7]. The lateral stresses immediately behind the shock front have been used, along with the known longitudinal stresses to determine the shear strength of the printed PLA. Usefully, the shear strength can be employed to help define the elastic–plastic transition. Above the elastic limit, the material behaves plastically and vice versa. By comparing the yield strength of the material to an elastic prediction given in Eq. 7, the Hugoniot Elastic Limit (HEL) can be obtained. This technique has been previously validated in Ref. [7] and employed to determine the HEL of PMMA. Employment of the technique in the determination of the shear strength is presented in Fig. 11. The elastic behaviour is represented by the solid line according to Eq. 7 [24].

$$2\tau = \frac{1-2v}{1-v}\sigma_x \tag{7}$$

where "v" is the poisons ratio. A linear line of best-fit has been put through the measured stress which intercepts the elastic prediction at longitudinal stress of ~ 0.9 Gpa. This can be taken as the Hugoniot Elastic Limit. In comparison with similar polymeric material like PMMA where the elastic limit has been placed in the range ~ 0.7–0.9 GPa. It is pertinent to note that the specimens employed here were fabricated with the build direction perpendicular to the shock direction and considering the fact that the mechanical properties of FDM built parts varies with built parameters [33] as well as the bulk material, the elastic limit obtained may vary with the different print settings and the bulk material; although this is only speculative.

From Fig. 11, it is apparent that shear strength increases with stress, as with other similar polymeric materials, PE and PVC. It is however interesting to note that the measured HEL of PLA is within similar range with PMMA which has been shown to have higher strength than basic polymers (particularly PE and PVC). This could be attributed in some ways to steric effect, arising from large chain structure due to the presence of multiple side chains and the presence of electronegative atom in the side group chain. While the presence of oxygen increases the electronegativity, allowing polar attraction to increase the bond strength, it's very likely that the dynamic response is controlled majorly by

Table 5 Experimental conditions and results of lateral stress gauges at 4 mm from the impact face

Flyer thickness (mm)/material	Impact velocity (m/s)	$\sigma_x(GPa)$	$\sigma_y(GPa)$	2τ (Gpa)
10/Cu	363	0.90	0.18	0.72
10/Cu	478	1.32	0.41	0.91
10/Cu	739	2.54	0.86	1.68
10/Cu	822	2.99	1.09	1.90

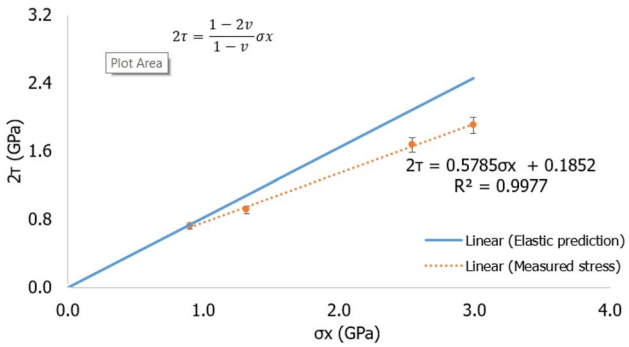

Fig. 11 The Shear strength versus longitudinal stress for Printed PLA

the interaction between adjacent polymer chains emanating from the inclusion of Methyl group and oxygen to the polymer chain, causing further tangling of the polymer chain structure.

Conclusion

Using the plate impact experiments, the dynamic response of 3D printed polylactic acid has been investigated over the impact velocity range of 200–900 m/s (corresponding to impact stresses of 0.30 to 4.00 GPa, respectively). A total of six plate-impact experiments were undertaken to determine the Hugoniot of commercially produced 3D printed PLA via the filament deposition technique. Both linear and non-linear Hugoniot was considered with the non-linear R^2 value tending to 1, giving it a non-linear equation of the form $U_s = 1.28 + 3.05U_p - 1.09U_p^2$. This non-linearity appears indicative of the underlying material structure. A change in slope in the plot of shear strength (2τ) at 0.7 GPa against longitudinal stress at 0.90 ± 0.05 GPa within similar range with PMMA was observed, attributed to both the increase chain entanglement and electronegativity of the polymer chain structure via the addition of methyl and oxygen atom respectively to the polymer chain.

Acknowledgements The authors wish to thank Mr Andrew Roberts and Mr David Miller for their assistance in undertaking the experimental work. This work was conducted as part of the PhD studies of the primary author, Henry Agu who was sponsored by Nigerian Air Force Grant under the leadership of Air Marshal Sadiq Abubakar, the Chief of the Air Staff.

Author Contributions HA designed, coordinated this research and drafted the manuscript, GJ Appleby-thomas conceived and carried out data analysis, AH participated in the research coordination and DW assisted with the analysis of the data obtained. The authors read and approved the final manuscript.

Funding This research was funded by the Chief of the Air Staff, Nigerian Air Force under the Grant Number 2016/2901/PHD.

Availability of Data and Materials All datasets and software used for supporting the conclusion of this article are available on demand.

Compliance with Ethical Standards

Conflict of interest The authors declare they have no competing interests.

References

1. Lasprilla AJR, Martinez GAR, Lunelli BH, Jardini AL, Filho RM (2012) Poly-lactic acid synthesis for application in biomedical devices—A review. Biotechnol Adv 30(1):321–328
2. Field JE, Walley SM, Proud WG, Goldrein HT, Siviour CR (2004) Review of experimental techniques for high rate deformation and shock studies. Int J Impact Eng 30(7):725–775
3. Giordano RA, Wu BM, Borland SW, Cima LG, Sachs EM, Cima MJ (1997) Mechanical properties of dense polylactic acid structures fabricated by three dimensional printing. J Biomater Sci Polym Ed 8(1):63–75
4. Song Y, Li Y, Song W, Yee K, Lee KY, Tagarielli VL (2017) Measurements of the mechanical response of unidirectional 3D-printed PLA. Mater Des 123:154–164
5. Carneiro OS, Silva AF, Gomes R (2015) Fused deposition modeling with polypropylene. Mater Des 83:768–776
6. Millett JCF, Brown EN, Gray GT, Bourne NK, Wood DC, Appleby-Thomas G (2016) The effects of changing chemistry on the shock response of basic polymers. J Dyn Behav Mater 2(3):326–336
7. Millett JCF, Bourne NK (2000) The deviatoric response of polymethylmethacrylate to one-dimensional shock loading. J Appl Phys 88(12):7037–7040
8. Carter W, Marsh P Hugoniot equationof state of polymers
9. Bourne NK (2016) On the shock response of polymers to extreme loading. J Dyn Behav Mater 2(1):33–42
10. Kim E, Shin Y-J, Ahn S-H (2016) The effects of moisture and temperature on the mechanical properties of additive manufacturing components: fused deposition modeling. Rapid Prototyp J 22(6):887–894
11. Sood AK, Ohdar RK, Mahapatra SS (2010) Parametric appraisal of mechanical property of fused deposition modelling processed parts. Mater Des 31(1):287–295
12. Gebisa AW, Lemu HG (2019) Effect of process parameters on compressive properties of ULTEM 9085 Produced by FDM Process, p. V002T02A056
13. Popovich A, Sufiiarov V, Polozov I, Borisov E, Masaylo D, Orlov A (2016) Microstructure and mechanical properties of additive manufactured copper alloy. Mater Lett 179:38–41
14. Wood DC, Hazell PJ, Appleby-Thomas GJ, Barnes NR (2011) Shock behaviour of a phenolic resin. J Mater Sci 46(18):5991–5999
15. Hazell PJ, Appleby-Thomas GJ, Trinquant X, Chapman DJ (2011) In-fiber shock propagation in Dyneema®. J Appl Phys 110(4):043504
16. Appleby-Thomas GJ, Hazell PJ, Stennett C, Cooper G, Helaar K, Diederen AM (2009) Shock propagation in a cemented tungsten carbide. J Appl Phys 105(6):064916
17. Appleby-Thomas GJ, Hazell PJ, Sheldon RP, Stennett C, Hameed A, Wilgeroth JM (2014) The high strain-rate behaviour of selected tissue analogues. J Mech Behav Biomed Mater 33(1):124–135
18. Millett JCF, Lowe MR, Appleby-Thomas G, Roberts A (2016) The mechanical and optical response of polychlorotrifluoroethylene to one-dimensional shock loading. Metall Mater Trans A 47(2):697–705
19. Ahn SH, Montero M, Odell D, Roundy S, Wright PK (2002) Anisotropic material properties of fused deposition modeling ABS. Rapid Prototyp J 8(4):248–257
20. Parker NG, Mather ML, Morgan SP, Povey MJW (2010) Longitudinal acoustic properties of poly(lactic acid) and poly(lactic-co-glycolic acid). Biomed Mater 5(5):055004
21. Wood A (1930) A textbook of sound: being an account of the physics of vibrations with special reference to recent theoretical

and technical developments by Wood, A. B. (Albert Beaumont). Macmillan, New York
22. Rosenberg Z, Yaziv D, Partom Y (1980) Calibration of foil-like manganin gauges in planar shock wave experiments. J Appl Phys 51:3702
23. Meyers MA (2014) Dynamic behavior of material. Wiley, Hoboken
24. Bourne N (2013) Materials in mechanical extremes; fundamentals and application. Cambridge University Press, Cambridge
25. Barker M, Hollenbach LE (1970) Shock-wave studies of PMMA, fused silica, and sapphire. J Appl Phys 41:4208–4226
26. Dattelbaum DM, Coe JD (2016) **The dynamic loading response of carbon-fiber-filled polymer composites**. In: Silberschmidt VV (ed) Dynamic deformation, damage and fracture in composite materials and structures. Woodhead Publishing, Sawston
27. Davison L, Graham RA, Davison L, Graham RA (1979) Shock compression of solids. Phys Rep 55(4):255–379
28. Hazell PJ (2016) Shock loading of polymer composites. Elsevier, Amsterdam
29. Rosenberg Z, Bourne NK, Millett JCF (2007) On the effect of manganin gauge geometries upon their response to lateral stress. Meas Sci Technol 18(7):1843–1847
30. Millett JCF, Bourne NK (2006) Shock and release of polycarbonate under one-dimensional strain. J Mater Sci 41(6):1683–1690
31. Shepherd CJ, Appleby-Thomas GJ, Wilgeroth JM, Hazell PJ, Allsop DF (2011) On the response of ballistic soap to one-dimensional shock loading. Int J Impact Eng 38(12):981–988
32. Painter JD et al (2012) On the importance of encapsulation environment for lateral gauges. AIP Conf Proc 1426:454–457
33. Alharbi N, Osman R, Wismeijer D (2016) Effects of build direction on the mechanical properties of 3D-printed complete coverage interim dental restorations. J Prosthet Dent 115(6):760–767

Appendix 2

Comparison of the microstructure of machined and laser sintered shaped charge liner in the hydrodynamic regime

Journal of Dynamic Behavior of Materials
https://doi.org/10.1007/s40870-019-00213-y

RESEARCH PAPER

Comparison of the Microstructure of Machined and Laser Sintered Shaped Charge Liner in the Hydrodynamic Regime

H. O. Agu[1] · **A. Hameed**[1] · **G. J. Appleby-Thomas**[1]

Received: 20 April 2019 / Accepted: 18 July 2019

Abstract
To gain further insight into the mechanisms underlying jet formation and elongation of laser sintered shaped charge liners under high strain rate deformation, Cu–Cr–Zr alloy liners fabricated by selective laser sintering process were deformed by explosive detonation. Their as-manufactured (liner) and resultant (slug) microstructure have been investigated in comparison with those of traditional machined liners employing both optical and scanning electron microscopy. The resultant slug microstructure of both machined and laser sintered liners revealed a smaller refined equiaxed grain size consistent with traditionally fabricated liners, characteristic of dynamic recrystallization. The disappearance of the (originally present) pores in the post-shot/recovered material microstructure was observed for laser-sintered liners. Comparison of the forward and rear region of the slug revealed variations in liner deformation, a result attributed to temperature variation across the slug. In contrast with the machined liner, a unique feature of precipitation, observed in the ending (slug) microstructure of the laser sintered liner is indicative of the associated extreme high strain and strain rate liner deformation which occurred during slug formation. The precipitates are likely compounds of Chromium and Zirconium which are constituents of the laser sintered copper alloy—the first time this observation is reported. This study provides a link between post charge evolution microstructure and liner manufacturing processes, potentially providing a new route to help optimise jet formation and effectiveness.

Keywords Liner · Laser sintering process · Shaped charge · Copper · Microstructure · Temperature

Introduction

It has become widely accepted that shaped charge liners undergo dynamic recrystallization during liner collapse and jet formation to produce refined microstructures [1–3]. Under high strain/strain rate conditions, severe plastic deformation of the liner gives rise to nucleation and growth of new grains by continuous accumulation of dislocations [4]. During this process, low angle boundaries are being transformed into high angle boundaries accompanied by subdivision of original grains into small, sometimes equiaxed grains with significant microstructural refinement [5]. Although the resultant microstructure is controlled by the degree of deformation [1], it is influenced majorly by the strain/strain rate as well as the deformation temperature (itself a function of the nature of load on the liner) which varies along the jet length [5, 6]. This variation, result in segments of the ending (slug) microstructure having higher deformation with apparently more refined microstructure than others [7]. Guo et al. observed that, in spite of the small equiaxed microstructure observed in recovered Tungsten slugs, significant variations in grain size were recorded at the centre, 0.5 and 1 mm away [7]. In short, the grain size of the slug appeared to change linearly outward with the smallest grains at the centre and the largest in the outer regions. A similar observation was reported by Murr et al., [2], where different grain sizes were observed at three concentric rings with the middle ring having the largest. Usefully, analysis of hydrocode simulations of a stretching shaped charge jet has revealed higher temperatures [6] and strain at the centre indicative of a higher degree of deformation. A relationship between the starting liner grain size (D_0) and the ending grain size (D_s), revealed that smaller starting liner grain sizes produce correspondingly smaller grain size ratios [1] because lower starting grain sizes are associated with dramatically higher levels of liner volumetric stored energy [8]. This implies that the

✉ H. O. Agu
henry.agu@cranfield.ac.uk

[1] Centre for Defence Engineering, Cranfield University, Defence Academy of the UK, Shrivenham SN6 8LA, UK

Published online: 30 July 2019

ending grain size is influenced not only by the starting grain size but by the degree of deformation.

In addition to the starting liner microstructure, other factors such as the liner material properties, particularly; thermal conductivity and heat capacity as well as processing route have been reported to have a significant influence on the ending microstructure [7]. As an example, Murr et al., [9] observed that the grain size ratio between the starting and ending microstructure of Tantalum differs widely from that of Copper (by a ratio of 10:1.5), something the authors attributed to inherent liner material properties. In a separate study, comparing differences in processing technique, it was observed that equiaxed and well-annealed Tantalum both showed similar slug microstructural features which were consistent with a forged Tantalum liner, but with variations in average grain size. While the forged liner showed a resultant grain size of 35 µm, the equiaxed and well-annealed liner averaged 5 µm. With regards to the effects of processing routes, similar microstructural differences have been reported for several processing techniques [10]. A case in point is the difference observed between OFE copper and electrolytic tough pitched copper (ETP). In contrast to OFE copper, the ETP copper showed significant voids [11], suggesting an effect of processing technique on the ending (slug) microstructure. Surprisingly, while several liner processing techniques has been examined [10], liners fabricated by selective laser sintered (SLS) process have yet to be considered. This study consequently deals with the characterization and analysis of slug recovered from explosively deformed laser sintered liner. In the present work, liners fabricated by both conventional machining and the selective laser sintering process were deformed by explosive loading to form jet and slug. We examined the microstructures of the liners and resultant slugs in comparison with machined OFC copper liner employing both optical and scanning electron microscope (SEM).

Experimental Method

Oxygen free copper (OFC) and CuCrZr alloy of grade C18150 were employed for the production of the machined and laser sintered liners respectively. The chemical composition of CuCrZr alloy of grade C18150 employed is detailed at Table 1.

Table 1 The chemical composition of CuCrZr grade C18150

Element	Content (%)
Copper (Cu)	98.12–99.27
Chromium (Cr)	0.5–1.2
Zirconium (Zr)	0.03–0.3

The liners design used was of 50-mm charge diameter and 1.5 mm liner wall thickness and was inclined at 42° (cone angle). The sintered liner was solution annealed at 960 °C for 3 h, water quenched and heat treated at 460 °C for 3 h, while the machined liners were used as produced. Figure 1 shows images of the produced liners. The liners were deformed in the plastic and hydrodynamic regimes upon detonation with Plastic Explosive Number 8 (PE8). The jet tip velocity produced by the machined liner was determined independently using AUTODYN 2D hydrocode to be 8.6 km/s. The jet was allowed to penetrate a mild steel target placed 3 charge diameters away. After firing, the resultant slugs were recovered, sectioned transversely to the slug axis, prepared and observed optically and in scanning electron microscope (SEM). Metallographic preparation involved successively finer (320 grit and then 800 grit) silicon carbide grinding followed by rough polishing using 3-micron diamond suspension and then a final polish using an alumina suspension. Ammonium hydroxide/hydrogen peroxide etch was then employed before both optical and SEM analysis (using an Olympus BX53M optical and Scanning Electron Microscope, Hitachi type SU3500 respectively).

For grain size measurement, three standard ASTM approaches were considered. These were: a comparison procedure which involved a direct comparison of the grain structure to a series of the graded image superimposed over the microstructure; the planimetric (or Jeffries) procedure which requires actual counting of the number of grains within a known area and the Intercept procedure. These approaches have been summarized in Ref. [12]. Of the three approaches, the intercept procedure which is faster and more convenient than the planimetric method was employed to determine the grain sizes of the starting (liners) and ending microstructure. Further, the intercept method has demonstrated reliability and efficiency for the determination of grain size and is particularly recommended for grains that depart from uniform equiaxed form [12]. The Heyn Lineal Intercept procedure backed by Image J software which

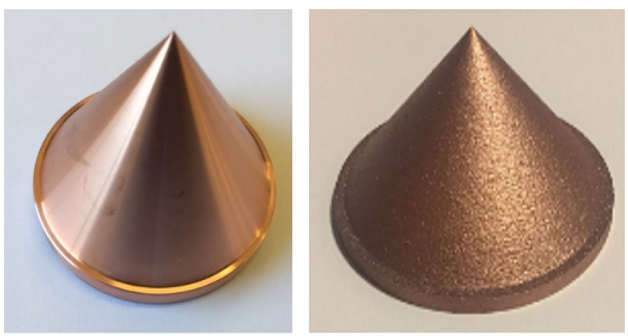

Fig. 1 Images of machined OFC liners (left) and Laser sintered liner (right) in their as-produced state

employs long straight lines was used. To ensure precision, counting was done on three long lines with low magnification from which the average was taken.

Results and Discussion

Figure 2 shows optical micrographs of the machined and laser sintered copper liner before deformation. The microstructure of the laser sintered liner (Fig. 3b) consists of elongated grains along the build direction. The density of the machined liner was measured using an XS 105 dual range analytical balance from Mettler Toledo as 8.91 ± 0.02 g/cm^3 while the laser sintered liner was found to be 8.77 ± 0.02 g/cm^3, comprising approximately 98–99% copper with 1–2% Chromium and Zirconium. The average measured grain size of the machined liner was ~ 54 µm ± 4 µm while the laser sintered liner after being solution annealed at 960 °C for 3 h, water quenched and heat treated at 460 °C for 3 h, exhibited elongated grain sizes ranging from circa 20 and 70 µm ± 6 µm along the horizontal and vertical axis respectively; an indication of a partially recrystallized structure arising from the sintering and post-production processes on the fabricated part. Essentially, fusion heat caused in situ recrystallization during the building process [13], resulting in partial recrystallization of the microstructure. Of particular significance is the presence of pores which is one of the common defects in SLS liners [14] and which are observable in the SEM image in Fig. 3. The pore sizes and shapes are irregular with no distinct pattern. In addition, there are characteristic lines running diagonally which likely correspond to the layer boundaries in areas of their fusion during sintering ('scan tracks'); this supposition is backed by their separation which nominally correspond to the laser sintered machine manufacturing tolerance of separation of ca. 100 mm per-sweep. However, it is not known whether the grain structure or chemical composition along the track would differ from other regions. Further work may be required in this regard to ascertain this.

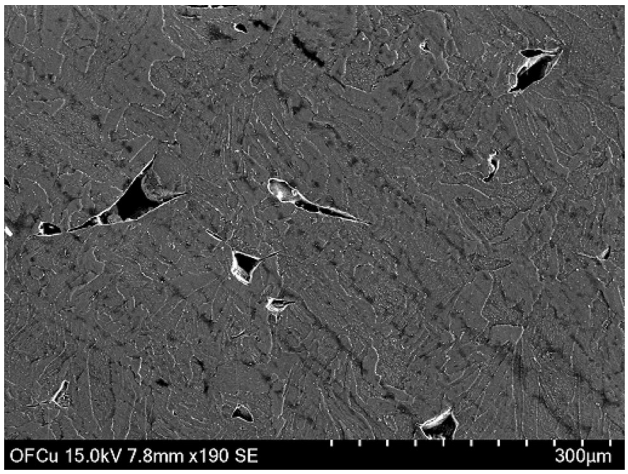

Fig. 3 SEM observation of the laser sintered liner microstructure revealing scan tracks and irregularly shaped pores before deformation

Optical Metallography of Slug Recovered from the Machined Copper Liner

It is pertinent to note that unlike the soft recovery process where the jet/slug is recovered in flight, interaction between the jet and mild steel plate could increase the strain and generate higher deformation temperature in the jet/slug, leading to higher grain refinement. Figure 4 shows optical metallographic observations of both the starting and ending microstructures of the machined copper liner and recovered slug for comparison. It is very convincing that there is a significant reduction in the grain size of the recovered slug compared to the starting liner material. The measured

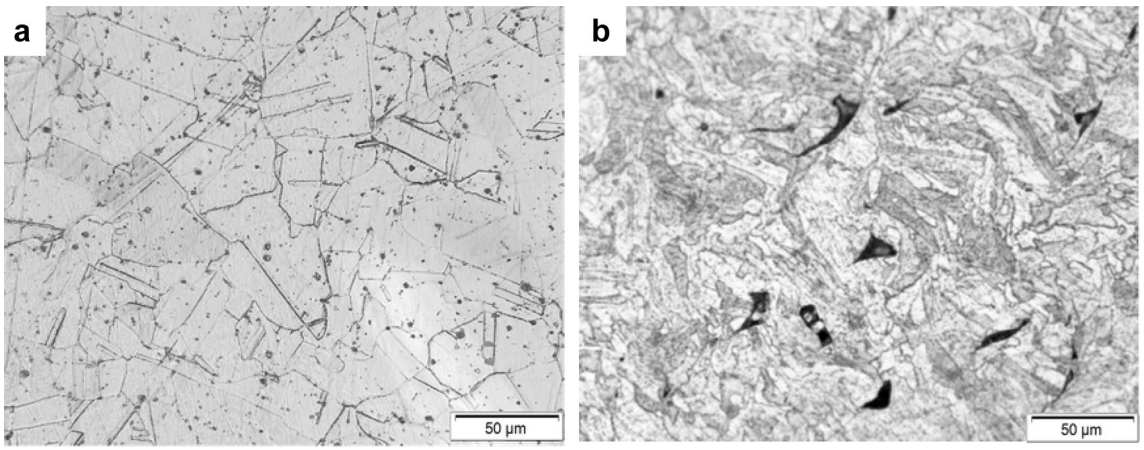

Fig. 2 Optical Images of the starting microstructure of **a** machined OFC Copper liner and **b** laser sintered Copper liner (×20 respectively)

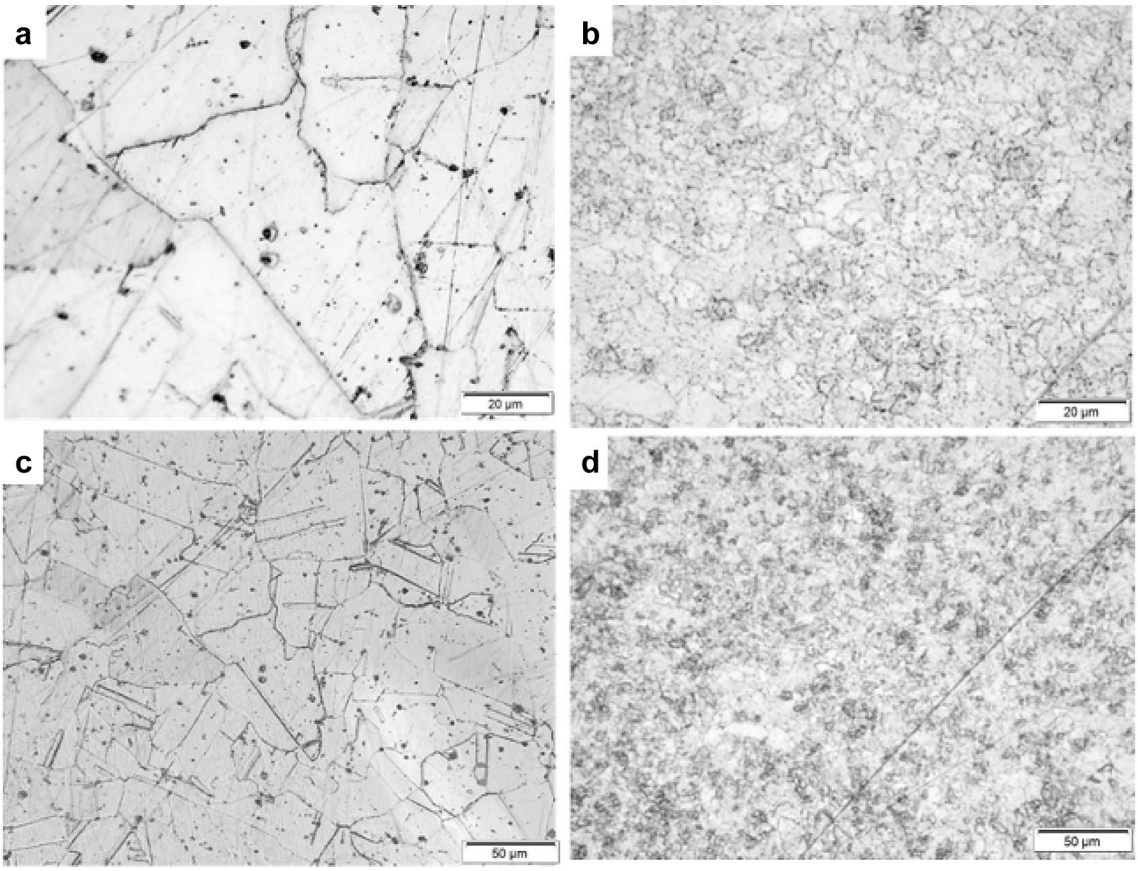

Fig. 4 Comparison of the initial and final microstructure of machined copper liner and slug; **a** The microstructure of starting copper liner × 50. **b** The microstructure of recovered copper slug revealing equiaxed microstructure and reduction in grain size × 50. **c** The microstructure of starting liner × 20. **d** Recovered copper slug x20

grain size of the recovered slug averaged 6 µm ± 2 µm This phenomenon (grain size reduction/refinement) has been reported extensively elsewhere [1, 8], consistent with the concept of dynamic recrystallization occurring at such high strain rates. In fact, Murr et al., observed a reduction in grain size by a factor of 10 for copper shaped charge liners. In this study, the measured recovered material grain sizes were equiaxed, consistent with previous work [2, 15] and varies from the initial liner grain size (an average of 54 µm) by a factor of 9. A similar study on Tungsten shaped charges liners revealed the role of dislocations in the refinement of the microstructure during dynamic recrystallization suggesting a link between strain and grain size of the recovered slug [7].

We have also observed variations in grain size refinement in various sections of the recovered slug. As an example, the forward (tip region) and the rear sections of the recovered slug detailed in Fig. 5 shows some variation in the grain sizes. Although slightly, it is apparent that there is a more refined microstructure with smaller grain sizes in the rear (Fig. 5a) of typical average grain size of 4 ± 2 µm than in the forward section (Fig. 5b) where a typical average grain size of 7 ± 2 µm is apparent (please note that no particular attention was placed on the distance/depth from the centre axis at which the samples were extracted from both positions). This provides further proof of the variation in the degree of deformation in the microstructure across the resultant slug. This observed apparent variation in the grain size refinement at different sections of the slug has been reported severally elsewhere [2, 9, 16]. However, in all the recovered slug sections for the machined copper liner, no melt-related phenomenon was observed on the samples analysed—strongly suggesting hydrodynamic behaviour (flow, rather than melt).

Optical Metallography of Slug Recovered from Laser Sintered Liner

Figure 6 shows an image of the recovered laser sintered slug while Fig. 7 shows optical metallographic observations of the starting and ending microstructures of the laser sintered copper liner and slug for comparison. In contrast with the elongated grains observed along the build direction of the starting liner microstructure, the recovered slug shows a more refined/microstructure with a reduction in the

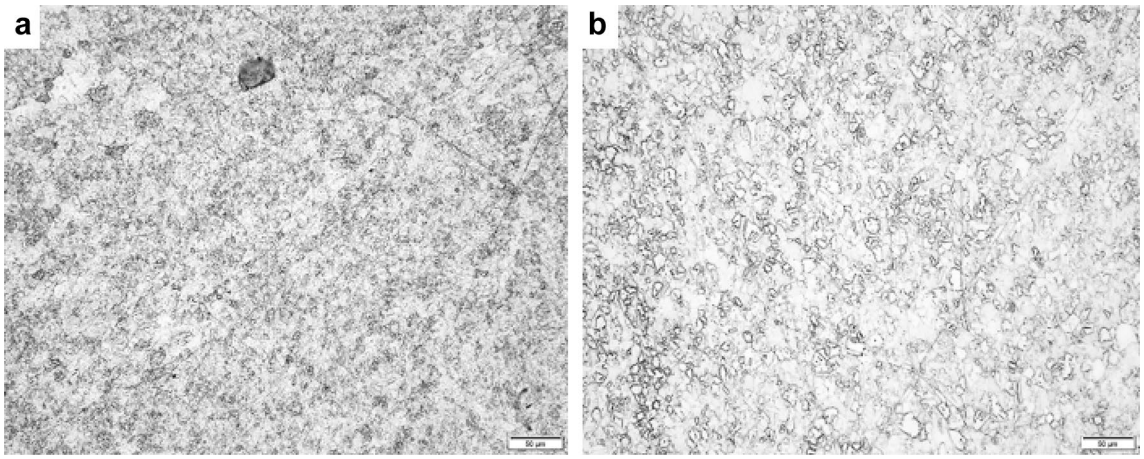

Fig. 5 Optical micrograph of slug recovered from the machined copper liner experiment. **a** The rear region (×20). **b** The forward region (×20)

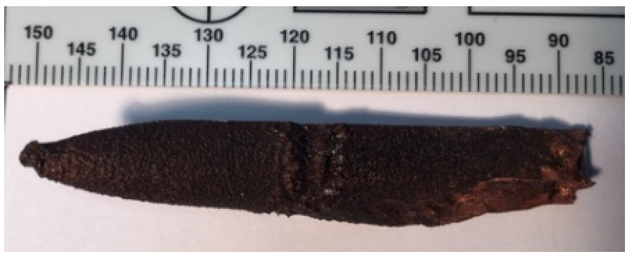

Fig. 6 Recovered laser sintered slug (mm)

average grain size from 20 ± 3 µm in the vertical direction to an average grain size of ~ 14 µm. As the final grain size is dependent on the initial grain size, the low reduction in variation between the initial and ending microstructures is attributed to the already reduced starting grain size resulting from the post-processing of the sintered liner part. More importantly, the pores which were observed in the starting liner are completely absent in the slug. While it is difficult to rule out any form of melting or melt-related phenomenon as reported in previous shaped charges studies [5], several precipitates, distributed randomly in the microstructure were visible and concentrated along the grain boundaries. A similar observation has been reported in Ref. [13] of a sintered CuCrZr alloy during high-temperature annealing. X-ray diffraction analysis of the precipitate revealed a high content of Cr and Zr with dimensions ranging from the nm to µm scale without forming any intermetallic compounds. While Cu_8Zr_3 precipitates were formed at higher temperatures, in contrast with $Cu_{10}Zr_7$, the variation in behaviour of the precipitates suggests the influence of temperature and annealing condition on the precipitation pattern. As a consequence, the apparent high temperature encountered during the jet formation process is a possible cause of the precipitation observed in this study. Whether the precipitate is a result of melt or melt related phenomenon is a subject of discourse. However, it is pertinent to point that, no melt or melt-related phenomenon has been reported in previous shaped charge studies [7] except for electroformed nano-sized nickel liners where melting was observed due to the high volumetric stored energy associated with small grains [8]. Hence, even though the liner flows hydrodynamically ('as fluid') under impact loading, it remains solid because the liner is not heated to its melting temperature [17]. In fact, at such extremely high strain/strain rate the liner deforms plastically and is drawn in the form of a wire with diameter much lower than the initial diameter. Under such conditions, it is very likely that the precipitates of Chromium and Zinc are evolved as Chromium is not soluble in Copper. Previous work on the heat treatment of CuCrZr at 450 °C indicates a high content of Cr and Zr located at the melt pool boundaries [13], something similar to the slug microstructure observed here which indicates that the particles have formed during the solidification of the melt pool. As such, we speculate that the formation of precipitates in the slug is an indication of adiabatic temperature rise during liner collapse and jet formation. However, as this is only a speculation, further work may be required may be required to confirm the compound formed.

A particularly interesting phenomenon is the further grain size reduction and precipitates observed in the rear slug (Fig. 7c) in comparison with the forward section; similar behaviour observed in the ending microstructure of machined liners. Although the depth from which the samples were collected were not considered (in both liner processing techniques), it is only an indication of the degree of deformation in various sections of the slug.

A comparison of the final/ending microstructure of the machined and laser sintered liners in Fig. 8 revealed two different ending microstructures. Firstly, as mentioned

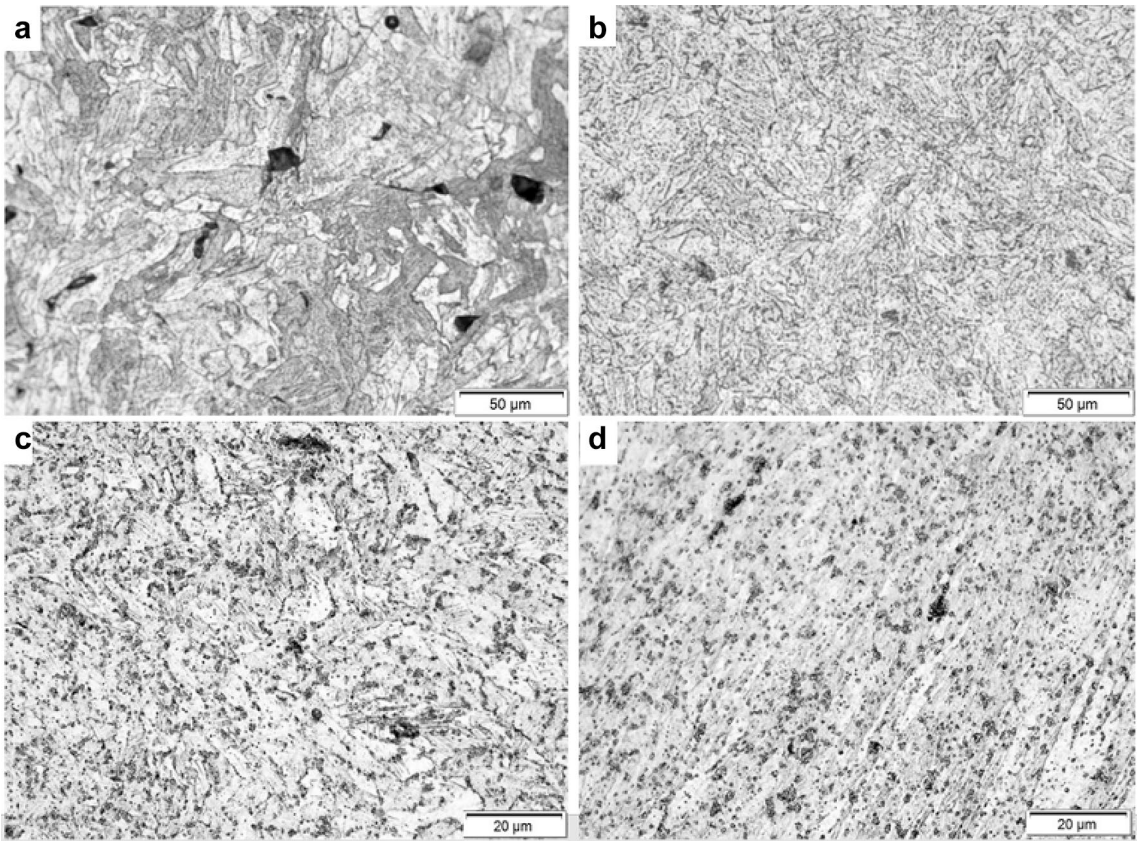

Fig. 7 Comparison of the initial and final microstructure of laser sintered copper liner and slug; **a** Starting laser sintered copper liner, **b** recovered slug, **c** forward region of recovered laser sintered copper slug. **d** Rear region of recovered laser sintered slug showing several precipitates. Magnifications are the same

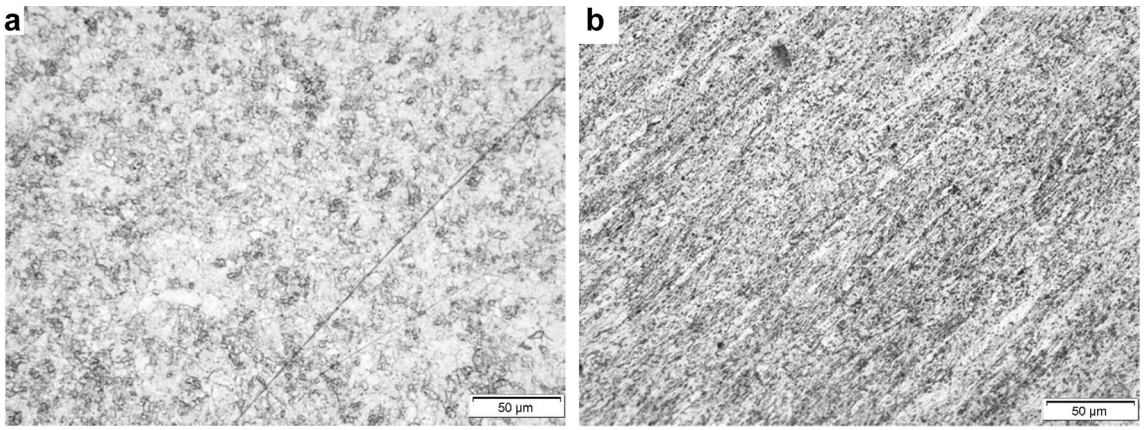

Fig. 8 Comparison of the ending microstructure of machined and laser sintered liner

earlier, while the machined liners showed an equiaxed grain size distribution, the microstructure of the resultant slug from the laser sintered liner showed the presence of precipitates distributed randomly. Although, the precipitates formed were not investigated in this study, previous work has shown that because of the low solubility of Chromium in Copper, the formation and growing of Chromium precipitates especially at grain boundaries (apparent in the recovered slug here) is triggered by high temperatures and exposure times [13] which suggest the

effect of temperature on liner deformation evaluated in the subsequent section.

Measurement of the Jet Temperature

The first attempt to measure the temperature of a shaped charges jet was by Von Holle and Trimble [17]. Employing infrared radiometry technique, properties of 81.3 mm diameter copper shaped charge jet loaded with Comp. B or Octol were determined. An average recorded jet temperature of 428 °C (701 K) was measured for Comp. B, while 537 °C (810 K) was recorded for Octol [18]. Subsequent measurement recorded by Lassila found an exterior jet temperature of 500 °C using CALE—an arbitrary Lagrange–Eulerian computer code [19]. Essentially, jet heating results from the interaction of the detonation waves with the liner (grazing detonation), plastic work during liner collapse, and jet elongation [19, 20]. In this study, an Autodyn 2D [21–23] numerical algorithm was used to study temperature variation in shaped charges. The use of Autodyn 2D to measure jet temperature was employed by Elshenawy et al., for a Zirconium shaped charge jet but was limited to the jet temperature for calculating the break-up time of Zirconium liners [6]. Here, the temperature at different sections of the jet was calculated to proffer a possible explanation to the variation in grain refinement in various sections of the jet. The hydrocode temperature calculations were first validated by modelling a BRL-81.3 mm shaped charge [24] in the multi-material Eulerian grid, employing the complete Mie–Gruneisen form of the equation of state which describes the heat capacity variations and thermodynamic properties with a reference temperature of 300 K and heat capacity 3.83 e–4 J/Kg K [25]. We derived the temperature of the jet due to severe plastic work, during jet elongation (as this has been shown to produce higher temperature increase in the jet), rather than the grazing detonation wave (occurring during liner collapse) [20] for an 81.3 mm shaped charge. The longitudinal section of Autodyn 2D shaped charge layout is shown in Fig. 9.

The jet temperature was recorded at three different times: 36 µs, 45 µs and 54 µs respectively during the jet elongation regime. From the resultant jet profiles in Fig. 10, it is apparent that temperature varies across the jet length with the highest temperature (up to 1500 K) on the jet axis while the outer surface temperature ranges from 795 K (522 °C) to 905 K (632 °C).

When the temperature and time are plotted in Fig. 11, it was observed that the jet temperature rises initially to a peak before equilibrating at a steady temperature of 710 K (437 °C). This recorded temperature agrees well with the temperature recorded by Von Holle and Trimble (720 K) [17]. The high temperature recorded on the jet central axis is likely a result of the high dynamic pressure at the collision point as the liners interact with each other. This extremely high-temperature phenomenon at the jet centre axis could account for the unique liner deformation patterns reported in the region around the jet axis. For instance, metallurgical examination by Lassila et al., [19] of soft recovered copper jet particles and slug indicate that a central region of approximately 10% of the jet's diameter was molten. Baoxiang et al. observed a wave pattern around the centre axis of the jet microstructure, characteristic of fluid instability which was speculated to cause jet break up [26]. More interestingly, the presence of a central hole at the jet centre axis [26] which was postulated to account for an unexplained 6.5% density deficit [27] in stretching shaped charge jets [26] was noted. Although these phenomena were attributed to high dynamic pressure (around 70 GPa recorded at a distance less than 1 mm from the axis and decaying to an average of approximately 15 GPa), which tends to resist further compression

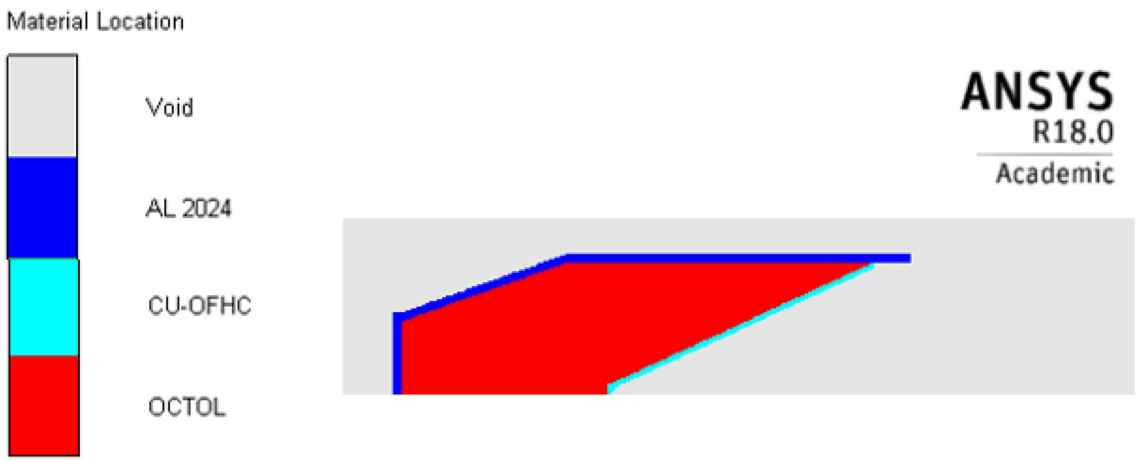

Fig. 9 Autodyn 2D Layout of an 81.3 mm charge diameter shaped charge in the multi-material Eulerian grid

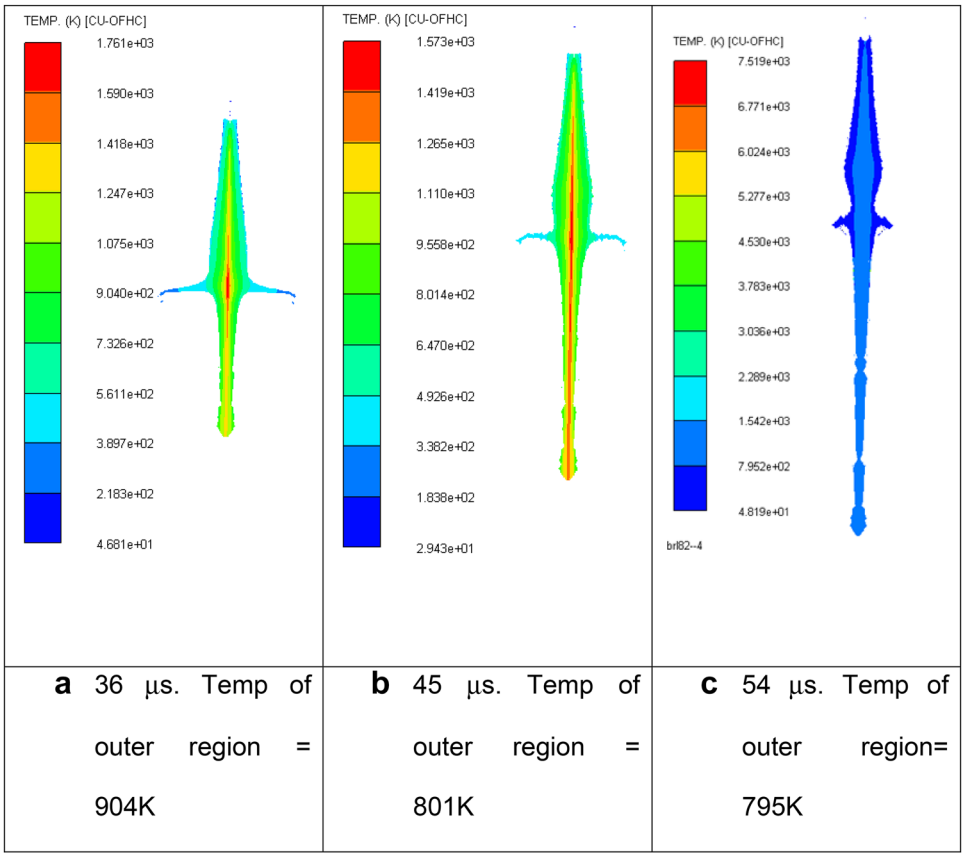

Fig. 10 Jet temperature for BRL 81.3 mm shaped charge at various times and before jet particulation

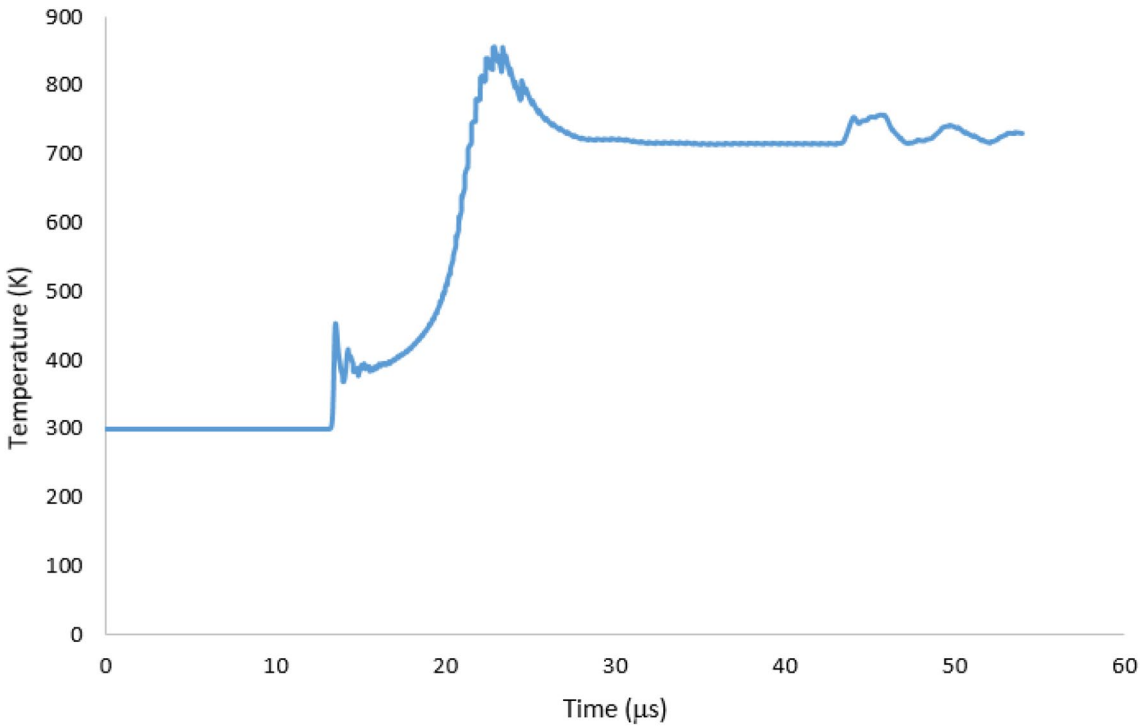

Fig. 11 Jet temperature variation with time recorded from Autodyn 2D simulation

of the liner towards the centre axis and possibly altering the deformation pattern [26], from the findings reported here, giving the high temperature recorded at the jet central axis, it is likely that the material in the central region of the jet and slug experiences melting (lasting for only a short time—a few microseconds) as the temperature's recorded are higher than the melting temperature of Copper—something observed by Lassila [19] to account for the 10% melt phenomenon recorded in her work. If this is true, and under such molten state, it is speculated that, the forward action of the travelling molten jet would invariably cause a corresponding backward motion of the fluid, leaving a space (centre hole in the jet and slug).

To verify temperature distribution across the jet length, moving temperature gauges were placed at the outer, middle and inner surfaces of the liner represented in Fig. 13. It is generally known that for conventional conical charges, the first 30–40% of the liner from the theoretical apex forms the tip of the jet [28]. Employing a simple Lagrangian coordinate, postulated by Carleone and Chou [21] in Fig. 12, we identified suitable positions of various segments of the jet and on the liner where our gauges were placed [21]. The axial liner position is described by coordinate "x" whereas the position of the jet is given by coordinate ξ in Eq. 1:

$$\xi(x,t) = \mathrm{Z}(x) + \left(t - t_o\right) V_j(x) \tag{1}$$

where $\mathrm{Z}(x)$ is the location of the formation, t_o is the time at which the liner element first arrives at the axis, and $V_j(x)$ is the jet velocity, which is a function of the liner position and time. Accordingly, we measured the jet temperature at various positions of the jet including the outer surface, mid-radius and jet centre. The temperature across the jet length was also evaluated by placing temperature gauges on defined

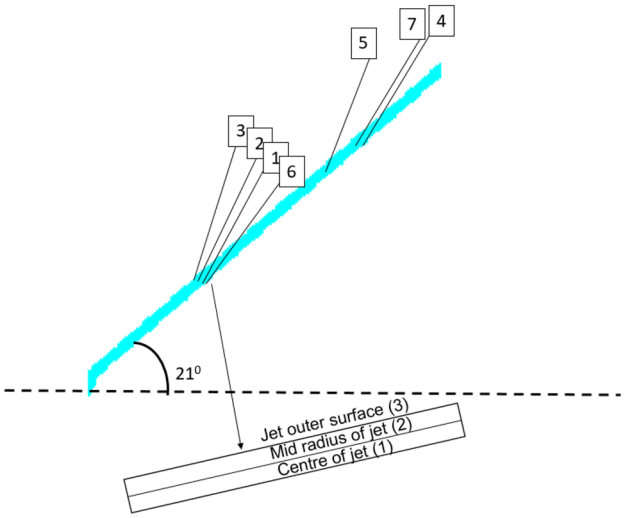

Fig. 13 The cross section of the liner showing gauge locations

areas on the liner as shown in Fig. 13 to obtain corresponding temperatures at the marked regions on the jet (Fig. 14).

From Fig. 15, it is apparent that the temperature across the jet width varies linearly outward. The highest temperature was recorded at the gauge trace closest to the inner centre axis (1100 K) and this was observed to decrease outward towards the surface, consistent with the jet profile (Fig. 9) suggesting that temperature decreases as the jet elongates. Hence the jet centre is heated higher than the outer surface providing evidence of temperature variation along the entire jet width with resultant variation in grain refinement.

To investigate how the temperature varies across the jet length, temperature gauges were placed at three different outer positions on the jet (gauges 4, 5 and 6, in Fig. 16). Adequate care was taken to ensure the gauges sat

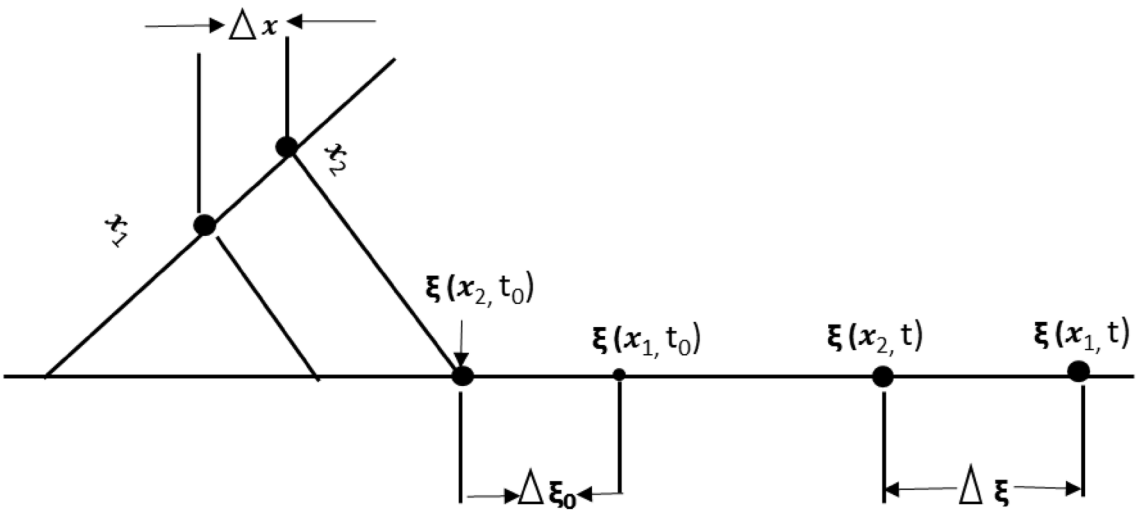

Fig. 12 Relationship between the liner coordinate × and the jet coordinate ξ adapted from Ref. [28]

Fig. 14 Corresponding gauge locations on the shaped charge jet during formation and elongation

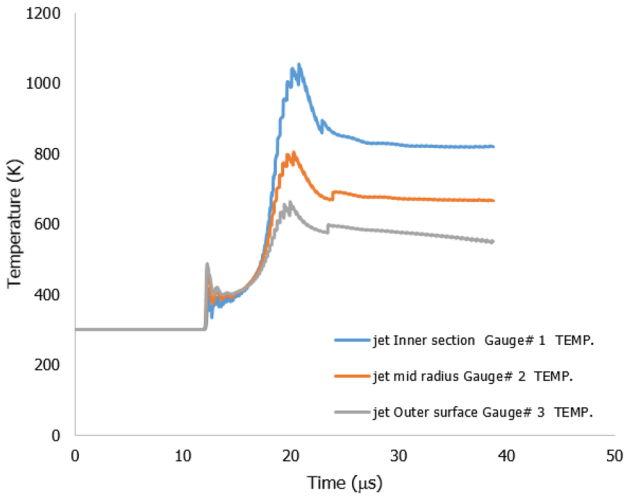

Fig. 15 The recorded temperature histories of tracers positioned at the outer middle and inner section of the liner

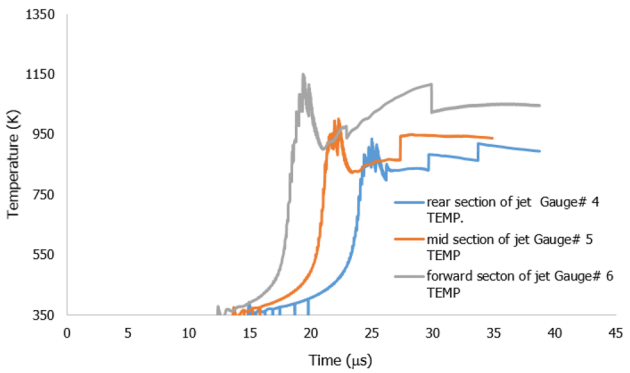

Fig. 16 The recorded temperature Histories at the forward, middle and rear sections of the jet

horizontally at the same depth on the outer surface. The highest temperature was found at the forward section of the jet and this decreases down to the rear as can be seen in Fig. 16; an indication of the temperature variation across the jet length. If this trend continues across the entire jet and slug length, it would therefore suggest that temperature across the outer surface of the jet length varies with the jet tip recording higher temperatures.

Conclusion

The starting microstructures for machined and laser sintered copper shaped charge liners have been compared with corresponding, recovered (ending) slugs—the first time the microstructure of recovered selective laser sintered slugs has been studied. It has been observed that:

a. Consistent with previous work [1, 2, 5, 9], a common feature of both processing techniques in terms of their end/post-employment microstructures is a reduction in grain size (slug), which is a classical feature of dynamic recrystallization.
b. Variation in grain refinement at different sections of the slug is an indication of differences in the degree of deformation attributed to temperature variation across the jet length and width.
c. According to jet temperature calculations, it has been shown that the jet central axis experiences a transient higher temperature exceeding the melting temperature of copper; this is speculated to account for the 10% melt reported by Lassila et al., [19], wave fluid like instability reported by Baoxiang et al., [26] and the observed hole in the centre of soft recovered jet.
d. The precipitates formed in the ending microstructure of recovered laser sintered slug are likely compounds of Chromium and Zirconium formed from an adiabatic temperature rise during liner deformation.

Acknowledgements Air Marshal Sadique Baba Abubakar is appreciated for sponsoring the PhD programme under which this project was carried out. The authors wish to thank Lt Col Liz Nelson for sponsoring the ATO study under which the shaped charge experiments were conducted. The authors would also like to acknowledge the support offered by the technical staff of the Schools' workshop in producing the shaped charge liners.

References

1. Murr LE et al (1995) Comparison of beginning and ending microstructures in metal shaped charges as a means to explore mechanisms for plastic deformation at high rates. J Mater Sci 30(11):2747–2758
2. Gurevitch AC et al (1993) Characterization and comparison of microstructures in the shaped-charge regime: copper and tantalum. Mater Charact 30(3):201–216
3. Murr LE, Shih H, Niou CS, Zernow L (1993) Dynamic recrystallization in the shaped charge regime. Scr Metall Mater 29:567–572
4. Sakai T, Belyakov A, Kaibyshev R, Miura H, Jonas JJ (2014) Dynamic and post-dynamic recrystallization under hot, cold and severe plastic deformation conditions. Prog Mater Sci 60(1):130–207
5. Murr L, Niou C, Garcia E (1997) Comparison of jetting-related microstructures associated with hypervelocity impact crater formation in copper targets and copper shaped charges. Mater Sci Eng 222:118–132
6. Elshenawy T, Ming Q (2013) Breakup time of zirconium shaped charge jet. Wiley, New York, pp 703–708
7. Guo W, Li SK, Wang FC, Wang M (2009) Dynamic recrystallization of tungsten in a shaped charge liner. Scr Mater 60(5):329–332
8. Yang F, Li C, Cheng S, Wang L, Tian W (2010) Deformation behavior of explosive detonation in electroformed nickel liner of shaped charge with nano-sized grains. Trans Nonferrous Met Soc China 20(8):1397–1402
9. Murr LE, Shih HK, Niou CS (1994) Dynamic recrystallization in detonating tantalum shaped charges: a mechanism for extreme plastic deformation. Mater Charact 33(1):65–74
10. Guo W, Li SK, Wang FC, Wang M (2009) Dynamic recrystallization of tungsten in a shaped charge liner. Scr Mater 60(5):329–332
11. Zernow L, Lowry L (1992) High strain rate deformation of copper in shaped charge jets. In: Meyers MA, Murr LE (eds) Shockwave and high-strain-rate phenomena in materials. Springer, Berlin
12. E 112-96 (2009) Standard test methods for determining average grain size 1. ASTM International, vol. 96, Reapproved 2004
13. Wallis C, Buchmayr B (2019) Effect of heat treatments on microstructure and properties of CuCrZr produced by laser-powder bed fusion. Mater Sci Eng A 744:215–223
14. Olakanmi E, Cochrane R, Dalgamo K (2015) A review on selective laser sintering/melting (SLS/SLM) of aluminium alloy powders: processing, microstructure and properties. Prog Mater Sci 74:401–477
15. Murr LE, Esquivel EV (2004) Observations of common microstructural issues associated with dynamic deformation phenomena: twins, microbands, grain size effects, shear bands, and dynamic recrystallization. J Mater Sci 39(4):1153–1168
16. Guo W, Li SK, Wang FC, Wang M (2009) Dynamic recrystallization of tungsten in a shaped charge liner. Scr Mater 60(5):329–332
17. Von Holle W, Trimble J (1976) No title. Sixth international symposium on detonation, Colorado, San Diego, pp 691–699
18. Flis WJ (2018) On temperatures in shaped-charge jet penetration
19. Lassila DH, Walters WP, Nikkel DJ, Kershaw RP (1996) Analysis of OSoft "recovered Shaped charge jet particles. This paper was prepared for submittal to the symposium structures under extreme loading conditions at the 1996 American Society of Mechanical Engineers pressure vessels and piping conference
20. Racah E (1988) Shaped charge jet heating. Propellants Explos Pyrotech 13:176–182
21. Agu HO, Hameed A, Appleby-Thomas GJ (2018) Application of shell jetting analysis to determine the location of the virtual origin in shaped charges. Int J Impact Eng 122:175–181
22. Malcolm C (1997) "AUTODYN® jetting tutorial, 3rd revision. Century Dynamics, USA
23. Elshenawy T, Elbeih A, Klapötke TM (2017) A numerical method for the determination of the virtual origin point of shaped charge jets instead of using flash X-ray radiography. Taylor & Francis, London, pp 1–14
24. Walters W, Zukas JA (1989) Fundamental of shaped charges. Springer, New York
25. Heuzé O (2012) General form of the Mie–Grüneisen equation of state. Comptes Rendus Mec 340(10):679–687
26. Baoxiang R, Gang T, Peng W, Changxing D, Chunqiao P, Hongbo M (2018) Analysis of the formation mechanism of the slug and jet center hole of axisymmetric shaped charges. Results Phys 9:135–141
27. Zernow L (1997) The density deficit in stretching shaped charge jets. Int J Impact Eng 20:849–859
28. Walters WP, Jonas Z (1989) Fundamentals of shaped charges. Springer, New York

Appendix 3

Application of shell jetting analysis for determination of the virtual origin in shaped charges

International Journal of Impact Engineering 122 (2018) 175–181

Contents lists available at ScienceDirect

International Journal of Impact Engineering

journal homepage: www.elsevier.com/locate/ijimpeng

Application of shell jetting analysis to determine the location of the virtual origin in shaped charges

H.O. Agu*, A. Hameed, G.J. Appleby-Thomas

Centre for Defence Engineering, Cranfield University, Shrivenham SN6 8LA, United Kingdom

ARTICLE INFO

Keywords:
Virtual origin
Cumulative jet mass
Jet velocity
Jetting analysis
Numerical simulation

ABSTRACT

Shaped charges are designed to produce high-velocity jets for penetration. During jet formation, the liner collapses and converges at a point source, also known as the virtual origin (VO), along the distance–time plane. The location of the VO must be known to allow the development of penetration analytical models. Here we determined the location of the VO using the ANSYS® Autodyn 2D shaped charge jetting technique. Jetting analysis was conducted for two shaped charges of 18 and 32 mm diameter. The explosive and casing were represented by Eulerian two-dimensional finite difference grids, whereas the liner was modelled using a shell formulation. The summary/history of the jetting analysis was used to determine the VO position in the shaped charges. Interpolating the point of intersection on the liner between the jet velocity (U-Jet) and the cumulative jet mass revealed the location of the VO at a distance equivalent to approximately two-thirds of the inner cone diameter of the shaped charges, in agreement with earlier studies based on different methods. Validation of this technique using the DiPersio, Simon and Merendino (DSM) model based on the Allison-Vitalli equation also showed good agreement with the numerical results.

1. Introduction

Shaped charges are used extensively against armoured vehicles and structures. Enhancing the performance of shaped charges by optimizing their parameters in experimental trials is expensive, so analytical formulae have been developed to predict their performance. DiPersio and Simon' [1] introduced explicit formulae taking into account the concept of a virtual origin (VO) [2] as proposed by Allison and Bryan [3] and developed by Allison and Vitalli [4] for continuous and particulate jets with a non-uniform jet velocity distribution [5]. In particular, given target density (ρ_t) and jet density (ρ_j), jet tip velocity (V_0), and cut-off velocity (V_c), DiPersio and Simon [1] applied Eqs. (1)–(3) to calculate the depth of penetration before, during, and after jet breakup [6,7].

Eq. (1) is used when the jet breaks before penetration:

$$\boldsymbol{P} = \boldsymbol{Z}_0\left[\left(\frac{V_0}{V_c}\right)^{1/\gamma} - \mathbf{1}\right] \text{ for } \mathbf{0} \le \boldsymbol{Z}_0 < \boldsymbol{V}_c\ \boldsymbol{t_b}\left(\frac{V_c}{V_0}\right)^{\mathbf{1}/\boldsymbol{\gamma}} \tag{1}$$

Eq. (2) is used when the jet breaks during penetration:

$$\boldsymbol{P} = \frac{(\mathbf{1}+\boldsymbol{\gamma})(V_0\ \boldsymbol{t_b})^{\frac{1}{(1+\gamma)}}\boldsymbol{Z_0}^{\frac{y}{1+y}-V_c\ t_b}}{\gamma} - \boldsymbol{Z_0} \text{ for } \boldsymbol{V_c}\ \boldsymbol{t_b}\left(\frac{V_c}{V_0}\right)^{1/\gamma} \le \boldsymbol{Z_0} < \boldsymbol{V_0}\ \boldsymbol{t_b} \tag{2}$$

Finally, Eq. (3) is used when the jet breaks before reaching the target:

$$\boldsymbol{P} = \left(\frac{(\boldsymbol{V_0} - \boldsymbol{V_c})}{\boldsymbol{\gamma}}\right)\boldsymbol{t_b} \text{ for } \boldsymbol{V_0}\ \boldsymbol{t_b} \le \boldsymbol{Z_0} < \infty \tag{3}$$

Although these formulae agree reasonably well with experimental results [8], one of their limitations is the *a priori* determination of Z_o, which is effectively the distance between the VO and the target surface b [9], also known as the effective jet length (Eq. (4)).

$$Z_o = VO - b \tag{4}$$

One of the methods established to locate the VO is the back-projection of the jet particles by X-ray radiography [10]. Although accurate, this technique is very expensive and requires specialised equipment such as an X-ray source, coolers, capacitors and isolated fibre optics. Even so, such techniques have been used to determine the VO of shaped charges [11]. For example, the VO for a large (150-mm calibre) shaped charge was located at a distance from the liner base equivalent to 64% of the charge diameter [12]. Several qualitative estimates have also been used for the computation of penetration depths, e.g. by assuming the VO is located about one-third of the distance from the apex to the base of the cone [12] or by estimating the position of the VO based on past experience (rule of thumb) as three-quarters of the liner height [13]. Also, Held [14] found that the VO was located at a distance of about two-thirds of the internal diameter of the liner. In a recent study, the back-projection technique was applied numerically using the

* Corresponding author.
E-mail address: henry.agu@cranfield.ac.uk (H.O. Agu).

https://doi.org/10.1016/j.ijimpeng.2018.04.014
Received 7 November 2017; Received in revised form 20 April 2018; Accepted 29 April 2018
Available online 25 July 2018
0734-743X/

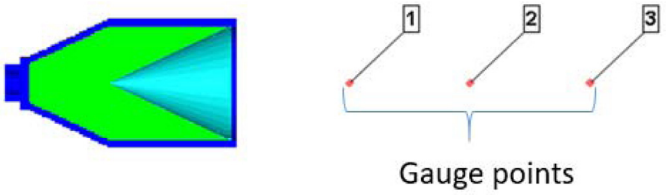

Fig. 1. Gauge points at 1, 2 and 3 cone diameters.

Euler solver method in ANSYS® Autodyn 2D to determine the locations of both the jet tip and the stagnation point at different times [11]. This technique requires the back-projection of the jet to be calculated at a defined time during jet motion.

Here, we developed a simple Lagrangian coordinate technique as postulated by Carleone and Chou [15] to map the position of the jet element on the liner, and thus to pinpoint the VO of shaped charges. By obtaining shaped charge parameters such as the cumulative jet mass and U-Jet (jet velocity) from a standard shell jetting analysis, the point where the jet velocity just overcomes the cumulative jet mass was marked as the VO, and this was related back to the exact position on the charge. A mesh sensitivity study was carried out first to determine the effect of mesh size and the density of shaped charges before the technique was tested on the 18-mm and 32-mm shaped charges.

2. Mesh sensitivity study

The ability of ANSYS® Autodyn 2D to simulate shaped charges has been verified in several studies [16,17], particularly the representation of jet velocity as a function of cumulative jet mass. A mesh sensitivity study was conducted with four uniform square mesh sizes of 0.2, 0.3, 0.5 and 0.7 mm to determine the effect of mesh size on jet tip velocity, penetration depth and the cumulative jet mass via a standard jetting analysis. A 32-mm shaped charge with a 1.2-mm OFHC copper liner at a half-cone angle of 26.84° was tested, incorporating a C4 explosive charge with a 2-mm thick aluminium 7039 casing. Material models for the OFHC copper liner and aluminium casing were taken from the Autodyn standard library whereas the inbuilt Jones-Wilkins-Lee equation of state was applied for the C4 explosive.

3. Effect of mesh size on jet tip velocity

The explosive, liner and casing were modelled in a Euler sub-grid. Nodal monitoring points (velocity gauges) were placed at intervals of 1–3 cone diameters (CDs) to obtain the jet velocity (Fig. 1).

The result of the simulations is summarized in Fig. 2, which clearly shows that the coarse mesh size (0.7 × 0.7 mm) produced the lowest jet tip velocity of 4.11 km/s, compared to a velocity of 5.9 km/s produced by the finest mesh size (0.2 × 0.2 mm). A gradual decrease in the tip velocity was observed for all mesh sizes, in agreement with experimental results described by Walters and Zukas [2]. The finest mesh size produced the most accurate result but required nearly three times longer than the 0.3 × 0.3 mm mesh to complete the simulation, and the difference between them in terms of the jet tip velocity was only 0.36 km/s (5.9%). The 0.3 × 0.3 mm mesh size was therefore selected for all simulations because the computational cost of the finer mesh was not justified by the diminishing returns in terms of accuracy.

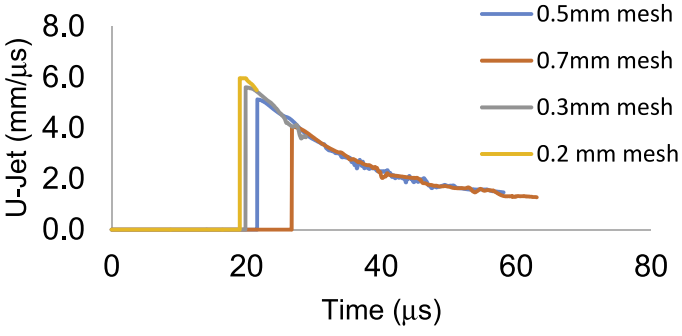

Fig. 2. The velocity–time histories for the jet at the gauge points for different mesh sizes.

4. Effect of mesh size on penetration depth

The jet formed from the Euler sub-grid was remapped for penetration into 1006 steel with a standard fixed mesh size of 0.5 × 0.5 mm producing results that compared favourably with previous experiments [8]. The simulation was allowed to run until the jet was eroded in the target. The penetration depths for the different mesh sizes are summarised in Table 1. The finest mesh size achieved the greatest penetration depth, reflecting the higher tip velocity.

A non-linear trend in mesh size and penetration depth was apparent, with increasing convergence as the mesh size was reduced. This is shown in Fig. 3, which plots the key numerical data from Table 1.

Fig. 3 clearly reveals a polynomial relationship between the calculated penetration depths and the mesh size. Extrapolating the corresponding best-fit curve to a theoretical mesh size of 0 mm provides a corresponding penetration depth of 160.75 mm. This suggests that, given a mesh size of 0.2 mm, the error in the calculated shaped charge performance is only ~12%. A further reduction in mesh size would therefore increase the accuracy, but the advantage would be minimal. Table 1 indicates that more time is required to run simulations with smaller mesh sizes, as highlighted in Fig. 4. Essentially, an additional 19 h was required to run the model using a 0.2 × 0.2 mm mesh rather than a 0.3 × 0.3 mm mesh with only a 3.54% increase in accuracy (relative to the nominal 0-mm mesh size baseline depth of 160.75 mm). The computational cost of simulations with mesh sizes of less than 0.3 × 0.3 mm is again unjustifiable given the diminishing returns, and the 0.3 × 0.3 mm mesh size was selected.

5. Mesh sensitivity for standard jetting analysis

Shaped charge jetting analysis is based on the use of continuum mechanics to estimate the non-uniform collapse velocity [19], and is applied to calculate other jetting parameters based on the Pugh, Eichelberger and Rostoker (PER) theory [20]. In the jetting setup, the

Table 1
The effect of mesh size on penetration depth.

Mesh size (mm)	0.2	0.3	0.5	0.7
Penetration depth (mm)	141	136	116	90
Time required (h)	32	13	5	2

The time required is based on a computer with an Intel® Core™ i7-6700HQ processor CPU at 2.6 GHz or 2592 MHz.

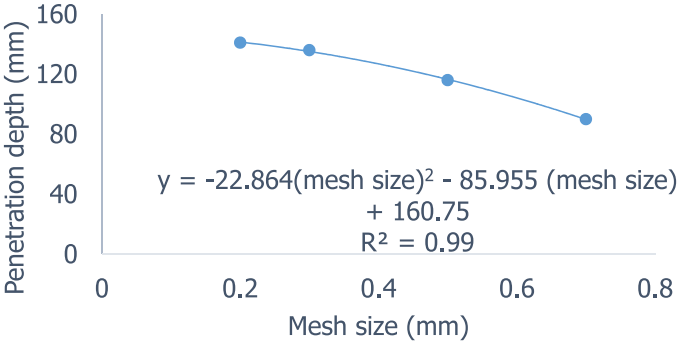

Fig. 3. Variation of penetration depth with mesh size.

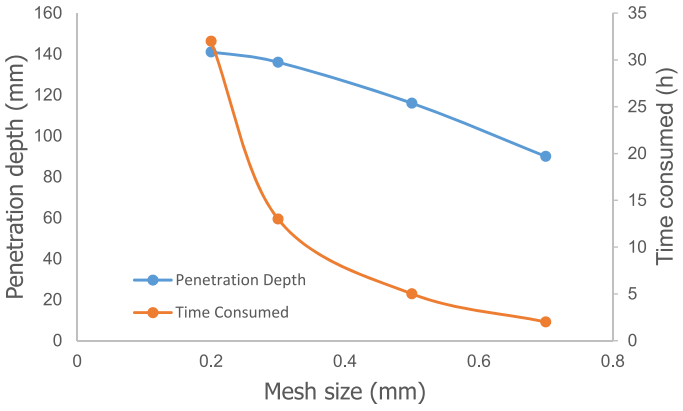

Fig. 4. Penetration depth and computation time for various mesh sizes.

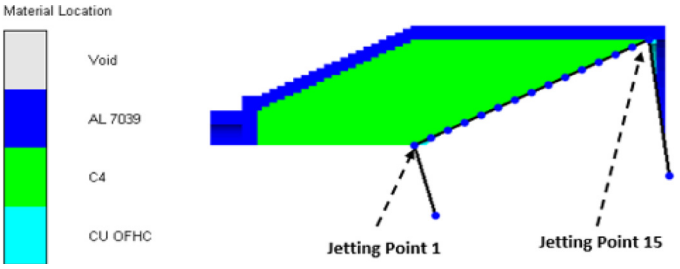

Fig. 5. Jetting points on the shell copper liner.

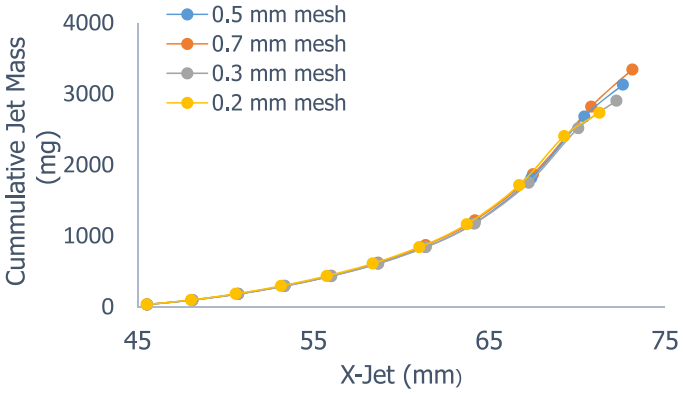

Fig. 6. Mesh sensitivity study for standard jetting analysis.

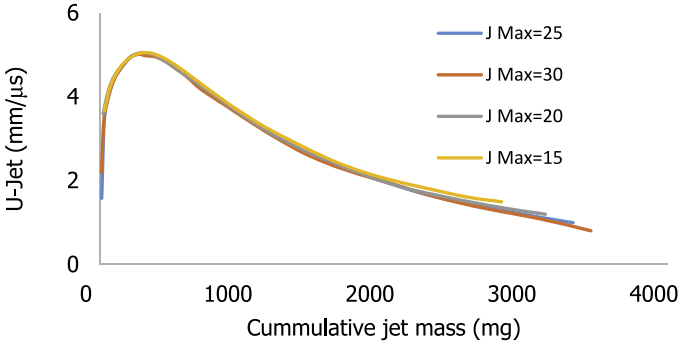

Fig. 7. Relationship between jet velocity and cumulative jet mass according to the number of nodes.

explosive is modelled in the Euler sub-grid whereas the liner is modelled in the shell formulation with the generation of jetting points, as shown in Fig. 5.

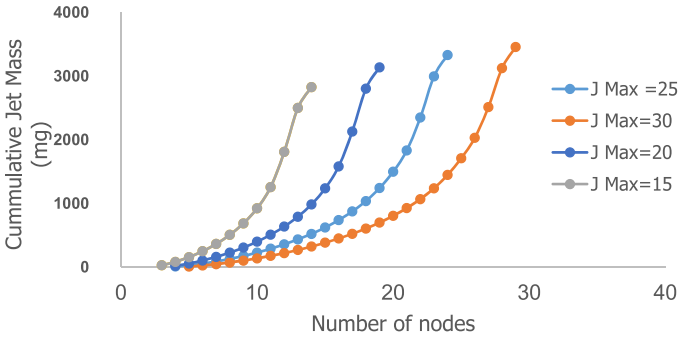

Fig. 8. Relationship between cumulative jet mass according to the number of nodes.

Jetting calculations were conducted for four mesh sizes: 0.2, 0.3, 0.5 and 0.7 mm. The detonation wave travelled along the liner surface with a decreasing collapse velocity from the apex to the base, with more liner material forming the jet. A summary of the jetting analysis, in which the cumulative jet mass is plotted against the axial x position (X-jet) for all four mesh sizes, is provided in Fig. 6. The relationship between the cumulative jet mass and the X-jet for all mesh sizes was similar, bearing the same shape at the beginning, up to a nominal coordinate distance of 55 mm. Beyond this point, variations in the curve were observed with a general convergence of the solution towards the 70 mm position for a mesh size of 0.3 mm x 0.3 mm. The accuracy and computational time of the 0.3 mm square mesh makes it suitable for the simulation and it was therefore used for the entire jetting analysis.

6. Effect of varying the number of nodes on the cumulative jet mass

Because this technique involves locating the VO using shell jetting analysis, it is necessary to investigate the effect of varying the number of nodal points on the U-Jet and cumulative jet mass. Four jetting calculations were conducted with similar charge configurations but a different number of nodes (J Max): 10, 15, 20 and 25. The effect of node variations on the U-Jet and cumulative jet masses are plotted in Figs. 7 and 8, respectively. From the jetting calculation, the maximum jet velocity remains the same in all four jetting calculations but the cumulative jet mass increases as the number of nodal points increases. This is because more liner material is added in the calculation, as shown in Fig. 8.

7. Method to determine the VO position

This technique applies a single Lagrangian coordinate to relate the position of the jet element back to its original position on the liner. The technique was first developed by Chou and Flis [21] and applied by Carleone and Chou [15] to calculate the strain, jet length and jet radius. The axial liner position is described by coordinate x whereas the position of the jet is given by coordinate ξ (Eq. (5)):

$$\xi(x,\ t) = Z(x) + (t - t_o)V_j\ (x) \tag{5}$$

where t_o is the time at which the liner element first arrives at the axis, $Z(x)$ is the location of the formation, and $V_j(x)$ is the jet velocity, which is a function of the liner position and time. The relationship is shown in Fig. 9.

Eq. (5) can be rearranged to derive Eq. (6):

$$Z(x) = \xi(x,\ t) - (t - t_o)V_j\ (x) \tag{6}$$

Applying the inverse velocity gradient based on the conservation of momentum, with respect to x when x is the VO, yields Eq. (7):

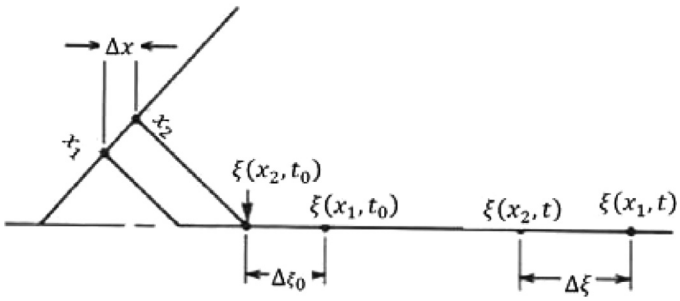

Fig. 9. Relationship between the liner coordinate x and the jet coordinate ξ [15].

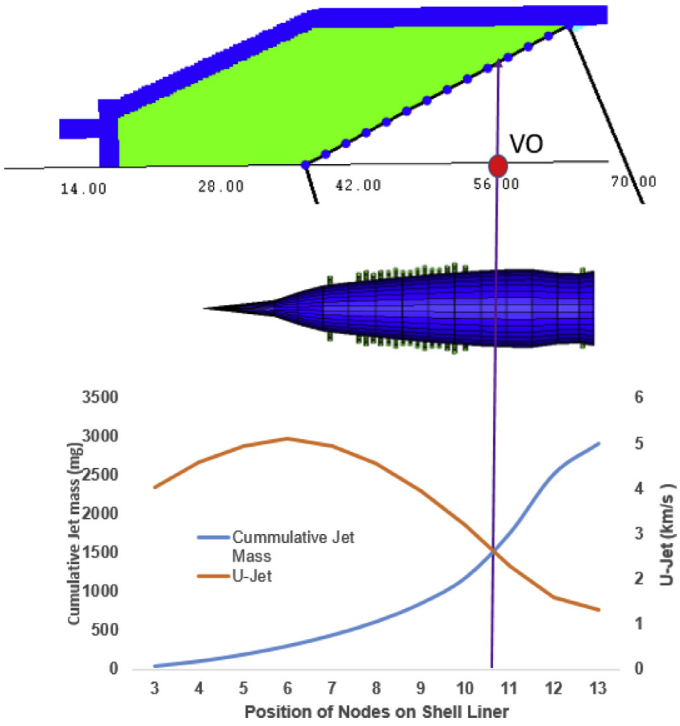

Fig. 10. Determination of the VO for the 32-mm shaped charge.

$$V_j(x) = V_j(VO) = \frac{\int_0^{X_{VO}} V_j\,(dm_j/dX)dX}{\int_0^{X_{VO}} V_j\,(dm_j/dX)dX} \tag{7}$$

By integrating the mass piled up along the jet velocity of the jet particles, a one-dimensional jet is observed when the U-Jet just overcomes the cumulative mass effect created by the pilling up. The point that the jet begins to protrude from the collapse matrix is the VO and this is shown in Fig. 10 as the intercept point between the U-Jet and cumulative jet mass. An example of the technique was applied to 18-mm and 32-mm shaped charges with C4 explosive in a 2-mm thick aluminium 7039 casing. Copper (OFHC) liners of constant thickness (0.5 and 1.2 mm) were used for the 18-mm and 32-mm shaped charges, respectively, with a half cone angle of 26.5° in both cases. Point initiation at the rear of the charge was assumed. The output jetting data, comprising the U-Jet, cumulative jet mass and nodal points/jetting points, were then extracted and reduced for subsequent analysis.

8. Results and discussion

The liner collapse data revealed that the amount of liner mass entering the jet increases towards the base of the liner while the jet

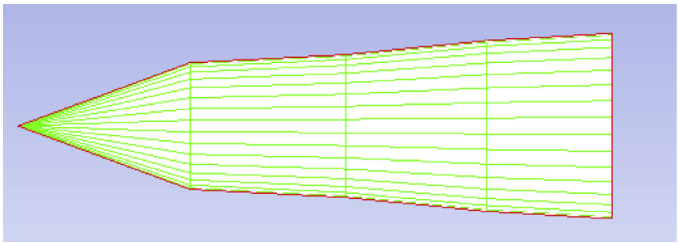

Fig. 11. Distorted liner collapse resulting from a low number of nodes (J Max = 5).

velocity (U-Jet) declines. The point at which the U-Jet intercepts the cummulative jet mass lies between the tenth and eleventh nodes on the 32-mm charge. To obtain this position on the *x*–*y* plane, the jetting points were numbered in ascending order and the position (between the tenth and eleventh nodes) was interpolated on the charge as shown in Fig. 10.

The VO was found to be at the 61.00 mm mark, which is 24.13 mm from the cone apex and 7 mm from the charge base. This position is 75.86% of the liner height (about three-quarters of the liner height from the conical apex and about one-quarter from the base), which is also two-thirds of the shaped charge liner base diameter. The same technique was applied to the 18-mm shaped charge and the VO appeared to flow in the same way. Our results were in agreement with the VO position reported by Held [14] who located the VO at about two-thirds of the inside diameter of the liner, and also DiPersio et al. [13] who located the VO at a distance equivalent to about three-quarters of the liner height from the cone apex.

9. Verification of the technique

To confirm the suitability of this technique, an experimental study is ideal but prohibitively expensive as stated earlier. Instead, verification can be achieved via other methods, one of which involves investigating

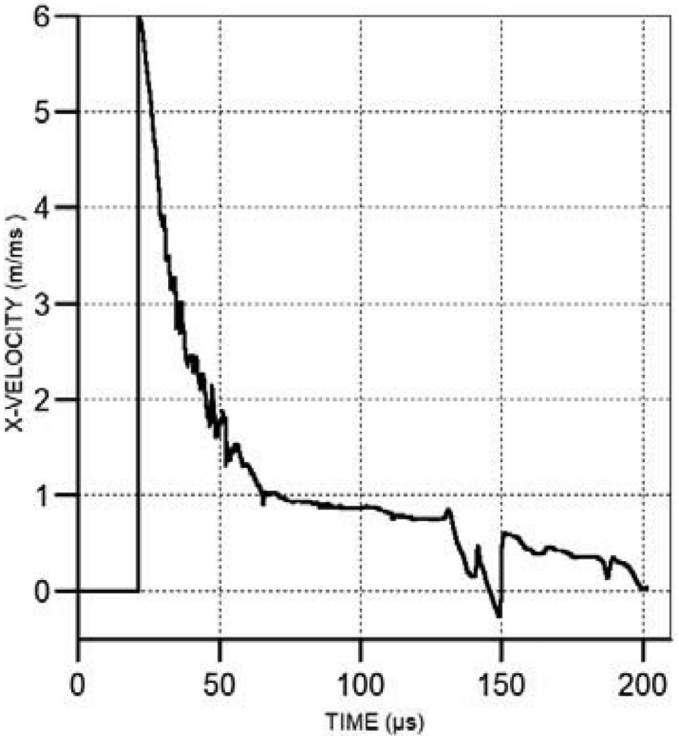

Fig. 12. Jet velocity recorded at 2CD for a 32-mm shaped charge (without tip correction).

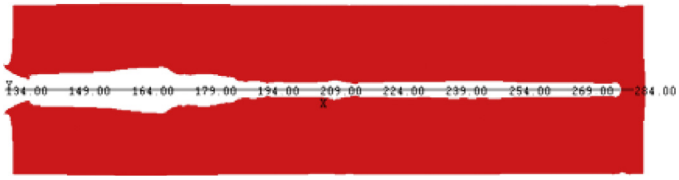

Fig. 13. The depth of penetration for 32-mm shaped charges was 141 mm.

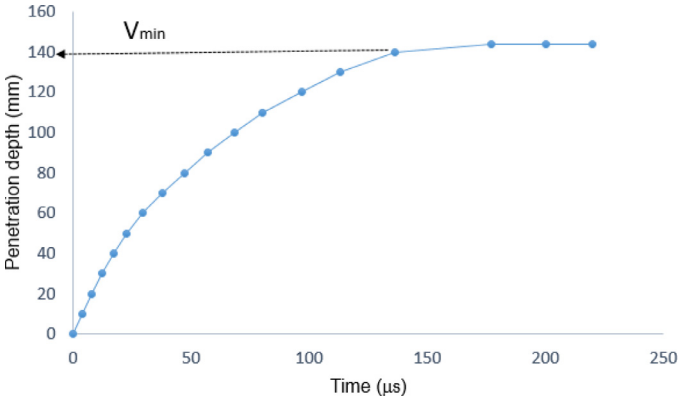

Fig. 14. Jet penetration–time history for the 32-mm shaped charge.

the effect of the number of nodes on the VO position. Four additional jetting calculations were conducted, with 5, 10, 14 and 20 nodes on the shell liner. As the number of nodes increased, we observed issues associated with tangled polygons and these were deleted from the simulations. Analysis of the results showed that when the maximum number of nodes is low (e.g. J Max = 5), the jet formation is distorted as shown in Fig. 11, pushing the VO position towards the apex (55% from the charge base). The effect of VO position on J Max is summarized in Appendix 1. A decrease in the proposed VO position was observed for an increase in the number of nodes. At higher values of J Max, the distance between the charge base and the VO decreased to the point at which a further increase in the number of nodes gave no change in the VO position. This point was regarded as the true VO location.

10. Verification of the VO position

The technique was also verified by computing the penetration depth of the effective and traditional stand-off distance using the DSM formula described in Eqs. (1)–(3). The jet tip velocity was determined at two cone diameters (2CD) with a nodal monitoring point/gauge as shown in Fig. 12. By applying the jet tip correction, when the U-Jet was plotted against the cumulative jet mass, the modified jet velocity was 5.096 km/s.

The depth of penetration was determined numerically using Autodyn 2D. The explosive, liner and casing were modelled in the Euler sub-grid whereas the target was modelled with the Langregian sub-grid. The jet from the Euler solver was remapped to the Langregian solver for penetration into 1006 steel until the jet element was completely eroded. Fig. 13 shows the depth of penetration for the 32-mm shaped charge.

According to Hirsch [22], the penetration of an ideal jet into steel becomes mostly ineffective below ~1.8 km/s, when the rate of target penetration becomes less than half the jet velocity. However, deviations from perfect symmetry and jet particulation accounts for the loss of penetration efficiency below 3 km/s. The cut-off velocities were determined from the penetration–time history (Fig. 14) of the shaped charge jet as described by Held [18,23].

Having satisfied the conditions for a continuous jet, Eq. (1) was applied. The parameters used to determine the penetration depth are in Table 2.

The depth of penetration for the numerical simulations and analytical equations using the derived and traditional SOD are summarized in Table 3. Higher penetration depths were observed for the effective SOD compared to the numerical simulations. The proposed VO technique shows only a 4.5% difference in penetration depth from the numerical simulation whereas the traditional SOD underestimates the VO by 5.6% compared to the numerical simulation. The ability of this technique to determine the location of the VO as well the improved predictions compared to the traditional SOD makes it valid for specifying the position of the VO.

11. Conclusion

In conclusion, we carried out a series of numerical simulations to investigate the ability of ANSYS® Autodyn 2D to predict the VO of shaped charges. The technique applies a simple Lagrangian coordinate for relating the position of the jet element on the liner. We found that:

a. Ignoring the distance between the charge base and the VO underestimates the depth of penetration.
b. The VO position can be reasonably estimated by shaped charge jetting analysis using ANSYS® Autodyn 2D.
c. The jet tip velocity remains the same irrespective of the number of

Table 2
Parameters used to determine the depth of penetration. SOD = stand-off distance.

V tip (m/s) corrected	*~$V_{(min)}$ (m/s)*	*SOD (mm)*	*Effective SOD (mm)*	*Solid jet density (g/cm^3)*	*Target density (g/cm^3)*	$y = \sqrt{\rho_t/\rho_j}$
5096	1787	64.00	71.00	8.96	7.85	0.93

Table 3
Comparison of the depth of penetration (DOP) determined by numerical simulations, SOD and derived SOD positions.

Numerical simulation at 0.3 mm mesh (mm	Using the traditional SOD (mm)	Using the Effective SOD (mm)	Difference in DOP between traditional SOD and numerical simulation.	Difference in DOP between effective SOD and numerical simulation.	Difference in DOP between traditional SOD and Effective SOP
141.00	133.43	148.02	7.67 (~5.4%)	6.92 (~4.5%)	14.59 mm

nodes or J Max in the shell jetting analysis.
d. When the number of nodes is low, the jet formation is distorted therefore moving the VO towards the apex.
e. The depth of penetration estimated using the derived VO deviates by only 4.5% from the numerical simulation, while the traditional SOD results in a 5.6% deviation.
f. The proposed technique agrees well with earlier works [12,13].

Acknowledgement

The authors wish to appreciate, Dr Tamer Elshenawy and Dr David Wood for their support.

Supplementary materials

Supplementary material associated with this article can be found, in the online version, at doi:10.1016/j.ijimpeng.2018.04.014.

Appendix 1. Effect of the number of nodes on the VO

J max = 5 nodes

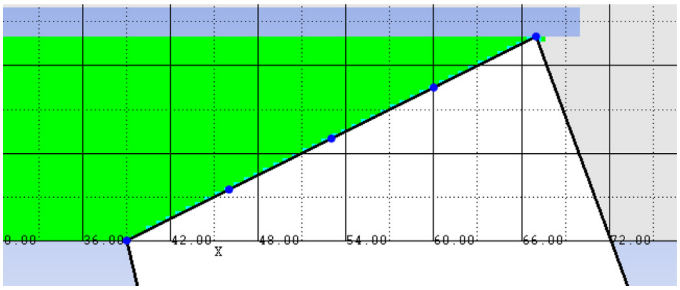

Intercept position = between the 2nd and 3rd node.
Interpolated on the liner = 52 mm
68 - 52 = 16 mm from the charge base.
VO = 55.17% from the charge base.

J max = 10 nodes

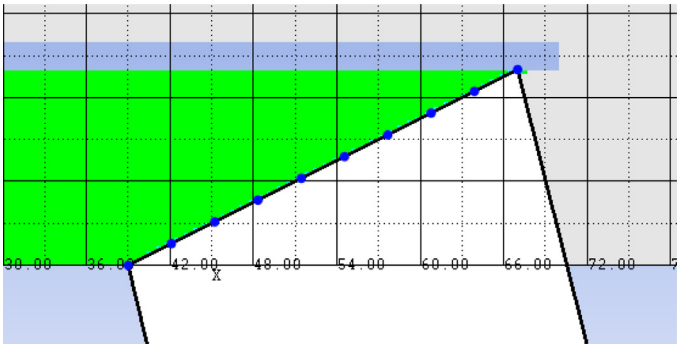

Intercept Position = 7th node
Interpolated on the liner = 58 mm
68–58 = 10 mm
VO = 34.48% of the cone height from the base

J max = 14 nodes

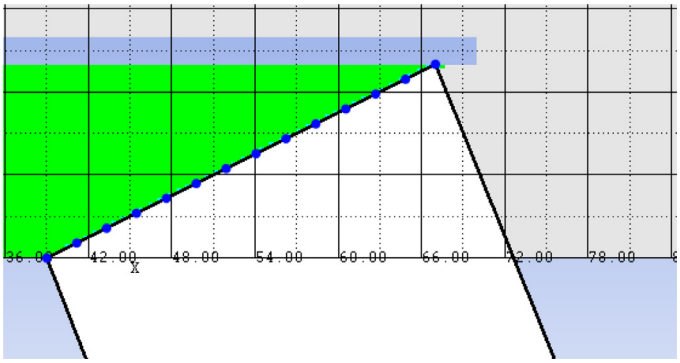

Intercept Position = 11th node,
Interpolated on the liner = 60 mm
68–60 = 8 mm from the charge base

VO = 27.58% from the charge base
J max = 20 nodes

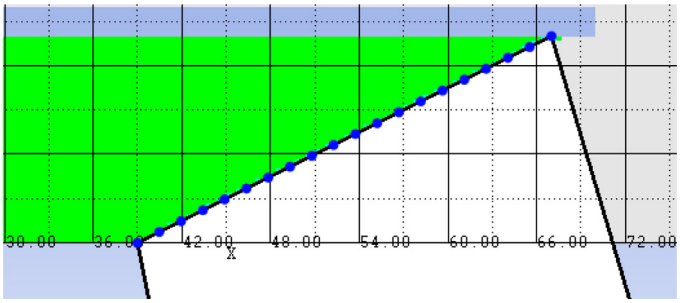

Intercept position = between the 15th and 16th node.
When Interpolated on the liner = 61 mm
68–61 = 7 mm from the charge base.
VO = 24.13% from the charge base.

References

[1] DiPersio J, Simon R. The penetration standoff relation for idealized shaped charge jets. Report No 1313. Ballistic Research Laboratory, Aberdeen Proving Ground, Maryland, USA, 1964.
[2] Walters WP, Zukas J. Fundamentals of shaped charges. New York, New York, USA: John Wiley & Sons; 1989. p. 179.
[3] Allison F, Brian GM. Cratering by a train of hypervelocity fragment. Proc Second Hypervelocity Impact Symp 1957;1:81.
[4] Allison FE, Vitali R. A new method of computing penetration variables for shaped charge jets. Report No 1184. Ballistic Research Laboratory, Aberdeen Proving Ground, Maryland, USA, 1963.
[5] Abrahamson GR, Goodier JN. Penetration by shaped charge jets of non-uniform velocity. J Appl Phys 1963;1:195–9.
[6] Dipersio R, Simon J, Merendino B. Penetration of shaped-charge jets into metallic targets. Report No 1296. Ballistic Research Laboratory, Aberdeen Proving Ground, Maryland, USA, 1965.
[7] Chou PC, Hirsch E, Walters WP. The virtual origin approximation of shaped charge jets. Proceedings of the sixth international symposium on ballistics. 1981.
[8] Elshenawy T, Elbeih A, Li QM. Influences of target strength on the penetration depth of shaped charges into RHA target. Int J Mech Sci 2018;136:234–42.
[9] Shear RE, Brundick FS, Harrison JT. A link between shaped charge performance and design. Aberdeen Proving Ground, Maryland, Technical Report ARBRL-TR-02361, USA, 1981.
[10] Robinson AC. SCAP – a shaped charge analysis program-user's manual. Sandia National Labs Report SAND85-0708, Albuquerque, New Mexico, USA, 1985.
[11] Elshenawy T, Elbeih A, Klapötke TM. A numerical method for the determination of the virtual origin point of shaped charge jets instead of using flash x-ray radiography. J Energ Mat 2018;16:127–40.
[12] Held M. Penetration cut-off velocities of shaped charge jets. Prop Expl Pyro 1987;13:111–9.
[13] DiPersio R; Simon J, Merendino B. Characteristics of jet from small calibre shaped charges with copper and aluminium liners. Report No 1866. Ballistic Research Laboratory, Aberdeen Proving Ground, Maryland, 1967.
[14] Held M. Hydrodynamic theory of shaped charge jet penetration. J Expl Prop (Taiwan) 1991;7:9–24.
[15] Carleone J, Chou PC. A one-dimensional theory to predict the strain and radius of shaped charge jets. Proceedings of the first international symposium on ballistics. Florida, USA: Orlando; 1974.
[16] Cheng W, Wen LX, Chung kim S. Penetration of shaped charge into layered and spaced concrete targets. Int J Impact Eng 2018;112:193–206.
[17] Pugh EM, Eichelberger RJ, Rostoker N. Theory of jet formation by charges with lined conical cavities. J Appl Phys 1952;23:532–6.
[18] Held M. Assessment of measurement of the cratering velocities of shaped charge jet. Int J Impact Eng 1997;20:349–61.
[19] Hayhurst CJ, Clegg RA, Livingstone IH, Francis NJ. The application of SPH techniques in Autodyn 2-D to ballistic impact problems. Proceedings of the 16th international symposium on ballistics. 1996.
[20] Century Dynamics Incorporated, AUTODYN® Explicit Software for Nonlinear Dynamics. Jetting tutorial revision v4.3, 2005.
[21] Chou PC, Flis WJ. Recent developments in shaped charge technology. Prop Expl Pyrotech 1986;11:99–114.
[22] Hirsch E. The penetration cut-off velocity of ideal jets. Rafael Ballistics Center, Haifa, Israel.
[23] Held M. Penetration of shaped charges in concrete and in sand in comparison to steel target. J Expl Prop (Taiwan) 1992;8:1–15.

Appendix 4

Liner design employed in Chapter 5 for the production of PLA and copper-fill Liners.

a. 1.5 mm liner thickness

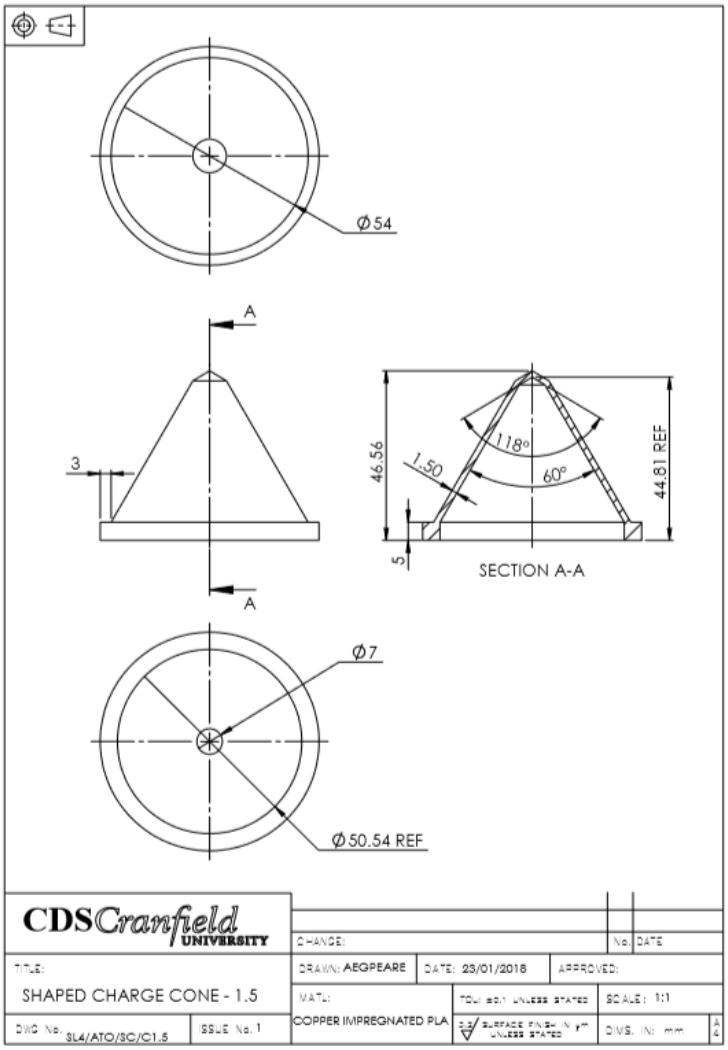

b. 3.5 mm liner diameter

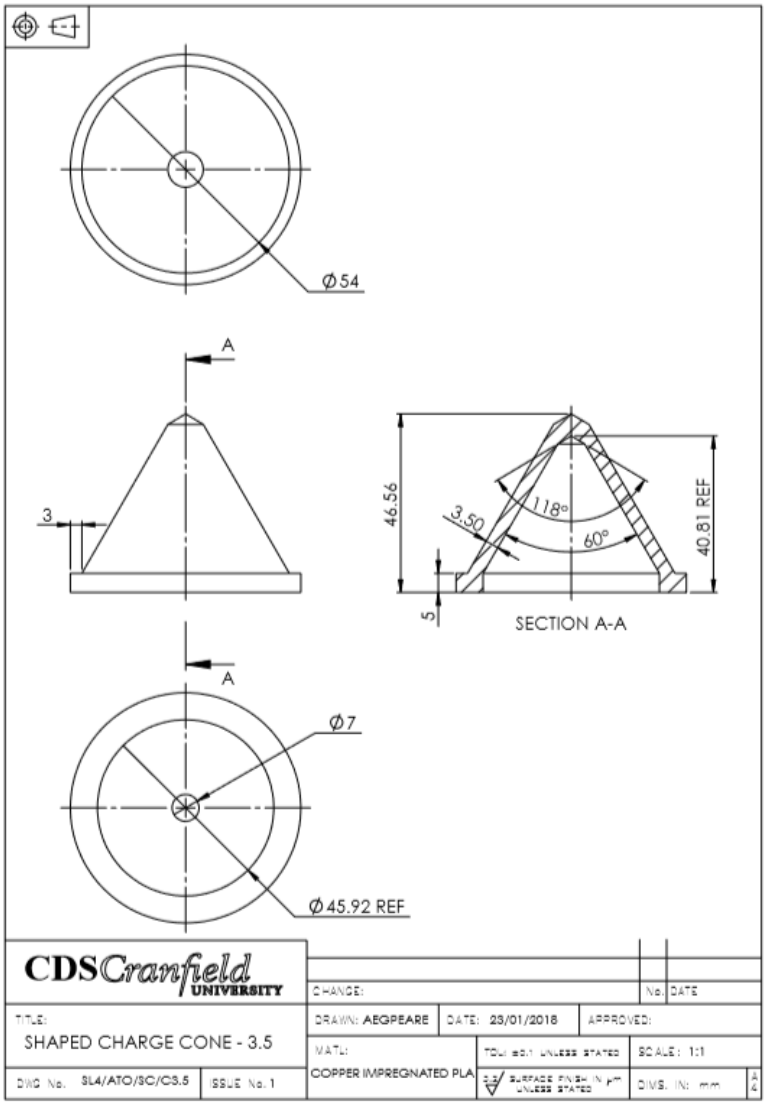

c. 5.5 mm Liner thickness

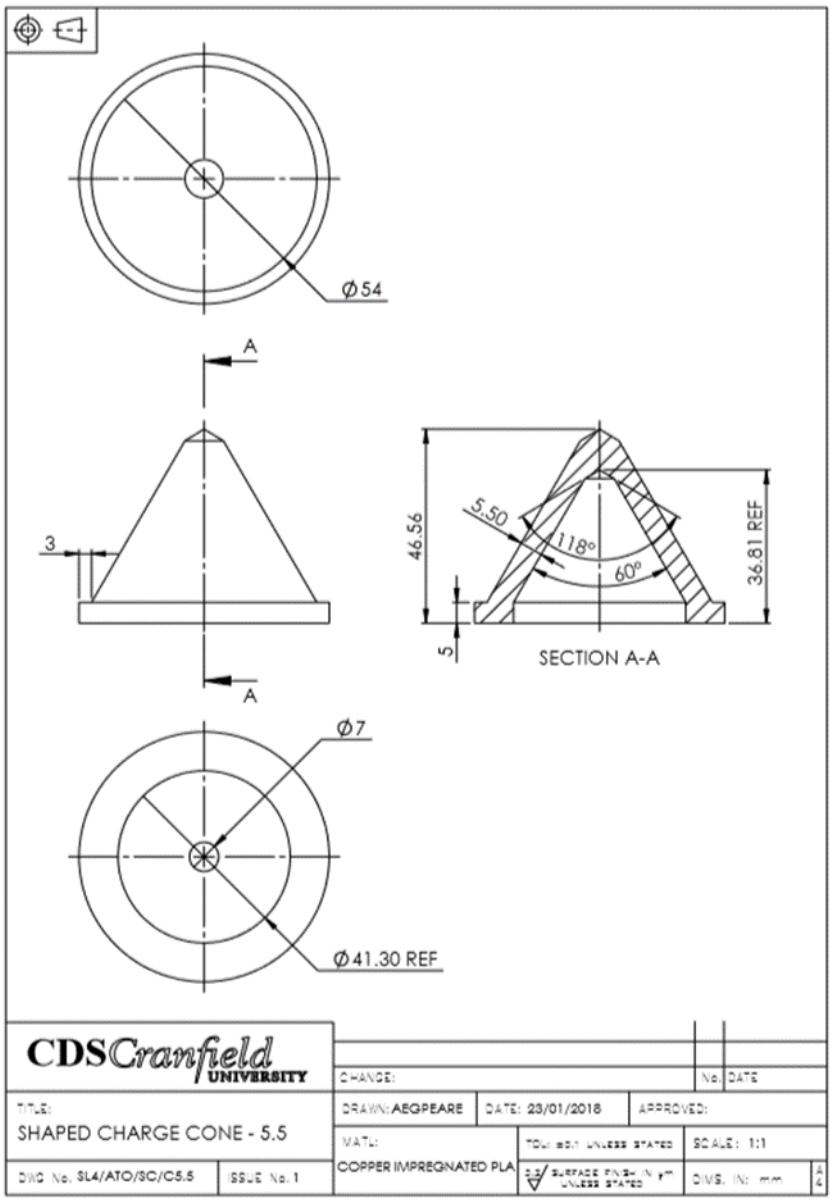

d. 7.5 mm liner thickness